Maastricht University

Multi-scale modeling and variability in cardiac cellular electrophysiology

Citation for published version (APA):

Clerx, M. P. É. (2017). *Multi-scale modeling and variability in cardiac cellular electrophysiology*. [Doctoral Thesis, Maastricht University]. Maastricht University. https://doi.org/10.26481/dis.20170420mc

Document status and date:
Published: 01/01/2017

DOI:
10.26481/dis.20170420mc

Document Version:
Publisher's PDF, also known as Version of record

Please check the document version of this publication:

• A submitted manuscript is the version of the article upon submission and before peer-review. There can be important differences between the submitted version and the official published version of record. People interested in the research are advised to contact the author for the final version of the publication, or visit the DOI to the publisher's website.
• The final author version and the galley proof are versions of the publication after peer review.
• The final published version features the final layout of the paper including the volume, issue and page numbers.

Link to publication

General rights
Copyright and moral rights for the publications made accessible in the public portal are retained by the authors and/or other copyright owners and it is a condition of accessing publications that users recognise and abide by the legal requirements associated with these rights.

• Users may download and print one copy of any publication from the public portal for the purpose of private study or research.
• You may not further distribute the material or use it for any profit-making activity or commercial gain
• You may freely distribute the URL identifying the publication in the public portal.

If the publication is distributed under the terms of Article 25fa of the Dutch Copyright Act, indicated by the “Taverne” license above, please follow below link for the End User Agreement:

www.umlib.nl/taverne-license

Take down policy
If you believe that this document breaches copyright please contact us at:

repository@maastrichtuniversity.nl

providing details and we will investigate your claim.

Download date: 20 Apr. 2024

Multi-Scale Modeling and Variability in Cardiac Cellular Electrophysiology

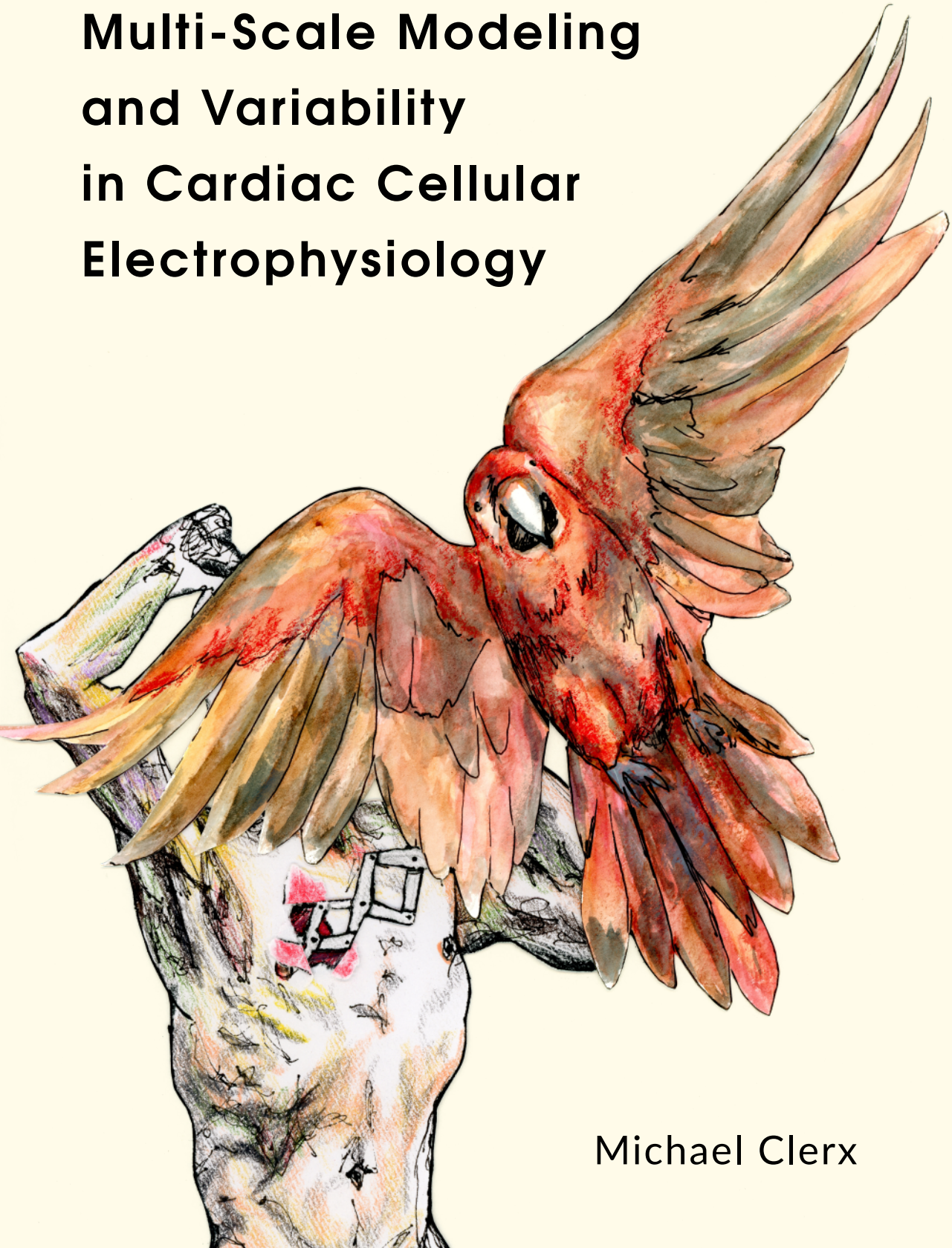

Michael Clerx

Multi-Scale Modeling and Variability in Cardiac Cellular Electrophysiology

DISSERTATION

to obtain the degree of Doctor
at Maastricht University,
on the authority of the Rector Magnificus,
Prof. dr. Rianne M. Letschert,
in accordance with the decision of the Board of Deans,
to be defended in public
on Thursday April 20th 2017, at 16:00

by

Michael Peter Éamon Clerx

Supervisors:
Prof. dr. ir. R.L.M. Peeters
Prof. dr. P.G.A. Volders

Co-supervisor:
Dr. P. Collins

Assessment Committee:
Prof. dr. T. Delhaas (*voorzitter*)
Prof. dr. H. Abriel (University of Bern)
Prof. dr. B. Rodríguez (University of Oxford)
Prof. dr. F. Thuijsman
Prof. dr. A. Zaza (Università degli Studi di Milano-Bicocca)

The research in this thesis was supported in part by the Transnational University Limburg (tUL), and by The Netherlands CardioVascular Research Initiative, CVON PREDICT. Financial support by the Dutch Heart Foundation for the publication of this thesis is gratefully acknowledged.

© Michael Clerx, 2017
ISBN 978-94-6295-626-1

Cover art and design © Debbie Young, 2017

Contents

1 Introduction **7**

2 Bioelectricity in the human heart **11**

3 Myokit: A simple interface to cardiac cellular electrophysiology **31**

4 Reducing simulation times with splines **61**

5 Variability in the dynamical properties of human cardiac I_{Na} **75**

6 Predicting changes to I_{Na} from missense mutations in *SCN5A* **107**

7 Using whole-ventricle simulations for regularization in ECGI **137**

8 Discussion **157**

A Summary **177**

B Valorization **181**

C Acknowledgments **185**

D Curriculum vitae and publications **189**

The workings of the heart

Normal cardiac electrophysiology represents the complex interplay among multiple, often redundant, components – Dan M. Roden (2010).

Diseases [...] represent emergent properties at the scale of the organism that result from dynamic interactions between multiple constantly changing molecular factors – James N. Weiss et al. (2015).

The role of modeling

A model is something simple made by a scientist to help him understand something complicated – Richard FitzHugh (1969).

The joy of experiments

Even though the extent of my ignorance and confusion was more clearly revealed, I was very pleased by the direct records of the amplitude and currents – Kenneth S. Cole (1968), about performing the first ever voltage clamp experiments.

and the impact of a novel concept

It is easy to fail to think of an idea that with hindsight seems very obvious. – Andrew Huxley (2002), about the concept of ion channels, which he did not have when he (co-)created the first ever models of ionic currents.

CHAPTER 1

Introduction

The rhythmic beating of the human heart powers our circulation, distributing oxygen and nutrients to the body and carrying off harmful waste. In line with this vital function, diseases of the heart and circulatory system are among the most common causes of death, accounting for 28% of all deaths in the Netherlands (Buddeke et al., 2015) and an estimated 31% worldwide (WHO, 2016). The heart's rhythm is regulated by electrical activation and recovery, and the study of these processes is known as *cardiac electrophysiology*. Understanding the rhythm of the heart requires dealing with its complexity: efficient contraction requires a coordinated action of the approximately five billion muscle cells (myocytes) in the heart. It involves the flow of ionic currents through channels formed by small macromolecular complexes, propagation of signals from cell to cell, and much larger structures such as the specialized conducting fibers connecting different parts of the heart. To handle the complexities inherent to cardiac function in health and disease, computational models have been introduced that describe the function of ion channels, cells, tissue, and the heart as a whole. The process of creating and analyzing models that connect these spatial scales, as well as the different time scales involved, is known as *multi-scale modeling* (Southern et al., 2008). A broader introduction to the computational modeling of cardiac electrophysiology is given in Chapter 2.

This thesis deals with the computational modeling of the electrical characteristics of cardiac myocytes, starting from a single healthy myocyte, and extending the analysis to include lower levels (such as ion channels and genes), higher levels (such as coupled cells and tissue), and disease mechanisms. The central question is how we can use computational tools to organize this problem, to make sense of the available experimental data and to try and reduce the resulting complexity without losing the ability to investigate the influences of microscopic changes. This is especially pertinent in the light of recent insights into the importance of cell-to-cell, person-to-person and even day-to-day *variability* in disease mechanisms and responses to treatment (Marder and Goaillard, 2006; Weiss et al., 2012).

Within this broader problem statement, five different topics are addressed. In Chapter 3, we review existing tools for modeling and simulation of the cardiac action potential (AP)

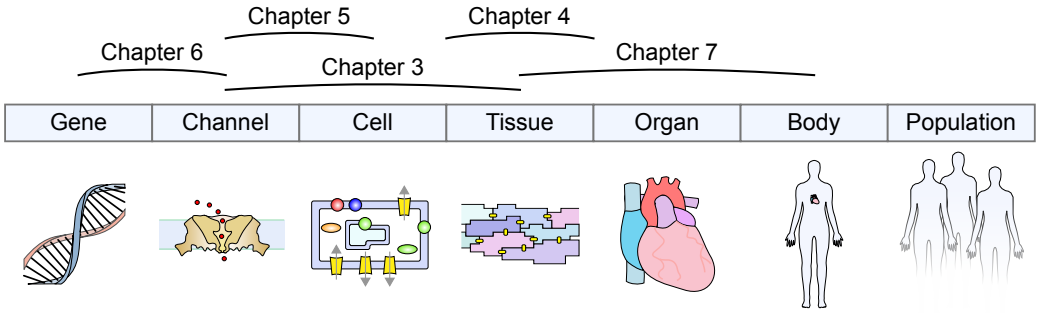

Figure 1.1: Graphical overview of the thesis chapters and the spatial scales they connect. In **Chapter 3** we show how our tool Myokit can be used to fit ion-current models to patch-clamp data, incorporate them into cell models and run simulations at the tissue level. **Chapter 4** then investigates methods to increase the size of simulated tissue patches. In **Chapter 5** we examine whether or not variability at the ionic current level can occur in the absence of variation in the underlying channel gene. **Chapter 6** investigates whether machine-learning methods can be used to predict the effects of genetic mutations on ion-current properties. Finally, in **Chapter 7** we use highly-simplified whole-heart models to link the cell level to the whole-organ level, and use *electrocardiographic imaging* to examine the heart from the body level.

and find there is room for a tool with a specific focus on AP model development. We then go on to describe *Myokit*, the result of our efforts to build such a tool. In Chapter 4 we investigate a potential method of speeding up calculations with the goal of extending our reach by simulating larger numbers of cells. We then focus on the ionic current I_{Na}, which has been linked to a wide variety of arrhythmias. In Chapter 5 we investigate if variability in the kinetics of I_{Na} can be observed, and in Chapter 6 we investigate if we can predict the changes to I_{Na} caused by genetic defects. Finally, in Chapter 7 we ask if AP models can be used to improve reconstructions of heart-surface potentials from noninvasive body-surface potential recordings, and we investigate the level of detail these models require to be successful. A graphical overview of the spatial scales addressed in the main chapters is given in Fig. 1.1.

1.1 Thesis outline

We now discuss the contents of the thesis in some more detail.

Chapter 2 discusses important background information: the role of bioelectricity in the heart is explained and models of the cellular AP and ion channels are introduced.

In **Chapter 3**, we present *Myokit*, a computational tool to simplify development and analysis of models of the cardiac AP. Models of the AP provide a unique bridge between the sub-cellular, cellular, and tissue-levels, allowing multi-scale modeling and investigation of cardiac function and disease. Given the overwhelming complexity of cardiac physiology and pathophysiology, providing easy-to-use tools is a critical task: it broadens the scope

of individual researchers, aids newcomers into the field and helps shift the focus from computational to biological complexity. In addition, Myokit experiments can easily be run on several models, which is a first step towards their systematic comparison and *synthesis*.

Following this, in **Chapter 4** we propose and investigate a novel method of speeding up simulations by replacing slow-to-evaluate mathematical expressions with faster approximations using *splines*. While a successful implementation would allow larger numbers of cells to be investigated, we find that splines provide a significant speed-up only for single-cell simulations with relatively small models of the AP. In addition, the benchmarking performed in this chapter provides insight into the workings and performance of the main simulation engines used in Myokit.

In **Chapter 5** we look at differences in I_{Na} measured in cells expressing the same channel DNA. Using novel measurements and results from identifiability theory we show that there is variability in the time constants of inactivation of I_{Na} and that this exceeds the variability expected from noise or imperfect experimental control. We conduct a literature review into reported midpoints of (in)activation for I_{Na} and find variability in individual studies, but an even greater variability *between* studies. This work provides modelers with quantitative data on cell-to-cell variability, which has been singled out as one of the most important future challenges for the modeling of cardiac cellular electrophysiology (Abriel et al., 2013; Mirams et al., 2016).

Chapter 6 addresses the question of genotype-phenotype relations in ion-channel related cardiac diseases. We hypothesize that the step from cell-level effect to clinical phenotype is affected by inter-subject variability, but that the step from gene to ion-current phenotype has a stronger deterministic character, especially when investigated in the controlled setting of expression system experiments. To test this hypothesis, we focus on missense mutations in *SCN5A*, the gene expressing the pore-forming alpha-subunit of the channel carrying I_{Na}. These mutations have been associated with a wide spectrum of clinical phenotypes (Remme, 2013). We collect a large number of I_{Na} measurements from the literature and then use visual inspection and machine learning techniques to show that, even in single-cell experiments in expression systems, the link between channel mutations and current-phenotype is difficult to characterize.

In **Chapter 7** we examine the cardiac electrical signals that can be measured on the body surface. With *electrocardiographic imaging* (ECGI) we can use these body-surface potentials to reconstruct the electrical potentials on the heart (Cluitmans, 2016). We show that, by simulating beats originating from different locations on the heart, we can create a basis of 'realistic' patterns of heart surface potentials that can be used to reduce the error in such reconstructions. By comparing detailed and simplified models, we show that for this purpose the resulting activation patterns on the heart surface are more important than the precise characteristics of the individual cellular APs.

In **Chapter 8** we discuss multi-scale modeling, simulation, and systems biology approaches to cardiac electrophysiology and pathophysiology. We highlight some of the challenges specific to this field, show uses of simulation at different scales, and discuss the reliability of such work. We conclude with a discussion of variability in multi-scale models of the cardiac AP.

1.2 Models and experiments

This thesis deals predominantly with *computational models* of the cardiac AP. Although the benefits of a combined modeling-experimental approach have been highlighted before (see for example Carusi et al., 2012; Heijman et al., 2015; Noble et al., 2012; Smith and Niederer, 2016) we now briefly discuss some of the advantages of modeling and the benefits of a tight integration of model and experiment (Noble and Rudy, 2001; Quinn and Kohl, 2013; Devenyi and Sobie, 2016).

Computational modeling allows the complex interplay between the various processes leading to the heart's contraction to be simulated and analyzed. This allows experimental scientists to work in a 'reductionist mode', gathering data on subprocesses (for example individual ion currents) and then combining their findings into an integrative model. As modern AP models are increasingly complex (Heijman, 2012) and contain many non-linear phenomena, the need to augment human intuition with simulations and numerical analysis steadily grows.

Models form a summary of years of experimental data and mechanistic insights. Using simulation, particularly with easy-to-use tools like Myokit, a modeler can quickly familiarize him- or herself with complex cellular functions. In contrast to physical experiments, all variables in such a simulation can be inspected simultaneously without interfering with the virtual experiment in any way. At the same time, if we *want* to interfere, any variable can be perfectly controlled.

Apart from the educational benefits, this perfect control allows simulations to be used to *test* our ideas, not by showing if a hypothesis is *correct*, but by showing if it is *plausible*. In other words, while we cannot test a hypothesis against biological reality using a model, we can test if it is internally consistent and does not clash with what we know so far. This brings us to the next point, which is the relationship between models and experiments.

Experiments can be time-consuming, expensive, and in the case of human testing or animal experiments, they require careful ethical consideration. Models and indeed simulated experiments are no substitute for this work, but they can help to interpret experimental findings, to extrapolate from the results, and to improve the design of experiments (see for example Clerx et al., 2015). In this way, modeling increases the power and value of experimental work, and may help reduce the need for human and animal testing.

CHAPTER 2

Background: Bioelectricity in the human heart

Abstract

This chapter provides some of the biological and modeling background needed to read this thesis. References to more detailed works are given throughout the text.

The heart uses bioelectrical signals called *action potentials* (APs) to coordinate its contraction. These signals originate at the cellular level, and are caused by the movement of charged particles (ions) through channels and transporters in the cell membrane. Action potentials propagate from cell to cell, creating traveling waves of excitation that trigger contraction of the heart muscle. The aggregate electrical currents through the billions of muscle cells in the human heart give rise to a signal powerful enough to be measured on the body surface: the electrocardiogram or ECG.

Using modern measurement techniques and novel pharmacological compounds, it has become possible to study the ionic currents through several distinct ion channels and transporters. Each of these currents can be described using numerical models, and models of currents can be combined into models of the cardiac cellular AP. These models describe the complex interplay between the currents and can even capture subcellular processes, including the release of Ca^{2+} which triggers the cell's contraction. Models of the single-cell AP can be combined into models of coupled cells, of patches of tissue and ultimately of the electrical system of the whole heart.

Contents

2.1 Bioelectricity in the human heart . . . 13
2.2 The cellular action potential . . . 14
2.3 Modeling the action potential . . . 15
2.4 Modeling ionic currents . . . 16
2.4.1 Hodgkin-Huxley models of ionic currents . . . 17
2.4.2 A note about identifiability . . . 19
2.4.3 Markov models of ionic currents . . . 19
2.4.4 Single-channel simulations . . . 20
2.5 Measuring currents and mutations . . . 21
2.6 Modern AP models . . . 23
2.7 The human ventricular epicardial AP . . . 24
2.8 Models of coupled cells and tissue . . . 26
2.9 Conduction velocity and reentry . . . 26
2.10 Bioelectricity on the body surface . . . 27
2.11 A personal note . . . 28

2.1 Bioelectricity in the human heart

For all its complexity, the heart functions as a two-sided pump. Its right side pumps blood into the lungs to be oxygenated (the *pulmonary* circulation), after which it returns to the left side of the heart which pumps it to the rest of the body (the *systemic* circulation). Each side has an *atrium*, which functions as a receiving chamber and a preloading pump for the larger *ventricle*, which performs the main pumping action. The heart's capacity to pump efficiently comes from its ability to perform coordinated contractions: First, both the left and right atrium (LA and RA) contract, filling the left and right ventricles (LV and RV). Next, the ventricles contract, sending blood into the aorta (from the LV) and pulmonary artery (from the RV). A schematic overview is given in Fig. 2.1.A.

This timed sequence of contractions arises from the individual contraction of each of the heart's muscle cells, which are known as *cardiac myocytes*. As the heart contains around five billion of these cells (Olivetti et al., 1995) this requires a high degree of synchronization. This is achieved through the use of *bioelectricity*. Like neurons, myocytes have evolved to sustain a brief electrical pulse and pass it on to their neighbors, causing the spread of an electrical signal in a 'Mexican wave' style (Welsh et al., 2017). This propagating cellular electrical signal is known as an *action potential* [1] (AP).

In addition, the heart contains smaller numbers of cells with specialized electrical functions: the cells of the *sinoatrial* (SA) node show spontaneous excitation (i.e., they spontaneously generate APs). This occurs about once per second, although this rate is regulated by different mechanisms in response to varying energy demand. In healthy conditions, the SA node sets the pace for the rest of the heart. From the SA node's location at the top of the right atrium, its electrical waves spread over the right and left atria through cell-to-cell conduction. This electrical excitation triggers contraction of the atrial muscle cells via *excitation-contraction coupling* (Bers, 2001).

The atria are electrically shielded from the ventricles, causing the propagating AP to halt at the atrial borders. Activation of the ventricles occurs via a second group of specialized cells which together form the *atrioventricular* (AV) node. Signals from the SA node reach the AV node, where they are slightly delayed while the atria contract and fill the ventricles. Next, the signals travel down conducting *Purkinje fibers* in the septum (the muscle wall which separates the LV and RV) towards the tip (or *apex*) of the heart. From there, they spread over the ventricular walls causing both ventricles to contract and perform a powerful pumping motion. A schematic overview of the heart's electrical conduction system is given in Fig. 2.1.B.

[1] Readers with a background in physics may wish to note that it is not a potential in the physical sense of the word, i.e., it is not a measure of energy or electrical potential but simply the name given to a short electrical event.

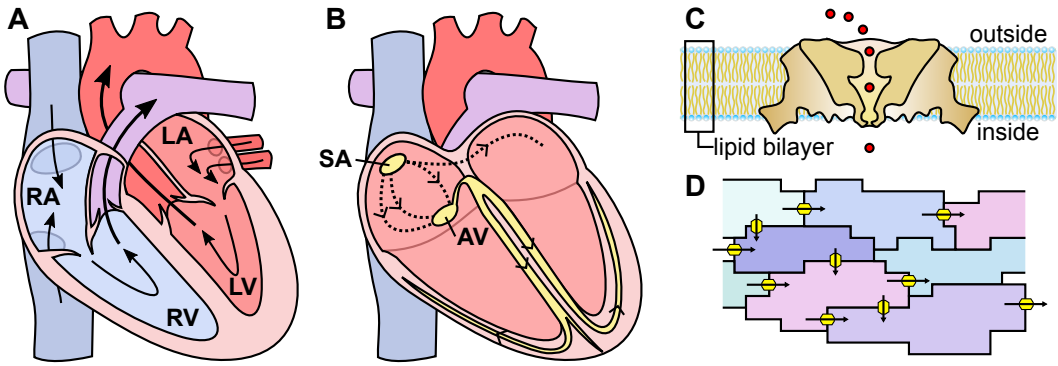

Figure 2.1: (*A*) Basic anatomy of the heart. Oxygen-depleted blood enters the right atrium (RA), is transported to the right ventricle (RV) and then pumped to the lungs. From the lungs, oxygen-rich blood enters the left atrium (LA) and then the left ventricle (LV) from where it is pumped into the aorta and then to the body. (*B*) A schematic overview of the heart's conduction system. Excitation starts at the sinoatrial node (SA) and travels over the atria before being propagated to the atrioventricular node (AV), where it is slightly delayed before being propagated to the ventricles. (*C*) A cross-section of a cell membrane, containing an ion channel. The shape of the channel is based on Payandeh et al. (2011). (*D*) A network of myocytes, connected by gap junctions.

2.2 The cellular action potential

How can cells conduct electrical waves? The answer depends crucially on the *cell membrane*, a thin water-insoluble layer that separates a cell's interior from its environment. The membrane is composed of phospholipids that have a polar (and hence hydrophilic) head and a non-polar (hydrophobic) tail. This property causes them to organize into a *lipid bilayer*, with heads pointing out and tails pointing in towards the center of the membrane (see Fig. 2.1.C). The non-polar core acts a strong electrical *insulator*, blocking the passage of any polar or charged particles, including naturally present ions such as sodium (Na^+), potassium (K^+) and calcium (Ca^{2+}). As a result, a cell can contain different concentrations of ions than the fluid outside it, allowing a difference in the density of electrical charge to arise. This charge imbalance can be expressed as an electrical potential difference called the *membrane potential*. Membrane potentials can be measured, and are usually in the order of tens of millivolts (about -100 to $+50$mV in a cardiac cell). When ions move in or out of the cell, the membrane potential changes, producing the so called action potential.

Wedged into the cell membrane of cardiac myocytes are several proteins, some of which have remarkable properties. *Ion channels* are large macromolecular complexes that, under certain conditions, can 'open' to form an aqueous pore that allows ions to pass through the membrane. Most ion channels are highly selective, and include a narrow funnel-like structure whose electrochemical properties are such that only a single species of ion can pass through. The direction of movement depends on the ion's concentration gradient and the membrane potential. Some channels open and close only after binding to certain chemicals, but this thesis deals exclusively with ion channels that open and close in a *voltage-dependent* manner.

A cartoon of an ion channel inside a cell membrane is shown in Fig. 2.1.C.

In addition to ion channels, the membrane contains so-called *pumps* that transport ions from one side of the membrane to the other. Pumps move ions *against* their chemical and/or electrical gradient, and the energy required to do so is obtained by breaking down ATP (adenosine triphosphate) into ADP (adenosine diphosphate). Similarly, *co-transporters* and *exchangers* move ions against their gradient, but they derive their energy from the simultaneous movement of a second type of ion, *along* its gradient. Pumps, exchangers and co-transporters are collectively known as *transporters* (Molleman, 2003).

Finally, myocytes are connected to their neighbors via special channels known as *gap junctions*. These form large, non-specific pores that allow strong ionic currents to pass between cells. Although gap junctions are weakly voltage sensitive, it is usually adequate to think of them as continuously open channels (Gros and Jongsma, 1996). Myocytes are around $140\mu m$ long and $25\mu m$ wide (Volders et al., 1998) and are usually arranged in a grid with similarly oriented cells. Most connections are at the short end of the cells, leading to faster AP propagation along the longitudinal axis of the fibers. A group of myocytes connected by gap junctions is shown schematically in Fig. 2.1.D.

2.3 Modeling the action potential

In a groundbreaking series of papers published in 1952, Alan Hodgkin and Andrew Huxley presented the first *computational model* of a cellular AP (Hodgkin and Huxley, 1952a,b,c,d). By carefully measuring the different currents passing through the membrane of a squid axon, they were able to create models for the three main components of the axon's AP: a current carried by Na^+, one carried by K^+, and a 'leakage' current carried by anything else. They found that the size and shape of each current is strongly dependent on the membrane potential. As the membrane potential is a direct result of the ionic concentrations in and outside the cell, it changes when ions move across the membrane. This creates a feedback loop, shown in Fig. 2.2 (left), where the membrane potential determines the transmembrane currents and the transmembrane currents determine the membrane potential. As a result, the process is best described as a *dynamical system*.

In computational models of the AP, variables are defined that represent the membrane potential, intracellular ion concentrations, and the state of all ion channels and transporters. Next, differential equations are defined that, given the model state at some time t, provide the derivatives of all variables. In other words, given the current state of the cell, they specify how it will *change*. This knowledge can then be used to make a prediction for the state of the model at time $t + \Delta t$, and by doing this repeatedly (with very small time steps Δt) simulations can be run (for a detailed overview of this and similar methods, see any book on *numerical integration* of *ordinary differential equations*).

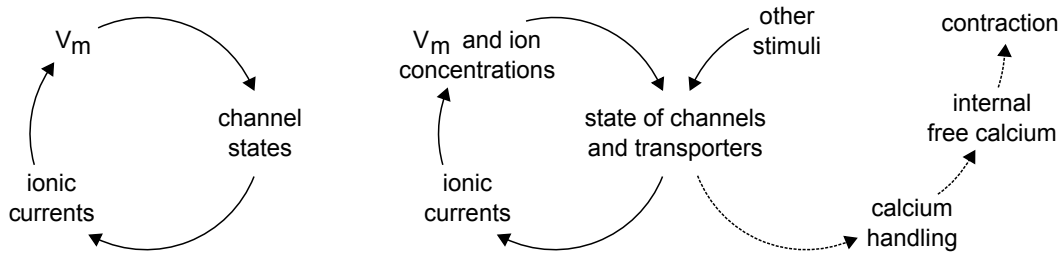

Figure 2.2: A classic (left) and updated (right) view of the feedback loop underlying models of the cellular action potential. In the classic view, the membrane potential V_m determines the channel states, which determine the ion currents through the membrane. The sum of the ionic transmembrane currents then determines the change in the membrane potential. To the right, an updated view is given where not only changes to V_m are modeled, but additional work is done to keep track of ionic concentrations in crucial parts of the cell. Ion channels, pumps, exchangers and even diffusion currents are modeled, all of which can be affected by stimuli from outside the cell. Particular attention is paid to the processes that determine the free Ca^{2+} concentration in the cell, which ultimately leads to contraction. Adapted from Hille (2001).

To give all this a mathematical representation, we define the membrane potential V_m as

$$V_m = V_{\text{in}} - V_{\text{out}}$$

where V_{in} and V_{out} are the electrical potentials inside and outside the cell respectively. Next, we define a *positive* current, as one that carries charge *out of the cell* (thus lowering V_{in}, raising V_{out} and decreasing V_m). The change this causes to the membrane potential is captured by the equation

$$\frac{dV_m}{dt} = -\frac{1}{C_m} I$$

where C_m is the membrane capacitance and I is the sum of all transmembrane currents. In Hodgkin and Huxley's model, this results in

$$\frac{dV_m}{dt} = -\frac{1}{C_m}\Big[I_{\text{Na}} + I_{\text{K}} + I_{\text{leak}}\Big].$$

Here, I_{Na}, I_{K} and I_{leak} represent the sodium, potassium and leak current respectively. Later models added new currents and refined the existing ones, leading to a more complicated equation but following the same general form (see Chapter 3). A detailed introduction to AP modeling can be found in Rudy and Silva (2006). The next step is to model the ionic currents, which is discussed in the following section.

2.4 Modeling ionic currents

Models of ionic currents start from Ohm's law $I = \Delta V/R$, where I is the current, R is an electrical resistance and ΔV is a difference in electric potential. Instead of using resistance, current modelers use *conductance* $G = 1/R$, with the S.I. unit *siemens* or *S*. The appropriate voltage difference ΔV is determined by a combination of electrical forces and *diffusion*:

When channels are open, ions can diffuse from the side with the higher concentration to the side with the lower. But since ions are charged they are also affected by the presence of any electrical field. Thus, ion currents depend on chemical as well as electrical gradients. Currents will flow until these two forces reach equilibrium at a potential E, known as the *Nernst* or *equilibrium* potential. In other words, they will flow until $\Delta V = V_m - E = 0$.

For convenience, a changing conductance is usually written as the product of a dimensionless time-variant term $g\big(V_m(t), t\big)$ and a fixed factor $\bar{g}$ that can be used to scale the current, for example to model different cell sizes, changes in the number of channels (due to regulation of genetic expression) or drug-induced block. This results in a general equation of the form

$$I = \bar{g} \cdot g \cdot (V_m - E)$$

There are two main formalisms used to model the variable conductance term g: *Hodgkin-Huxley style models* and *Markov models*. Both will be discussed below. For a major reference work on ion channels and ion channel models, see Hille (2001).

2.4.1 Hodgkin-Huxley models of ionic currents

The current models introduced by Hodgkin and Huxley (HH) describe the conductance term g as the product of one or more dimensionless variables, whose value can vary between 0 and 1. Each variable can appear in the product once or multiple times (i.e., some variables are raised to an integer power). For example, for the sodium current I_{Na}, HH introduced the variables m and h, with m appearing three times, to obtain:

$$I_{\mathrm{Na}} = \bar{g}_{\mathrm{Na}} \cdot m^3 \cdot h \cdot (V_m - E_{\mathrm{Na}})$$

where E_{Na} is the reversal potential for Na^+, which depends on the Na^+ concentrations in and outside the cell. Intuitively, the term $m^3 \cdot h$ can be thought of as a series of three synchronized m-type gates, followed by a single h-type gate, where the m and h-type gates open and close independently of each other. The variables m and h then represent the proportion of gates in the membrane that are in the open state. If all gates are open ($m = h = 1$) the current is at its peak, but no current can flow if either m or h is zero.

Opening and closing of a gate is modeled as a chemical reaction:

$$\text{closed} \underset{\beta}{\overset{\alpha}{\rightleftharpoons}} \text{open}$$

where α and β are the opening and closing rates (in units 1/second). We can then write an equation that shows how a proportion such as m changes over time (we use m in the example, but equations of the same form are used for h or any other gating variable):

$$\frac{dm}{dt} = \alpha_m(1 - m) - \beta_m m$$

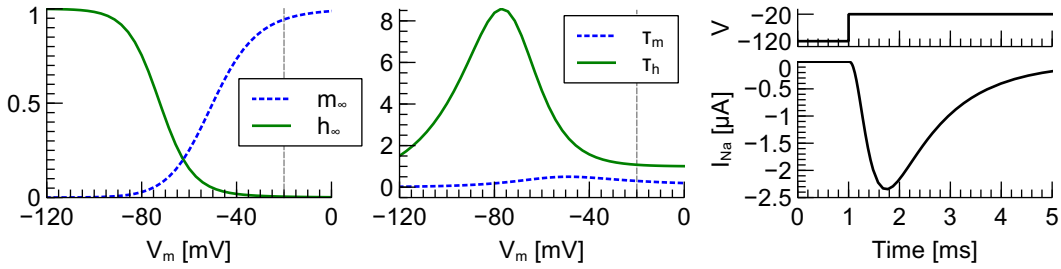

Figure 2.3: The steady states (left) and time constants (center) for gating variables m and h, calculated from the equations for the sodium current given in (Hodgkin and Huxley, 1952d). The current elicited by a voltage step from −120mV to −20mV is shown on the right. Before the voltage step ($t < 1$) a low membrane potential $V_m = -120$mV is maintained. At this voltage, the model is not activated ($m = 0$) and completely recovered from inactivation ($h = 1$), as can be seen in the left panel. At $t = 1$ms, the potential is quickly raised to −20mV causing the model to activate ($m \to 1$) with a speed dictated by τ_m. It also immediately starts inactivating ($h \to 0$) but this happens at a lower speed than activation (center panel), leading to the temporary appearance of an ionic current (lower right panel). After a few milliseconds at −20mV, the model is fully activated ($m = 1$) but also fully inactivated ($h = 0$) so that a current can no longer be observed.

This is often rewritten in the form $dm/dt = (m_\infty - m)/\tau_m$ with $m_\infty = \alpha_m/(\alpha_m + \beta_m)$ and $\tau_m = 1/(\alpha_m + \beta_m)$. With this formulation, it can be seen that every gate variable (in this case m) approaches a steady state value (m_∞) with a speed determined by some time constant (τ_m). The steady state and time constant are taken to be the voltage dependent parts of the system, so that

$$\frac{dm}{dt} = \frac{m_\infty(V_m) - m}{\tau_m(V_m)}$$

The process of fitting a HH-style model to a current, then, is the process of: 1. Postulating the number of gate types (typically using the smallest number that can fit the observed data). 2. Measuring the steady states and time constants for a range of values of V_m. 3. Choosing equations to fit this data and finding the parameters that give the best match. 4. Tweaking the result by adding powers to the gating variables (again, using the smallest power that gives an adequate fit).

The steady state and time constant curves obtained by HH for the sodium current in the squid axon are shown in Fig. 2.3. These curves were highly influential for the methodology and terminology of cellular electrophysiology. The variable m became known as an *activation* variable, with the transition from $m = 0$ to $m = 1$ known as activation and the reverse process sometimes known as deactivation. Similarly, the decrease in h seen at higher potentials is now known as *inactivation*, while its transition back to 1 is called recovery from inactivation, or simply recovery. The potential at which $m_\infty = 0.5$ is known as the *midpoint of activation* and the point at which $h_\infty = 0.5$ is the *midpoint of inactivation*. These terms have stuck, and are often used outside the context of modeling or even when discussing competing current model formalisms.

2.4.2 A note about identifiability

The steady states and time constants of HH-style models cannot be measured directly, but must be inferred from recordings of the current. This raises concerns about the model's *identifiability*, i.e., the possibility of finding the 'true' model parameters based on recordings of I. In their analysis, Hodgkin and Huxley relied on the crucial assumption that the time constant of m is much smaller than that of h, causing m to change much faster. The difference in speed allows the start of a recording to be used to estimate the parameters for m, while the end can be used to estimate the parameters of h. This is discussed further in Chapter 5.

2.4.3 Markov models of ionic currents

When Hodgkin and Huxley created their model of currents and the AP, the mechanism by which ions moved through the membrane was still unknown. Later, as the recognition of ion channels grew, models emerged that attempted to describe changes in channel protein conformation as a means of predicting currents. These became known as *Markov models*[2].

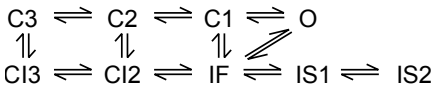

Figure 2.4: A Markov model structure for I_{Na} introduced by Clancy and Rudy (2002).

An example of a Markov model structure for the cardiac sodium current is shown in Fig. 2.4. It defines 9 states, one of which is the open state (O). In addition, there are three closed states (C3, C2, C1), two closed-inactivated states (CI3 and CI2), a 'fast' inactivated state (IF) and two 'slow' inactivated states (IS1 and IS2). Like in the HH formalism, transitions between states are governed by voltage-dependent chemical reaction rates. Using this model, the sodium current through a cell membrane is modeled as:

$$I_{\mathrm{Na}} = \bar{g}_{\mathrm{Na}} \cdot O(V_m) \cdot (V_m - E_{\mathrm{Na}})$$

where $O(V_m)$ is the proportion of channels in the open state.

This model shares similarities with the I_{Na} model introduced by Hodgkin and Huxley. To activate, the model makes three jumps ($C3 \rightarrow C2 \rightarrow C1 \rightarrow O$) after which inactivation can set in ($O \rightarrow IF$). It is also possible for the model to be deactivated ($m = 0$) and inactivated ($h = 0$) at the same time (CI3 and CI2). However, the Markov model structure allows for the introduction of dependencies between state transitions: the inactivated states IS1 and IS2 can only be reached via the state IF. These states were introduced to represent an

[2]Readers familiar with statistical Markov chains should note that the models used in cell electrophysiology use chemical reaction rates instead of transition probabilities, leading to slightly different mathematics.

experimentally observed slow inactivation process, where channels that were kept at high potentials for an extended period needed a long time to recover (Clancy and Rudy, 2002).

Markov models have long been investigated as a way to connect ion-channel characteristics to measurable currents (Armstrong and Bezanilla, 1977). This has been succesfully used to extrapolate from changes in single-channel function to clinically relevant changes in the AP (Clancy and Rudy, 1999). Conversely, it can be used to learn about channel properties (for example state-dependent effects of channel-blocking drugs) by inspecting differences in measured currents (Clancy et al., 2007).

If a channel's kinetics can be well described as discrete transitions between a limited number of states, and *if* we can identify those states, write down equations and parametrize the resulting model, then Markov models present a unique bridge between molecular-level effects and whole-cell currents. However, like the problem of finding the number of gates and the powers in HH-style models, the problem of determining the structure of a Markov model is still unsolved, although good estimates can be made by combining different sources of information (Armstrong, 2006). Similarly, the shape of the equations that describe the rate constants is chosen freely by the modeler (but equations based on *Eyring rate-theory* have also been used, see Irvine et al., 1999). Finally, simulations with Markov models are slower than those using HH-style models, especially when tricks are used to reduce the run-time (see Rush and Larsen, 1978, and Chapter 4). For a recent overview of the differences between HH-style and Markov models, see Carbonell-Pascual et al. (2016).

2.4.4 Single-channel simulations

The discovery of ion channels allowed Hodgkin and Huxley's ion current models to be interpreted as descriptions of the current carried through the membrane by *all* channels of a certain type. When the current through *individual* channels was measured in the 70s (see Section 2.5) it confirmed earlier suspicions[3] that they opened and closed stochastically, with opening and closing probabilities dictated by the membrane potential. By selecting the appropriate algorithm, Markov models can be used to simulate both the stochastic single-channel currents (Gillespie, 1976) and the idealized aggregate current through large numbers of channels.

Fig. 2.5 shows the stochastic opening and closing of cardiac sodium channels, simulated with the model by Clancy and Rudy (2002) (using *Myokit*, see Chapter 3). According to this model, channel openings are relatively rare events, even at potentials leading to strong aggregate currents. As the number of channels increases, the probability of multiple channels being open at the same time increases. For larger numbers of channels, the sum of the stochastic openings increasingly resembles the idealized aggregate current.

[3] In fact, good estimates of the number of channels and their individual conductances had already been made using statistical models, see for example Hille (1970) or Katz and Miledi (1972).

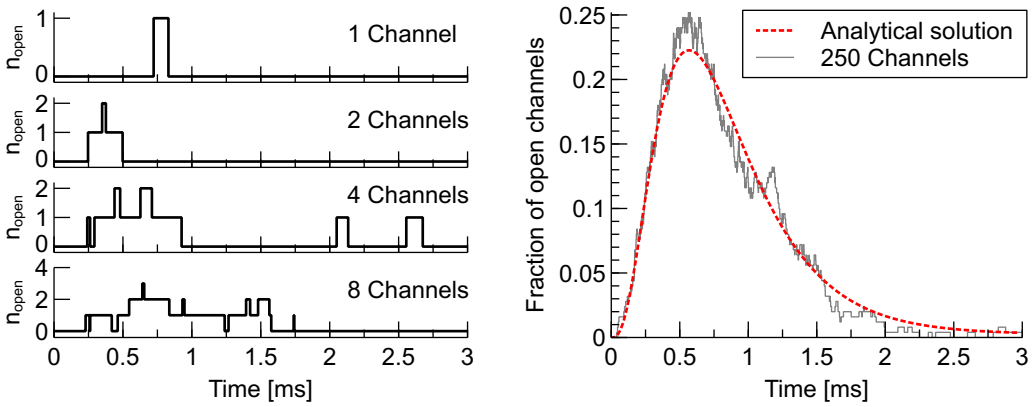

Figure 2.5: Stochastic sodium channel openings, simulated using the model by Clancy and Rudy (2002) for a single voltage step from −120mV to −20mV. (*Left*) The total number of open channels, simulated in a model with 1, 2, 4 or 8 channels. (*Right*) The fraction of open channels in a stochastic simulation with 250 channels (noisy line) and the idealized aggregate curve (smooth line).

2.5 Measuring currents and mutations

The first (indirect) recording of an AP occurred as early as 1868, when the German physiologist Julius Bernstein invented the "differential rheotome" and used it to measure impulse propagation in frog nerve (Schuetze, 1983). He hypothesized that his findings could be explained if cells had an electrically isolating membrane, occasionally permeable to potassium ions (Seyfarth, 2006). Direct recording of ionic currents became possible in 1947, when George Marmont and Kenneth S. Cole realized that a feedback amplifier could be used to control the membrane potential while simultaneously measuring transmembrane currents[4]. In their early experiments they used the giant axon of the squid *Loligo pealeii* (now known as *Doryteuthis pealeii*), an unusual cell type which had the advantage of being large enough to allow the insertion of a metal electrode directly into the axon. This technique of controlling the membrane potential with a feedback amplifier became known as *voltage clamping* (Cole, 1968; Huxley, 2002; Verkhratsky et al., 2006).

Later, voltage clamping was applied to other cell types by using glass *micropipettes* (with a very sharp tip) to penetrate the cell membrane. Provided the pipette tip is small enough for the membrane to survive the perforation, an electrical connection with the cell interior can be made by filling the pipette with a buffered salt solution and inserting an electrode into its wider end (Graham and Gerard, 1946). Combined with voltage-clamp, this technique can be used to measure APs and transmembrane currents (see also Hodgkin, 1950) and in 1949 the first micropipette measurements of the cardiac AP were reported by Coraboeuf and Weidmann (1949).

[4] Guitar players might be interested to learn that, while the transistor had been developed in the very same year, the first voltage-clamp amplifiers were in fact tube amplifiers.

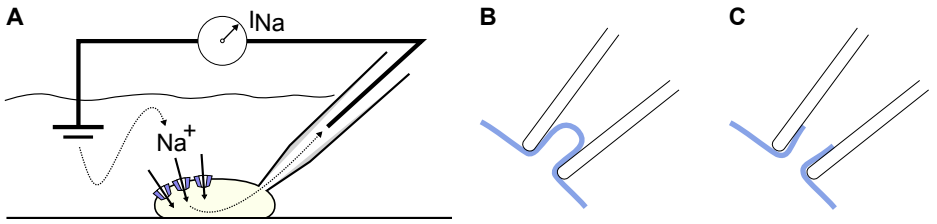

Figure 2.6: (*A*) A schematic overview of the whole-cell patch-clamp configuration. (*B*) Pipette attached to a cell. Some suction is applied, causing the membrane to enter the pipette and form a tight seal. (*C*) After applying another short burst of suction, the membrane ruptures but stays attached to the inside of the pipette.

In 1976, Neher and Sakmann discovered they could use a pipette with a larger tip (a *low-resistance electrode*) to electrically isolate a small patch of membrane, allowing the recording of currents through a single channel (Neher and Sakmann, 1976). Different variations on this concept appeared in the years following their discovery, which collectively became known as *patch clamping*. A popular method, employed in Chapter 5, is the 'whole-cell configuration' which measures aggregate whole-cell currents instead of single-channel currents. In this set-up, shown schematically in Fig. 2.6.A, a pipette is placed *against* the cell membrane (using a microscope and a mechanical micro-manipulator on a stabilized table). Some suction is then applied, causing a small patch of tissue to enter the pipette and form a tight seal (Fig. 2.6.B). Once the seal has stabilized, a second short burst of suction (or 'kiss') is applied that, if successful, ruptures the membrane but leaves it attached to the inside of the pipette, allowing electrical access to the cell interior (Fig. 2.6.C).

The next big advance occurred when genes encoding ion-channel subunits were identified and cloned. In 1984, Noda et al. were able to transcribe the DNA sequence for the sodium channel of the electric eel *Electrophorus electricus* (Noda et al., 1984). Electric eels were the ideal candidate as their *electroplax* (the electric organ used to shock prey with) contains a very high density of sodium channels. Two years later they artificially inserted this DNA into *Xenopus* oocytes (frog eggs), and managed to record currents from the ion channels then expressed by these cells (Noda et al., 1986).

The technique of inserting cloned channel DNA into such an *expression system* was further developed to allow the study of *artificially mutated genes*. This has had a great impact on medicine, as it allows mutations in channel genes identified in a clinical setting to be recreated and studied in the laboratory. In Chapter 5 we use measurements in cell-expression systems to investigate the possibility of variability in the kinetics of I_{Na}. In Chapter 6 we analyze a large number of patch-clamp experiments on mutated sodium channels in expression systems, and attempt to predict how the mutations affect the ionic current.

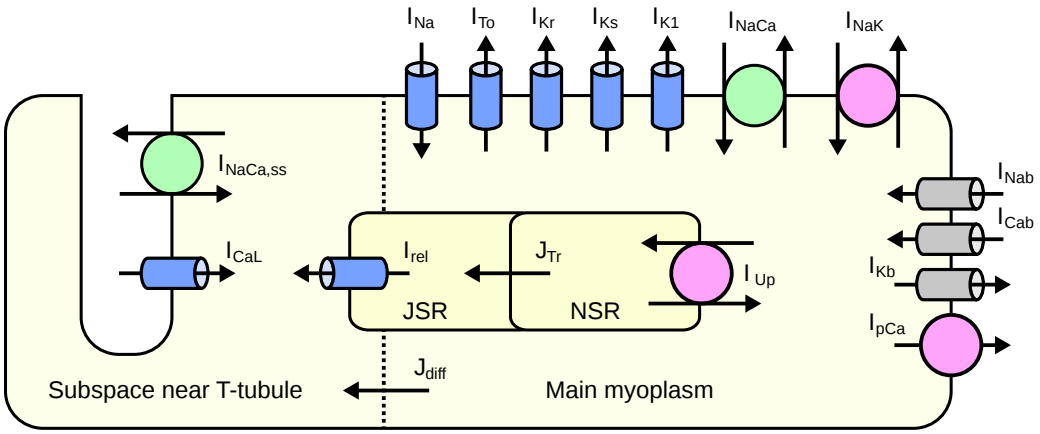

Figure 2.7: Simplified schematic of a model of the ventricular action potential (O'Hara et al., 2011). The cell is split into the main myoplasm, the area near the t-tubules and two compartments relating to Ca^{2+} storage and release (the JSR and NSR, see text). Channels are shown in blue, pumps in red and exchangers in green. Background currents are indicated as gray channels.

2.6 Modern AP models

In 1962, ten years after Hodgkin & Huxley's model of the squid axon, the first computational model of a cardiac cell was developed by Denis Noble (1962). This model described the AP of cells from the Purkinje fibers. Like the HH model, it used just three currents (sodium, potassium and leak) and made no predictions about ion concentrations in the cell. In 1977, a model of the (mammalian) ventricular AP was introduced by Beeler and Reuter (1977), which included a Ca^{2+} current and a method for tracking the internal Ca^{2+} concentration. The model also split the potassium current into two distinct components. This trend of tracking concentrations and adding or refining currents continued in the next decades, causing models to grow larger and ever more specific. 'Mammalian' models were replaced with species-specific ones (dog, rabbit, mouse, human, etc.) and different models were created for cells from the SA node, the atria, Purkinje fibers, the LV and RV, and even for cells from the outer (*epicardial*) or inner (*endocardial*) layer of the LV. For a detailed overview, see Noble et al. (2012).

Fig. 2.7 shows a schematic overview of a modern model of the ventricular epicardial AP (O'Hara et al., 2011). It includes a fast sodium current (I_{Na}) and a three-part leak (or background) current ($I_{\mathrm{Nab}} + I_{\mathrm{Cab}} + I_{\mathrm{Kb}}$). The potassium current has been split into four different parts, each through a different channel type with its own distinctive characteristics. In addition, a Ca^{2+} current (called I_{CaL}) has been introduced, along with several pumps and exchangers.

The cell interior is divided into several compartments, and the model tracks ionic concen-

trations (particularly Ca^{2+}) in each of these, as well as the diffusion between them. The *network* and *junctional sarcoplasmic reticulum* (NSR and JSR) are structures inside the cell that play a crucial role in *Ca^{2+}-induced Ca^{2+} release*, a process whereby the entry of a small amount of Ca^{2+} through the membrane triggers the release of large amounts of Ca^{2+} from the sarcoplasmic reticulum (Bers, 2001). Ventricular myocytes are known to have an extensive network of *t-tubules*; places where the membrane folds inwards to create deep "invaginations" that bring the sarcoplasmic reticulum into close proximity with the extracellular fluid (see Soeller and Cannell, 1999, for 3-dimensional images of the t-tubular network). In the model shown here, the area near the t-tubules is modeled as distinct from the bulk intracellular fluid (or *myoplasm*). These detailed channels, transporters and compartments are crucial in modeling the complex processes of excitation-contraction coupling that lead to contraction of the muscle cell. An updated version of the cyclic interaction between membrane potential, channel states and currents is shown in Fig. 2.2 (right).

The development of complex models such as these has led to the need for tools that simplify model implementation, exchange, and comparison. In Chapter 3, *Myokit* is introduced as a toolkit for development and rapid simulation of modern models of the AP. For a comparison of the complexity of modern models, see Heijman (2012).

2.7 The human ventricular epicardial AP

One of the advantages of computational modeling is the ability to simulate and visualize the complex interaction between model components. Fig. 2.8 shows how currents in the model by O'Hara et al. (2011) act together to shape the human ventricular epicardial AP. For the sake of simplicity, some of the smaller currents are omitted, and no details of the internal currents and diffusion are shown. While model- and cell-specific, the main components for this model are similar to those in many cardiac myocytes, and will be discussed below as a general introduction to the different currents and their role in shaping the AP.

At the start of the simulation shown in Fig. 2.8, the cell is fully relaxed (not contracted) and V_m is at a stable *resting potential* of around -88mV. After 30ms, a short pulse is applied to the cell (i.e., a small inward current is injected). This raises the membrane potential just enough for the sodium current I_{Na} to activate, triggering a significant rise in the membrane potential. As the sodium current begins to inactivate, the increase in membrane potential slows down, eventually leading to a peak of around 35mV. At this high potential, the transient outward potassium current I_{To} activates and then rapidly inactivates, causing a small notch in the AP that is characteristic for epicardial ventricular cells. The next currents to activate are the L-type calcium current I_{CaL} and the rapid delayed rectifier potassium current I_{Kr}. These currents act in opposing directions, causing the membrane potential to stay relatively stable for a period of about 200ms known as the *plateau phase*. During the

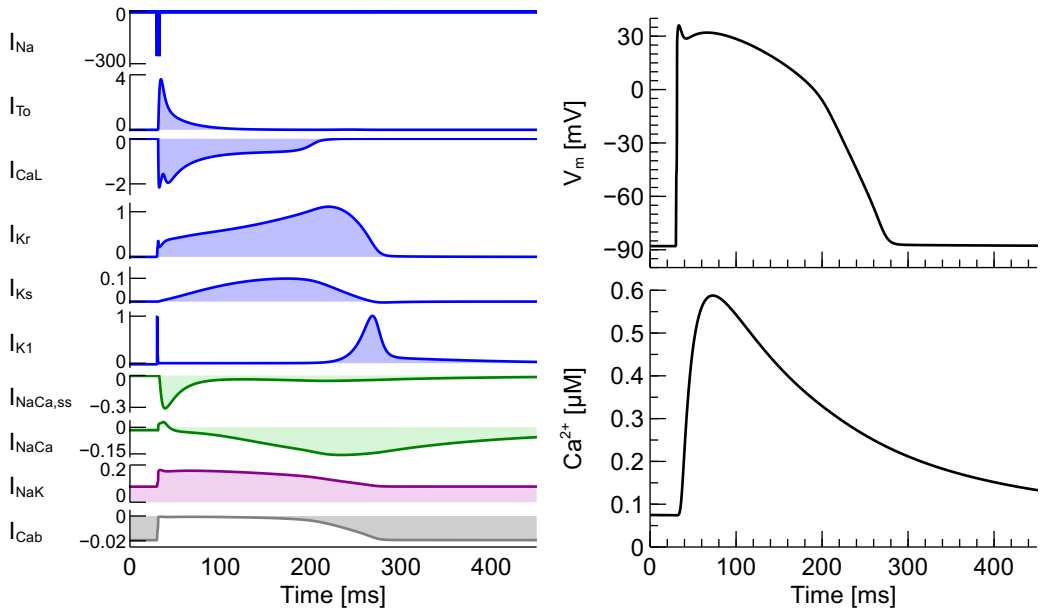

Figure 2.8: (*Left*) Currents through the cell membrane, simulated with the model by (O'Hara et al., 2011). For simplicity, some of the smaller currents are omitted. Note the wide variety of time-scales, shapes and amplitudes. (*Right*) The resulting action potential (top) and Ca^{2+} transient (bottom).

plateau phase, I_{Kr} grows steadily, while I_{CaL} begins to inactivate, eventually causing the membrane potential to drop. At around -50mV, the inward rectifier potassium current I_{K1} becomes active and brings V_m back down to the resting potential.

Once the cell is back at its resting potential (once it has *repolarized*, in electrophysiology lingo) the ion channel currents largely disappear. Instead, the membrane potential is determined by the balance of the sodium-potassium pump current I_{NaK}, the sodium-calcium exchange current I_{NaCa} and the sodium and calcium background currents, one of which (I_{Cab}) is shown Fig. 2.8. The current I_{K1} is also active in this phase, but as it has a reversal potential very close to the resting membrane potential, the current is typically small. However, if any minor deviations in V_m occur, they are immediately compensated by an increase in I_{K1}.

A final current visible in the figure is the slow delayed rectifier potassium current I_{Ks}. During a normal AP, it has a very low amplitude, and can be blocked entirely without apparent consequence. However, if an AP is prolonged excessively or if adrenaline is present (e.g., when something triggers the body's 'fight-or-flight' response), I_{Ks} can grow to become a dominant force in restoring the resting potential (Volders et al., 2003). This is an example of redundancy in the cellular AP, an area where nature has introduced multiple mechanisms that appear to have the same function but can in fact act as back-up systems for each other. This is discussed further in Chapter 8.

2.8 Models of coupled cells and tissue

Once an AP model has been defined, it can be extended into a model of cardiac tissue. To create a model of two cells, the AP model's equations are duplicated, leading to two V_m's, two sodium currents, two Ca^{2+} concentrations etc. A gap junction current is introduced to couple both cells:

$$I_{1\to 2} = g_{12} \cdot (V_1 - V_2)$$
$$I_{2\to 1} = g_{21} \cdot (V_2 - V_1) = -I_{1\to 2}$$

where $I_{1\to 2}$ is the current from cell 1 to 2, $I_{2\to 1}$ is the current from 2 to 1, V_1 and V_2 are the membrane potentials of cell 1 and 2 and $g_{12} = g_{21}$ is a fixed conductance indicating the strength of the connection. $I_{1\to 2} = -I_{2\to 1}$, indicating that this is a charge conserving connection. The exchange of ions between cells associated with this current is not commonly modeled. This scheme can be extended to any number of cells and allows arbitrarily complex networks of connections.

Modeling each cell individually, however, is not a particularly *fast* way of modeling tissue. This issue is solved in the *monodomain* model, which ignores the distinction between cells and uses AP models to describe *points in space*, connected by a resistance dictated by a continuous scalar field. Instead of the ordinary differential equations (ODEs) of single or coupled cell models, this results in partial differential equations (PDEs). The computational speed-up is achieved by solving the PDE on a grid with points spaced further apart than individual cell lengths (Leon and Horáček, 1991). The *bidomain* model is like the monodomain model, but has the additional benefit of incorporating extracellular conduction, which can be useful to model defibrillation (Keener and Sneyd, 2009). The relation between the monodomain model and the coupled cell approach is discussed in the appendix to Chapter 3. For a detailed guide to large-scale tissue modeling, see Clayton and Panfilov (2008).

2.9 Conduction velocity and reentry

In systems of coupled cells, APs can propagate from cell-to-cell, causing waves of excitation to spread over the tissue. The speed at which they travel is called the *conduction velocity* (CV) and is an important tissue-level parameter. The CV is determined by the characteristics of the cardiac fast sodium current I_{Na}, the number of the gap junctions connecting the cells, and the presence of any fibrotic (non-conductive) material between cells. The number of gap junctions and the amount of fibrosis are both modeled by the cell-to-cell conductance terms specified by the tissue model. The influence of I_{Na} is an example where the tissue-level behavior depends on the properties of the individual cells. As a result, validating a cell model, or even a current model, also requires inspecting tissue-level behavior.

In normal cardiac conduction, waves propagate from one side of the ventricles (or atria) to the other and then die out. But under certain conditions *spiral waves* can occur that rotate around a fixed or moving locus, and can continue for extended periods of time (a detailed overview is given in Kléber and Rudy, 2004). This phenomenon is known as *reentry* and was described and analyzed as early as 1913 (Mines, 1913). Reentry severly disrupts the pumping function of the heart, and occurs in some of the most serious forms of arrhythmia. An example of a reentrant wave is shown in Chapter 3.

2.10 Bioelectricity on the body surface

The combined electrical action of all cardiomyocytes creates a signal strong enough to be measured at the body surface, using electrodes placed on the skin. The resulting signal is called the *electrocardiogram* or ECG and is one of the most important diagnostic tools in clinical cardiology. In Chapter 7 we exploit the fundamental relationship between the cellular AP and the ECG to improve the quality of heart-surface potential reconstructions based on body-surface measurements. To do this, we use a heuristic method based on the coupled-cell approach (see Section 2.8) to perform highly simplified 'whole-heart' simulations, which we compare to fine-grained simulations performed using the monodomain model.

2.11 A personal note

Occasionally, people have been surprised to hear of electricity as a central feature of the heart, of the biological applications of mathematical theory, or of the intrusion of computer scientists into the biomedical world (and vice versa!). This 'crossing-borders' aspect is one of the things that makes computational cardiac electrophysiology rewarding and fun. At the same time, its inter-disciplinary nature doesn't always fit well with administrative or educational systems (not to mention the difficulty of explaining your job at dinner parties). Sometimes, whether due to nurture or nature, a certain cultural difference also seems to exist between holders of engineering and biomedical degrees.

And yet a brief glance at history shows that the interplay between these fields can be very fruitful indeed. For example, both Hodgkin and Huxley (see Chapter 2) had a strong background in physics; Huxley had even intended to graduate in this discipline before switching to physiology. During the war, both were involved in the development and application of radar (Nobel Media, 1963a,b). The papers that resulted in their 1963 "Nobel prize in physiology or medicine" (shared with John Eccles) not only describe physiology experiments but also provide the building plans for the electrical devices needed to perform them (Hodgkin et al., 1952). A second Nobel prize for physiology or medicine was awarded to Neher and Sakmann in 1991 for their invention of the single-channel recording technique. Again, this work was highly technical in nature, and again the authors wrote in the accompanying biography about their love of biology and physics and the difficulty of choosing one over the other when applying for university (Nobel Media, 1991a,b).

Leaving Nobel prizes aside, it is fascinating to see how quickly technological advancements have influenced biology. Sticking with mid-twentieth century examples, the electronic negative-feedback amplifier concept was developed in the 1930s (Kline, 1993), patented in 1937 (Black, 1937), and formed the electronic basis of the voltage-clamp in 1947 (Huxley, 2002; Cole, 1968). When Hodgkin and Huxley performed their simulations in 1952, they used "a hand-operated calculating machine", but by 1960 both Richard Fitzhugh and Denis Noble had simulated APs on an analog (Fitzhugh) and a digital (Noble[5]) computer (Huxley, 2002; Fitzhugh, 1960; Noble, 1960). Before computational models were introduced, Balthazar van der Pol and Jan van der Mark used a system of flashing Neon tubes to model the normal heartbeat, sinoatrial block, and the impossibility of creating extra systoles by stimulating during the heart's refractory period. They published their findings with this electronic model in 1928 (Van der Pol and Van der Mark, 1928).

There are multiple conclusions we can draw from these examples, but the few I'd like to highlight are (1) there is a close and historical relationship between the mathematical sciences and biology, cardiac electrobiology in particular, (2) becoming proficient in more than one

[5]In fact, Noble used one of only *two* such devices available in the United Kingdom at the time.

subject should be encouraged at every level, and (3) investments in science can pay off in unexpected ways. These points may be relevant to those in charge of university structure, university curricula, and scientific funding.

CHAPTER 3

Myokit: A simple interface to cardiac cellular electrophysiology

This chapter is based on:

Michael Clerx, Pieter Collins, Enno de Lange and Paul G.A. Volders (2016). Myokit: A simple interface to cardiac cellular electrophysiology. In *Progress in Biophysics and Molecular Biology*. Volume 120, issues 1–3, pages 100–114.

Michael Clerx, Paul G.A. Volders and Pieter Collins (2014). Myokit: A Framework for Computational Cellular Electrophysiology. Presented at *Computing in Cardiology, Boston 2014*. Volume 41, pages 229–232.

Abstract

Myokit is a new powerful and versatile software tool for modeling and simulation of cardiac cellular electrophysiology. Myokit consists of an easy-to-read modeling language, a graphical user interface, single and multi-cell simulation engines and a library of advanced analysis tools accessible through a Python interface. Models can be loaded from Myokit's native file format or imported from CellML. Model export is provided to C, MATLAB, CellML, CUDA and OpenCL. Patch-clamp data can be imported and used to estimate model parameters. In this chapter, we review existing tools to simulate the cardiac cellular action potential to find that current tools do not cater specifically to model development and that there is a gap between easy-to-use but limited software and powerful tools that require strong programming skills from their users. We then describe Myokit's capabilities, focusing on its model description language, simulation engines and import/export facilities in detail. Using three examples, we show how Myokit can be used for clinically relevant investigations, multi-model testing and parameter estimation in Markov models, all with minimal programming effort from the user. This way, Myokit bridges a gap between performance, versatility and user-friendliness.

Contents

3.1 Introduction . . . 33
3.1.1 Tools for sharing models . . . 34
3.1.1.1 Combining models . . . 35
3.1.1.2 Comparing model results . . . 35
3.1.2 Sharing methods . . . 36
3.1.3 User-friendliness . . . 37
3.1.4 Tools used in model development . . . 38
3.1.5 Myokit . . . 38
3.2 Functionality . . . 39
3.2.1 Models of the cardiac cellular AP . . . 40
3.2.1.1 Multi-cell and tissue simulations . . . 41
3.2.2 Models in Myokit . . . 41
3.2.3 File format . . . 42
3.2.3.1 Model syntax . . . 43
3.2.3.2 Protocols . . . 44
3.2.3.3 Scripts . . . 44
3.2.4 Import and export . . . 45
3.2.5 Single and multi-cell simulation . . . 45
3.2.6 Advanced simulation and analysis . . . 46
3.2.7 Fitting patch clamp data . . . 46
3.2.8 Graphical user interfaces . . . 47
3.2.9 Implementation . . . 47
3.3 Usage . . . 49
3.3.1 A multi-scale experiment . . . 49
3.3.2 Multi-model testing . . . 51
3.3.3 Parameter estimation . . . 52
3.4 Discussion . . . 53
3.4.1 Dynamical systems . . . 53
3.4.2 Multi-cell modeling . . . 54
3.4.3 Sub-cellular modeling . . . 54
3.4.4 CellML support . . . 54
3.4.5 Direct editing and generic experiments . . . 55
3.5 Conclusions . . . 55
3.A Tools used in AP-model development . . . 56
3.B Coupled cells and the monodomain model . . . 57
3.C An example of a full model . . . 59

3.1 Introduction

Numerical models of the electrical processes in cardiac myocytes have been successfully used to elucidate the mechanisms of action potential (AP) formation, electrical propagation from cell to cell, and abnormal impulse formation and conduction in the heart (Noble et al., 2012). These models provide a vital bridge between drug targets, for example ion channels or receptors, and the dynamical factors leading to heart-rhythm disorders, such as pathologically altered conduction or repolarization (Weiss et al., 2015). The application of new and refined experimental methods has led to an increased level of detail and specialization in AP models, which may now include elements such as stretch-sensitive channels (Niederer and Smith, 2007), ion-channel phosphorylation (O'Hara et al., 2011) or signaling pathways (Heijman et al., 2011). Conversely, the growing awareness of the need to integrate models on different scales combined with the increased availability of computing power has broadened the scope for application of AP models considerably. As a result, AP models have more users and more uses than ever before, but also a far greater mathematical complexity and a greater reliance on the model builder's correct interpretation of complex multi-modal experimental data. Collaboration between experts from a wide range of disciplines is vital to further refine models and experiments and therefore the knowledge we obtain from them (Abriel et al., 2013).

Software tools can aid researchers using AP models in several ways. Firstly, the definition of open and unambiguous formats for model description allows models to be exchanged, inspected, compared, improved and revised. Publishing a model in a widely recognized format is an invitation for external feedback and can assist widespread adoption and recognition of modeling results. Comparison can be automated, allowing models to be tested against previous results from model or experiment each time a change is made. This way, models can be continuously refined without the danger of losing past results.

Secondly, sharing software for simulation and analysis is a way of sharing effort and expertise so that researchers may benefit directly from each other's work. Of particular importance in this respect, is the role of fiber and tissue simulations for the development of single-cell models. Many of the properties that a single-cell model should capture only emerge when cells are coupled, making such simulations a vital part of AP model development. However, the programming effort required to set up these simulations may deter some modelers from going down this route. By sharing software tools such barriers are taken away.

Finally, if tools are not just efficient but also easy to use then the time needed to set up experiments is decreased while the number of people able to do so (or willing to learn) is increased. This can aid collaboration by drawing more non-experts into computational biology while giving experts time to step outside their disciplines.

So how far have these benefits been realized in current software tools? In the next sections we

review existing software with a focus on the three goals of sharing models, sharing methods and user friendliness. We discuss the usefulness of these tools for model development and make two central observations: (1) Existing tools cater to AP-model use, more than to model development. These two goals have different, sometimes directly opposite needs. (2) There is a wide gap between easy-to-use simulation software with limited capabilities and powerful simulation tools that require considerable effort and programming skill from the user. Finally, we present Myokit, a tool for model development and analysis which aims to fill this gap.

3.1.1 Tools for sharing models

The most widely used language for sharing models of the cardiac AP is CellML (Hedley et al., 2001; Cuellar et al., 2003). While there are other exchange formats such as SBML (Systems Biology Markup Language, see Hucka et al., 2003) in which AP models can be formulated, CellML has broad support in the AP modeling community and a freely accessible repository containing over 160 models of the cardiac AP (`http://models.cellml.org`). The first specification (version 1.0) was finalized in 2001 and a second (version 1.1) was given definitive status in 2002. An overview of tools capable of working with CellML is available online (`http://www.cellml.org/tools`). The goal behind CellML is to facilitate universal exchange and re-use of mathematical models, particularly models of the electrophysiological and biochemical processes inside a cell.

A number of tools have been published to convert CellML to other languages, allowing CellML models to be used with a variety of tools. The CellML advanced programming interface (API) defines a number of ways to interact with a model, including translating it to other languages (Miller et al., 2010). An implementation of the API is available on the CellML website and can be used to translate CellML models to C, MATLAB and Python. Another conversion tool is AGOS (Barbosa et al., 2006), which can create simulation code for C++. It was modified by Amorim et al. (2010) to generate simulation code that can be run on graphical processing units (GPUs), thereby facilitating fast multi-cell simulations. PyCml (`http://chaste.cs.ox.ac.uk/cellml`) is a Python based utility that can be used to read and stringently validate CellML files before creating C++ model definitions.

The CellML language is specified using XML (eXtensible Markup Language), a widely used format for sharing documents over the internet. The choice for XML makes it easy for developers of software tools to incorporate a CellML import into their programs, as software libraries to work with XML documents are freely available for many different platforms. A downside of XML is that, while it is *human-readable* as well as *machine-readable*, it is not necessarily compact, nor easy to read or to write by hand. CellML equations in particular are specified in a subset of MathML (Mathematical Markup Language), which is unambiguous but highly verbose. In addition, good model definitions for archiving and

exchange are written out with consistent units, are well annotated with information about all the variables and define a rigid interface through which the model can interact with other models. These features, which are undoubtedly good for exchange formats, can be a hindrance to users wishing to rapidly experiment with different model formulations, making CellML less suited to model development.

3.1.1.1 Combining models

A major benefit of having models publicly available in a shared format is that models can be *combined*. For example, a model of the cardiomyocyte can be incorporated into an integrative model of the cardiovascular system. This is one of the key ideas behind the IUPS Human Physiome project, which seeks to connect the many specialized mathematical models used in biology (Bassingthwaighte, 2000; Hunter, 2004). The need for such model integration has driven the development of many of the tools discussed here.

A tool for combining models on the molecular level is Virtual Cell, also known as VCell (Moraru et al., 2008). It can model electrophysiology, reaction kinetics, membrane transport and diffusion processes to create a 3D model of a cell that can be related to experimentally obtained images. On a larger scale, tools such as CHeart (`http://cheart.co.uk`), Continuity (`http://continuity.ucsd.edu`) and OpenCMISS (Nickerson et al., 2015) can be used to create combined models of electrophysiology, contraction and the resulting fluid dynamics inside the heart.

A key idea in creating these combined, multi-scale models is that the resulting system is *modular*, i.e., that any model of a subsystem (for example a model of the cardiac cellular AP) can be replaced or updated without requiring changes to the other subsystem models. This requires that the models, at least in part, adhere to some well-defined structure about which there is a widespread consensus. Such fixed structures (called *ontologies* in software terms) contrast sharply with the creative aspects of model development where variables, for example currents, are continuously added, removed, split up and redefined. As a result, the aim of integrating different levels of physiology is not always compatible with the aim of accurately incorporating new experimental data.

3.1.1.2 Comparing model results

AP models represent theories on the electrophysiological functioning of the cell. As such, it should always be possible to compare model results with experimental data or predictions from competing models. A standard defining the Minimum Information for a Cardiac Electrophysiology Experiment (MICEE) has been approved by a large consortium of cardiac electrophysiologists (Quinn et al., 2011). Similarly, a standard defining the Minimum Information About a Simulation Experiment (MIASE) has been created by Waltemath et al. (2011a). SED-ML, the Simulation Experiment Description Markup Language, is a format

for sharing simulation experiments designed to meet the requirements set out in MIASE. It describes how a simulation should be designed and run in a manner that allows the results to be replicated on different systems. At the time of writing this manuscript, the standard does not yet meet the requirements needed to compare the output of different models or to compare the output of arbitrary models to experimental data. *Functional curation* is a standard proposed by Cooper et al. (2011, 2015b) to describe experiments and post-processing operations independently of a model. Such a standard can be of great use for systematic model development. For example, by creating a series of tests that a model must pass and regularly (re-)running them, a model builder can focus on highly specific subsystems (for example the influence of an intracellular calcium concentration on a particular current) without inadvertently changing other parts of the model. Comparing model output can also be useful to identify differences in emergent model properties[1] or to identify areas where different models disagree, which can be promising targets for investigation. A freely accessible on-line implementation of the functional curation standard was recently presented in the form of the Cardiac Electrophysiology Web Lab (Cooper et al., 2015a).

3.1.2 Sharing methods

Common methods employed in cellular electrophysiological research and model development include single-cell simulation, multi-cell simulation, large scale tissue- and whole-organ simulations as well as parameter estimation and sensitivity analysis. Tools for working with AP models can be divided into tools that work from a graphical user interface (GUI) and tools made available as programming libraries.

A good example of a GUI-based tool is OpenCOR (Garny and Hunter, 2015), a merger of the older tools COR and OpenCell/PCEnv. It provides an interface through which CellML models can be loaded, single-cell simulations are run and the results may be visualized. OpenCOR has full CellML 1.1 support and support for SED-ML and Python scripting is planned. Multi-cellular simulations are not supported.

CESE Plus 2.0 (Simulogic Inc., Halifax, NS, Canada) is a proprietary tool that provides a graphical environment from which single-cell simulations can be run using a selection of annotated cell models. Parameters can be modified and some graphical analysis tools are provided.

JSim (Butterworth et al., 2013) is a Java-based tool for simulation and analysis of mathematical models including various types of differential equations. It is mentioned here because it can import and export CellML models and provides methods for parameter estimation and sensitivity analysis. However, it does not cater specifically to models of the cardiac AP.

[1] Emergent properties are properties that are not explicitly encoded in a model but arise from the interplay of various elements. An example in cardiac AP models is the action potential duration, which is not set by the modeler but emerges as a result of the balance of depolarizing and repolarizing currents.

CSim (http://code.google.com/p/cellml-simulator) is a stand-alone utility for running single-cell simulations intended for use as a back-end to other more elaborate packages. As such, it has no graphical front-end and does not provide any further modes of analysis.

DENIS (Castro et al., 2016) is a recently developed project that aims to build a large network of volunteers whose computers can be used during "idle time" to perform electrophysiological simulations. In its first implementation DENIS is focusing on single-cell models only, but work is in progress to extend the project to include multi-cellular GPU simulations.

The C++ library Chaste (Mirams et al., 2013; Cooper et al., 2014) is the first tool discussed here that performs single and multi-cell simulations. Chaste uses models encoded in C++ (optionally converted from CellML using PyCml) to run high-performance single-cell, monodomain or bidomain simulations. Before running, many intermediate optimizations are applied to reduce computation times. The first (and so far only) implementation of functional curation is based on Chaste. A downside to Chaste is that it requires some programming effort to use. For model development, users can modify either C++ or CellML code.

Large scale tissue and organ simulations face additional problems that do not occur on the cellular level, for example fiber orientation, mesh generation and the creation of patient-specific heart geometries. These tools usually assume that the user is a skilled programmer who uses the tool to set up complex simulations that need to be run on high-performance distributed computing systems. Good examples are CARP (Vigmond et al., 2003), Continuity and OpenCMISS. At this scale, detailed cellular electrophysiology is often sacrificed for computational speed and the ability to investigate higher-level properties such as mechanical stress and strain or fluid dynamics.

Finally, a number of tools exist that tackle the numerical complexity of whole-heart simulations not by addressing state-of-the-art hardware and software, but by creating simplified cell models that can be combined into a high-performance model of the whole heart. This is an interesting and fruitful area of research, but as it concerns building specialized models rather than creating model-independent software tools, it lies outside the scope of this review.

3.1.3 User-friendliness

A number of tools have been released to make working with AP models more user-friendly and less time-consuming. OpenCOR contains a graphical interface for running single-cell simulations, changing parameter values and annotating models. Equations can be changed by editing CellML either directly or via a friendlier short-hand syntax using the recently re-introduced "CellMLTextView". Another friendly tool is CESE Plus 2.0, which uses annotated models that hide the equations from the user completely. CESE's interface can

be used to run single-cell simulations and change model parameters, but model equations are fixed. JSim features a GUI and uses its own "Mathematical Modeling Language" to represent model equations but has no specific focus on modeling the AP, which means users will need to implement their own methods using JSim's mathematical tools.

Other tools for working with CellML models are available, such as CellMLGUIgo (http://www.cellml.org/tools), which provides a minimalistic graphical representation of the components in a CellML model and allows raw MathML to be modified. CellMLViewer (Wimalaratne et al., 2009) can visualize the structure, but not the equations of a model in CellML. Finally, educational tools such as eSolv (http://www.esolv.nl) provide an intentionally limited set of simulation options that let students use modeling to explore the current understanding of the cardiac AP.

3.1.4 Tools used in model development

From the review above, it becomes clear that none of the tools discussed are targeted specifically at AP-model development and that tools for simulation of the cardiac AP are either user-friendly and simple, allowing only single-cell experiments, or very powerful but more difficult to use. We investigated the tools used by model developers by conducting a review of the AP models listed in the recent overview provided by Noble et al. (2012). Models from this overview were only included in our analysis if they were published in 2002 or later, i.e., after the first CellML version was finalized. In this subset of 60 models, we found most developers favored a custom implementation using either MATLAB, C, C++ or Fortran. The full table is given in Section 3.A.

The choice for these languages is not surprising: C and Fortran stand out as programming languages due to the availability of established, well-tested, numerical tools. In particular, the Fortran library LSODE (Hindmarsh, 1983) and the later C version CVODE (Hindmarsh et al., 2005) have been used by several groups. Any C routine can also be run in C++ which has additional advantages when creating complex programs or using libraries written specifically for C++. MATLAB provides wrappers around many C and Fortran routines, making them easier to use from a graphical environment, and also provides visualization and scripting options as well as thorough documentation. However, such custom implementations do not benefit from the previous work by other researchers and require the user to fully understand both the model and the programming techniques required to best implement and solve them. Most importantly, this situation makes it more difficult for researchers to compare models and reproduce results without requiring model translation, which is an error-prone process.

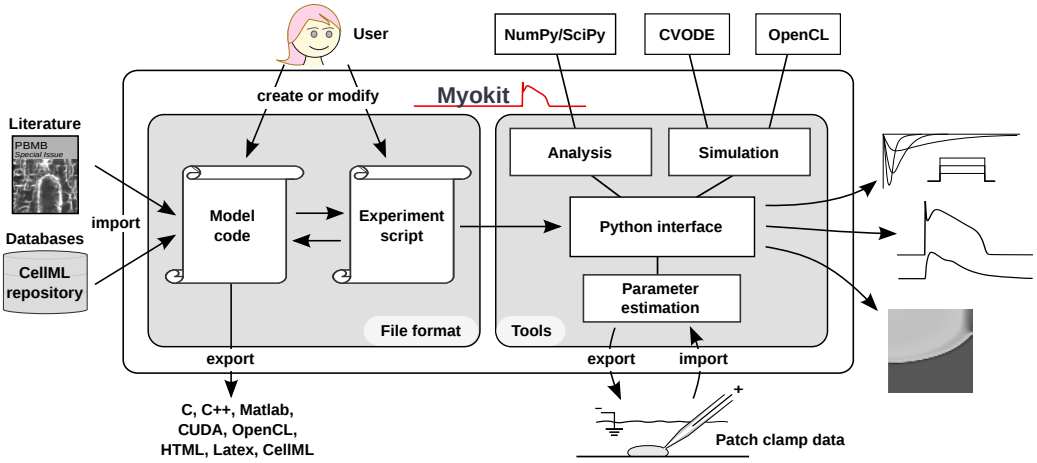

Figure 3.1: A schematic overview of Myokit's main functionality. Models are created, transcribed from literature or loaded from a database and written in a compact, easy-to-read syntax. The experiment to be performed is specified in a script which accesses the various tools provided through Myokit's Python interface. Behind the scenes the framework makes use of existing external libraries to provide high performance. The results can be processed directly or stored for later analysis. Export of model files is provided to allow interaction with existing software.

3.1.5 Myokit

In this chapter we present Myokit, a tool specifically created for AP model simulation, analysis, and development that bridges the gap between hard-to-use powerful libraries and user-friendly but limited simulation tools. Myokit uses an easy-to-read model definition language that allows users to interact directly with model equations without the drawbacks of working in a low-level programming language or an XML-based annotated exchange format. Simple simulations can be run directly from a graphical user interface while advanced experiments are easily set up using the popular scripting language Python. High performance is guaranteed by using on-the-fly compilation of generated C code, allowing Myokit to exploit CVODE for single-cell simulations and use OpenCL for parallelized multi-cell simulations. Tools for reading and writing of electrophysiology experimental data formats are included along with routines for parameter estimation. Myokit can be integrated with NumPy/SciPy (Jones et al., 2001) to create a powerful scientific computing environment similar to MATLAB or Octave. Models can be manipulated directly from the Python interface so that experiments can be fully automated or written in a model-independent fashion. Finally, CellML import and export is provided, as is import from SBML and ChannelML, and export to C, MATLAB and others. Myokit's main components are illustrated schematically in Fig. 7.1 and described in detail in the remainder of this chapter.

3.2 Functionality

We now describe Myokit's main features, including its model definition language, simulation engines and import/export facilities. A short description of Myokit's implementation is also provided.

3.2.1 Models of the cardiac cellular AP

Models of myocyte electrophysiology are commonly formulated as systems of ordinary differential equations (ODEs) that provide formal, testable hypotheses about the cellular processes that interact to form the cardiac AP. Examples of action potentials generated from six cell models are shown in Fig. 3.2. A general mathematical form of a model describing the cardiac single-cell AP is

$$\frac{\mathrm{d}V}{\mathrm{d}t} = -\frac{1}{C}\big(I_{\mathrm{ion}}(V,u,p) + I_{\mathrm{stim}}\big) \tag{3.1}$$

$$\frac{\mathrm{d}u}{\mathrm{d}t} = f(V,u,p) \tag{3.2}$$

Here, V is the transmembrane potential, C is the membrane capacitance and t represents time. The vector u holds the time variant quantities describing the current state of the cell, which typically consists of intracellular ion concentrations and variables describing channel configurations such as activation, inactivation or Markov model states. Model parameters, for example fixed concentrations or myocyte dimensions are contained in the vector p. The change in membrane potential $\mathrm{d}V/\mathrm{d}t$ depends on the sum of currents passing through the cell membrane. Currents due to an external stimulus, commonly applied to excite the cell, are represented by I_{stim}. The sum of the remaining transmembrane currents (sodium currents, calcium currents, the sodium-potassium pump current etc.) is written as I_{ion}. The size of these currents depends on V, on the ion concentrations and channel states contained in the vector u and on the parameters p. All transmembrane currents are defined using the common convention that a positive current has the net effect of carrying positive charge *out* of the cell. The time dependent behavior of the variables in u is specified by the function $f(V,u,p)$. The exact definition of f is what makes a cell model unique.

3.2.1.1 Multi-cell and tissue simulations

To set up multi-cellular simulations, the equations for a single cell are duplicated and the cells are coupled by introducing a diffusion current. Each cell i in the system is then described by

$$\frac{\mathrm{d}V_i}{\mathrm{d}t} = -\frac{1}{C}\big(I_{\mathrm{ion},i}(V_i,u_i,p_i) + I_{\mathrm{stim},i} + I_{\mathrm{diff},i}\big) \tag{3.3}$$

$$\frac{\mathrm{d}u_i}{\mathrm{d}t} = f(V_i,u_i,p_i) \tag{3.4}$$

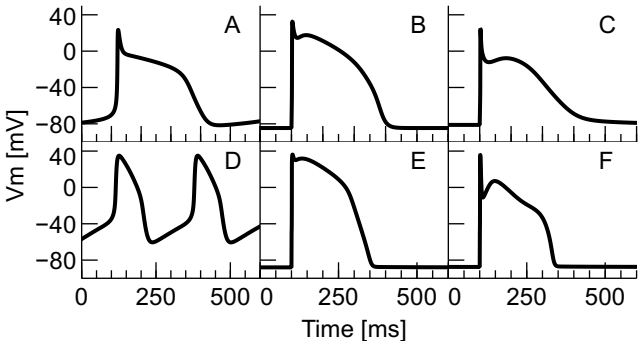

Figure 3.2: Action potentials generated from various models using Myokit. (*A*) Purkinje fiber, Noble (1962) (*B*) Mammalian ventricular myocardial fiber, Beeler and Reuter (1977) (*C*) Human atrial myocyte, Courtemanche et al. (1998) (*D*) Rabbit sino-atrial node cell, Demir et al. (1999) (*E*) Human ventricular myocyte, O'Hara et al. (2011) (*F*) Canine epicardial myocyte, Heijman et al. (2011)

Currents passing between connected cells i and j are assumed to follow Ohm's law, so that

$$I_{\text{diff},ij} = g_{ij}(V_i - V_j) \tag{3.5}$$

where g_{ij} is the conductance of the connection between the two cells and $I_{\text{diff},ij}$ is the current flowing from cell i to j. The total current $I_{\text{diff},i}$ for each cell i is then given by

$$I_{\text{diff},i} = \sum_j g_{ij}(V_i - V_j) \tag{3.6}$$

Note that this formulation allows for arbitrary connections between the cells, allowing complex geometries to be captured in this form. In the equations above, the parameter values p_i may be varied from cell to cell to introduce tissue heterogeneities. The constants g_{ij} can be varied spatially to model heterogenous conduction, or they may be replaced by variable conductances to incorporate detailed models of gap junction behavior. In a further extension on this scheme, we can allow the function f and the size and meaning of the vector u to vary from cell to cell. This allows simulations with multiple models to fit in this scheme, for example to investigate AP propagation at the Purkinje-ventricular junction. Under certain conditions, solutions to the monodomain model can also be made to fit this form (see Section 3.B).

3.2.2 Models in Myokit

A model in Myokit is simply a set of equations, where each equation uniquely defines a variable. Models are divided into *components*, which indicate a functional or conceptual relationship among a group of variables. For example, a component may hold all variables relating to the fast sodium current or calcium dynamics. Variables, in turn, can have child variables visible only to themselves. This allows long equations to be split into parts and facilitates the re-use of common variable names such as `alpha` or `beta`. Myokit uses a

declarative rather than a *procedural* language: details such as variable types and the order in which to evaluate the equations are not specified by the user but determined automatically by the software. As such, users specify the model to be solved, not the procedure by which to do this.

Models, components and variables can have plain text *meta-data* properties associated with them. For example, a model can define a property "description" with information about the model's origins. Units can be added to variables and numbers appearing in equations. Methods are provided to check for unit consistency, but this is not required for simulation.

A model's variables can be annotated using a system of *labels* (for output) and *bindings* (for input). A Myokit model is self-contained: every variable that the model uses must be contained within the model itself. However, a variable may define a *binding* to an external value. Simulation engines that recognize this binding can then replace the variable's equation with the provided value. For example, multi-cell simulations use the binding `diffusion_current` to identify the model variable representing I_{diff} and use it to insert the calculated current.

Variables that may be needed outside of the model are indicated with *labels*. For example, the label `membrane_potential` is used to indicate the model variable representing V. Multi-cell simulations read this variable's value and use it to calculate the diffusion currents between connected cells.

3.2.3 File format

Experiments in Myokit are defined in three parts: a model, a stimulus or voltage clamp protocol and a script. This is reflected in Myokit's file format, which can contain a `model`, a `protocol` and a `script` section. Each of the sections is optional, so that it is possible to have a file with a reference version of a model and several other files containing only scripts that load this model and use it in an experiment. Alternatively, a file containing all three sections is a compact and full description of an experiment which can be archived or shared with students and colleagues. Even for reference implementations of models it is often useful to include a short demonstration in the experiment section so that users downloading the model can immediately see it in action. Myokit files use the extension `.mmt` and are written in plain-text. Using plain text files has a number of advantages: (1) users can open them in any editor, (2) models and experiments can be emailed without security warnings, and (3) versioning systems (such as Git or Subversion) can track changes and efficiently store plain text files. The syntax used in each section is briefly discussed below. The full technical specification of the file format is found in the online documentation (`http://docs.myokit.org`). Examples of a (partial) model, protocol and script are given in Fig. 3.3, and a full model is given in Section 3.C.

```
[ina]
use membrane.V as V
gNa = 4 [mS/cm^2]
ENa = 50 [mV]
INa = gNa * m^3 * h * (V - ENa)
    in [uA/cm^2]
    desc: The fast sodium current
dot(m) = alpha * (1 - m) - beta * m
    alpha = (V + 47) / (1 - exp(-0.1 * (V + 47)))
    beta = 40 * exp(-0.056 * (V + 72))
dot(h) = alpha * (1 - h) - beta * h
    alpha = 0.126 * exp(-0.25 * (V + 77))
    beta = 1.7 / (1 + exp(-0.082 * (V + 22.5)))
```

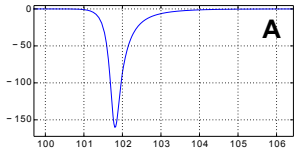


```
# Level  Start    Length   Period   Multiplier
1.0      100      0.5      1000     0
```

B

```
import myokit
# Get the embedded model
# and protocol
m = get_model()
p = get_protocol()
# Create a simulation
s = myokit.Simulation(m, p)
# Simulate 1000ms
d = s.run(1000)
# Use maplotlib to visualize the results
import matplotlib.pyplot as pl
pl.figure()
pl.plot(d['engine.time'], d['membrane.V'])
pl.show()
```

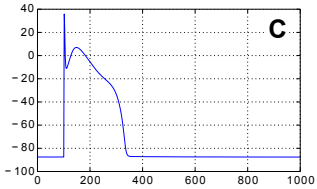

Figure 3.3: (*A*) An example of a fast sodium current component in Myokit. The inset shows the resulting current during a normal AP. (*B*) A pacing protocol specifying a 0.5ms pulse every 1000ms, with the first pulse occurring at t=100ms. (*C*) A basic Python script using Myokit and the resulting simulated membrane potential.

3.2.3.1 Model syntax

Myokit models are written in a clear and unambiguous syntax. An example of a component representing the sodium current is given in Fig. 3.3.A. The component is defined by writing its name enclosed in square brackets. Directly below this header, variables and component-level meta-data can be added. The component declares two constants, an intermediary variable `INa` and the states `m` and `h`, which are defined through their time derivative indicated using the `dot()` operator. Nested variables, units and variable meta-data are indicated by writing them below the parent variable on an indented line. For example, the current variable `INa` has a meta-data property "desc" which provides a description of the variable's meaning. A unit for `INa` is declared using the `in` keyword. The variable `ENa` does not have a variable associated with it directly, but one can be derived from its defining equation. Variables from other components can be used by specifying their component name, for example `x = 5 + membrane.V`. In this example an *alias* is defined for `membrane.V`, allowing the usage of the shorthand `V`. An example of a full model specification is given in Section 3.C, and further examples are provided in the supplementary materials. The full, technical specification of Myokit's model language, and many more models and examples can be found online at http://myokit.org.

3.2.3.2 Protocols

Protocols in Myokit are used to create the signals used to periodically stimulate or voltage clamp a model. An example of a simple periodic pacing protocol is shown in Fig. 3.3.B. A protocol contains one or more *events*, where each event has a specified starting point, duration, and amplitude. Events can be set to repeat indefinitely with a certain period or to occur a fixed number of times. This allows the various pacing protocols commonly used in AP-model experiments to be implemented, as well the step protocols needed to voltage clamp a cell. Having the protocol separated from the model has two main advantages. Firstly, it allows models and protocols to be easily exchanged: a model can be run with multiple protocols and the same protocol can be applied to many different models. Secondly, having a separate protocol specification makes it easier for simulation engines to deal with the discontinuities created by the protocol. Models of cells displaying automaticity can be used without a protocol.

3.2.3.3 Scripts

The script section of a Myokit file is used to store a short Python program to set up and run an experiment. This script can access the model and protocol stored in the same file, but may also load models and protocols from external files. Scripts have access to Myokit's full range of capabilities through a Python API. In addition, scripts can import any number of existing Python modules, such as the popular NumPy/SciPy stack which provides a wealth of tools for numerical analysis and the Matplotlib library (Hunter, 2007) for data visualization. The result is a powerful open-source modeling environment which is a viable alternative to proprietary frameworks such as MATLAB and is specifically tailored to the needs of cardiac cellular electrophysiology.

An example of a simple script running a single-cell simulation is shown in Fig. 3.3.C. First, the Myokit module is loaded (line 1). Next, the model and protocol are read from the other sections of the file (lines 4 and 5). These are then used to create a simulation engine (line 7) whose `run()` method is called to perform a 1000ms simulation (line 9). The results are returned to the user as a dictionary containing the logged data for all variables. The example finishes by loading a visualization library (line 11) and using it to create a plot of the results (lines 12-14).

Models can be edited by modifying the model code directly, but also *programmatically* from the experiment script. For example, in Fig. 3.3.C, after loading the model (line 4) a change could be made to the model before passing it to the simulation (line 7). This way the simulation would be run with a modified version of the model contained in the file. Programmatically modifying models allows experiments to be automated, for example to explore or optimize a set of parameter values.

3.2.4 Import and export

Models can be imported from the exchange formats CellML, SBML (Hucka et al., 2003) and ChannelML (Gleeson et al., 2010). Model import from CellML gives users access to nearly 200 cardiac AP models listed in the CellML model repository and allows modelers to find the model that's best suited to a particular experiment, or to test their hypotheses in a multitude of models. Myokit model definitions can be exported to several formats including CellML, MathML, C, C++, MATLAB/Octave, CUDA and OpenCL for analysis. For presentation purposes, equations can be exported to LaTeX or MathML, allowing PDF and HTML documents to be created. Model equations can be imported from and exported to the computer algebra system SymPy (Joyner et al., 2012), allowing advanced symbolic manipulation. Data from patch-clamp recordings can be read from ABF, ATF, WCP and CSV formats. Simulated waveforms can be exported to protocol files usable with Axon software or WinWCP (Strathclyde Electrophysiology Software).

3.2.5 Single and multi-cell simulation

Myokit's single-cell simulation engine uses the implicit adaptive multi-step solver CVODE. This solver provides excellent performance on stiff systems of differential equations which arise naturally in cellular electrophysiology (see Cooper et al., 2014, and Chapter 4). The solver can be stopped or restarted at any time, allowing simulation results to be saved to disk so that the simulation can be restarted later. Threshold-crossing detection is provided which can be used to accurately measure action potential durations.

A versatile parallelized forward-Euler solver similar to Sato et al. (2009) is implemented in Myokit for multi-cellular simulations. This engine uses OpenCL (Stone et al., 2010) to simulate large numbers of cells in parallel on multi-core CPUs (Central Processing Units), GPUs or FPGAs (Field-Programmable Gate Arrays). By default, it is set up for rectangular grids of homogeneous cells, coupled with a uniform conductance g_x for 1-dimensional simulations, and an additional conductance g_y for simulations in 2-d. However, users can also specify the individual connections between cells, allowing heterogenous conduction properties and more complex geometries to be used. Further heterogeneity of tissue properties can be introduced by varying model parameters from cell to cell. Additionally, by disabling cell-to-cell conduction, users can exploit the engine's parallelization to perform a large number of single-cell simulations with different parameters. Finally, under certain conditions the engine can be used to find solutions to the monodomain model (see Section 3.B). For users who do not wish to install an OpenCL driver, a simpler one-dimensional forward-Euler solver for single core CPU is supplied.

3.2.6 Advanced simulation and analysis

In addition to fast single and multi-cell simulations Myokit provides a number of specialized tools for advanced analysis and simulation. A method based on automatic differentiation (Griewank and Corliss, 1991) is included that can numerically approximate an AP model's Jacobian matrix for any point reached during a simulation. This can be used to evaluate the system's stability (i.e., the robustness of the AP against small perturbations) which can be relevant when investigating phenomena such as early afterdepolarizations.

A specialized simulation engine is provided that combines automatic differentiation with a simple forward-Euler scheme to calculate partial derivatives of model variables with respect to model parameters. In Section 3.3.1 this is used to show how the membrane potential's sensitivity to a particular current changes over time. A different use is illustrated in Clerx et al. (2015), where this capability is used to investigate parameter identifiability using the method described by Fink and Noble (2009).

In a second simulation engine, automatic differentiation is employed to calculate the derivative of the state with respect to the initial conditions. This can be useful when investigating periodicity, for example to evaluate the stability of a periodic orbit or as part of a scheme to find such orbits. However, the practical feasibility of applying these methods to complex AP models has not yet been fully explored.

Finally, a method is provided to perform fast simulations of currents described by Markov models during voltage step protocols. In this method, Myokit's SymPy import/export is utilized to check if a user-supplied set of model states can be rewritten as a linear system of differential equations for a fixed membrane potential. If this condition is met, the currents elicited during a piecewise-linear voltage-step protocol can be calculated using eigenvalue decomposition. The performance boost this provides compared to ODE-integrating methods is particularly useful in the context of parameter estimation, which may require thousands of such simulations.

3.2.7 Fitting patch clamp data

Import facilities are provided for patch-clamp data in the formats used by Axon and Strathclyde Electrophysiology software. The data is made available to the user in the same format as simulation data, allowing direct comparison of the two. Users can then define an error function to be minimized (see also Section 8.2.1.1). To this end, two global heuristic-based derivative-free optimization methods are provided: particle search optimization and a genetic search algorithm. Both methods have been shown to perform well for global estimation of ion-channel model parameters (Wilhelms, 2013). Solutions can be further refined using the local derivative-free optimization methods provided by SciPy. Parameter estimation in Markov models can be sped up using Myokit's fast Markov model simulations for step

protocols. Finally, parameter sensitivity analysis can be used to test if a given protocol is able to uniquely identify all parameters in a model. This can be used as a tool for model development and protocol design.

3.2.8 Graphical user interfaces

An integrated development environment (IDE) is provided to edit `mmt` files and run simulations, as shown in Fig. 3.4. It displays the model, protocol and script sections of an `mmt` file on different tabs and contains several functions to visualize the structure of the model. Equations can be visualized by selecting them with the cursor and using the "graph variable" option. Single-cell simulations can be run without scripting by using the "Explorer". This opens up a separate window that lets users run simulations and inspect the results. Parameters can be changed in the model code in-between explorer simulations, allowing the results to be compared. A GUI for visualizing one- and two-dimensional simulation results is also included.

3.2.9 Implementation

Myokit is written in Python, a language that was originally designed for educational purposes and which has an easy-to-read, uncomplicated syntax. For high-performance tasks such as simulations, Myokit automatically generates and compiles code in C or C++. This allows simulations to run at the speed normally associated with low-level languages without requiring low-level programming from the user.

All GUI components are based on the PyQt library (http://www.riverbankcomputing.co.uk). These modules are built as *extensions* to Myokit, and are explicitly not part of its core. This ensures that Myokit can safely be used with other GUI toolkits, in standalone Python scripts, or within scientific environments such as Spyder (http://github.com/spyder-ide/spyder). Similarly, while some of Myokit's methods are designed to work with the Python graphing package Matplotlib, none of the core functions rely on it so that Myokit can be safely used with alternative packages.

Myokit requires a C99 compatible compiler such as GCC, which is commonly found on any Unix-based system (including Linux and OS X). Users of Microsoft Windows may need to install a GCC based version of Python. The Myokit website contains detailed instructions on how to install and uninstall Myokit.

Myokit is open-source and licensed under the GNU General Public License (GPL). It runs on Linux, Windows and OS X. Source code, example files, full documentation and a Windows installer can be downloaded from the Myokit website (http://myokit.org).

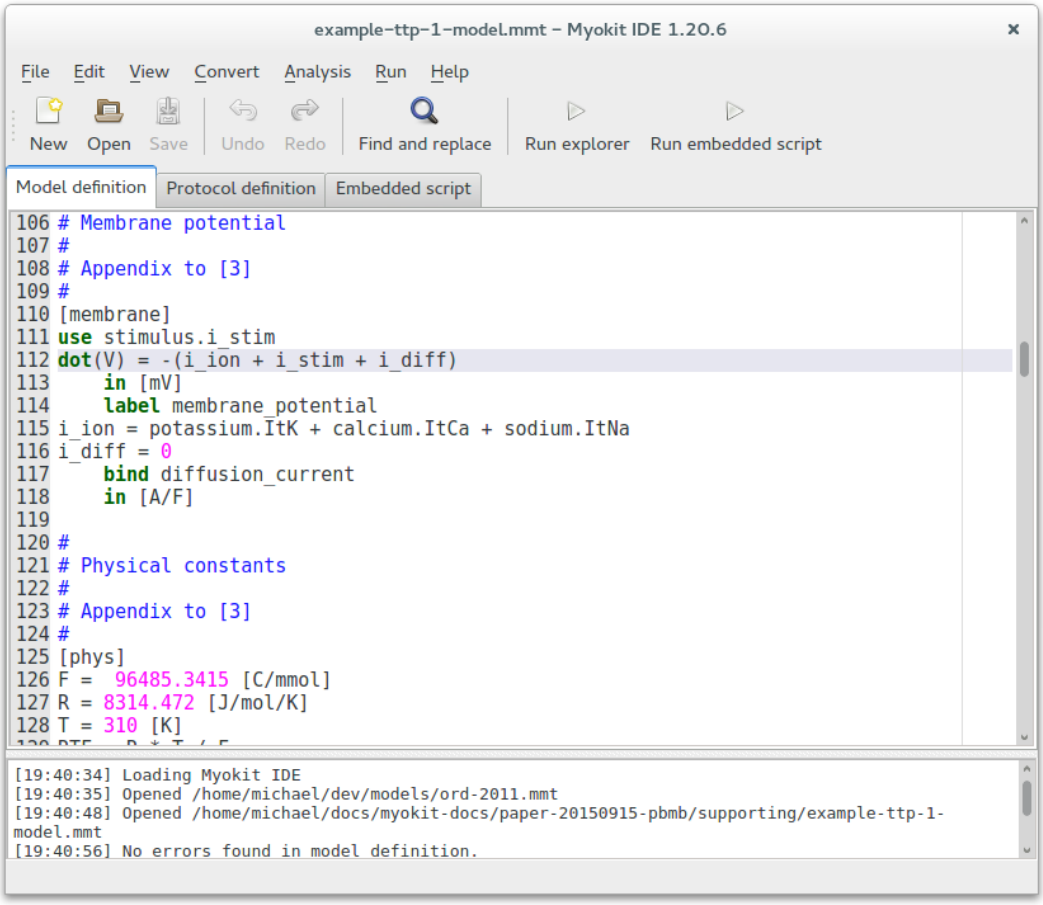

Figure 3.4: The Myokit IDE, open on the model definition tab. Using the IDE, users can edit the model, protocol and script sections of `mmt` files and run simulations using the Explorer or the script.

3.3 Usage

We now provide a few examples of how Myokit can be used in AP modeling practice. The `mmt` files for all examples presented here are included as supplementary materials to the published paper (Clerx et al., 2016) and can be run or modified in the Myokit IDE. To run the multi-cellular simulations in the first example an OpenCL driver must be installed. The parameter estimation example requires SciPy and SymPy to be installed; these are included by default in many Python distributions.

3.3.1 A multi-scale experiment

In this first example we demonstrate the power of Myokit to run multi-cellular simulations of clinically relevant situations. While the results shown here are not novel *per se*, we use them to illustrate how such simulations can be set up in Myokit with only a few lines of scripting code, thereby paving the way for further analysis.

Transmural differences of the right-ventricular myocardium have been linked to Brugada syndrome and VT/VF (Yan and Antzelevitch, 1999). In particular, changes to the balance between fast sodium current I_{Na}, transient outward current I_{To} and L-type calcium current I_{CaL} may lead to alternating loss of dome in epicardial cells, which can trigger a reentrant wave originating from the epicardium (Yan and Antzelevitch, 1999; Dumaine et al., 1999; Nademanee et al., 2011). We now demonstrate how Myokit can be used to investigate the mechanism underlying this phenotype on the cell, fiber and tissue level.

We selected the model of the human ventricular AP by ten Tusscher and Panfilov (2006), or TTP-2006, as it incorporates transmural differences in ion currents and has been shown to recreate both physiological and pathological propagation. The model was downloaded from the CellML repository and imported into Myokit. After importing the hard-coded stimulus current was replaced by a stimulus using Myokit's pacing mechanism and the three models; epicardial, endocardial, and midmyocardial were merged into a single file with a cell-type switch (see *example-ttp-1-model.mmt* and *example-ttp-2-transmural-differences.mmt*).

An epicardial AP generated by Myokit from TTP-2006 is shown in Fig. 3.5.A. To recreate the observed pathological behavior, we changed the balance between inward and outward currents in the early phase of the AP by modifying the I_{To} conductance parameter g_{To}. APs generated for increasing values of g_{To} are plotted in Fig. 3.5.B: the notch is seen to gradually deepen, eventually leading to a complete loss of dome (see *example-ttp-3-gto.mmt*). Further analysis of the influence of g_{To} on the model AP is presented in Fig. 3.5.C. Here, the top panel shows the current itself while the lower panel displays the derivative of the membrane potential with respect to the conductance g_{To}. This illustrates the size of the effect small changes in g_{To} will have on the AP at different points in time. This quantity, though not easy to verify experimentally, can be highly illustrative of model behavior: it shows clearly

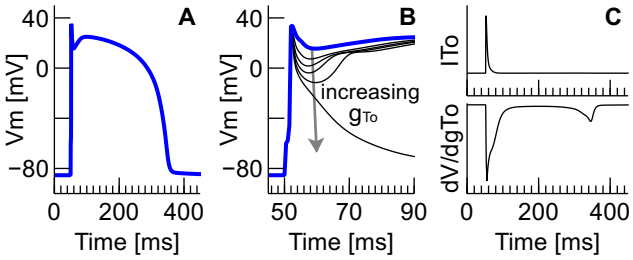

Figure 3.5: (*A*) The baseline epicardial AP generated from TTP-2006. (*B*) Effect of increasing g_{To} on the notch in the AP. The original unchanged AP is shown as the thick line at the top, successive increments push it to more negative potentials, eventually leading to a complete lack of dome (bottom line). (*C*) I_{To} current density and sensitivity of the AP to small changes in g_{To}. Slight changes in g_{To} affect the early and late stages of the AP, long after the current itself has inactivated.

that the current's effects last much longer than the current itself as it influences both notch depth and action potential duration (see *example-ttp-4-sensitivity.mmt*).

We then set up a multi-cellular simulation to study transmural propagation. Following Bébarová et al. (2008) we used a fiber consisting of 60 endocardial, 45 mid-myocardial and 60 epicardial cells with a stimulus applied at the endocardial end. The cell-to-cell conductance was set to match a transmural conduction velocity of approximately 50 cm/s (Taggart et al., 2000). The APs from cells in different parts of the fiber are shown in Fig. 3.6.A. Under baseline conditions the traces are almost indistinguishable: a slight delay between the activation of the endocardial and epicardial cells can be seen, and APs from mid-myocardial and epicardial cells display a slight notch. The strong coupling between the cells creates an almost homogeneous action potential duration throughout the strand, so that midmyocardial cells no longer display a prolonged AP. A pathological case was created by reducing cell-to-cell conductance, decreasing g_{CaL} to 50% (Antzelevitch et al., 2007), increasing epicardial and midmyocardial g_{To} to 250% and adding a shift in I_{To} voltage dependence. With these modifications the epicardial cells alternate between a delayed dome

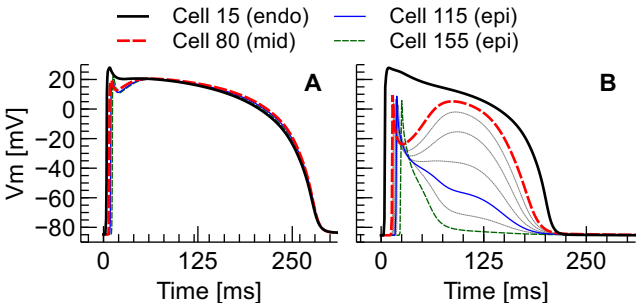

Figure 3.6: (*A*) Baseline action potentials from different cells in a transmural fiber simulation are almost indistinguishable. (*B*) APs from cells in a transmural strand with increased g_{To} and reduced g_{CaL}. Selected cells between cell 80 and 155 are shown in gray to illustrate transmural development of loss-of-dome.

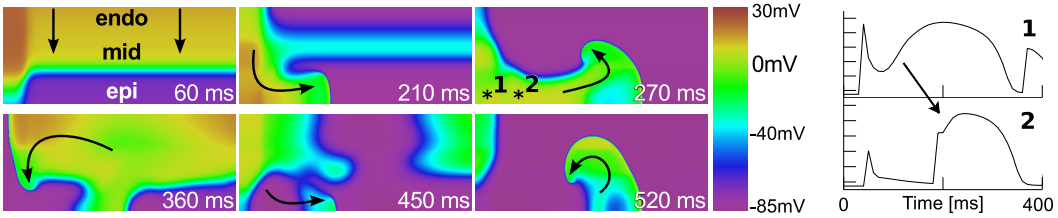

Figure 3.7: (*left*) Reentrant wave in a transmural plane of 400x165 cells. A stimulus is applied endocardially and seen to travel towards the epicardium. Heterogeneous g_{CaL} causes conduction block in all but the left-most epicardial cells. The epicardial cells that do depolarize then cause a wave that propagates through the epicardium before reentering the repolarized endocardium, triggering a spiral wave. (*right*) Calcium-driven conductance from a delayed-dome cell to a loss-of-dome cell initiates an ectopic AP in the tissue simulation. The location of the cells is indicated by *1* and *2* in the top-right panel (270 ms).

and complete loss of dome. A loss-of-dome beat is shown in Fig. 3.6.B (see *example-ttp-6-transmural-modified.mmt*)

To see how transmural loss of dome can lead to reentry, the fiber experiment was extended to a simulation of a transmural plane measuring 400 by 165 cells. Again, I_{To} was increased (this time only in the epicardial cells) and the conduction speed was lowered. I_{CaL} conductance g_{CaL} was set to 75% for the left 10% of cells and to 30% for the remainder. Under these conditions, a severely delayed dome in the left 10% can trigger a new depolarization in a neighboring loss-of-dome cell. The resulting reentrant wave is visualized in Fig. 3.7 and a video is included in the supplement.

3.3.2 Multi-model testing

In the previous example, changes to models were made directly in the `mmt` model definition. In this example, which is included in the supplementary materials as *example-multi-model-testing.mmt*, we show how to run experiments whilst only making changes from the script. This can be of great practical use when comparing models or during incremental model development. Twelve `mmt` files are used, each containing either a human or canine model or a model variant for a specific cell type. The example script loads each of these models, creates an appropriate protocol (1000ms cycle length) and runs a simulation. The model files are annotated with labels for the membrane potential and the L-type calcium current, allowing the script to identify these variables and modify them. The membrane potential variable is tracked by the simulation to calculate an action potential duration (APD). Next, the defining equation for the L-type calcium current is modified to be 50% of its original value. A second simulation is then run with this updated model and the APD is measured again. The resulting APD differences are plotted in Fig. 3.8. While the human models agree an APD shortening should occur, there is no consensus about the degree of shortening or the transmural differences. The canine models are divided about the direction of the change, but generally favor a smaller change than the human models.

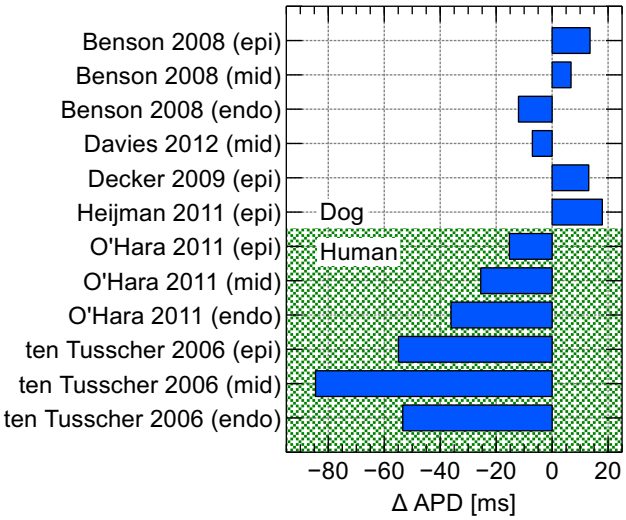

Figure 3.8: Action-potential duration prolongation (positive) or shortening (negative) due to blocking of the L-type calcium current, tested in several models. The top six results are in the canine ventricular models of Benson et al. (2008), Davies et al. (2012), Decker et al. (2009) and Heijman et al. (2011). The lower six results are from the human ventricular models published by O'Hara et al. (2011) and ten Tusscher and Panfilov (2006). Results are included for epicardial (epi), mid-myocardial (mid) and endocardial (endo) cells.

3.3.3 Parameter estimation

As a final example, we show how Myokit can be used for parameter estimation in Markov models, a common step in model development. Two examples are provided: The first, given in the supplementary material as *example-parameter-estimation.mmt*, uses simulated data while the second, given as *example-parameter-estimation-2.mmt*, uses currents obtained from a patch-clamp experiment.

In both examples, a cell model is loaded and the variable representing membrane potential is identified. The membrane potential is clamped to $V = -140mV$ and the model is simulated for 30 seconds to let the sodium channels move into a steady state. Next, a number of parameters of the Markov model for I_{Na} are selected and Myokit's `MarkovModel` class is used to extract a parametrizable, linear Markov model from the cell model. A set of reference currents is then obtained, either through simulation or by loading and pre-processing a patch-clamp data file. The experimentally obtained currents are shown in Fig. 3.9.A.

Next, a score function is defined that takes a set of parameter values as input, calculates the resulting currents and returns the sum of squares difference with the reference currents. A wide set of boundaries is defined for all parameters and a global search for the smallest error is run starting from random positions within these bounds. Using particle search optimization a set of parameters providing a good fit is found. This solution is then refined using a

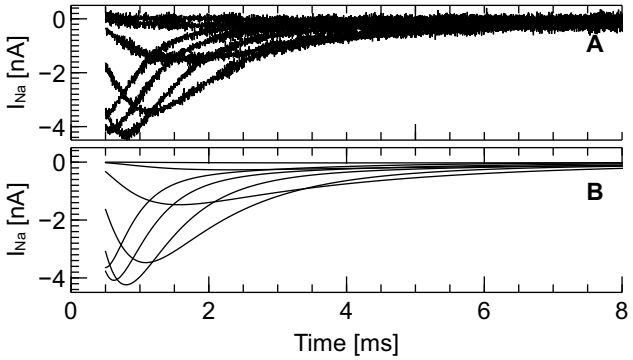

Figure 3.9: Sodium currents elicited by a voltage step protocol. (*A*) Experimentally obtained currents in a Chinese hamster ovary cell stably transfected with *SCN5A*. (*B*) Currents calculated with the values found by the parameter estimation method.

local search method, in this case the Nelder-Mead simplex algorithm provided by SciPy. Simulated currents from the model fit to the experimental data are shown in Fig. 3.9.B.

3.4 Discussion

The strengths and weaknesses of any well-implemented software tool are due in large part to the priorities set by its authors. Myokit aims to be a tool not just for simulation and analysis, but also for model *development*. This may include the creation of a whole new model but more often means fitting models to new data, adding new components or refining existing ones. It frequently includes changing equations in deeper ways than changing parameter values and so an easy-to-work-with modeling language is required. To explore the results of altering the model equations Myokit supports fast single-cell simulation. It is highly scriptable to allow systematic investigation of model properties. Because multi-cell phenomena emerge from single-cell models and are a crucial tool for model validation, support is included for fast parallelized multi-cellular simulations. In this section we discuss Myokit's strong points, discuss its (intentional and unintentional) limitations and describe directions for future development.

3.4.1 Dynamical systems

Myokit provides support for first order ODEs. Higher order ODEs can be included by rewriting them as systems of first order ODEs: for example $\ddot{x} = f(x)$ can be rewritten as $\dot{x} = y$ with $\dot{y} = f(x)$. No general support for partial differential equations (PDEs) is provided, but Myokit can be used to solve the most common PDE in cardiac electrophysiology, the monodomain equations, albeit only on a rectangular grid (see Section 3.B). Support for differential algebraic equations (DAEs) is not included as these are not very common in

cardiac AP models. Stochastic ODEs can be useful to model phenomena such as stochastic channel openings or calcium sparks. Support for this may be added in future versions of Myokit.

3.4.2 Multi-cell modeling

Myokit's focus is on single-cell simulations and systems of coupled cells. Bidomain models and whole-heart simulations lie outside of its intended scope. Nevertheless, the OpenCL based simulation method included in Myokit can rapidly simulate 1 and 2-dimensional grids of connected cells in parallel on personal computers' GPUs. Connections between cells can be specified manually, allowing simulations of arbitrary geometries to be set up and run. An interesting direction for the future would be to optimize Myokit's tissue simulation to run large scale simulations on high-performance clusters. Since Myokit maintains a symbolic version of the model equations, models may be optimized for large scale simulations, for example using lookup tables (Cooper et al., 2014), splines (Chapter 4) or more advanced techniques such as automated application of the Rush-Larsen method (Marsh et al., 2012). Myokit's capability of generating model code can also be used to provide cell models for existing large-scale simulation libraries. Using Python's ability to call on compilers, Myokit could be set up as a front-end to such tools.

3.4.3 Sub-cellular modeling

AP models have included sub-cellular compartments for a long time, and these can easily be incorporated into models in Myokit. Recently, models have also appeared that treat a single cell as a system of many sub-cellular elements, each described by their own system of ODEs (Nivala et al., 2012; Voigt et al., 2014). An interesting open question is in how far such models can be simulated using the coupled-cell approach described in this chapter. Alternatively, such simulations may be facilitated by adding a vector data type to Myokit. Both options are viable targets for future investigation.

3.4.4 CellML support

Myokit is not a CellML tool *per se*, but it can read and write CellML 1.0 files for cardiac AP models. Instead of relying on the official CellML API, Myokit converts CellML files directly to Myokit models. The implementation is focused entirely on the features present in the bulk of cardiac AP models: as such, DAEs and the `<reaction>` element used to define biochemical pathways are not supported. The optional CellML features scripting and automatic unit conversion are not supported either, although warnings will be raised if a model with inconsistent units is loaded. Finally, Myokit does not support the import statement introduced in CellML 1.1 or the MathML `factorial` element. Despite these limitations, Myokit can read 163 out of the 165 cardiac models in valid CellML 1.0 available

in the CellML repository, and 163 out of the 168 valid cardiac CellML 1.1 files.

3.4.5 Direct editing and generic experiments

Myokit's file format allows a whole experiment to be contained in a single file so that model and experiment can easily be archived. This encourages direct interaction with the models, allowing users to familiarize themselves with the models by making changes and examining the results. Alternatively, models can be loaded from separate files and changed using scripting, without modifying the model file. This way, Myokit supports both the direct experimentation typical of model development and the systematic approach required when running experiments with previously established models. Ideally, it will act as a bridge between the two worlds, allowing scientists from both domains to benefit from each other's work.

The ability to make changes programmatically also enables the creation of generic experiments that can be run on an annotated set of reference models. Support for functional curation (which accomplishes the same in a program-independent manner) is not included but work is in progress to enable Myokit to interact smoothly with the tools provided by Cooper et al. (2015a). Support for SED-ML, which is less versatile, is not currently planned.

3.5 Conclusions

Recent tools for AP modeling and simulation do not cater to model development. Furthermore, there is a gap between easy-to-use but limited simulation tools and more powerful software packages that require greater skill from the user. Myokit is a new tool that bridges this gap, allowing users to directly access their models and providing an easy-to-use interface in which to do so. Models can be shared via import and export of common exchange formats and the numerical methods implemented in Myokit can be used to set up and run complex simulations and analyses with minimal programming effort. Scientists can use Myokit to model and simulate, and thereby better understand the cardiac cellular action potential as a basis for a multi-scale understanding of the beating of the heart.

Acknowledgments

Paul G.A. Volders is supported by a Vidi grant from the Netherlands Organization for Scientific Research (ZonMw 91710365). The authors thank Ralf L.M. Peeters, Ronald L. Westra and John Walmsley, all from Maastricht University, for our valuable discussions.

3.A Tools used in AP-model development

Table 3.1 lists the 60 models or model extensions published after 2001 (when CellML 1.0 was finalized) as found in the overview by Noble et al. (2012). While the list is slightly out of date and not all papers we investigated mention the tools that were used, we believe this gives a reasonable impression of the software used in modern AP-model development. The first column gives the index from Noble et al. (2012), the second gives the reference and the third column lists the used tools and, where possible, the ODE solver. The final column highlights instances where CellML was used either before, during or after the modeling process.

Table 3.1: Post-CellML modeling papers and the tools they use.

Index	Model	Tools	CellML
2-32	Aslanidi et al. (2009a)	C (MPI)	Pre
1-25	Aslanidi et al. (2009b)	C (MPI)	
4-77	Aslanidi et al. (2012)	C	Pre
4-63	Benson et al. (2008)	C (OpenMP)	
4-37	Bernus et al. (2002)	C++	
1-21	Bondarenko et al. (2004)	Fortran	
2-29	Bueno-Orovio et al. (2008)	Fortran	
4-43	Cabo and Boyden (2003)	Unknown	
4-78	Carro et al. (2011)	Fortran	Post
4-61	Cherry et al. (2007)	Java, C, Fortran	
2-14	Clancy and Rudy (2002)	MATLAB, C	
1-29	Corrias et al. (2011)	Chaste	Post
1-24	Cortassa et al. (2006)	MATLAB, C++ (CVODE)	
4-49	Coutu and Metzger (2005)	C++	
4-72	Decker et al. (2009)	MATLAB, C++	
4-39	Fenton et al. (2002)	Java, C, Fortran	
4-51	Fink et al. (2006)	MATLAB (ode15s)	
4-64	Fink et al. (2008b)	MATLAB	
4-52	Flaim et al. (2006)	MATLAB (ode23t)	
2-15	Fox et al. (2002)	C	
3-3	Garny et al. (2003)	C, Fortran, CMISS, COR	During
4-75	Grandi et al. (2010)	MATLAB (ode15s)	
4-79	Grandi et al. (2011)	MATLAB (ode15s)	
4-41	Greenstein and Winslow (2002)	C/Fortran	
4-53	Greenstein et al. (2006)	MATLAB	
4-80	Heijman et al. (2011)	MATLAB, C++	
2-20	Hund and Rudy (2004)	MATLAB, C++	
1-26	Inada et al. (2009)	C++	
2-24	Iribe et al. (2006)	MATLAB (ode15s)	Post
1-22	Iyer et al. (2004)	Fortran (LSODE)	
4-42	Kneller et al. (2002)	C	
2-16	Kurata et al. (2002)	MATLAB	
1-27	Li et al. (2010)	MATLAB	Post
1-30	Li and Rudy (2011), 2011	C++	
2-27	Livshitz and Rudy (2007)	MATLAB	
2-21	Lovell et al. (2004)	MATLAB, Octave, C (CVODE)	
4-73	Koivumäki et al. (2009)	MATLAB (ode15s)	
2-30	Mahajan et al. (2008)	C	
4-74	Maleckar et al. (2008)	Unknown	
2-25	Mangoni et al. (2006)	Unknown	
2-17	Matsuoka et al. (2003)	Unknown	
2-23	Michailova et al. (2005)	MATLAB	
4-44	Mitchell and Schaeffer (2003)	Unknown	
2-28	Niederer and Smith (2007)	COR	During
1-31	O'Hara et al. (2011)	MATLAB, C++	
4-45	Pandit et al. (2003)	C (RK-Merson)	
2-26	Pásek et al. (2006)	MATLAB (ode15s)	
4-66	Pásek et al. (2008)	MATLAB (ode15s)	
1-28	Sampson et al. (2010)	Fortran (LSODE)	
2-18	Sarai et al. (2003)	Unknown	
4-57	Sato et al. (2006)	C	
2-19	Saucerman et al. (2003), 2003	Berkeley Madonna	
4-67	Saucerman and Bers (2008)	MATLAB (ode15s)	
4-46	Seemann et al. (2003)	C	
2-22	Shannon et al. (2004)	C (CVODE)	
4-58	Simitev and Biktashev (2006)	Fortran (NAG)	
2-31	Stewart et al. (2009)	COR	During
1-23	ten Tusscher et al. (2004)	C++	
4-59	ten Tusscher and Panfilov (2006)	C++	
4-69	Wang and Sobie (2008)	MATLAB (ode15s)	

The number of times each tool was mentioned is given in Table 3.2. Note that some papers used multiple tools.

Table 3.2: Tools, sorted by popularity.

Tool	Mentions
MATLAB	22
C	17
C++	12
Fortran	10
COR	3
Java	2
Octave	1
Chaste	1
CMISS	1
Berkely Madonna	1
Unknown	6

3.B Coupled cells and the monodomain model

Myokit provides a simulation engine for systems of coupled cells, connected through currents following Ohm's law. In this appendix we show how, under certain conditions, the same simulation engine can be used to calculate solutions to the monodomain model.

In a coupled cell simulation, each cell's transmembrane potential V_i changes according to

$$\begin{aligned} \frac{\mathrm{d}V_i}{\mathrm{d}t} &= -\frac{1}{C}\left(I_{\mathrm{ion},i} + I_{\mathrm{stim},i} + I_{\mathrm{diff},i}\right) \\ I_{\mathrm{diff},i} &= \sum_j g_{ij}(V_i - V_j)\,. \end{aligned}$$

Here the summation is taken over all cells j connected to cell i. While the simulation engine allows arbitrary cells to be connected, in this section we assume the cells are arranged in a regularly spaced rectangular grid and conductance only happens in orthogonal directions x and y, parallel to the rectangle's sides. Cells at the grid boundaries simply have fewer neighbors and do not communicate with points outside the grid.

The monodomain equations (Leon and Horáček, 1991) are used to model *tissue*, where each infinitesimal point in the tissue is described using:

$$\begin{aligned} \frac{\partial V}{\partial t} &= -\frac{1}{C}\left[I_{\mathrm{ion}} + I_{\mathrm{stim}} - \frac{1}{\chi}\frac{k}{k+1}\nabla \cdot D\nabla V\right] \\ &= -\frac{1}{C}\left(I_{\mathrm{ion}} + I_{\mathrm{stim}} + I_{\mathrm{diff}}\right)\,. \end{aligned}$$

Here we have re-arranged the terms and changed the sign of I_{stim} (called I_{app} in the cited source) to match the sign convention for transmembrane currents. Again, we only allow

horizontal or vertical conduction and assume points at the edges of the tissue do not communicate with the outside world ("zero-flux boundary conditions"). If we then define a regularly spaced rectangular grid with horizontal step size Δx and vertical step size Δy and we apply a finite-difference approximation, the system takes on the same form as the coupled cell simulation described above. For a node in the center of a 1-dimensional grid, we find:

$$\begin{aligned} I_{\text{diff},i} &= -\frac{1}{\chi}\frac{k}{k+1}\nabla \cdot D\nabla V_i \\ &\approx -\frac{1}{\chi}\frac{k}{k+1}\sigma_x \frac{V_{i-1} - 2V_i + V_{i+1}}{\Delta x^2} \\ &\approx \frac{\sigma_x}{\chi \Delta x^2}\frac{k}{k+1}\Big((V_i - V_{i-1}) + (V_i - V_{i+1})\Big) \\ &\approx \sum_j g_x (V_i - V_j)\,. \end{aligned}$$

This shows that, to use Myokit's coupled cell simulation for monodomain simulations on a rectangular grid, we can set the "node-to-node conductance" as

$$g_x = \sigma_x \frac{1}{\chi}\frac{1}{\Delta x^2}\frac{k}{k+1}\,.$$

Similarly, in a 2-dimensional grid we set

$$\begin{aligned} g_x &= \sigma_x \frac{1}{\chi}\frac{1}{\Delta x^2}\frac{k}{k+1} \\ g_y &= \sigma_y \frac{1}{\chi}\frac{1}{\Delta y^2}\frac{k}{k+1}\,. \end{aligned}$$

3.C An example of a full model

```
[[model]]
name: Tran-2009
# Initial values
membrane.V = -84.3801107371
ica.d      = 0.00302126301779861
ica.f      = 0.999967936476325
ik.x       = 0.0417603108167287

# Membrane potential
[membrane]
dot(V) = -(i_ion + i_stim)
    in [mV]
i_stim = engine.pace * stim_amplitude
    stim_amplitude = -73 [uA/cm^2]
i_ion = ica.i_si + ik.i_K + ik1.i_K1 + ikp.i_Kp + ib.i_b

# Slow inward calcium current
[ica]
use membrane.V as V
E = 80 [mV]
g = 0.09 [mS/cm^2]
i_si = g * d * f * (V - E)
    in [uA/cm^2]
dot(d) = (alpha * (1 - d) - beta * d)
    alpha = 0.095 * exp(-0.01 * (V - 5)) / (1 + exp(-0.072 * (V - 5)))
    beta  = 0.07 * exp(-0.017 * (V + 44)) / (1 + exp(0.05 * (V + 44)))
dot(f) = (alpha * (1 - f) - beta * f)
    alpha = 0.012 * exp(-0.008 * (V + 28)) / (1 + exp(0.15 * (V + 28)))
    beta  = 0.0065 * exp(-0.02 * (V + 30)) / (1 + exp(-0.2 * (V + 30)))

# Time dependent potassium current
[ik]
use membrane.V as V
i_K = g_K * x * xi * (V - E_K)
    in [uA/cm^2]
E_K = -77 [mV]
g_K = 0.282 * sqrt(parameters.Ko / 5.4)
    in [mS/cm^2]
xi = if(V > -100, xibar, 1)
xibar = 2.837 * (exp(0.04 * (V + 77)) - 1) / ((V + 77) * exp(0.04 * (V + 35)))
dot(x) = (alpha * (1 - x) - beta * x) / gamma
    alpha = 0.0005 * exp(0.083 * (V + 50)) / (1 + exp(0.057 * (V + 50)))
    beta  = 0.0013 * exp(-0.06 * (V + 20)) / (1 + exp(-0.04 * (V + 20)))
gamma = 1

# Time-independent potassium current
[ik1]
use membrane.V as V
E = parameters.RTF * log(parameters.Ko / Ki)
g = 0.6047 * sqrt(parameters.Ko / 5.4)
    in [mS/cm^2]
Ki = 145 [mM]
i_K1 = g * (alpha / (alpha + beta)) * (V - E)
    in [uA/cm^2]
    alpha = 1.02 / (1 + exp(0.2385 * (V - E - 59.215)))
    beta = numer / denom
        numer = (0.49124 * exp(0.08032 * (V - E + 5.476)) + exp(0.06175 * (V - E - 594.31)))
        denom = (1 + exp(-0.5143 * (V - E + 4.753)))

# Plateau potassium current
[ikp]
use membrane.V as V
i_Kp = g * Kp * (V - ik1.E)
g = 0.0183 [mS/cm^2]
Kp = 1 / (1 + exp((7.488 - V) / 5.98))

# Background current
[ib]
i_b = g * (membrane.V - E)
    in [uA/cm^2]
E = -59.87 [mV]
g = 0.03921 [mS/cm^2]

# External values
[engine]
time = 0 bind time
pace = 0 bind pace

[parameters]
Ko = 5.4 [mM]
RTF = 26.712 [mJ/C]
```

Figure 3.10: A Myokit representation of the simplified model by Tran et al. (2009).

CHAPTER 4

Reducing run-times of AP model simulations by automatically replacing computationally expensive functions with splines

This chapter is based on:

Michael Clerx, Pieter Collins (2014). Reducing run-times of excitable cell models by replacing computationally expensive functions with splines. Presented at *Mathematical Theory of Networks and Systems, Groningen 2014* (peer reviewed proceedings). Volume 21, pages 84–89.

Abstract

Numerical simulation of muscle cells and tissue is an established tool in cardiac electrophysiology, where the electrical behavior of excitable heart muscle cells is commonly modeled as a stiff, non-linear system of ordinary differential equations. A common feature of this system's right-hand side is the heavy use of computationally expensive univariate functions of the membrane potential. We investigated the performance benefits of replacing these functions with cubic spline approximations in an automated model simplification process. Clear performance gains were found when evaluating the right-hand side in isolation and when performing multi-cellular simulations using a simple forward Euler method. Single cell simulations run with an adaptive method saw smaller gains due to an increase in overhead and a decrease in the number of function evaluations. A parallel multi-cellular simulation was also investigated, but the overhead of the implementation overshadowed the evaluation time of the right-hand side.

Contents

4.1 Introduction . . . 63
4.2 Methods . . . 64
4.2.1 Models of the AP . . . 64
4.2.2 Single cell simulations . . . 65
4.2.3 Multi-cell simulations . . . 65
4.2.4 Selecting expressions for approximation . . . 66
4.2.5 Spline fitting procedure . . . 66
4.2.6 Benchmarking . . . 66
4.3 Results and discussion . . . 67
4.3.1 Potential benefits of using splines . . . 67
4.3.2 Accuracy of fit versus performance . . . 68
4.3.3 Performance gain in complex models of the AP . . . 68
4.3.3.1 RHS Evaluation times . . . 70
4.3.3.2 Single cell simulation run-times . . . 71
4.3.4 Multi-cell simulation . . . 71
4.4 Conclusion . . . 73

4.1 Introduction

Since their introduction in the second half of the 20th century, ODE models of the cardiac action potential (AP) have become increasingly complex. From a computational efficiency point of view modern AP models contain many expensive-to-evaluate functions, especially univariate functions of the membrane potential V making heavy use of the exponential function (Heijman et al., 2011; O'Hara et al., 2011; Mahajan et al., 2008; Stewart et al., 2009). As more is learned about the complexity of the mammalian heart, the number of equations used to model a single cell is growing. This conflicts with the need to run simulations fast and the desire to create personalized models of the whole human heart, which contains roughly $5 \cdot 10^9$ of such cells (Olivetti et al., 1995).

For this chapter we investigated the performance gain to be had from replacing computationally expensive parts of the right-hand-side (RHS) of the differential equations with faster-to-evaluate approximations. Numerical experiments were run in which selected equations were replaced with cubic spline approximations, and the effects on the RHS evaluation times were measured. We examined the influence of using a simplified RHS in three scenarios: single cell simulations using an advanced numerical solver, multi-cell simulations without parallelization, and multi-cell simulations run in parallel on a graphics processing unit (GPU).

To the best of our knowledge, no similar attempts have been reported. Although Mirin et al. (2012) report using rational function approximates for the same purpose as part of a larger effort to simplify the model by ten Tusscher and Panfilov (2006), our approach differs in two ways: Firstly, in our approach we use splines, which are more stable and flexible when approximating functions with strong localized variations and may evaluate faster, and secondly, instead of simplifying one specific model we have described and implemented a generic approach. Cooper et al. (2010) did implement an automated system, but used look-up tables instead of function approximation.

4.2 Methods

All simulations and benchmarks were carried out using Myokit (see Chapter 3). The used models were either re-implemented from the published equations, or imported from the CellML (Cuellar et al., 2003) model repository (`http://models.cellml.org`).

4.2.1 Models of the AP

As described in Section 3.2.1, an AP model's RHS can be broken down into two parts:

$$\frac{\mathrm{d}V}{\mathrm{d}t} = -\frac{1}{C}\left(I_{\mathrm{ion}}(V,u,p) + I_{\mathrm{stim}}\right) \tag{4.1}$$

$$\frac{\mathrm{d}u}{\mathrm{d}t} = f(V,u,p) \tag{4.2}$$

Here, $f(V,u,p)$ is a non-linear and typically stiff system of equations. In electrophysiological terms, it contains both fast and slow currents. For example the *fast sodium current* rises and falls in a time span of < 5ms, whereas the *slow delayed rectifier potassium current* can take several seconds to reach its peak. More details are given in Section 3.2.1.

For a classic example of a cardiac myocyte model and the accompanying equations see Beeler and Reuter (1977) or Luo and Rudy (1991). A good example of the complexity of modern models is found in the detailed appendix to Heijman et al. (2011). In Table 4.1 an example of a reduced AP model is presented. These equations describe the Morris-Lecar model (Morris and Lecar, 1981), a reduced form of the original neuronal model by Hodgkin and Huxley (1952d), which contains only two state variables. In this example, an external input forcing the system is given as the dimensionless value *pacing*.

Table 4.1: The reduced Morris-Lecar model

$\frac{dV}{dt} = -\frac{1}{C}\left[I_{ion} + I_{\mathrm{stim}}\right]$	$\frac{dw}{dt} = 0.04\,\frac{w_{\mathrm{inf}} - w}{w_{\mathrm{tau}}}$
$C = 20$	$I_{Ca} = g_{Ca}\,(V - E_{Ca})$
$I_{ion} = I_{\mathrm{K}} + I_{\mathrm{Ca}} + I_{\mathrm{leak}}$	$E_{Ca} = 120$
$I_K = g_K\,(V - E_K)$	$g_{Ca} = 4.4 m_{\mathrm{inf}}$
$E_K = -84$	$m_{\mathrm{inf}} = \frac{1}{2}\left[1 + \tanh\left(\frac{V+1.2}{18}\right)\right]$
$g_K = 8w$	$I_{\mathrm{leak}} = 2\,(V + 60)$
$w_{\mathrm{inf}} = \frac{1}{2}\left[1 + \tanh\left(\frac{V-2}{30}\right)\right]$	$I_{\mathrm{stim}} = -80 \times pacing$
$w_{\mathrm{tau}} = 1/\left[\cosh\left(\frac{V-2}{60}\right)\right]$	
$V(t=0) = -60.86$	$W(t=0) = 0.015$

A characteristic feature of AP models is that they contain many computationally expensive functions that depend only on the membrane potential V. We automatically identify these functions and replace them by spline approximations which are faster to evaluate. Most

of these functions are found in ion channel models, which are a phenomenological class of models so that no valuable information is lost by altering the form of the expression. Furthermore, the precision of cell models is limited, and, as we illustrate in the next two sections, the stability of the ODE integrator takes precedence over the accuracy of the evaluation of the RHS.

4.2.2 Single cell simulations

For detailed modern single-cell models the RHS is a costly function to evaluate and the system of equations is stiff. As a result, higher-order adaptive schemes that require multiple RHS evaluations or suffer from reduced stability fail to produce any performance benefits. Implicit methods offer greater stability and therefore bigger step sizes, but the need to approximate the next solution often involves more RHS evaluations which can counteract this benefit. In addition, the Jacobian of an AP model is not typically available analytically. For some good examples of complex models see Heijman et al. (2011), Mahajan et al. (2008) or O'Hara et al. (2011). As a result, the explicit forward Euler method has remained a competitive choice. A difficult to implement, but much faster approach is to use an implicit adaptive multi-step method, e.g., CVODE (Hindmarsh et al., 2005, see Section 3.2.5). The multi-step approach means only a limited number of RHS evaluations per time step are required; in most cases a single evaluation per step is sufficient (see Fig. 4.2.D). Cardiac AP models are typically *paced* (forced) periodically with a block wave stimulus, which introduces two discontinuities per cycle. At these points, it is necessary to reset the simulation routine, leading to a higher number of steps around those points.

4.2.3 Multi-cell simulations

Single cell models can be used for multi-cellular simulations by simply duplicating the single cell state vector. Without any interaction between the cells, the system's Jacobian takes on a diagonal block structure. Connections between the cells are then introduced in the form of a diffusion current. For details see Section 3.2.1.1.

The most common strategy for running multi-cell simulations is to use the explicit forward Euler method. There are a number of reasons for this. First of all, in a multi-cell simulation, the evaluation time of the duplicated RHS becomes extremely high so that methods requiring multiple evaluations all incur a strong increase in overhead. Secondly, in the single cell case the system's fast dynamics are highly localized in time (about 5ms per 1000ms for a heart rate of 60bpm) and occur at the onset of excitation. In a multi-cell scenario each cell's excitation triggers its neighbors' excitation with a small delay, causing the fast dynamics (and the need for a small step size) to be spread out over a much larger time. In extreme cases (which are often of high scientific interest) some part of the tissue is undergoing rapid changes at any given time (e.g., during *re-entry*, see Fig. 3.7). This limits the utility of

adaptive methods. Finally, when performing parallelized multi-cellular simulations on GPU devices the cost of memory access and synchronization is such that a simple forward Euler scheme is almost always faster than a more complex approach requiring the storage of multiple state or derivative vectors.

Garcia et al. (2011) report experimenting with different adaptive Runge-Kutta pairs before selecting the simplest tested method: an explicit Euler / Heun pair. They report a 25% speed-up over fixed size forward Euler. Unfortunately, few details are given and we were unable to reproduce this result.

4.2.4 Selecting expressions for approximation

As a first step in model simplification, a model was chosen and a number of expressions were selected for approximation. A symbolic version of the model's equations was obtained (using Myokit, this is automatically available) and scanned for univariate functions of V. Care was taken to include functions both directly and indirectly dependent on V. For these functions, a spline was calculated using the methods described in Section 4.2.5 and accepted or rejected based on the accuracy of the fit. The approximated equation was then removed from the symbolic model and replaced with a piecewise polynomial with the calculated spline coefficients. Finally, the new symbolic model was exported to standard C or OpenCL and used for benchmarking either the RHS or a full simulation.

4.2.5 Spline fitting procedure

A cubic spline function $g(V)$ was fit to each selected function $f(V)$ on the interval $I = [-100\text{mV},\ 150\text{mV}]$. Spline coefficients were set by imposing $\frac{df}{dV} = \frac{dg}{dV}$ at the endpoints of I, setting $g(x_i) = f(x_i)$ at each knot x_i and then solving the resulting linear system. The absolute and relative errors in the fit were estimated by sampling both functions at 1000 evenly spaced points on the selected interval and calculating

$$e_{\text{abs}} = \max|f - g| \tag{4.3}$$

$$e_{\text{rel}} = \max|f - g|/(\max f - \min f) \tag{4.4}$$

over the full sample. The tolerance was set to $e_{\text{abs}} \leq 10^{-3}$ and $e_{\text{rel}} \leq 10^{-5}$. Whenever these limits were exceeded an extra knot was added at the point with the highest error. If a set maximum number of pieces (100) was reached the procedure was halted and an error returned, marking the function as unfit for approximation.

4.2.6 Benchmarking

Single and multi-cell simulations were benchmarked by recording the times just before and after a simulation was run. Single-cell simulations were run using a simulation built on

Myokit's `Simulation` class, which creates, compiles and executes C code using CVODE to integrate the ODE.

RHS evaluation times were measured using the following procedure: A simulation was run and the state vector was saved for every position. Next, a benchmarking tool revisited each state multiple (tens of thousands) times and measured the average execution time. For this purpose, a class `RhsBenchmarker` was added to Myokit that performs either full RHS evaluations or partial ones, allowing the evaluation time of selected equations to be measured.

4.3 Results and discussion

4.3.1 Potential benefits of using splines

To demonstrate the performance benefits of spline approximations, cubic spline approximations using 32-piece[1] splines were created for the following functions:

$$f_0(V) = \exp(V/100) \tag{4.5}$$
$$f_1(V) = \exp(0.01V) \tag{4.6}$$
$$f_2(V) = 1/[1 + \exp((V + 40)/-10)] \tag{4.7}$$
$$f_3(V) = 1/[7\exp((V + 12)/35) + 9\exp(-(V + 77)/6)] \tag{4.8}$$
$$f_4(V) = 1/[1 + \exp(-0.1(V + 40))] \tag{4.9}$$
$$f_5(V) = 1/[7\exp(0.03(V + 12)) + 9\exp(-0.2(V + 77))] \tag{4.10}$$

The first function is a minimal example of an exp function, scaled to the range I. The second function shows the performance benefit of multiplication over division, compared to the run-time of an exp evaluation. The third and fourth equations are adapted from the fast sodium channel formulation of (O'Hara et al., 2011) and are typical examples of the kind of equation we hoped to simplify. The function f_2 represents the steady-state value of one of the state variables, m, and defines a sigmoid curve. The function f_3 is the voltage dependent time constant with which m approaches its steady state value and defines a "hat" or "bell" shape over I. The final two equations show the effect of replacing division operations with multiplication in f_2 and f_3.

The performance gains are shown in Table 4.2. Here, the original evaluation time of the equation is given as T_{eq} while the spline evaluates in T^s_{eq}. The resulting speed-up is given by $F^s_{\text{eq}} = T^s_{\text{eq}}/T_{\text{eq}}$. As can be seen, the performance of the splines is invariant with respect

[1] Splines with 32 pieces provided accurate fits in each of these examples. As can be seen in Fig. 4.1.B, the evaluation time of a full spline depends only weakly on the number of pieces used and using, for example, a 64-piece spline gives roughly the same results.

Table 4.2: Performance gains for single function approximation.

Function	T_{eq} **(ns)**	T^s_{eq} **(ns)**	F^s_{eq}
f_0	25.9	5.08	20%
f_1	23.8	5.07	21%
f_2	27.4	5.10	19%
f_3	53.8	5.07	9%
f_4	24.4	5.10	21%
f_5	48.3	5.10	11%

to the run-time of the original function, leading to large speed-ups for complex expressions. This illustrates the potential advantage of spline approximations in the RHS.

4.3.2 Accuracy of fit versus performance

Experiments were run to asses the trade-off between spline accuracy and run-time using the reduced Morris-Lecar model for excitable cells (see Table 4.1). The expressions for w_{inf}, w_{tau} and m_{inf} were each selected for simplification: spline approximations were generated for each with an increasing number of segments (from 2 to 200). For each generated spline, a single cell simulation was run using CVODE. All simulations were started from a common set of initial values.[2] Results are shown in Fig. 4.1.

As can be seen, increasing the number of pieces reduces the error of fit almost without affecting the RHS evaluation time, which shows a reduction to about 13% of the evaluation time of non-optimized case. The difference between state variable w with and without the approximation was tracked and seen to stabilize around 10 pieces. Similarly, the number of steps taken by the adaptive solving scheme and the total number of RHS evaluations performed in a simulation reached a stable average at about 5 pieces.

From these results we conclude that (1) Increasing the number of pieces in a spline below the minimum number required to achieve acceptable accuracy does not dramatically affect RHS evaluation time. As a result, no special strategy to keep the number of pieces in a spline to a minimum is required. (2) Using spline approximations increases the number of steps taken by the adaptive solver, but the increase does not seem to be affected by the number of pieces. (3) The accuracy of the produced result increases significantly as the spline quality increases but then stabilizes once the maximum relative error of fit has gone below 10^{-3}.

We speculate that the unusually high and seemingly random variation in the number of RHS evaluations and integrator steps was caused by the higher-order discontinuities at the spline knots. This is discussed briefly in Section 4.3.3.2.

[2] A similar test was run where models were "pre-paced" for 10^5 periods before the steps taken were measured, but no significant difference with the pre-pacing free case was found.

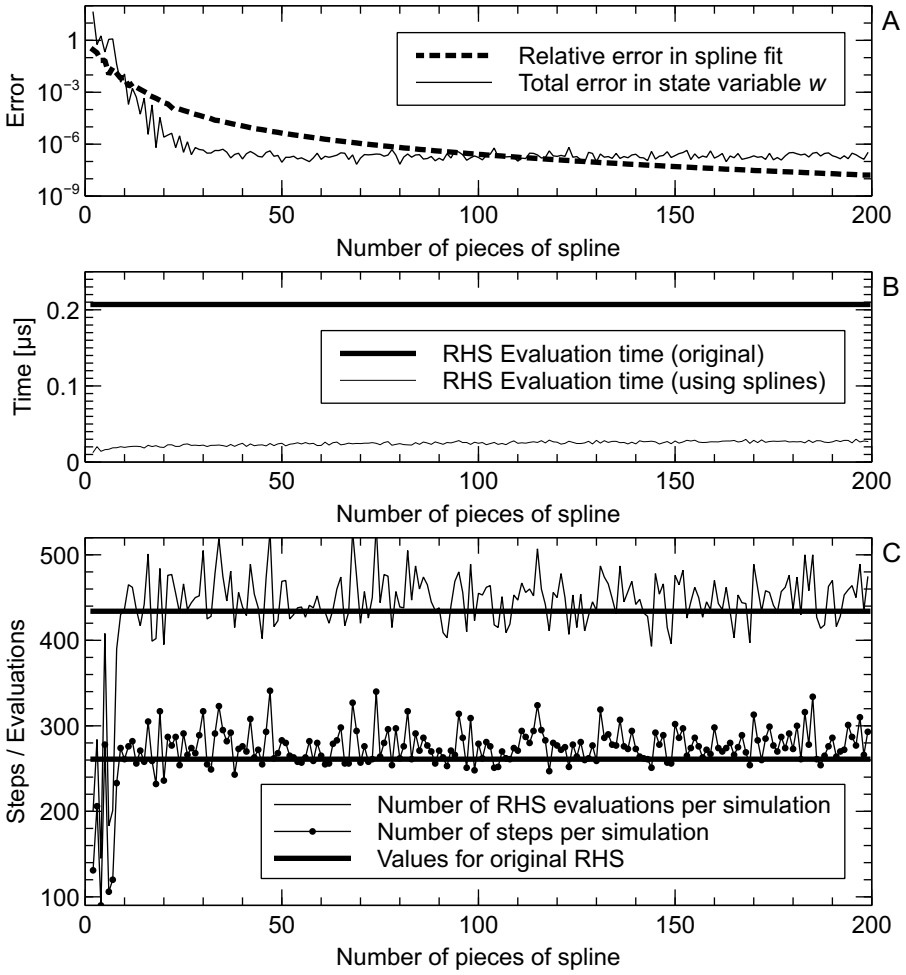

Figure 4.1: Effects of the number of pieces in a spline, measured in the reduced Morris-Lecar model. *(A)* The relative error in the spline approximation and the resulting total error in state variable w during a full simulation, calculated as $\sum_i (w_i^s - w_i)^2$ where w_i^s and w_i are the values of w at a 1000 linearly spaced points during the simulation with and without splines respectively. *(B)* The average RHS evaluation time with approximations using an increasing number of pieces and for the unmodified RHS. *(C)* The number of steps taken by an adaptive solver and the number of RHS evaluations performed during a simulation. Thick lines indicate the corresponding values for the unoptimized RHS.

Table 4.3: Model run times and performance.

Model	N_s	N_e	N_r	F^b_{RHS}	F^s_{RHS}	T_0	F^s_0	M_0	M^s_0	F^s_1
Tran et al. (2009)	4	24	11	28%	17%	0.5ms	69%	359	350	-
Luo and Rudy (1991)	8	37	17	30%	24%	1.7ms	56%	847	773	25%
Stewart et al. (2009)	20	106	38	50%	48%	3.7ms	80%	942	991	51%
O'Hara et al. (2011)	41	249	67	53%	64%	12ms	98%	1483	2586	-
Decker et al. (2009)	48	204	48	74%	72%	13ms	88%	1646	1594	73%
Sampson et al. (2010)	81	299	107	39%	85%	38ms	97%	3277	3209	78%
Heijman et al. (2011)	145	514	61	80%	88%	83ms	98%	4165	4071	89%

4.3.3 Performance gain in complex models of the AP

Next, we applied our automated spline simplification routine to seven increasingly complex models of the cardiac AP. The resulting performance gains are shown in Table 4.3. In this table, N_s and N_e are the number of state variables and equations in each model respectively, while N_r is the number of those equations that could be simplified. F^b_{RHS} is an estimate of the best performance achievable through spline approximation. It was calculated by measuring the full RHS evaluation time, T_{RHS}, and the RHS time when the N_r selected equations were omitted entirely, T^b_{RHS}, and then calculating the ratio $F^b_{\text{RHS}} = T^b_{\text{RHS}}/T_{\text{RHS}}$. The actual performance was evaluated by replacing the N_r selected equations with splines and measuring the new evaluation time T^s_{RHS} before calculating the ratio $F^s_{\text{RHS}} = T^s_{\text{RHS}}/T_{\text{RHS}}$.

The time required to perform a one-second single-cell simulation with the *unoptimized* models is given as T_0. As can be seen, this increases with an increasing model size (as indicated by N_s and N_e). The performance increase when using splines in these simulations is given as $F^s_0 = T^s_0/T_0$ where T^s_0 is the run-time of a one-second single-cell ("zero dimensional") simulation using splines. The adaptive step-size algorithm treats the optimized and unoptimized models differently, as is shown by the number of RHS evaluations in the unoptimized model M_0 and in the optimized one M^s_0. Finally, $F^s_1 = T^s_1/T_1$ represents the speed-up gained in an unparallelized fixed step-size cable simulation.

Note that the *smaller* the F-value, the *larger* the performance gain using splines. The time taken to perform the spline approximations was not included in any of the benchmarks.

4.3.3.1 RHS Evaluation times

The results in Table 4.3 show that employing spline approximation decreased the RHS evaluation time in each case: F^s_{RHS} is always less than 100%. However, the utility of function approximation is seen to decrease with increasing model complexity. This can be attributed to two factors: the inclusion of more multivariate equations (for example signaling, intracellular diffusion processes or calcium concentration dependent currents) and a shift towards models that contain more equations but of a simpler form (for example Markov model formulations of ion channel currents instead of Hodgkin-Huxley type ones).

For small models, the performance of the spline-based RHS sometimes exceeds our calculated estimate F^b_{RHS}. This is a side-effect of the many optimizations employed by modern compilers and hardware, which make it difficult to get consistent benchmarking results when comparing short run-times.

4.3.3.2 Single cell simulation run-times

The results for single-cell simulations show a smaller speed-up than expected on the basis of the RHS performance alone. We initially hypothesized that this may be due to the higher-order discontinuities created at the knots, but this would suggest a strong relation between the number of pieces used and the number of steps taken. No such relation was found, as can be seen in Table 4.3. Experiments using splines with higher orders of continuity failed to show a consistent performance gain in terms of number of steps. By comparing the number of RHS evaluations taken in simulations with and without spline approximations, given in Table 4.3 as M_0 and M^s_0, it can be seen that even with a reduced number of evaluations the performance gain is not proportional to that in the RHS evaluation times. This suggests overhead of the ODE solver is a bigger factor in these simulations and the impact of RHS run-time reduction is reduced.

To gain insight into the adaptive behavior of the CVODE solver, we implemented a tracking mode that logs the number of evaluations taken and the system time at each step of a simulation. Fig. 4.2 shows the results for a one-second simulation using the model by Decker et al. (2009). As can be seen from the top half of the figure, most of the work done during a simulation occurs during the action potential, the period when the membrane potential is elevated from its usual resting state of around −80mV. This example, which is typical for ventricular myocyte models, shows how most of the system's fast dynamics are localized around the start and finish of the AP. The lower half of the figure clearly shows why this method is efficient in terms of RHS evaluations: the most common number of evaluations needed at each step is 1 with occasional short bursts of around 50 evaluations, leading to an average of 3.1 evaluations per step throughout the simulation. This average ranges from 1.6 to 6.0 evaluations per step for the models described in Table 4.3.

4.3.4 Multi-cell simulation

Non-parallel multi-cellular simulations were run using Myokit's `Simulation1D` class, which uses an explicit forward-Euler method to integrate the ODE. As described in Section 4.2.3, this is often the best approach for multi-cellular simulations. Without a step-size choosing algorithm or other complicating factors, the performance boost in this scenario matches that seen in single RHS evaluation times. This can clearly be seen in Table 4.2, where the speed-up F^s_1 closely follows F^s_{RHS}. In two models, no wave propagation was observed so no speed-ups could be measured.

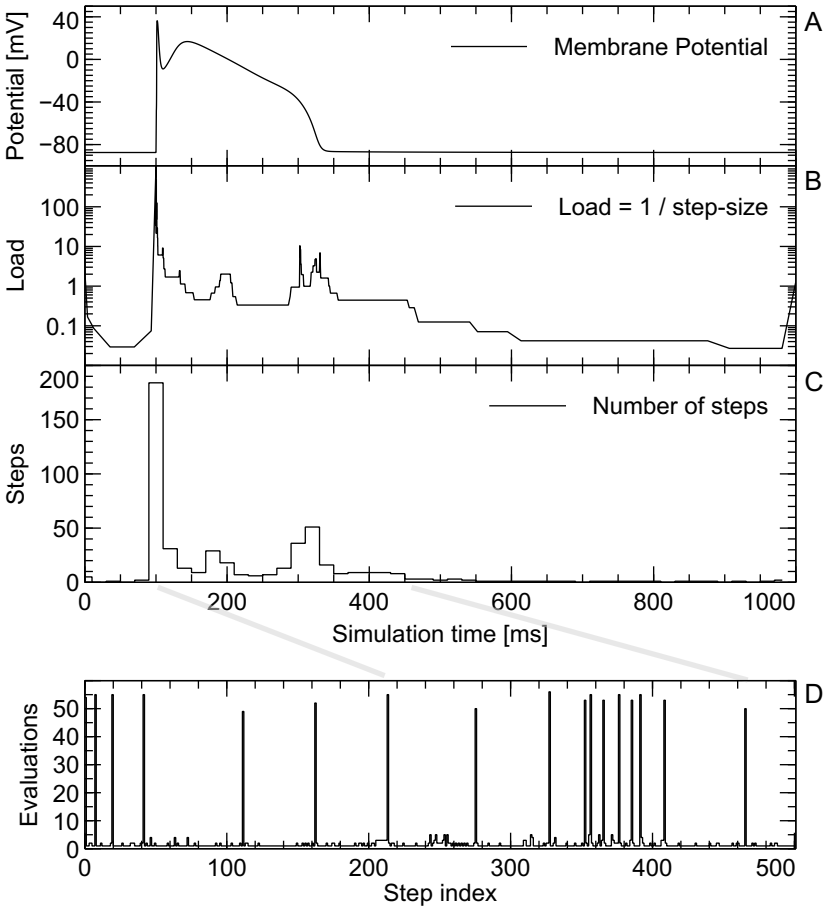

Figure 4.2: Number of steps taken and number of RHS evaluations performed by the CVODE adaptive solver during a 1000ms simulation using Decker et al. (2009) (A) The simulated membrane potential plotted against the simulated time. (B) The load on the solver, calculated as the inverse of the used step-size at each simulated point in time, shown on a logarithmic axis. (C) A histogram of the number of steps taken by the solver plotted against the simulated time. (D) The number of RHS evaluations taken at each step of the simulation. The full simulation is shown; note that the x-axis does not scale linearly to the axes of the figures above.

An OpenCL-based parallel version of this simulation was implemented, but was unable to produce any speed-ups on a GPU. Indeed, we found that eliminating the simplified calculations from the RHS entirely only lead to marginal speed-ups, indicating that the RHS evaluation time is of little importance in our parallel implementation. We suspect that the overhead of memory access and synchronization in this case is a bottleneck in our calculations.

4.4 Conclusion

Splines are a natural candidate for providing simplified approximations to univariate functions occurring in the right-hand side of a differential equation model of excitable cells. In this chapter, we show that the use of cubic spline approximations can reduce the time needed to evaluate an AP model's RHS. Further, the lack of higher-order smoothness at the spline knots does not negatively affect the number of RHS evaluations needed by the sophisticated implicit multi-step method used by the ODE solver CVODE. The time benefit of this optimization was seen directly in unparallelized multi-cell simulations, but failed to materialize fully in single cell simulations using CVODE, and had no effect on parallel multi-cell simulations using the forward Euler method run on the GPU. We suggest that the RHS evaluation time is overshadowed by overhead resulting from the solver in the former case, and from overhead of memory access due to the hardware architecture in the latter.

Given the speed-ups obtained in the evaluation of the RHS, we believe that this method may still be useful in situations where RHS evaluation time is a dominant factor, either in the field of cellular electrophysiology or in other domains. If memory access can be made cheaper in GPU simulations, the method may provide considerable speed-ups.

Acknowledgments

The authors would like to thank Dr. Enno de Lange for our valuable discussions on AP models, model implementations and running parallelized simulations.

CHAPTER 5

Variability in the dynamical properties of human cardiac I_{Na}

This chapter is based on:

Michael Clerx, Roel L.H.M.G. Spätjens, Cristina Altrocchi, Sandrine R.M. Seyen, Pieter Collins, Enno de Lange, Ralf L.M. Peeters, Paul G.A. Volders (2016). Variability in the dynamical properties of human cardiac I_{Na}. *Manuscript in preparation.*

Michael Clerx, Pieter Collins, Paul G.A. Volders (2015). Applying novel identification protocols to Markov models of I_{Na}. Presented at *Computing in Cardiology, Nice 2015*. Volume 42, pages 889–892.

Abstract

Recent work has shown the increased predictive power of cardiac action-potential models that include variability in their parameters. Yet quantitative data on variability in the kinetics of ionic currents is scarce. We investigated and quantified variability in one of the major ionic currents, the cardiac fast sodium current I_{Na}. Using a simple voltage step experiment, we found that time constants of inactivation varied between roughly one-half and twice the most common value. This suggests that a skewed, perhaps lognormal, distribution is appropriate when modeling variability in time constants. Time constants of fast and slow inactivation were linearly correlated (R=0.66). Next, we performed a literature review and found that midpoints of activation and inactivation were reported over a 40mV range. Midpoints of activation and inactivation were both approximately normally distributed. Midpoint of activation and inactivation showed a linear correlation (R=0.82) and linear regression suggested an average distance of approximately 40mV between midpoints. Fluctuations in the distance between midpoints also appear approximately normally distributed. By reviewing the literature on sources of variability in patch-clamp experiments such as temperature, time since membrane rupture and liquid junction potential, we showed that the observed variability exceeds that which can be expected from experimental conditions alone. Finally, we used computational models to show that the observed variability affects the cellular action potential, and leads to variability in the automaticity of isolated Purkinje cells.

Contents

5.1 Introduction . . . 77
5.2 Methods . . . 78
5.2.1 Experimental set-up . . . 78
5.2.2 Electrophysiological measurements . . . 78
5.2.3 Quantifying time constants of inactivation . . . 80
5.2.4 Computational methods . . . 81
5.2.5 Review of midpoints of (in)activation . . . 81
5.3 Results . . . 82
5.3.1 The time constants of inactivation vary from cell to cell . . . 82
5.3.1.1 Slow and fast inactivation are not independent . . . 84
5.3.1.2 The time constants do not correlate with time since rupture . . . 84
5.3.1.3 The influence of noise is limited . . . 84
5.3.1.4 Variability is not explained by temperature . . . 85
5.3.2 The midpoints of (in)activation vary from cell to cell . . . 86
5.3.2.1 The mean midpoints of (in)activation vary from study to study . . . 86
5.3.2.2 The midpoint of activation and inactivation are not independent . . . 87
5.3.2.3 Cell-type and channel-variant do not explain study-to-study variability 87
5.3.3 The observed variability affects the cellular AP . . . 90
5.4 Discussion . . . 91
5.4.1 Time constants of inactivation . . . 91
5.4.2 Midpoints of activation and inactivation . . . 92
5.4.3 Correlation between kinetical parameters . . . 92
5.4.4 Implications for cardiac modeling . . . 93
5.4.5 Implications for reporting of cell-electrophysiological data . . . 93
5.4.6 Limitations . . . 93
5.4.7 Comparison to previous work . . . 94
5.5 Conclusion . . . 95
5.A Extended methods . . . 96
5.A.1 Time constants are identifiable . . . 96
5.A.2 Membrane charging interferes with activation . . . 97
5.A.3 Repeated-fit experiments confirm our analysis . . . 100
5.B Additional results . . . 101
5.B.1 Time-constant experiments . . . 101
5.B.2 Midpoints of (in)activation in the biggest subgroup . . . 102
5.B.3 β1-subunit coexpression . . . 103
5.C Studies used in the literature review . . . 103

5.1 Introduction

Variability in the maximum conductance and in the dynamical properties of cardiac ion channels has been linked to critical differences in the response to antiarrhythmic drugs (Sarkar et al., 2012; Britton et al., 2013), and may be a factor explaining the diverse arrhythmias sometimes observed between different carriers of the same mutation (Remme et al., 2008; Weiss et al., 2012, 2015). Incorporating variability into models of the action potential (AP) has been identified as one of the key challenges in the future of cardiac cellular electrophysiology (Abriel et al., 2013) and was the subject of a white-paper featured recently in the Journal of Physiology (Mirams et al., 2016). Yet, studies with an experimental basis that quantify the variability in even the major cardiac ion currents are scarce.

In the present study, we have investigated variability in the kinetical parameters of the cardiac fast sodium current I_{Na}, which is responsible for the initial rapid upstroke of the AP, and plays a major role in AP propagation. Abnormalities in I_{Na} have been linked to long-QT syndrome (type 3), Brugada syndrome, cardiac conduction disease, atrial and ventricular fibrillation, 'overlap syndromes' and more (Amin et al., 2010). While some studies of variability in ionic currents have focused entirely on changes in maximum conductance (Sánchez et al., 2014; Chang et al., 2015; Passini et al., 2016), others have shown the predictive power of including variability in kinetic parameters such as time constants of (in)activation (Romero et al., 2009; Sarkar and Sobie, 2011; Britton et al., 2013). In contrast to changes in maximum conductance, which can be explained by variable ion channel expression levels and measured using protein counting techniques, measuring variability in kinetics requires cellular-electrophysiological experiments and a careful analysis of the experimental factors influencing these results.

Our study proceeds in three parts. First, we perform simple voltage-step experiments and fit a mathematical model to the results to quantify variability in the time constants of inactivation. With these experiments we show that variability between cells occurs even under controlled conditions. Next, we conduct a review of previously reported midpoints of activation and inactivation. This provides an insight into the variability in repeated measurements in and between different laboratories, over a time span of several years. Finally, we incorporate the observed variability into computational models and show the effect of variability on the AP of ventricular and Purkinje cells. By comparing our results to estimates of the uncertainty due to experiment and analysis, we argue that this variability is not experimental noise but an inherent property of the channels. A graphical overview of the study is given in Fig. 7.1.

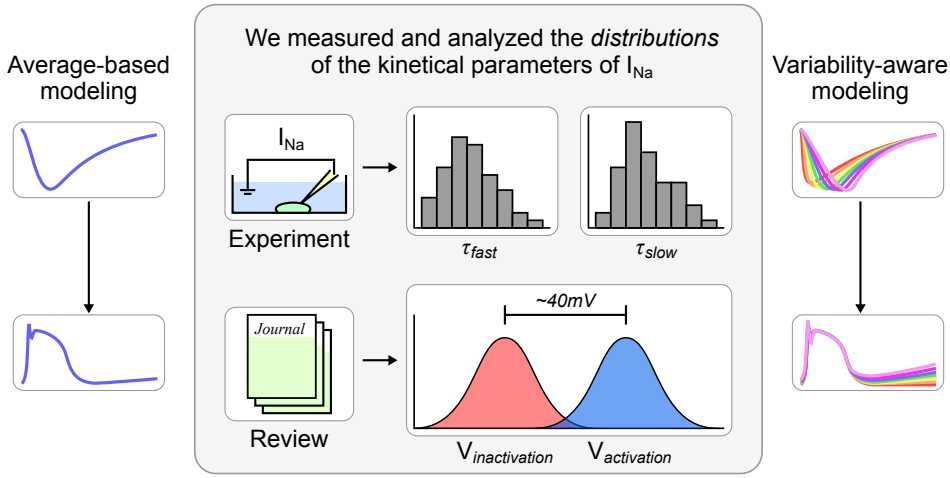

Figure 5.1: Graphical overview of this study. We performed patch-clamp experiments to characterize and quantify variability in the time constants of I_{Na} inactivation, after transfection of wild-type *SCN5A*. Next, variability in midpoints of activation and inactivation was studied by reviewing the existing literature. With this knowledge in hand, we can move from conventional average-based modeling to variability-aware modeling, which predicts not just a single outcome but a biologically realistic range of outcomes.

5.2 Methods

5.2.1 Experimental set-up

To determine whether variability could be observed in a simple, well-controlled experiment, we investigated the currents elicited by applying a single voltage step to cells expressing human *SCN5A*. To quantify the results, a Hodgkin-Huxley style model was fit to the data using whole-trace fitting, which gives more reliable results than the conventional 'disjoint' method of analysis (Willms et al., 1999). Based on the results of an analysis by Walch and Eisenberg (2015), we concentrated on the time constants instead of the steady-states, as the latter cannot be determined uniquely (i.e., variability in fitted parameters may be observed even for identical currents) unless the initial state of the system is known exactly. Finally, we chose to focus on inactivation alone because the membrane-charging process can interfere with recordings of I_{Na} activation (Sherman et al., 1999). A further description of the last two points is provided in the Supplement.

5.2.2 Electrophysiological measurements

Chinese hamster ovary (CHO) cells were cultured in 35 mm dishes with Ham's F-12 medium, supplemented with 10% fetal calf serum and 1% penicillin/streptomycin. Cells were transiently transfected with human WT *SCN5A* (NCBI reference sequence NM_000335.4, isoform b) and green-fluorescent protein (2.5μg pIRES-WT-SCN5A-GFP) using Fugene 6 (Promega

Benelux, Leiden, The Netherlands) as transfection agent. Fluorescence was boosted by adding an additional 0.25μg of DNA coding for fluorescent protein (0.25μg pIRES-empty-GFP).

The cells were then incubated for 24 hours at 37°C, briefly trypsinized and washed twice in culture medium. They were then placed on an inverted microscope in a bath perfused continuously with a solution containing (in mmol/L): 145 NaCl, 4 CsCl, 1 $MgCl_2$, 1.8 $CaCl_2$, 10 HEPES, and 11.1 glucose (pH=7.4 with CsOH). Pipettes were filled with (in mmol/L): 10 NaCl, 120 CsCl, 20 TEACl, 5 MgATP, 5 EGTA, and 5 HEPES (pH=7.2 with CsOH). Patch pipettes were pulled and fire-polished using a DMZ-Universal-Puller (Zeitz-Instruments Vetriebs GmbH, Martinsried, Germany) from 2mm borosilicate glass capillaries (Science Products GmbH, Hofheim, Germany). Experiments were performed at room temperature, which was measured as 22 ± 1.5°C.

Data was collected using three set-ups: An Axopatch 200B amplifier, Digidata 1322A digitizer and Clampex 8.2.0, an Axopatch 200B amplifier, Digidata 1440A digitizer and Clampex 10.2.0, and an Axopatch 1D amplifier, Digidata 1322A digitizer and Clampex 8.2.0 (all Molecular Devices, Sunnyvale, CA, USA). Green fluorescent protein was used to identify cells with successful transfection, which were then patch-clamped in the whole-cell configuration. Access resistance was below 8MΩ for all cells. Cell capacitances ranged from 5.5pF to 47pF. Series resistance compensation (60 to 80%) was employed, with 'prediction' enabled on the amplifiers that provided this (see Sherman-Gold and Maertz, 2012). Data was filtered at 1kHz using the analog low-pass 4-pole Bessel filter on the amplifiers and subsequently digitized at 20kHz.

Directly after rupturing the membrane, cells were stimulated repeatedly with a single voltage step, until the observed peak current had stabilized. Subsequently, a protocol with increasing voltage steps was run (used to characterize voltage-dependent activation). From this data the current elicited by a step from −120mV to −20mV was extracted. All steps were preceded by a few seconds at −120mV to inactivate the channels.

Capacitance artefacts were filtered digitally by omitting data from the first t_a milliseconds after each change in potential. The value for t_a was set manually for each recording, and was in the order of 0.5ms. To estimate the leak in each signal, we fit a simple biexponential curve to the decaying part of the current: $I_{\text{fit}} = I_{\text{leak}} + c_1 e^{-t/\tau_1} + c_2 e^{-t/\tau_2}$. Here, I_{leak}, c_1, c_2, τ_1 and τ_2 were cell-specific parameters that were determined by minimizing the sum-of-squares error between I_{fit} and the recorded I using a downhill simplex method (Nelder and Mead, 1965). The entire signal was then corrected by subtracting the estimated I_{leak}.

5.2.3 Quantifying time constants of inactivation

To quantify differences between experimental recordings, a Hodgkin-Huxley style model of I_{Na} was fit to each recording. We used the equations by Beeler and Reuter (1977), but without the constant term g_{NaC} that was intended to capture background sodium current. The resulting model includes slow and fast inactivation, and has the form:

$$I_{\mathrm{Na}}(t) = m^3 \cdot h \cdot j \cdot g \cdot (V - E) \tag{5.1}$$

$$dm/dt = (m_\infty(V,p) - m)/\tau_i(V,p) \tag{5.2}$$

$$dh/dt = (h_\infty(V,p) - h)/\tau_h(V,p) \tag{5.3}$$

$$dj/dt = (j_\infty(V,p) - j)/\tau_j(V,p) \tag{5.4}$$

Here, g is the fixed maximum conductance, V is the membrane potential and E is the reversal potential for I_{Na}. The model has a single activation variable m, a fast inactivation variable h and a slow inactivation variable j. After a change in membrane potential, each of these variables approaches a voltage-dependent steady state (m_∞, h_∞ and j_∞) with a speed determined by its time constant (τ_m, τ_h and τ_j). The steady states and time constants are all functions of V and a vector of parameters p. When $m_\infty(V,p)$ is plotted against voltage it forms a sigmoid curve and the voltage at which it passes through 0.5 is the midpoint of activation. The midpoint of inactivation is the voltage at which $h_\infty(V,p)$ passes through 0.5. We used the equations for the steady states and time constants from Beeler and Reuter and rewrote them in a parametrizable form, leading to a model with 16 parameters (not including the reversal potential E or maximum conductance g). The complete equations are given in Section 5.A.

When a voltage step is applied to a cell, its membrane potential approaches the applied command potential in a process well approximated by:

$$\frac{dV}{dt} = \frac{V_{\mathrm{cmd}}(t) - V}{\tau_{\mathrm{c}}} \tag{5.5}$$

where $V_{\mathrm{cmd}}(t)$ is the desired command potential, V is the actual membrane potential and τ_{c} is a time constant dependent on the membrane capacitance, series resistance, and amplifier series-resistance compensation settings (Sigworth, 1995). For I_{Na}, this charging time is in the same order as the time constant of activation, even when applying series-resistance compensation (Sherman et al., 1999). We therefore included V_{cmd} in our model as an instantaneous voltage step and modeled V using the above equation. The time constant of the compensated charging process τ_c was added as an additional model parameter to be estimated in our model fitting procedure (see also Clerx et al., 2015).

Model parameters were estimated from measured currents by minimizing a score function $f(p) = \sum_t \left[I_{\mathrm{sim}}(p) - I_{\mathrm{ref}}\right]^2$, where the sum was taken over all sampled instances. Function

minimization was performed using a parallelized particle swarm optimization (PSO) method (Eberhart and Kennedy, 1995). This method requires no derivatives, can deal well with non-smooth functions, and has been reported to perform well on ion-channel model fitting tasks (Loewe et al., 2013, 2016). PSO uses many (pseudo-)random steps, which means it may not always return the same value when re-applied, especially on noisy data. Our parameter vector included the 16 parameters determining the model's time constants and steady states, the maximum conductance g, and the membrane charging time constant τ_c. The reversal potential E was held constant at $E = 50\text{mV}$. A small number of heuristic modifications were made to the score function to ensure good fits for all cells: First, based on our analysis of the error introduced by the slowly charging membrane, we fit only to the signal starting approximately halfway into the initial downslope. Next, we added a number of constraints to ensure the variables took on the role of activation and (fast and slow) inactivation. We used $m_\infty(-20, p) \geq 0.5$, $h_\infty(-20, p) \leq 0.5$ and $j_\infty(-20, p) \leq 0.5$ and constrained the time constants with $\tau_m(-20, p) < \tau_h(-20, p) < \tau_j(-20, p)$ and the heuristics $\tau_h/\tau_m \leq 75$ and $\tau_j/\tau_m \leq 400$.

5.2.4 Computational methods

Simulations of the cellular AP were performed using the human ventricular model by Grandi et al. (2010) and the human Purkinje model by Stewart et al. (2009). Both models include an I_{Na} formulation based on the human ventricular model by ten Tusscher and Panfilov (2006). All simulations were carried out using Myokit (see Chapter 3). Patch-clamp data preprocessing and ion-current model fitting were performed using Myokit and NumPy/SciPy (Jones et al., 2001).

5.2.5 Review of midpoints of (in)activation

In the second part of our research, we conducted a review of published midpoints of activation and inactivation of I_{Na}. These midpoints are widely reported, allowing a large number of experiments to be compared. In addition, they are measured and calculated in a more uniform way than time constants or other channel characteristics. Peak current was not investigated as it varies strongly with channel density, activation and inactivation kinetics, and measurement factors such as temperature, sampling rate, and the applied voltage protocol.

Published recordings of I_{Na} in human myocytes are limited, with notable exceptions being Sakakibara et al. (1992); Schneider et al. (1994); Feng et al. (1996) for atrial myocytes and Sakakibara et al. (1993) for ventricular cells. By contrast, studies with cloned human sodium channels in expression systems are far more common. Typically, these studies investigate the changes caused by a mutation, but also report midpoints measured with wild-type (WT) DNA. This allowed us to collect a large number of reports of WT midpoint of activation

Table 5.1: Collected reports of either midpoint of activation, midpoint of inactivation or both, split by α-subunit. Where possible, GenBank accession numbers are provided. The total number of reports using each α-subunit is given as N. For every subtype, the number of reports made with β1-subunit co-expression is given as β1. Finally, the number of reports N (with and without β1-subunit) is broken down according to the expression system used (HEK293 or tsA201, Xenopus oocytes and CHO cells). The totals for each subgroup are given on the bottom row.

Code	**Description**	**Acc. No.**	**N**	**β1**	**HEK**	**Ooc.**	**CHO**
a	Isoform a (Q1077)	AC137587	25	4	23	0	2
b	Isoform b (Q1077del)	AY148488	28	7	23	1	4
a*	hH1 (R1027Q)	M77235	67	42	49	16	2
b*	hH1a (T559A; Q1077del)	None	6	3	6	0	0
?	Unknown	None	41	24	38	2	1
			167	80	139	19	9

and inactivation.

Table 5.1 shows the number of reports from expression system experiments collected in our study. The pore-forming, α-subunit expressed in these experiments differed slightly, and included the 2016 amino-acid long reference sequence (isoform a), the naturally more common isoform with a deletion at position 1077 (isoform b) and variants of both a and b with a slight variation not commonly found in human DNA, which we dubbed a* and b* (Makielski et al., 2003; Ye et al., 2003). In addition, we included experiments with and without the β1-subunit, made in human embryonic kidney (HEK) cells (including tsA201), Xenopus oocytes or CHO cells. The complete list of publications is given in Section 5.C.

All reported midpoints included in our analysis were specified as (1) the mean midpoint of (in)activation, (2) the corresponding number of measurements (i.e., the number of cells) and (3), the corresponding standard error of the mean (SEM). Using this data, we calculated the standard deviation (SD) for each report and constructed a probability density function (PDF) assuming that the measurements in each report followed a normal distribution. The different PDFs were then multiplied by the number of measurements, discretized (so that they resembled fine-grained histograms) and summed to create the combined PDFs seen in Fig. 5.5.

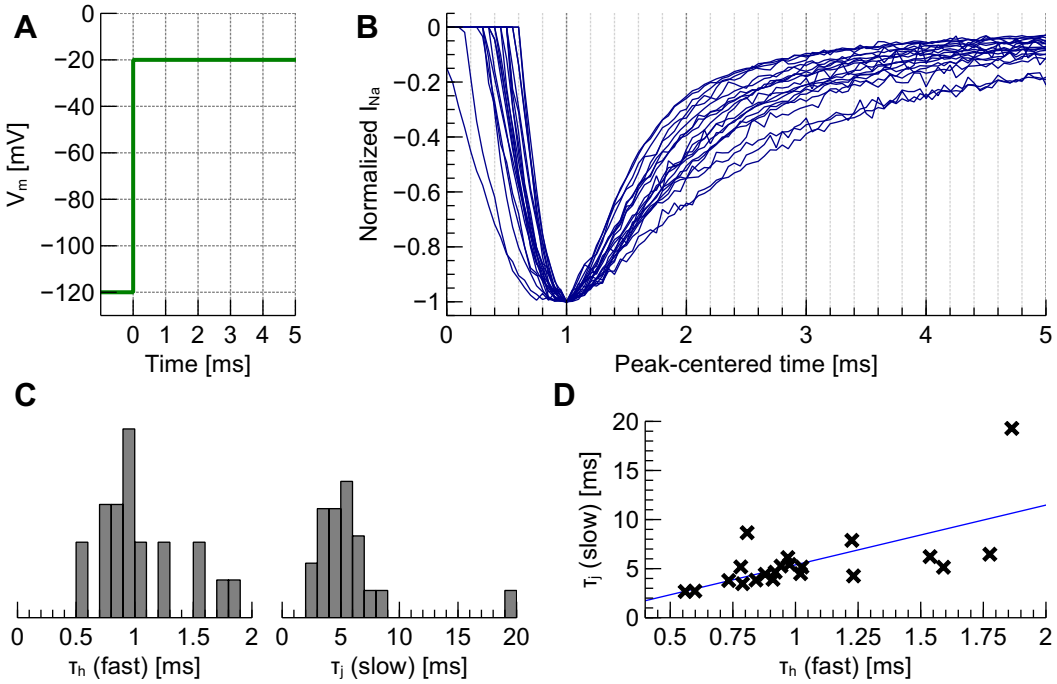

Figure 5.2: (*A*) A simple step protocol from −120mV to −20mV. (*B*) The resulting I_{Na}current, measured in 21 cells. All data was leak-corrected and had the capacitance artefacts removed, leading to the initial flat (zero) response. Data was time-shifted so that the peak occurred at $t = 1$ms. (*C*) Time constants of fast and slow inactivation, measured by fitting models to the data from each cell. (*D*) The correlation between the time constants of fast and slow inactivation.

5.3 Results

5.3.1 The time constants of inactivation vary from cell to cell

Fig. 5.2.B shows the current measured in 21 cells, normalized to a peak current of −1, and time-shifted to have its peak at $t = 1$ms. The initial downward slope and the time to peak varies from cell to cell (see also the alternative views in Section 5.B.1). Once the peak is reached, the current inactivates with a time course that varies from cell to cell. This variability was quantified by fitting a model of I_{Na}, and the resulting time constants of fast and slow inactivation are shown in Fig. 5.2.C. The distribution appears skewed, possibly lognormal, with values ranging from about half to twice the most common value (or mode), although the distribution for slow inactivation shows an outlier at around 4 times the mode.

5.3.1.1 Slow and fast inactivation are not independent

Fig. 5.2.D shows the relation between the slow and fast time constants. A moderate linear correlation was found, with a Pearson correlation coefficient $R = 0.64$. Linear regression

yielded $\tau_j \approx -0.7 + 6.1\tau_h$. The small offset suggests that perhaps the relation between the time constants is best expressed as the ratio τ_j/τ_h. Calculated per cell, this had a mean of 5.4 and a standard deviation of 1.9.

5.3.1.2 The time constants do not correlate with time since rupture

The time between membrane rupture and application of the step protocol varied between the experiments. It is possible that slow changes in membrane potential occurred during this time, e.g., due to a drifting liquid junction potential (Hanck and Sheets, 1992). Fig. 5.3 shows that the largest and smallest time constants were all measured around 500ms after membrane rupture, and there is no clear correlation between time since rupture and the time constants (Pearson correlation coefficient -0.039 for τ_h and time, 0.082 for τ_j and time). In addition, we obtained recordings at a second point of time for a subset of cells but generally saw only small differences between both measurements (see Section 5.B.1).

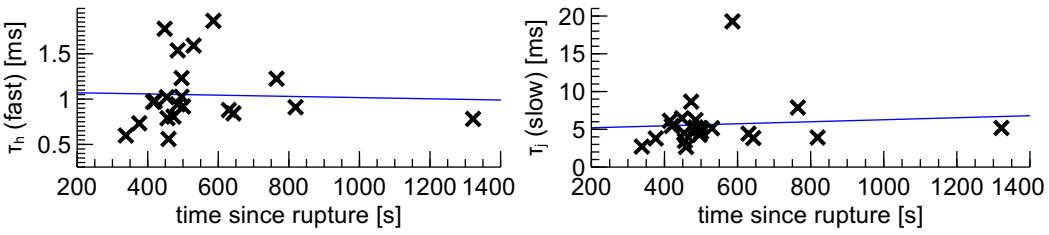

Figure 5.3: The fast (τ_h) and slow (τ_j) time constants of inactivation, plotted against the time between rupturing the membrane and performing the voltage step and current measurement. No clear relation between the time and the time constants can be seen, as indicated by the almost horizontal regression lines.

5.3.1.3 The influence of noise is limited

We estimated time constants by searching for the values that gave the best fit to our data using a pseudo-randomized approach (see Section 5.2.3). However, in the presence of noise, this procedure may not return a unique result, as multiple parameter sets can be found that will give different but almost equally good results, so that the 'best fit' chosen depends on details of the algorithm and score function used, rather than the underlying biology. To investigate the resulting noise-induced variability, we ran the analysis procedure several times for each cell. Because our dataset contained 21 cells, we performed 21 fits per cell so that the variability between cells and between fits could more easily be compared.

Fig. 5.4 shows the values obtained this way for each cell, alongside the values obtained by a single fit to each cell. For most cells, the variability between repeated fits was far smaller than the variability between cells. A numerical analysis supports this observation. Between cells, τ_h had a mean of 1.0ms and a standard deviation of 0.36ms, while the mean and standard deviation for τ_j were 5.7ms and 3.4ms respectively. The mean standard deviation

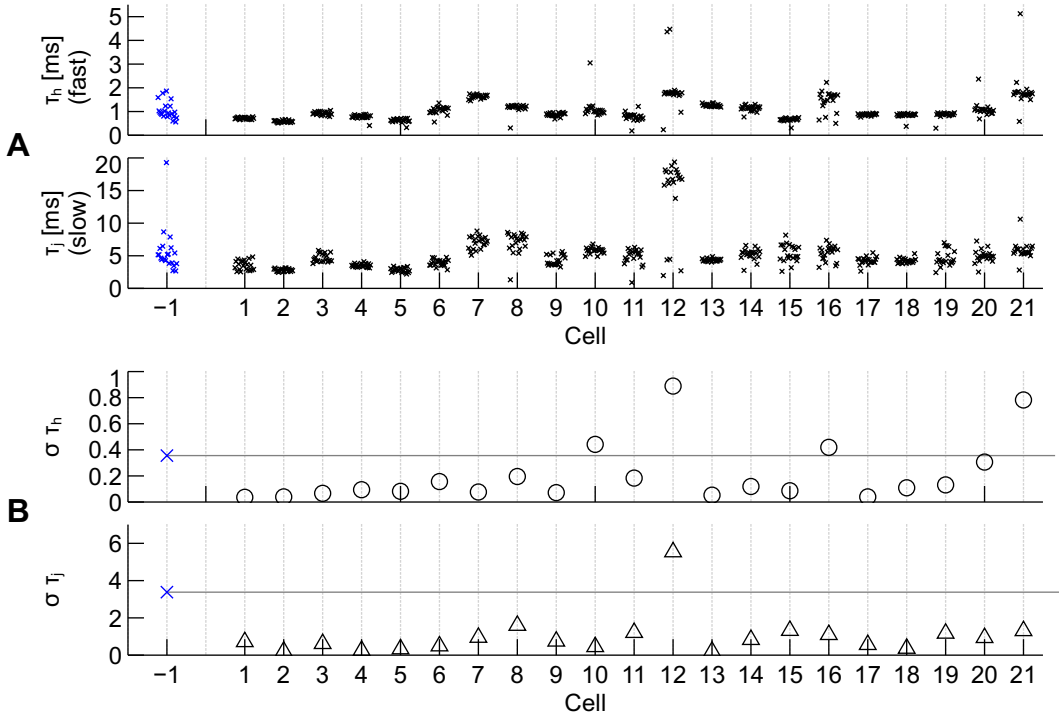

Figure 5.4: **Variability between cells exceeds variability in repeated fits.** (*A*) Fast (*top*) and slow (*bottom*) time constants of inactivation. The data points at position -1 each represent a single fit to a different cell. The subsequent signs at position 1, 2, 3, etc. indicate the outcomes of repeated fits to cells 1, 2, 3, etc. (*B*) The standard deviation of fits to different cells (position -1) and of repeated fits to the same data (positions 1, 2, 3, etc.).

observed in repeated fits was 0.21ms for τ_h and 0.99ms for τ_j. If we assume both standard deviations (between cells and between fits) describe independent distributions, we can use $\sigma^2_{x+y} = \sigma^2_x + \sigma^2_y$ to correct the inter-cell standard deviations for the fitting error to find $\sigma_h = 0.29$ms and $\sigma_j = 3.2$ms.

5.3.1.4 Variability is not explained by temperature

Temperature was kept within a ±1.5°C bracket during the recordings. If temperature alone induced the observed variability, this should cause the ratio between our highest and lowest time constants to be $0.5^{-3/10} \approx 1.23$, for both slow and fast inactivation (Nagatomo et al., 1998). However, the ratio seen in our data was closer to 4 for both, suggesting temperature differences may partly, but not fully explain the observed variance.

5.3.2 The midpoints of (in)activation vary from cell to cell

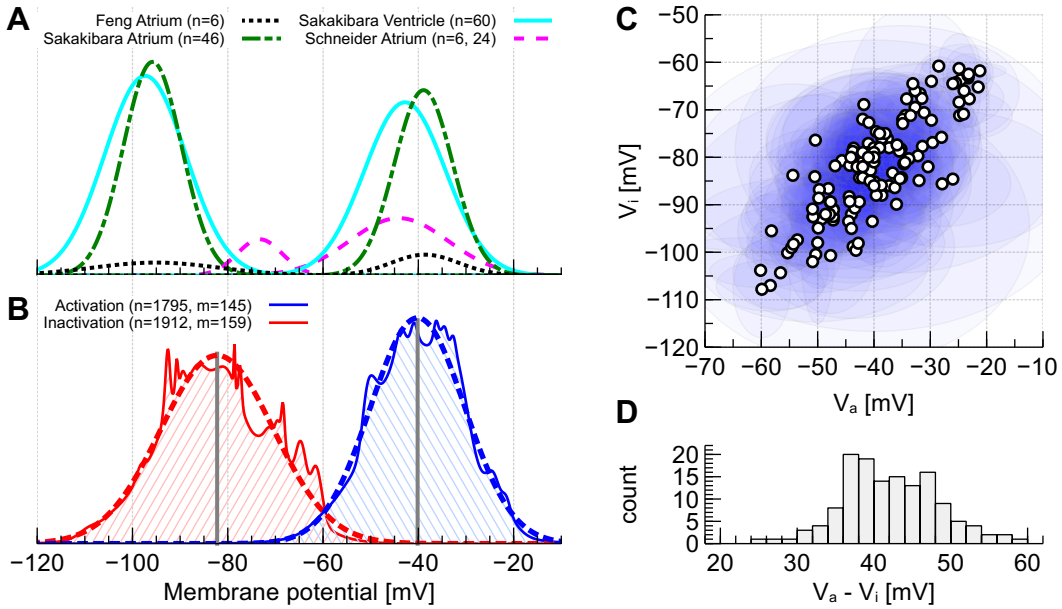

Figure 5.5: (*A*) The midpoints of activation and inactivation reported in human myocyte studies on n cells. All four studies show large variability, represented here as a normal curve with the reported mean and standard deviation, and an area under the curve equal to the number of measured cells. (*B*) Distribution of reported midpoints of activation and inactivation based on measurements in expression systems. The shaded areas shows the summed distribution constructed from the reported data for n cells in m individual reports. The thick dashed lines indicate a normal distribution with the corresponding mean and SD. The vertical grey lines indicate the mean of the inactivation and activation distributions. (*C*) Correlation between reported midpoints of activation (V_a) and inactivation (V_i), shown for studies that reported both. The white dots indicate a reported pair of mean midpoints, with the corresponding $\pm 2\sigma$ range indicated by the blue ellipses. (*D*) A histogram of the difference between midpoints of activation and inactivation.

Fig. 5.5.A shows the distributions of V_i and V_a obtained from studies with human myocytes, one with ventricular myocytes and three with atrial samples. All studies show large variability in outcome, independent of the number of cells being used. Similar variation was seen in the expression system data. In these reports, the standard deviation of V_a ranged from 0.4mV to 22mV, with a mean standard deviation of 4.5mV. Standard deviations of V_i ranged from 0.13mV to 15mV, with a mean of 4.0mV. Assuming a normal distribution, this indicates a spread of ±8mV (95% interval) is not uncommon in a single run of experiments.

5.3.2.1 The mean midpoints of (in)activation vary from study to study

Fig. 5.5.B shows the distribution of cellular V_a and V_i constructed by summing the distributions from multiple studies. Both distributions show a spread of approximately ±20mV (95% interval), indicating a much larger variance between studies than within studies. Even the smaller peaks, which indicate the means of individual reports, occur over a range of ±20mV

for both activation and inactivation. Both reconstructed distributions are reasonably well approximated by a normal distribution.

5.3.2.2 The midpoint of activation and inactivation are not independent

Fig. 5.5.B shows the distributions for V_i and V_a overlap. However, physiologically it seems likely some distance between V_i and V_a is required and that the two distributions are not independent. Fig. 5.5.C shows the midpoint of inactivation plotted against the midpoint of activation from the same study. Studies reporting only the midpoint of activation or only inactivation had to be omitted for this figure, but no other filtering was performed, leading to a total of 138 data points. A strong linear correlation is seen between the reported midpoints of activation and inactivation (Pearson correlation coefficient R=0.82). Using unweighted least-squares based linear regression, we found an offset of -42.06mV and a slope of 1mV/mV (1.000046).

To separate the simultaneous variance of V_a and V_i from their individual variance, we calculated the quantity $V_a - V_i$ (using only the means, not the reconstructed distributions) and plotted its distribution in Fig. 5.5.D. Here, we found a standard deviation of 6.3mV (the corresponding standard deviations for V_a and V_i in this dataset were 8.8mV and 10.8mV respectively). This indicates that, despite their strong linear relation, both midpoints also fluctuate independently.

5.3.2.3 Cell-type and channel-variant do not explain study-to-study variability

Fig. 5.5.B incorporates data from all reports included in our analysis, and so contains data from different expression systems, with and without the β1-subunit and with slightly different α-subunits. To remove these influences, Fig. 5.6.A was made using only data from the largest subgroup: The a* α-subunit, co-expressed with β1-subunit in HEK cells. As can be seen, this created a slight shift in the mean of the distribution, but did not significantly reduce the observed spread. A quantitative view of the midpoint data is given in Table 5.2. This table shows the mean V_a and V_i for the combined data, as well as for various subgroups. Here it can be seen that, while the standard deviation of V_a is slightly smaller in the biggest subgroup, the standard deviation of V_i is actually increased.

α-subunit: Fig. 5.6.B shows the data split by α-subunit. Papers that did not explicitly mention the subunit used were excluded for this figure. Note that the number of reports (m) and the number of cells (n) varies between the subgroups. The number of reports for isoform b* in particular may be too low for a good estimate of the real distribution. Interestingly, the means of the distributions do not differ strongly between subgroups. The groups with the largest number of measurements show the largest spread, indicating that either these cohorts are still too small to estimate the underlying distribution or that larger groups are more prone to capture the effects of some underlying confounding factors.

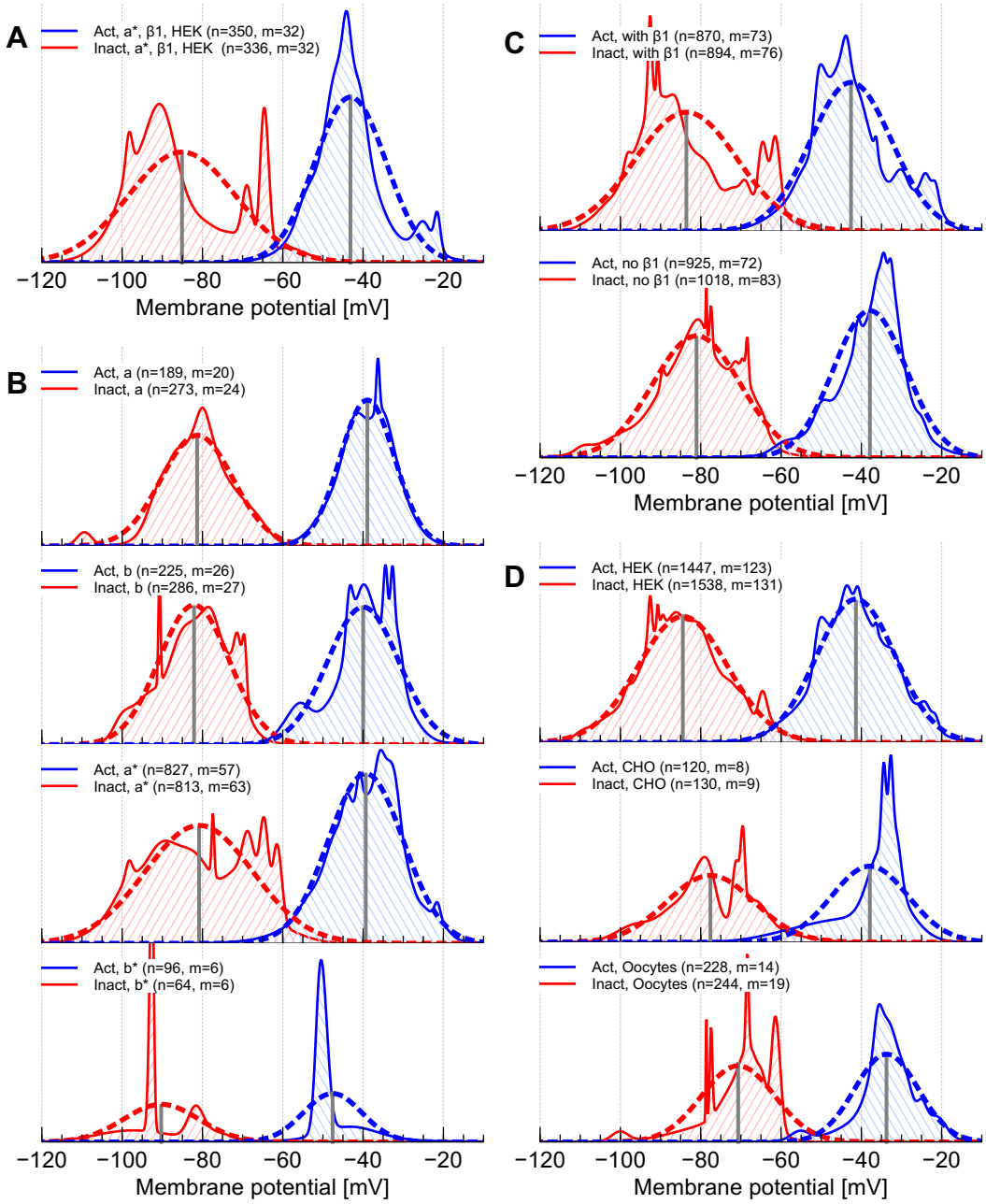

Figure 5.6: (*A*) Reconstructed distribution of midpoints of activation (red) and inactivation (blue) for the largest subgroup (a* α-subunit, with β1-subunit, expressed in HEK cells). The shaded areas indicate the summed distributions. The dashed lines indicate normal distributions with the equivalent mean and standard deviation. The mean is indicated by the solid grey line. (*B*) The distributions split by α-subunit: a (Q1077), b (Q1077del), a* (R1027Q) and b* (T559A; Q1077del). (*C*) The distributions split by co-expression of β1-subunit. (*D*) The distributions split by expression system.

Table 5.2: Ranges of midpoint of activation (left) and inactivation (right). The subgroup mean midpoints of activation and inactivation are indicated as μ_a and μ_i respectively, with the corresponding standard deviations shown as σ_a and σ_i. The 2-sigma range around each mean is shown in the columns $r_{2\sigma,a}$ (activation) and $r_{2\sigma,i}$ (inactivation). For each subgroup, the number of reports (m) and total number of measurements (n) is given.

	Activation					Inactivation				
	μ_a	σ_a	$r_{2\sigma,a}$	m	n	μ_i	σ_i	$r_{2\sigma,i}$	m	n
Combined	-40.2	9.88	-59.9, -20.4	145	1795	-82.2	11.8	-106, -58.5	159	1912
HEK, a*, β1	-43.1	8.90	-60.9, -25.3	32	350	-85.1	13.3	-112, -58.4	32	336
Isoform a	-38.9	6.79	-52.5, -25.4	20	189	-81.3	8.95	-99.2, -63.4	24	273
Isoform b	-40.0	8.86	-57.7, -22.3	26	225	-82.1	8.74	-99.6, -64.6	27	286
Isoform a*	-39.3	9.3	-58.0, -20.6	57	827	-80.8	13.4	-108, -53.9	63	813
Isoform b*	-47.6	7.28	-62.1, -33.0	6	96	-90.3	9.38	-109, -71.5	6	64
Unknown	-40.7	11.9	-64.5, -16.8	36	458	-84.1	11.6	-107, -60.9	39	476
With β1	-42.6	10.1	-62.9, -22.3	73	870	-83.6	12.7	-109, -58.2	76	894
Without β1	-37.9	9.04	-56.0, -19.8	72	925	-81.0	10.9	-103, -59.2	83	1018
HEK	-41.4	9.76	-60.9, -21.8	123	1447	-84.5	11.1	-107, -62.2	131	1538
CHO	-37.9	9.54	-57.0, -18.8	8	120	-77.6	10.9	-99.3, -55.9	9	130
Oocyte	-33.7	7.90	-49.5, -17.9	14	228	-70.1	9.10	-88.9, -52.5	19	244

Inclusion of β1-subunit: Fig. 5.6.C shows the distributions of midpoints with and without the β1-subunit. Papers that did not explicitly mention co-expression of the β1-subunit were assumed to fall into the 'no β1-subunit' category. Here, the means seem to indicate a shift to more negative potentials when the β1-subunit is co-expressed (-4.7mV for activation, -2.6mV for inactivation, see Table 5.2). However, the minimum and maximum values reported do not reinforce this pattern.

Expression system: Fig. 5.6.D shows the influence of the expression system on the measured midpoints. The overwhelming majority of measurements were performed using HEK cells, making the resulting distributions difficult to compare. However, it seems measurements in HEK cells and CHO cells are comparable, whereas oocyte experiments show a shift towards the positive.

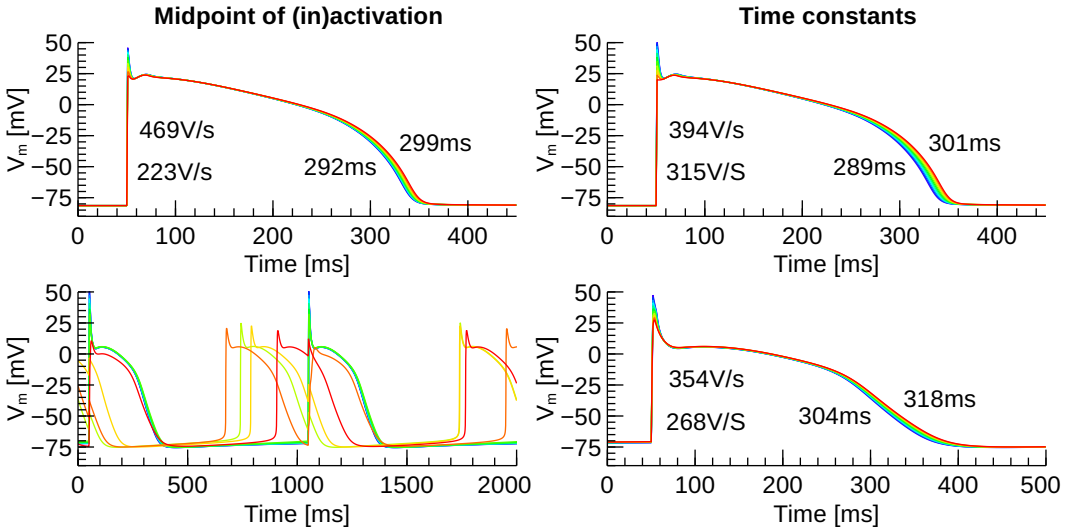

Figure 5.7: Simulations of the ventricular (*top*) and Purkinje (*bottom*) AP, incorporating variability in the midpoints of activation and inactivation (*left*) and time constants of inactivation (*right*). In all cases, the size of the initial upstroke and action potential duration were affected. In the Purkinje model, varying the midpoint of inactivation and activation also affected the cells' automaticity.

5.3.3 The observed variability affects the cellular AP

To investigate the effects of the observed variability on the cellular AP, we ran simulations using a model of the human ventricular AP and the Purkinje AP. In a first simulation, we varied the midpoints of activation and inactivation simultaneously (reflecting their strong linear correlation) by −5mV to +5mV in 1mV steps. The results are shown in the left panels of Fig. 5.7. In both models, this had a strong effect on the maximum upstroke velocity (even doubling it in the ventricular model) and a smaller effect on the action potential duration (APD). In the Purkinje cell model, moving the midpoints of (in)activation also lowered the threshold for activation, leading to automaticity at higher frequencies, causing the cells to depolarize ahead of the pacing signal.

In a second simulation, we varied both time constants of inactivation simultaneously from 0.5 to 2 times the original value in 11 logarithmically spaced steps. This had a much smaller effect on the upstroke velocity in both models, but a greater effect on the APD. Purkinje automaticity was unaffected by changes to the time constants. In all simulations, models were pre-paced at 1s intervals for 1000 beats after each change to the parameters.

5.4 Discussion

Despite the importance of including cell-to-cell variability in the parameters of computational models of the cardiomyocyte AP, data on such variability is scarce. In this study, we showed new evidence of variability in the time constants of inactivation in I_{Na} and reviewed existing evidence for variability in the midpoints of (in)activation. Using models of ventricular and Purkinje AP, we showed that variability has an impact on the shape and duration of the cellular AP.

5.4.1 Time constants of inactivation

We observed a variability between time constants of inactivation that is larger than can be expected from experimental sources of error alone. Hanck and Sheets (1992) showed the time between rupture of the cell membrane and performing the experiment could affect the time constants measured in Purkinje cells. However, we saw no correlation of our measurements with the time between rupture and experiment in our CHO cell measurements. Similarly, Abriel et al. (2001) saw no correlation in HEK cell recordings. Noise in the recordings was quantified using a repeated-fit strategy, and found to explain only a small part of the observed variability. Temperature is known to affect measurements of time constants of I_{Na}, but we saw a larger variance than would be predicted based on the results of Nagatomo et al. (1998), while the data of Keller et al. (2005) would suggest an even smaller temperature-based variation. Other factors, such as the internal and external solutions used, were constant throughout our experiments. We note also that, near -20mV, the time constants of inactivation are weakly voltage-dependent (see for example Beeler and Reuter, 1977), so that any factor leading to small transient changes in the potential across the channel will not have a strong influence. Taken together, these findings suggest the origin of the observed variability was not experimental error, but a fundamental feature of I_{Na} in expression systems.

Table 5.3 shows that the standard deviations in our measurements closely match those of previous studies in expression systems and isolated cardiomyocytes. The means too, are very similar to those reported by Wan et al. (2001a) in HEK cells, but both fast and slow time constants are approximately half the value found in myocytes by Sakakibara et al. (1992, 1993). While we cannot see the shape of the distribution of the time constants in these publications, the size of the standard deviations suggests that our results are representative for this type of experiment.

5.4.2 Midpoints of activation and inactivation

Some measure of cell-to-cell variability was seen in all reviewed reports of the midpoints of (in)activation, with a mean standard deviation of approximately 4mV and a maximum of

Table 5.3: Time constants of inactivation at −20mV.

	$\mu_{fast}(\tau_h)$	σ_{fast}	$\mu_{slow}(\tau_j)$	σ_{slow}	
This study	1.0	0.36	5.7	3.4	CHO cells
Wan et al. (2001a)	0.79	0.34	5.1	1.6	HEK cells
Sakakibara et al. (1992)	2.6	0.40	12	2.8	Atrial myocytes
Sakakibara et al. (1993)	2.1	0.47	12	3.3	Ventricular myocytes

15mV for V_i and 22mV for V_a. Assuming a normal distribution, this would lead to a range of 16mV within two standard deviations of the mean, within the average study. Note that systematic errors made within a single laboratory would not show up in this figure, nor would factors such as α-subunit, β1-subunit co-expression, or differences in the internal solution used. Again, temperature fluctuations could play a role. Nagatomo et al. (1998) recorded a shift in the midpoint of activation of +0.43mV per degree Celsius, and a +0.47mV shift for inactivation, but no such shifts were observed by Keller et al. (2005). Even assuming a 0.5mV/°C shift and a bath temperature ranging over 10°C, this would only explain a 5mV difference in midpoints. Time since rupture may also have varied from cell to cell and affected the recordings. In the Purkinje-cell recordings by Hanck and Sheets (1992), the midpoints of (in)activation changed over time with a rate of approximately 0.5mV/min. If a similar phenomenon occurs in expression systems, this could explain a part of the observed variability, if the standard deviation in time-to-experiment was approximately 8min in the average study (i.e., 32min within the 95% interval). However, Abriel et al. (2001) saw no time-dependent shifts in their data measured in HEK cell experiments, which were the predominant form of experiment in our data. In addition, our own data, though perhaps not representative, showed a standard deviation of 3.5min in the time-to-experiment. This suggests there is some measure of inherent variability in the midpoints of (in)activation.

The difference *between* studies extends over a much larger range, with reported mean midpoints varying over a range of 40mV for both activation and inactivation (see Fig. 5.5.C). In contrast to variability *within* studies, this variability may be partially explained by systematic differences between studies and laboratories. However, it is interesting to note that factors such as α-subunit and β1-subunit expression only cause small differences in the mean. Note also that some studies, for example the one by Tan et al. (2005) already report *multiple* mean midpoints, to allow pairwise comparison with mutated currents made under similar seasonal conditions. However, the difference seen between the midpoints in the study by Tan et al. was at most 3mV for activation, and 7mV for inactivation. Further work is needed to clarify the origins of these large inter-study differences.

5.4.3 Correlation between kinetical parameters

Fig. 5.5.C shows a striking linear correlation between V_i and V_a. A moderate correlation between the fast and slow time constants of inactivation was also found. Such correlations could be caused by some hidden variable affecting both parameters simultaneously. This

could be an experimental error, but is also consistent with the idea of regulation of channel function. However, it is unclear how this would arise, especially in expression systems that do not natively express I_{Na}.

5.4.4 Implications for cardiac modeling

Our results show that variability in the kinetical parameters of I_{Na} exists and has an effect on the AP. For computational studies that include variability in AP model parameters, perhaps the most important finding is that parameters are *correlated*. This implies that variability in the different parameters cannot be simulated by sampling from independent distributions, but that the covariance of the different model parameters must be taken into account. Alternatively, relations such as $\tau_j/\tau_h \approx 5$ and $V_a - V_i \approx 40\mathrm{mV}$ can be exploited to reformulate the parameters in terms of independent random variables. For example, assuming normally distributed midpoints of activation, $V_a = X_1, V_i = V_a + 40 + X_2$, where X_1 and X_2 are variables drawn from a normal distribution. Similarly, assuming lognormally distributed time constants, $\tau_h = Y_1, \tau_j = 5 \cdot \tau_h \cdot Y_2$ where Y_1 and Y_2 are drawn from a lognormal distribution. A further simplification was made in Section 5.3.3, where we set $X_2 = 0$ and $Y_2 = 0$. A physiological meaning can be attributed to these variables: in our example X_1 represents variability in the current's steady-state voltage dependence, while X_2 represents variability in the 'window' that gives rise to the 'window' current.

5.4.5 Implications for reporting of cell-electrophysiological data

The recognition of cell-to-cell variability in channel kinetics has a direct impact on any study investigating I_{Na} channelopathies, and may be a factor explaining phenomena such as ectopic beats in some, but not all, areas of the Purkinje system (for example via increased automaticity such as seen in Section 5.3.3). This has important implications for the way cell-electrophysiological results are reported. For instance, instead of only giving means and standard errors of the mean, data points corresponding to each individual cell should be given (see also Drummond and Vowler, 2011). Ideally, the data points should be labeled per cell so that correlations between the different parameters can be established. Most importantly, based on this study, it appears the variability in kinetical parameters is more than just noise, and could be a relevant physiological parameter.

5.4.6 Limitations

Future work could focus on increasing the sample size of the experiments, which would improve the accuracy of the results. Such a dataset might be obtainable with automated patch-clamp experiments, and could be performed cheaply if run as a baseline test done before a secondary experiment. While we chose to focus on I_{Na}, one of the major cardiac ionic currents, similar investigations into all other currents are needed to gain a full picture

of variability in the processees underlying the cardiac cellular AP.

We simulated the effects of I_{Na} variability on single cells. In tissue, the kinetics of I_{Na} are also likely to affect the conduction velocity and the safety factor of propagation. However, this will depend strongly on whether the coupled cells differ from each other, or if perhaps their shared environment and electrotonic coupling will cause them to function in a similar way.

The presented literature review was based entirely on reported means and standard deviations (calculated from reported standard errors of the mean). Future work could focus on obtaining data from individual cells, which will allow cell-to-cell variability to be reviewed more directly. Since the dataset contains many publications by the same groups, we also cannot exclude the possibility that some cells appear in the dataset more than once, so that the real number of cells is smaller than reported and some points in the distribution are over-represented. It is also possible there are still other confounding factors causing the observed variability in the measured results, that do not occur naturally on the same scale. For example, while the CHO cells we tested were all treated the same way, it is possible that naturally arising differences in stretch affected the ion channel characteristics (Morris and Juranka, 2007). Finally, the exact α-subunit used in a study is not always easy to determine, as many papers do not list an accession number or were written before the existence of variation between available plasmids was widely known.

5.4.7 Comparison to previous work

A study by Pathmanathan et al. (2015) fit multiple models of I_{Na} to data on the steady-state of inactivation in canine datasets, and investigated the effects of the different inactivation curves on the single-cell level. This work focused on the mathematical methodology of incorporating variability in I_{Na}, which contrasts with our focus on identifiability and possible experimental origins of variance. Interestingly, Pathmanathan et al. used two datasets from the same lab but made at different times, and found differences between the two datasets. This matches well with the large inter-study differences seen in our pooled midpoint data, and underscores the need to perform large studies of variability over longer periods of time.

Table 5.2 shows the mean midpoints of activation and inactivation measured in CHO cells occurred at higher potentials than in HEK cells (but note the different sizes of the datasets). This is consistent with earlier findings by Watanabe et al. (2011b) for I_{Na} and Fernandez et al. (2003) for Kv3.3. The collected data on midpoints also allows us to investigate the influence of factors such as the expression system used and co-expression of the β1-subunit. As there is no consistency in the size or direction of the shifts reported by individual studies investigating β1-subunit (see the table in Section 5.B.3) this may provide a useful 'consensus' view of its effects.

5.5 Conclusion

The fast and slow time constants of I_{Na} inactivation show variability that can not be explained by experimental error alone. A review of data reported in the literature suggests this is also the case for the midpoints of (in)activation. Simulations of Purkinje and ventricular electrophysiology show the observed variability has a notable effect on the cellular AP, and may lead to increased automaticity in isolated Purkinje cells. A moderate corelation was seen between the fast and slow time constants of inactivation, and a strong correlation between midpoint of activation and inactivation was observed. This suggests simulations incorporating variability in kinetical parameters should not vary these parameters independently but adapt their modeling strategy to incorporate these correlations. Finally, the recognition of cell-to-cell variability as a biological feature implies it should receive increased attention as a possible arrhythmogenic influence. Consequently, electrophysiological data should be reported in a manner that highlights where cell-to-cell variability and correlations between parameters occur.

Acknowledgments

The work of PGAV is supported by The Netherlands CardioVascular Research Initiative, CVON PREDICT. The authors would like to thank Ronald Wilders, Antoni van Ginneken and Jordi Heijman for our valuable discussions.

5.A Extended methods

The complete equations used to model I_{Na} are given below.

$$I_{\mathrm{Na}}(t) = m^3 \cdot h \cdot j \cdot g \cdot (V - E) \tag{5.6}$$
$$dm/dt = (m_\infty - m)/\tau_i \tag{5.7}$$
$$dh/dt = (h_\infty - h)/\tau_h \tag{5.8}$$
$$dj/dt = (j_\infty - j)/\tau_j \tag{5.9}$$
$$dV/dt = (V_{\mathrm{cmd}} - V)/\tau_{\mathrm{c}} \tag{5.10}$$

Time constants and steady-states (for $x \in \{m, h, j\}$):

$$\tau_x = 1/(\alpha_x + \beta_x) \tag{5.11}$$
$$x_\infty = \alpha_x/(\alpha_x + \beta_x) \tag{5.12}$$

and

$$\alpha_m = (V + p_1)/(1 - \exp(-p_2 * (V + p_1))) \tag{5.13}$$
$$\beta_m = \exp(-p_4 * (V + p_3)) \tag{5.14}$$
$$\alpha_h = \exp(-p_6 * (V + p_5)) \tag{5.15}$$
$$\beta_h = p_9/(1 + \exp(-p_8 * (V + p_7))) \tag{5.16}$$
$$\alpha_j = \exp(-p_{11} * (V + p_{10}))/(1 + \exp(-p_{13} * (V + p_{12}))) \tag{5.17}$$
$$\beta_j = p_{16}/(1 + \exp(-p_{15} * (V + p_{14}))) \tag{5.18}$$

The parameters to be identified were $p_1, p_2, ..., p_{16}, g, \tau_c$. We used $E = 50\mathrm{mV}$, as determined by the internal and external solutions.

Note that for a fixed membrane potential, all time constants and steady-states are constants, so that $p_1, p_2, ..., p_{16}$ can be dropped in favor of $\tau_m, \tau_h, \tau_j, m_\infty, h_\infty, j_\infty$.

5.A.1 Time constants are identifiable

If a model can be made to fit the same data in different ways (i.e., if it gives the same result with different parameter values) it is said to be *unidentifiable*. In such a case, variability in the parameters obtained by fitting a model can not be used to show variability in the underlying process. Walch and Eisenberg (2015) performed a detailed analysis of the identifiability of Hodgkin-Huxley style models, such as the one given above and used in this study. For voltage-step protocols (with constant voltage steps) and long noise-free current recordings, they found that time constants can be uniquely identified but steady-state values are fundamentally unidentifiable.

5.A.2 Membrane charging interferes with activation

When a voltage change is applied to a cell, the membrane potential does not change instantly but requires a short charging time, with a duration dependent on the membrane capacitance and access resistance. For I_{Na}, which can activate and inactivate in well under 5 milliseconds, this is an important effect. Most patch-clamp amplifiers contain compensation circuitry that temporarily injects extra current in an attempt to shorten the membrane charging time (Sigworth, 1995; Sherman et al., 1999). However, since the membrane capacitance varies between cells and the exact amount of compensation used is set using analog controls, this may introduce variability in the recordings.

If no compensation is used, membrane charging can be modeled as a simple capacitor charging circuit. This means that an updated model including membrane charging should be able to recreate currents recorded without compensation exactly. Unfortunately, not using compensation would lead to longer capacitance artefacts resulting in an unacceptable loss of signal. We therefore measured the compensated and uncompensated behavior of our amplifier (Axopatch 200B) to check if compensated behavior could still be approximated well by a simple charging capacitor circuit. To this end, we constructed the model cell shown in Fig. 5.8. It consists of two 22MΩ resistors which represent the access (pipette) resistance encountered in a normal experiment and a single 500MΩ resistor that represents the membrane resistance. A 22pF capacitor is included as a substitute for membrane capacitance. These values are consistent with those given in Sigworth (1995). To measure the model cell's charging time, a patch-clamp amplifier in voltage-clamp mode was attached to terminal A1 and used to perform a voltage step. A second patch-clamp amplifier in a voltage-measuring mode was then attached at terminal A2 and used to measure the potential over the resistor representing the membrane.

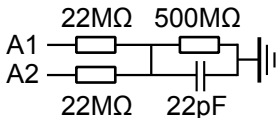

Figure 5.8: The model cell used to investigate the delayed changing of the membrane potential following a voltage step, with and without amplifier compensation.

Fig. 5.9 shows the potential over the model cell during a step from 0mV to 10mV. The recordings reveal a few milliseconds delay at the start of each step, followed by a quick jump in voltage, and finally settling into a simple exponential form. The potential then converges to something very near the desired potential, but not exactly, due to the voltage drop across the series or access resistance. With series resistance compensation enabled, this voltage drop is minimized and the charging process is accelerated. In the traces on the right panel of Fig. 5.9 the voltage drop has been artificially removed by rescaling the potentials. In this

case, we found the process could be well approximated as

$$\frac{dV}{dt} = \frac{V_{\mathrm{cmd}}(t - t_0) - V}{\tau_{\mathrm{c}}} \tag{5.19}$$

where $V_{\mathrm{cmd}}(t)$ is the desired command potential, V is the actual membrane potential, τ_{c} is a time constant dependent on the series resistance, membrane capacitance and amount of compensation, and t_0 is a remaining, unexplained latency. The quality of fit is shown in the right panel of Fig. 5.9.

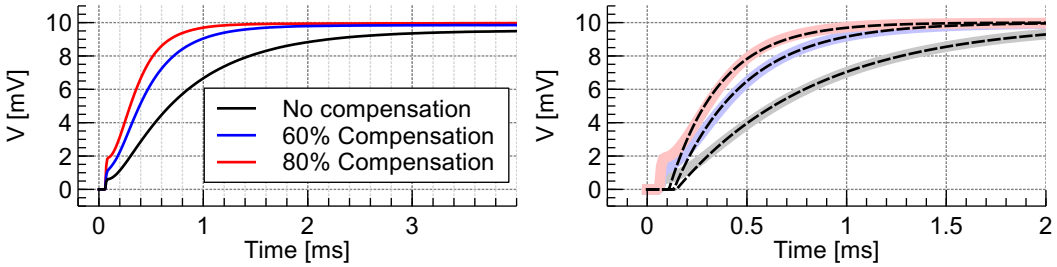

Figure 5.9: (Left) Membrane charging behavior measured in a model cell, during 'patch-clamp experiments' with 0%, 60% and 80% compensation. (Right) The charging behavior of a model cell can be modeled as an exponential convergence to the command potential and a slight delay. The thick, shadowed lines are the original traces from the left panel, the thin dashed lines are the fitted curves.

We found $\tau_{\mathrm{c}} \approx 0.70$ms uncompensated, $\tau_{\mathrm{c}} \approx 0.35$ms with 60% compensation and $\tau_{\mathrm{c}} \approx 0.26$ms with 80% compensation. By comparison, the values given by Beeler and Reuter's model for I_{Na} at -20mV are $\tau_m \approx 0.032$ms, $\tau_h \approx 1.1$ms and $\tau_j \approx 4.3$ms. This indicates that, even with good compensation, membrane charging will strongly interfere with the activation process, making τ_m more difficult to identify. With 'prediction' enabled (Sherman-Gold and Maertz, 2012), the situation is slightly more complex, as is shown in Fig. 5.10. However, for moderate prediction, the charging process is still reasonably well approximated by an exponential charging curve.

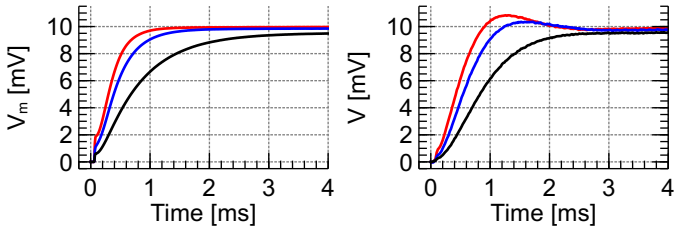

Figure 5.10: Uncompensated membrane charging (black) and charging with moderate (blue) or strong (red) compensation (left) or compensation/prediction (right).

To estimate the effects of membrane charging on I_{Na}, we updated our model of I_{Na} to include

a slowly charging membrane with $\tau_c \approx 0.3$ms. To reduce the number of extra parameters, the small latency t_0 seen in the model cell experiments was not included in the updated model. Because τ_c is not voltage-dependent we treated it as a single-valued parameter to be determined by the fitting procedure, and added it to the parameter vector p. With this updated model, we could simulate the effects of the membrane charging time on the fast sodium current. This is shown in Fig. 5.11 (left panel), which was made using the default model parameters given by Beeler and Reuter (for similar experiments using real cells, see Sherman et al., 1999). In the right panel, we show the ideal trace (i.e., with an instantaneously changing V) with a small time delay. This shows that the decaying part of the current is relatively unaffected by the slow membrane charging. By contrast, the time-to-peak, initial downward slope and peak current are all strongly affected.

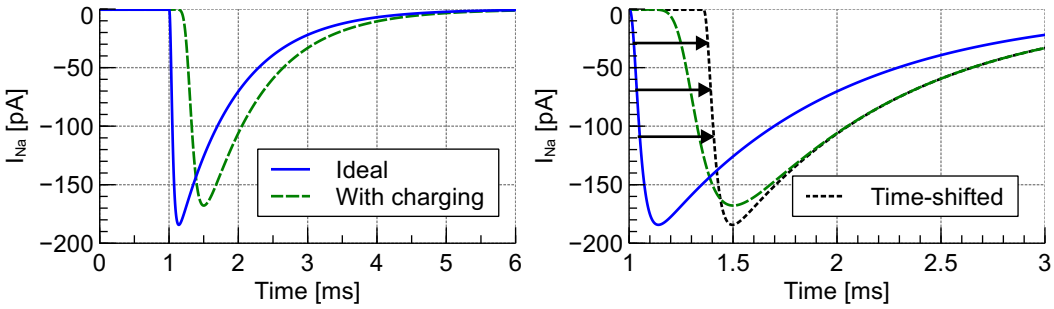

Figure 5.11: (Left) Simulated I_{Na} with ideal, instantaneous changes in membrane potential (blue, solid line) and with a realistic, series resistance compensated charging time (green, dashed). The charging time affects both the timing and the size of the peak. (Right) Time-shifting the ideal trace to overlap with the realistic trace reveals that the decaying phase is delayed, but otherwise unchanged (black dotted line).

The membrane charging time is not just an experimental issue, it also changes the identifiability of the model, making it more complex than the situation analyzed by Walch and Eisenberg. In their analysis, a single voltage step is considered so that V is piecewise constant, and the steady-state values and time constants for each V are single-valued parameters. Different step potentials V can then be applied and the appropriate constants worked out separately for each potential. Taking membrane charging time into account means adding a new variable to the model, but also means that, to accurately simulate a step from -120mV to -20mV, all values of the time constants and steady state values between -120mV and -20mV need to be identified simultaneously. However, provided the membrane charging time is short enough, only the activation process should be affected by this issue, as can be seen in the right panel of Fig. 5.11. To accommodate the changing V during activation, we used the full voltage-dependent parameters when fitting the model, allowing it to match the start of the experimental recording, even if in a non-unique way. Once the membrane is charged, the potential can once again be regarded as fixed. Based on the foregoing simulations and analysis we hypothesized that it should still be possible to

find reasonably accurate values for the time constants of inactivation. Similarly, the inaccuracy of dropping t_0 and not modeling the compensation/prediction curve will not affect inactivation measurements as long as the initial delay can be accommodated.

5.A.3 Repeated-fit experiments confirm our analysis

The top panel of Fig. 5.12 shows the variability observed between cells (i.e., single fits to different cells). It shows low variability in the steady-state values, but high variability for all time constants. The lower panel shows a similar graph for the variability observed between repeated fits to the same data from a representative cell ('cell 2'). Here it can be seen that, for the time constant of activation, the variability between repeated fits is similar to that observed between cells, so that no strong claims about inter-cell variability in activation can be made. Similarly, the variability observed in the determined steady-states can be explained as experimental error alone. By contrast, for the time constants of inactivation the variability between repeated fits is much lower than the inter-cell variability.

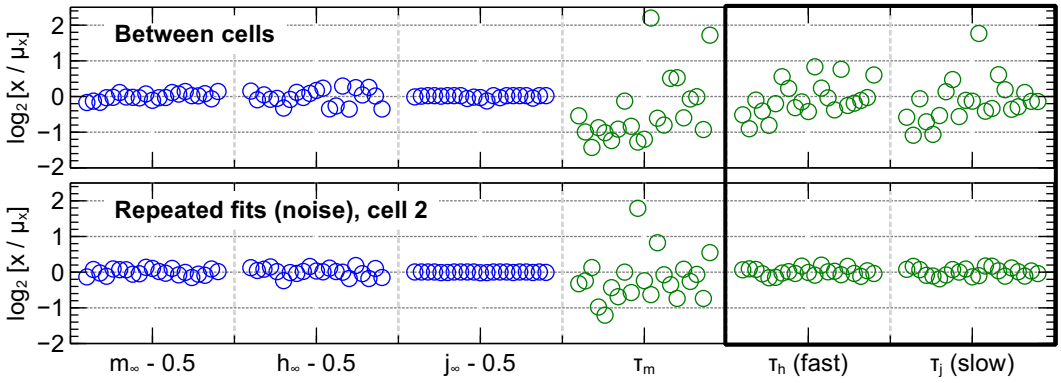

Figure 5.12: (*Top*) The variability in the parameters obtained by fitting our model to each of the 23 cells. For each parameter we show the $\log_2$ of its distance from the mean. The steady state parameters (m_∞, h_∞ and j_∞) were shifted by 0.5 to avoid dividing by zero, since $h_\infty \approx j_\infty \approx 0$. (*Bottom*) Variability in the parameters obtained by repeatedly fitting our model to the data from a single recording in cell 2 (data is shown from 23 re-runs).

5.B Additional results

5.B.1 Time-constant experiments

Fig. 5.13 shows alternative views of the I_{Na} measurements from Fig. 5.2. As can be seen, the maximum conductance varies widely, due to cell size, transfection success rate and differences in the kinetics of I_{Na} (as evinced by the different shapes of the curves, which are not simple linear multiples of each other).

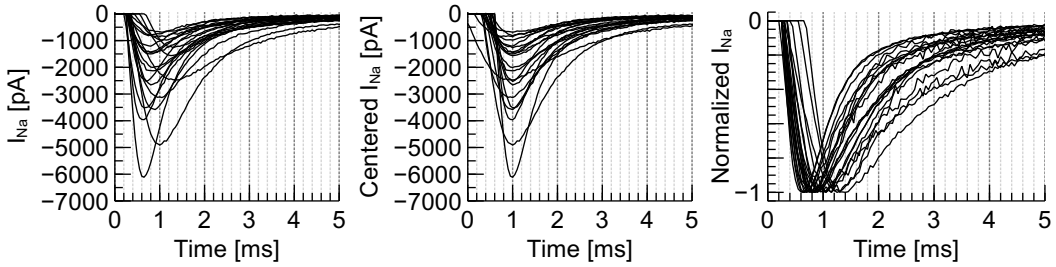

Figure 5.13: Alternative views of the single voltage-step experiments. (*Left*) The (pre-processed) data, without time-shifting or normalization. (*Middle*) The same data, time-shifted so that each peak occurs at $t = 1$ms. (*Right*) The same data, normalized to a peak-height of 1, without time-shifting.

Fig. 5.14 shows an example of the quality of fit obtained with the model including charging time.

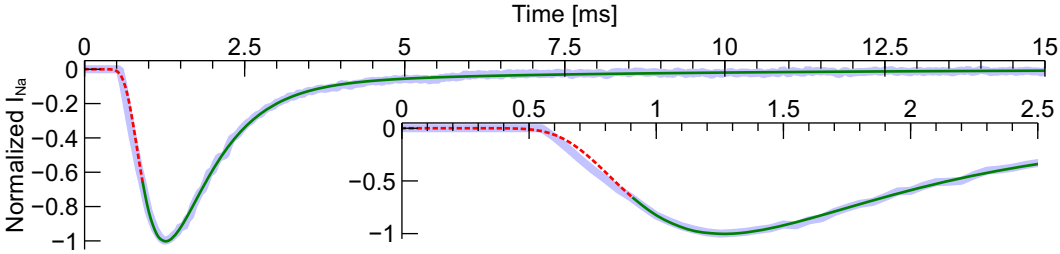

Figure 5.14: An example of the quality of fit obtained with the model including charging time. The raw data is shown in shaded blue. The model fit is shown as the solid green line. The dashed red lines indicates the part of the simulation that was not taken into account when calculating the score function. The inset gives a closer view of the same data during the initial downslope.

For 15 cells, we had two recordings made with a protocol containing a step from −120mV to −20mV. Fig. 5.15 shows the mean time constant determined using repeated fits to the recording from the first and second protocol for each of these cells. As can be seen, with a few exceptions, the cell behavior stayed constant during the experiment. Where values do vary, the direction of the change differs from cell to cell. This is inconsistent with the idea of

a slowly changing membrane potential due to flow of charged particles between the pipette and the cell, which would result in changes of a similar sign. On the basis of this figure, we also considered discarding the three cells that appear as 'outliers' in the top left of the left panel. However, the recordings showed no obvious deficiencies in leak or access resistance so that no objective criterion for rejecting them could be found. Removing these cells had a negligible effect on the corrected inter-cell standard deviations given in Section 5.3.1.3.

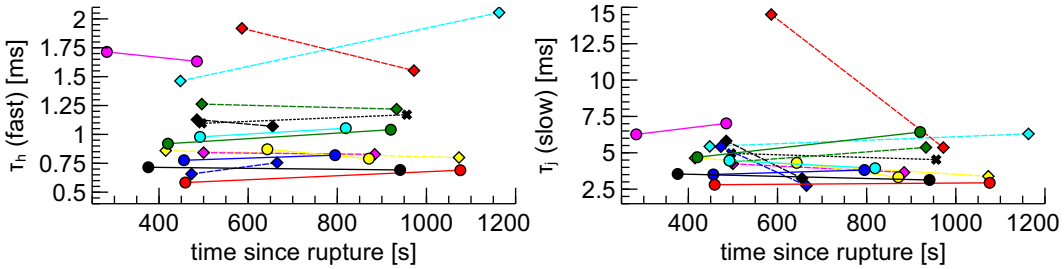

Figure 5.15: Changes in the time constants (determined as the mean constant using repeated fits) over time in 15 cells. Two time points are shown for each cell, connected by a line. Colors and markers are consistent between the left panel (fast inactivation) and the right (slow inactivation).

5.B.2 Midpoints of (in)activation in the biggest subgroup

Fig. 5.16.A shows the correlation between midpoint of activation and midpoint of inactivation for experiments in the largest subgroup. Regression coefficients were very similar to those found in the full dataset, with a slope of 1.13mV/mV and an offset of −38.3mV. The figure contains 28 points and has a slightly higher Pearson correlation coefficient than the full dataset (R=0.89). A distribution similar to Fig. 5.5.D but for the largest subgroup is shown in Fig. 5.16.B. Although there are fewer data points in these figures, the overall pattern is very similar.

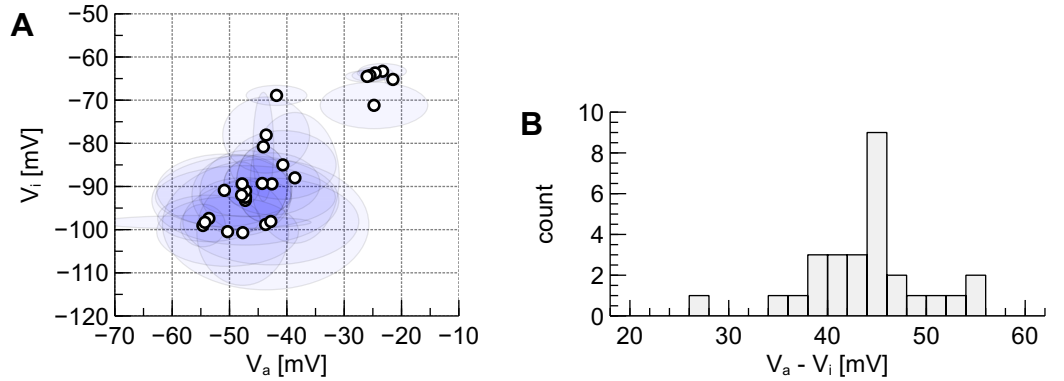

Figure 5.16: (*A*) Correlation between V_a and V_i in the largest subgroup. White dots indicate mean midpoints, blue ellipses indicate the corresponding $\pm 2\sigma$ range (*B*) A histogram of $V_a - V_i$ in the biggest subgroup.

5.B.3 β1-subunit coexpression

Table 5.4 shows the results from studies measuring midpoints of (in)activation of I_{Na} with and without β1-subunit. The table shows a variety of signs and magnitudes of reported shifts.

Table 5.4: Studies reporting midpoint of activation or inactivation with and without β1-subunit.

Midpoint of:	Activation [mV]			Inactivation [mV]				
	-β1	+β1	Shift	-β1	+β1	Shift	α	Cell type
An et al. (1998)				-70.2	-58.7	+11.5	a*	HEK
Bezzina et al. (2003)	-35.2	-39.9	-4.7	-78.3	-85.2	-6.9	a*	Oocyte
Calloe et al. (2011)	-34.4	-31.4	+3.0	-71.2	-77.7	-6.5	b	CHO
Groenewegen et al. (2003b)	-40.6	-38.63	+1.97	-82.75	-75	+7.75	a*	Oocyte
Wei et al. (1999)				-74.1	-63.2	+10.9	a*	Oocyte
Wan et al. (2000)	-33.4	-33.8	-0.4	-84.8	-79.3	+5.5	b*	Oocyte

5.C Studies used in the literature review

Table 5.5 shows all midpoints of (in)activation used in this study, along with the standard deviation (σ), number of cells (n) and the cell-type, α-subunit, and presence of β-subunit.

Table 5.5: Midpoints of (in)activation

Publication	V_a	σ_a	n_a	V_i	σ_i	n_i	Cell	α	β1
Abe et al. (2014)	-50.5	5.81	15	-84.1	5.03	15	HEK	b	no
Abriel et al. (2000)				-66.2	1.8	4	HEK	a*	yes
Abriel et al. (2001)	-21.5	0.735	6	-65.2	0.721	13	HEK	a*	yes
Abriel et al. (2001)	-23.3	2.08	3	-63.3	0.894	5	HEK	a*	yes
Abriel et al. (2001)	-24.6	1.56	3	-63.7	0.671	5	HEK	a*	yes
Abriel et al. (2001)	-25.5	1.56	3	-64.3	0.671	5	HEK	a*	yes
Abriel et al. (2001)	-26	1.91	3	-64.5	0.671	5	HEK	a*	yes
Aiba et al. (2014)	-43.3	4.76	7	-80.1	4.8	9	HEK	?	yes
Akai et al. (2000)	-44.1	0.9	9	-80.8	6.3	9	HEK	a*	yes
Albert et al. (2008)	-28.5	1.5	9	-60.8	0.959	23	Ooc.	a*	yes
Amin et al. (2005)	-36.7	6.96	10	-83.3	5.69	10	HEK	?	yes
An et al. (1998)				-70.2	5.36	17	HEK	a*	no
An et al. (1998)				-58.7	4.8	16	HEK	a*	yes
Bankston et al. (2007a)	-24.9	1.9	7	-61.3	3.67	5	HEK	?	yes
Bankston et al. (2007b)	-24.8	4.69	13	-71.2	2.7	9	HEK	a*	yes
Baroudi et al. (2000)				-101	5.63	22	HEK	a*	no
Baroudi et al. (2000)				-67.9	1.7	8	Ooc.	a*	no
Baroudi and Chahine (2000)	-47.2	8.15	23	-93.2	5.18	21	HEK	a*	yes
Baroudi et al. (2001)	-47.2	4.02	5	-92.5	2.26	4	HEK	a*	yes
Bébarová et al. (2008)	-31.8	4.8	16	-66.6	3.1	15	CHO	a	no
Beckermann et al. (2014)	-37.3	2.24	14	-86	1.33	11	HEK	?	yes
Beyder et al. (2010)	-33	22	6				HEK	b	no
Beyder et al. (2014)	-58.2	3	9	-95.5	3.9	9	HEK	b	no
Bezzina et al. (2003)	-35.2	14.7	8	-78.3	13	8	Ooc.	a*	no

Publication	V_a	σ_a	n_a	V_i	σ_i	n_i	Cell	α	$\beta 1$
Bezzina et al. (2003)	-39.9	8.6	4	-85.2	7.6	4	Ooc.	a*	yes
Calloe et al. (2011)	-34.4	0.566	8	-71.2	0.9	9	CHO	b	no
Calloe et al. (2011)	-31.4	1.26	10	-77.7	1.8	9	CHO	b	yes
Calloe et al. (2013)	-32.7	0.529	7	-69.5	0.529	7	CHO	b	no
Casini et al. (2007)	-38.6	3.87	15	-88	7.57	13	HEK	a*	yes
Chang et al. (2004)	-58.4	4.8	9	-107	2.7	9	HEK	?	yes
Chen et al. (2016)	-45.7	2.62	14	-80.7	4.5	12	HEK	?	yes
Cheng et al. (2010)	-32.2	3.2	16	-79.7	3.71	17	HEK	b	no
Cheng et al. (2010)	-31.1	3.43	6	-70.6	3.11	8	HEK	a	no
Cheng et al. (2010)	-34.9	3.6	9	-72	2.65	11	HEK	b	no
Cheng et al. (2010)	-34.9	2.01	5	-72.9	2.65	7	HEK	a	no
Cheng et al. (2011)	-37.6	3.39	8	-76.1	4.5	7	HEK	b	no
Cheng et al. (2011)	-39.6	5.59	5	-74.6	4.23	7	HEK	a	no
Clatot et al. (2012a)	-44.3	6.6	17	-81.7	1.9	10	HEK	b*	no
Cordeiro et al. (2006)	-49.3	1.05	15	-93	0.538	10	HEK	b*	yes
Crotti et al. (2012)	-50.8	10.3	33	-92.5	4.21	17	HEK	?	yes
Deschênes et al. (2000)	-53.6	4.47	5	-97.4	2.69	6	HEK	a*	yes
Detta et al. (2014)	-40.3	1.53	11				HEK	a*	yes
Ellinor et al. (2008)	-21.2	2.32	15	-61.8	0.825	17	Ooc.	a*	yes
Ge et al. (2008)	-35.5	5.05	13	-78.7	6.63	26	HEK	a	yes
Glaaser et al. (2012)				-69.1	9.9	9	HEK	?	no
Gosselin-Badaroudine et al. (2012)	-55.3	2.28	7	-100	2.04	7	Ooc.	b	yes
Groenewegen et al. (2003b)	-40.6	6.08	15	-82.8	6.62	15	Ooc.	a*	no
Groenewegen et al. (2003b)	-38.6	8.77	8	-75	6.36	8	Ooc.	a*	yes
Groenewegen et al. (2003a)	-37.3	6.22	8	-78	4.05	7	Ooc.	a*	no
Gütter et al. (2013)	-35.1	3.75	88	-84.3	4.95	68	HEK	a*	no
Gütter et al. (2013)	-33.5	3.62	82	-71.2	3.7	28	Ooc.	a*	no
Gui et al. (2010a)	-34.7	3.36	23	-81.4	3.43	24	HEK	a*	no
Gui et al. (2010a)	-34.2	2.81	22	-67.7	2.78	31	Ooc.	a*	no
Gui et al. (2010b)	-33.8	2.32	11	-80.3	3.12	12	HEK	a*	no
Hayashi et al. (2015)	-43.8	6.8	16	-80	2.4	16	CHO	?	yes
Holst et al. (2009)	-30.4	2.24	14	-82	4.69	13	HEK	?	no
Hoshi et al. (2014)				-79.5	2.55	18	HEK	a	no
Hsueh et al. (2009)	-42.6	2.56	10	-84.3	3.79	10	HEK	a	yes
Hu et al. (2007)	-50.8	1.03	33	-92.5	0.412	17	HEK	b*	yes
Hu et al. (2010)				-92.5	4.21	17	HEK	?	yes
Hu et al. (2014)				-92.5	3.85	22	HEK	b	yes
Hu et al. (2015)	-41	3.9	9	-80	6.97	19	HEK	b	no
Hu et al. (2015)	-41	8.65	13	-80	9.35	14	HEK	a	no
Huang et al. (2006)	-59.9	2.55	8	-108	5.09	8	HEK	?	no
Huang et al. (2009)	-50.3	6.18	9	-100	4.02	9	HEK	a*	yes
Itoh et al. (2005a)	-39.9	7.5	25				HEK	a*	yes
Itoh et al. (2005b)	-40.6	6.42	21				HEK	a*	yes
Itoh et al. (2007)				-90.9	3.3	9	HEK	a*	yes
Juang et al. (2014)	-36.3	0.4	4	-86.4	1.4	4	HEK	a	yes
Kato et al. (2014)	-54.4	8.91	18	-83.8	9.62	21	CHO	a*	yes
Keller et al. (2005)	-41	6.9	9	-77.1	3.58	5	HEK	b*	yes
Keller et al. (2006)	-60.1	4.49	10	-104	1.81	8	HEK	?	yes
Li et al. (2009)	-56.6	4.21	6	-104	3.87	6	HEK	?	no

Publication	V_a	σ_a	n_a	V_i	σ_i	n_i	Cell	α	$\beta 1$
Lin et al. (2008)	-54.6	1.96	7	-99	2.46	8	HEK	a*	yes
Liu et al. (2002)				-73.3	6.2	4	HEK	a*	yes
Liu et al. (2003)	-50.4	4.38	11	-76.4	4.8	16	HEK	?	no
Liu et al. (2005)				-97	4.2	9	CHO	b	no
Lupoglazoff et al. (2001)	-47.2	7.85	19	-92.5	3.65	11	HEK	a*	yes
Makita et al. (1998)				-68.7	4.31	11	Ooc.	a*	no
Makita et al. (2002)	-47.2	3.97	13	-91	4.69	13	HEK	a*	yes
Makita et al. (2005)	-48.1	3.92	19	-86.6	3.71	17	HEK	?	yes
Makita et al. (2008)	-49.7	6.22	32	-86.8	5.5	25	HEK	?	yes
Makiyama et al. (2008)	-43.6	3.79	23	-78.1	4.41	22	HEK	a*	yes
Marangoni et al. (2011)	-44	8	16	-92	7.21	13	HEK	?	yes
Medeiros-Domingo et al. (2007)	-43.8	2.86	5	-78.8	3.51	10	HEK	?	no
Medeiros-Domingo et al. (2009)	-38.6	3.49	15	-76	5.23	19	HEK	b	no
Mohler et al. (2004)	-41.8	2.65	7	-68.9	1.16	15	HEK	a*	yes
Mok et al. (2003)	-47.2	5.6	4	-91.1	0.693	3	HEK	?	yes
Moreau et al. (2013)	-47.9	4.33	13	-92	4.69	13	HEK	a*	yes
Murphy et al. (2012)	-50.9	10.3	20	-102	6.32	10	HEK	a*	no
Nakajima et al. (2015)	-38.7	3.1	15	-85.9	2.47	17	HEK	b	yes
Neu et al. (2010)	-50.9	5.89	12	-90.9	4.2	9	HEK	a*	yes
Nguyen et al. (2008)	-47.8	1.58	10	-89.4	2.53	10	HEK	a*	yes
O'Leary et al. (2002)				-78.6	0.134	5	Ooc.	?	no
Olesen et al. (2012)	-27.9	6.1	22	-85.6	4.5	25	HEK	?	no
Otagiri et al. (2008)	-44.4	4.26	37	-88.3	4.87	37	HEK	?	yes
Pfahnl et al. (2007)	-50	1.55	15	-98	8.52	15	HEK	b*	no
Poelzing et al. (2006)							HEK	a	no
Rivolta et al. (2001)	-23.3	2.24	5	-62.8	3.12	12	HEK	?	yes
Rook et al. (1999)	-35.9	0.949	10	-77.4	0.316	10	Ooc.	a*	no
Rossenbacker et al. (2004)	-24.1	0.894	5	-70.9	1.4	4	HEK	?	yes
Ruan et al. (2007)	-23.2	1.92	5	-62.5	2.15	10	HEK	?	yes
Ruan et al. (2010)	-23.1	1.77	9	-67.7	3.01	12	HEK	?	yes
Saber et al. (2015)	-24	4.9	6	-66	4.9	6	HEK	?	yes
Samani et al. (2009)	-36	5.03	7	-89.9	5.4	9	HEK	b	yes
Sarhan et al. (2009)				-109	1.85	7	HEK	a	no
Shinlapawittayatorn et al. (2011b)				-91.9	4.5	7	HEK	a	no
Shinlapawittayatorn et al. (2011a)				-91.2	2.77	12	HEK	a	no
Shirai et al. (2002)	-49.9	2.38	7	-94.9	6.37	6	HEK	a*	no
Shuraih et al. (2007)	-43.4	0.794	7	-90.7	0.265	7	HEK	b	yes
Shy et al. (2014)	-29.6	3.68	8	-76.9	6.96	10	HEK	?	no
Smits et al. (2005a)	-42.6	4.2	9	-89.4	3.6	9	HEK	a*	yes
Smits et al. (2005b)	-43.7	9	9	-98.8	7.57	13	HEK	a*	yes
Sottas et al. (2013)	-29.8	1.99	11	-72.2	1.66	11	HEK	?	yes
Splawski et al. (2002)	-26.6	3.68	8				HEK	?	no
Surber et al. (2008)	-31.5	7.27	27	-67.6	3.7	28	Ooc.	a*	no
Surber et al. (2008)	-42.2	3.37	14	-79.4	3.43	6	HEK	a*	no
Swan et al. (2014)	-28	3.39	8	-75.8	4.9	6	HEK	b	yes
Tan et al. (2001)	-48.6	3.17	7	-92	4.5	7	HEK	?	yes
Tan et al. (2002)	-40.3	2.88	13	-93.5	4.33	13	HEK	a*	no
Tan et al. (2005)	-39	4.9	6	-75	5.66	8	HEK	b	no
Tan et al. (2005)	-38	4.9	6	-75	6	9	HEK	b	no

Publication	V_a	σ_a	n_a	V_i	σ_i	n_i	Cell	α	$\beta 1$
Tan et al. (2005)	-42	2.91	5	-81	4.2	9	HEK	b	no
Tan et al. (2005)	-41	3.39	8	-79	5.31	11	HEK	b	no
Tan et al. (2005)	-42	2.55	8	-79	4.2	9	HEK	b	no
Tan et al. (2005)	-40	9.55	6	-78	7.83	5	HEK	b	no
Tan et al. (2005)	-40	1.39	3	-81	4.68	3	HEK	b	no
Tan et al. (2005)	-39	4	4	-75	5.66	8	HEK	a	no
Tan et al. (2005)	-39	4	4	-78	2.83	8	HEK	a	no
Tan et al. (2005)	-42	3.96	8	-82	4.85	12	HEK	a	no
Tan et al. (2005)	-40	8.49	18	-79	8.49	18	HEK	a	no
Tan et al. (2005)	-43	2	4	-82	6.2	4	HEK	a	no
Tan et al. (2005)	-42	3.39	8	-82	3.6	9	HEK	a	no
Tan et al. (2005)	-40	5.66	8	-80	4.8	9	HEK	a	no
Tan et al. (2005)	-41	1.8	4	-80	1.2	4	HEK	a	no
Tan et al. (2006)	-46.9	3.39	8	-81.8	3.68	8	HEK	b	no
Tan et al. (2006)	-44.1	5.06	10	-80	4.74	10	HEK	a	no
Tarradas et al. (2013)	-32	1.27	18	-84.9	2.85	10	HEK	a*	no
Tester et al. (2010)	-42	4	4	-72	2.24	5	HEK	b	no
Tsurugi et al. (2009)	-39.6	3.39	8	-88	2.55	8	HEK	?	no
Valdivia et al. (2004)	-42	7.75	15	-84.3	4.47	20	HEK	b	no
Vatta et al. (2002a)				-89.5	0.49	6	HEK	?	no
Vatta et al. (2002b)	-24.9	1.13	8	-68.4	0.332	11	Ooc.	?	no
Viswanathan et al. (2003)	-40.7	4.64	11	-85	3.98	11	HEK	a*	yes
Wang et al. (1996)	-43.2	6.85	13	-99.6	2.92	11	HEK	a*	no
Wang et al. (2002)	-47.7	4	16	-101	6.1	19	HEK	a*	yes
Wang et al. (2007a)	-44.3	2.24	14	-89.3	4.4	16	HEK	a*	yes
Wang et al. (2007b)	-46	6.93	5				HEK	a*	yes
Wang et al. (2008)	-44.3	2.24	14	-89.3	4.4	16	HEK	a*	yes
Wang et al. (2011)				-93.9	2.65	11	HEK	?	no
Wang et al. (2015)	-40.9	0.63	9	-72.7	2.49	7	HEK	a*	no
Wang et al. (2016)	-44.5	4.8	36	-93.5	4.08	34	HEK	?	yes
Watanabe et al. (2011c)	-35.4	3	25	-84.5	4.9	24	CHO	a	no
Watanabe et al. (2011c)	-47.7	4.4	16	-89.4	3.05	19	HEK	a	no
Wedekind et al. (2001)	-42.8	7.67	7	-98.1	5.03	7	HEK	a*	yes
Wehrens et al. (2003)	-29.8	1.13	8	-64	2.26	8	HEK	?	yes
Wei et al. (1999)				-63.2	4.11	10	Ooc.	a*	yes
Wei et al. (1999)				-74.1	2.38	7	Ooc.	a*	no
Winkel et al. (2012)	-26	10.3	17	-84.6	7.2	16	HEK	?	no
Yang et al. (2002)	-54.3	9.26	7	-98.3	0.794	7	HEK	a*	yes
Ye et al. (2003)	-44	15.8	10	-95	14.4	9	HEK	a*	no
Ye et al. (2003)	-40	18.5	7	-86	15.3	7	HEK	b*	no
Yokoi et al. (2005)	-49.8	3.68	8	-88.6	3	9	HEK	?	no
Young and Caldwell (2005)	-32.7	5.81	20	-66	8.94	20	CHO	a*	no
Zeng et al. (2013)	-34.5	4.24	8	-81.1	4.69	13	HEK	a	yes
Zhang et al. (2008)	-33.1	2.24	5	-64.5	0.98	6	Ooc.	a*	no
Zhang et al. (2015)	-28.1	5.03	15				HEK	?	no

CHAPTER 6

Predicting changes to I_{Na} from missense mutations in *SCN5A*

Abstract

We investigated the possibility of predicting changes in I_{Na} resulting from single nucleotide missense mutations in the underlying α-subunit channel gene *SCN5A*. An exhaustive list of nonsynonymous missense *SCN5A* mutations was compiled and annotated with the reported qualitative and quantitative changes to whole-cell I_{Na}. Specifically, we focused on changes to activation, inactivation, the late component of inactivation, and mutations that caused a complete absence of current. Mutations were characterized by their position on the gene and the difference in physical properties of the old and new amino acid (e.g., the difference in the acid's charge or hydrophobicity). Clinically investigated mutations were found to occur with uneven density across the gene, with a particularly high mutation density in the voltage sensing segments. The site of mutations could be correlated to channel function, showing a high number of activation-affecting mutations in the voltage sensor, and many current-blocking mutations in the pore-forming linker between segments 5 and 6. We were unable to link the physical properties of the exchanged amino acids to the resulting changes in I_{Na}. The dataset was then investigated using machine-learning techniques. The resulting predictions showed an accuracy only modestly better than chance, but with improved sensitivity and specificity, characterized by an increased area under the receiver-operating curve and a positive Matthews correlation coefficient. Although we were able to find published cell electrophysiology data for over 200 missense mutations, further work is needed to increase the size of this dataset and address issues with its bias and internal inconsistency. In addition, methods of interpreting the change in physical properties due to the amino-acid substitution need to be developed.

Contents

6.1 Introduction . . . 109
6.2 Methods . . . 109
6.2.1 Finding mutations in the literature . . . 109
6.2.2 Numbering of amino acids . . . 110
6.2.3 Electrophysiological characterizations . . . 110
6.2.4 Experimental set-up . . . 110
6.2.5 Substitution frequency ratios . . . 111
6.2.6 Machine-learning datasets . . . 111
6.2.7 Machine-learning features . . . 112
6.2.8 Machine-learning methods . . . 113
6.2.9 Other software tools . . . 113
6.3 Results . . . 114
6.3.1 Positional properties . . . 116
6.3.2 Amino-acid properties . . . 118
6.3.3 Midpoints of (in)activation . . . 121
6.3.4 Machine-learning results . . . 122
6.4 Discussion . . . 123
6.4.1 Comparison to previous work . . . 124
6.4.2 Future work: improving predictions . . . 125
6.4.2.1 Increasing dataset size . . . 125
6.4.2.2 Reducing dataset bias . . . 125
6.4.2.3 Improving internal consistency . . . 126
6.4.2.4 Finding suitable features . . . 126
6.5 Conclusion . . . 127
6.A Supplementary results . . . 128
6.A.1 Reported mutations over time . . . 128
6.A.2 Reporting of experimental conditions . . . 128
6.A.3 Inconsistencies in the dataset . . . 129
6.A.4 Information gain per feature . . . 129
6.A.5 EP-data overview . . . 131

6.1 Introduction

The human gene *SCN5A* encodes the pore-forming α-subunit of the cardiac sodium channel $Na_V1.5$ which carries the fast sodium current I_{Na}. I_{Na} is responsible for the initial rapid upstroke of the cellular action potential (AP) and a major determinant of electrical propagation in the heart (Kléber and Rudy, 2004). Mutations in *SCN5A* have been linked to several arrhythmogenic phenotypes, including Brugada syndrome, long-QT syndrome and conduction disorders (Wilde and Brugada, 2011). However, the relationship between channel genotype and disease phenotype is not fully understood and predictions of the pathogenicity of *SCN5A* mutations are generally less accurate than those in other channel genes (Leong et al., 2015; Kapa et al., 2009). In this study, we aimed to establish statistical links between *SCN5A* missense mutations and I_{Na} properties. We hypothesized that the reduction in complexity this entails compared to genotype-clinical phenotype correlations, could improve the accuracy of predictions. Mechanistic modeling methods could then be used to estimate the pathogenicity of the predicted I_{Na} effects at the tissue and organ level (see for example Hoefen et al., 2012).

To investigate this hypothesis, we conducted an extensive literature review of reported mutations in *SCN5A* for which cellular electrophysiology (EP) data was available. We focused only on non-synonymous missense mutations. As a simple initial definition of a current phenotype, we used the presence or absence of changes to activation, inactivation (including recovery), or the late component of I_{Na}. In addition, we noted which mutations abolished the current completely. We then evaluated the power of *machine-learning* techniques (Deo, 2015) to make genotype-I_{Na} predictions using this dataset. Finally, we investigated if *quantitative* predictions could be made by applying the same methods to the problem of predicting shifts in midpoints of activation and inactivation.

6.2 Methods

6.2.1 Finding mutations in the literature

To find publications on *SCN5A* missense mutations, we scanned through all PubMed results for the term '*SCN5A* mutation'. In addition, we screened previously published overview papers by Kapplinger et al. (2015, 2010); Hedley et al. (2009); Zimmer and Surber (2008); Ackerman et al. (2004); Moric et al. (2003); Napolitano et al. (2003). From the selected papers, we listed all nonsynonymous missense mutations for which cellular EP data was known, or which were associated with a pathological clinical phenotype. Because we focused on changes to channel function, we did not distinguish between nucleotide changes that resulted in the same amino-acid change.

6.2.2 Numbering of amino acids

In numbering the mutations, we used the position on the full, 2016 residue long sequence for human *SCN5A* (Isoform 1, GenBank accession number AC137587). In some cases this meant adjusting the numbering used in the paper.

6.2.3 Electrophysiological characterizations

Where possible, we collected information about the changes to whole-cell I_{Na} resulting from each mutation. First, we asked whether or not the mutated channel conducted a current large enough to measure (making no distinction between blocked pores and other factors such as trafficking defects). For conducting channels, we then looked if activation, inactivation (including recovery) and the late component were affected. Each of these fields was recorded as 'measured and affected', 'measured and not affected', or 'not measured'. The distinction between affected and not affected was made based on the significance (p-value) given in the paper and the wording used by the authors. Only homozygous measurements were included. Where possible, we calculated shifts in midpoint of activation and inactivation from the data given in the paper.

6.2.4 Experimental set-up

Every measurement recorded in the EP database was annotated with three fields: the type of α-subunit, the cell-type, and the presence of β1-subunits. In order of descending frequency the cell types were HEK (HEK293 and tsA-201), *Xenopus laevis* oocytes and CHO, but we also found a small number of measurements in COS cells and transgenic mouse myocytes. Some papers failed to mention the cell type and were listed as 'unknown'.

Many papers did not give precise information about the type of α-subunit used. We found at least five different subunits. First, some papers used a construct corresponding directly to either isoform 1 or isoform 2. Isoform 1 was denoted as *a*; it has a glutamine at position 1077 (Q1077) and is 2016 amino acids long (GenBank accession numbers AC137587 and NM_198056). Isoform 2 was denoted *b*; it lacks the 1077 glutamine (Q1077del) making it 2015 amino acids long (GenBank accession numbers AY148488 and NM_000335). Isoform 2 is now held to be the most common isoform, making it the preferred isoform for electrophysiological investigations (Makielski et al., 2003; Ye et al., 2003). A number of α-subunit clones have historically been used that turned out to contain unintended variants. The most common of these is often called 'hH1' (GenBank accession number M77235) and is equal to isoform 1 except for the rare variant R1027Q. We labeled this α-subunit *a**. All papers mentioning 'hH1' as the only reference were recorded as using *a**. A less common variant corresponding to isoform 2 with a T559A mutation was labeled *b**. Finally, some of the earliest papers had isoforms that turned out to contain additional rare and/or common

Table 6.1: α-subunit types of the I_{Na} channel, found in our literature search. The code for each type is given, as well as a description and, where possible, a GenBank accession number.

Code	Description	Acc. No.
a	Isoform a (Q1077)	AC137587
b	Isoform b (Q1077del)	AY148488
a*	hH1 (Q1077; R1027Q)	M77235
b*	hH1a (T559A; Q1077del)	None

variants, and in many cases the exact α-subunit type was not mentioned in the paper. An overview of the four main α-subunit types found is given in Table 6.1.

6.2.5 Substitution frequency ratios

Each mutation included in our database replaced one amino acid with another. To visualize the frequency with which each substitution was made, we calculated the *observed frequency* as the number of times a substitution occurred divided by the total number of substitutions in our database. Because *SCN5A* does not contain equal amounts of each amino acid, and because some transitions are more likely than others, we calculated a second measure for the *expected frequency*: First, we listed all possible single nucleotide changes in *SCN5A* and computed the resulting amino-acid substitutions. Next, we filtered out all nonsense and synonymous substitutions and used the remaining list as the list of expected mutations. From this, the expected frequency was calculated the same way as before. Finally, we calculated the ratio between the observed and the expected frequencies. This should be 1 if the mutation occurs with the expected rate, greater than 1 if it occurs more often, and less than 1 if it occurs less frequently than expected. Two additional modifications were made to allow visualization of the results: First, any substitution for which the expected frequency was 0 was assigned a ratio of 1. Secondly, to allow logarithmic plotting of the ratios, any substitution that was expected but never observed (and so should have ratio 0) was assigned a ratio equal to the lowest naturally observed non-zero ratio.

6.2.6 Machine-learning datasets

We created two types of datasets used to test the power of machine-learning algorithms to predict cellular EP. Both contained a number of *features* describing each mutation (see below). In addition, each dataset contained an *outcome* field describing the outcome to predict. We used both qualitative and quantitative outcomes.

A dataset was created for each of the qualitative outcomes 'activation', 'inactivation', 'late' and 'zero', where each outcome was listed as either 'affected' or 'unaffected'. Only mutations for which the outcome was known were included. Where multiple EP recordings were available, conflicts were resolved by a majority vote. Mutations with an equal number of reports claiming 'affected' and 'unaffected' were not included in the dataset.

For (semi-)quantitative predictions, we created a dataset of shifts in midpoint of activation or inactivation. Instead of using numerical voltages, we discretized the voltage shifts by assigning them to one of three intervals: $(-\infty, -3\text{mV}), [-3\text{mV}, 3\text{mV}], (3\text{mV}, \infty)$. Where multiple values were available, we selected a single recording by looking at the experimental conditions used. First, recordings co-expressing β1-subunits were preferred. Secondly, we looked for recordings made with the α-subunit 'b'. Thirdly, we prioritized recordings in HEK cells over others (since these were the most common in our dataset). Finally, any remaining conflicts were resolved by selecting the most recent recording.

6.2.7 Machine-learning features

Each mutation in the machine-learning datasets was specified by its index and a number of features intended to capture aspects of its physical consequences. First, we added features based on the annotations for *SCN5A* found on http://www.ncbi.nlm.nih.gov. These were: *side* (cytoplasmic, transmembrane, extracellular), *segment type* (terminus, segment, linker, domain linker) or *region type* (N-terminus, segment 1, segment 2, ..., segment 6, segment linker 1-2, ..., segment linker 5-6, domain linker 1-2, ..., C-terminus). In addition, we added the distance (in amino-acid counts) of each position to selected regions of the protein, namely the 4th, 5th, and 6th segment, the linkers between segments 4 and 5 and segments 5 and 6, the nearest transmembrane segment, the linker between domains 3 and 4, and the C-terminus.

Next, we added features describing physical properties of the substituted amino acids (e.g., their charge). Instead of adding the old and new properties directly, we only added the change in each property (e.g., the charge of the original residue minus the charge of the new residue). We added the change in average residue mass, percentage of buried residues, van der Waals volume, and polarity ranking (all from Simpson, 2003), amino-acid charge, hydrophobicity ranking (Kovacs et al., 2006) and α-helix propensity (Pace and Scholtz, 1998). Next, we added a measure of amino-acid similarity (Grantham, 1974) and of substitution likelihood (Gonnet et al., 1992)

Finally, we added a measure of conservedness for each position in the amino acid. This was calculated by performing a sequence alignment of human sodium channel genes and isoforms, as listed in Table 6.2. To further emphasize the functionally most important positions, two non-human sequences were added that have a history in cell electrophysiology: the eel sequence by Noda et al. (1984) and the sequence by Rosenthal and Gilly (1993) of *Doryteuthis opalescens*, a squid formerly known as *Loligo*. Sequences were aligned using Clustal 2.1 (Larkin et al., 2007) using the 'Gonnet-250' scoring matrix. The resulting conservedness score for each position of *SCN5A* was then added to the set of machine-learning features.

Table 6.2: All used human sodium channel isoforms.

Name	Accession number	Name	Accession number
SCN1A, isoform 1	NP_001189364.1	*SCN5A*, isoform 3	NP_001092874.1
SCN1A, isoform 2	NP_008851.3	*SCN5A*, isoform 4	NP_001092875.1
SCN1A, isoform 3	NP_001159436.1	*SCN5A*, isoform 5	NP_001153632.1
SCN2A, isoform 1	NP_001035232.1	*SCN5A*, isoform 6	NP_001153633.1
SCN2A, isoform 2	NP_001035233.1	*SCN7A*	NP_002967.2
SCN3A, isoform 1	NP_008853.3	*SCN8A*, isoform 1	NP_055006.1
SCN3A, isoform 2	NP_001075145.1	*SCN8A*, isoform 2	NP_001171455.1
SCN3A, isoform 3	NP_001075146.1	*SCN9A*	NP_002968.1
SCN4A	NP_000325.4	*SCN10A*	NP_006505.2
SCN5A, isoform 1	NP_932173.1	*SCN11A*	NP_001274152.1
SCN5A, isoform 2	NP_000326.2		

6.2.8 Machine-learning methods

Weka 3.7.12 (Hall et al., 2009) was used to quickly experiment with different machine-learning methods. To increase our chance of success, we experimented with methods based on very different underlying principles. We used a tree-based 'Random forest' classifier (Breiman, 2001), a Bayesian-statistics based 'Naive Bayes' classifier (John and Langley, 1995), a classifier based on a multilayer perceptron (a type of neural network), a support-vector machine classifier (Chang and Lin, 2011) and a nearest-neighbor classifier, which is an example of an instance-based learning method (Aha et al., 1991).

Performance was assessed using 10-fold cross-validation. Success was evaluated using several measures: the percentage of correct guesses (or accuracy, ACC), sensitivity (or true positive rate), specificity (or true negative rate), the area under the receiver operating characteristic (or area-under-curve, AUC, Mason and Graham, 2002), and the Matthews correlation coefficient (MCC).

As a baseline for each measure a Zero-R classifier was used. This simply assigns the most common class in a dataset to every new instance it evaluates. Thus, when a dataset contains 90 instances where the current is affected and 10 where it is not, the Zero-R classifier always predicts 'affected' and so has an accuracy of 90%. Using this baseline, another method with an apparently high accuracy of 91%, can be seen to have only made a small improvement over pure chance.

To see which features of the data were most useful for classification, we ranked them according to their *information gain*. See the Weka documentation (`http://www.cs.waikato.ac.nz/ml/weka/`) for details.

6.2.9 Other software tools

All gathered data was stored in an SQLite database, and analysis was performed using Python. Statistical tests were carried out using SciPy (Jones et al., 2001).

6.3 Results

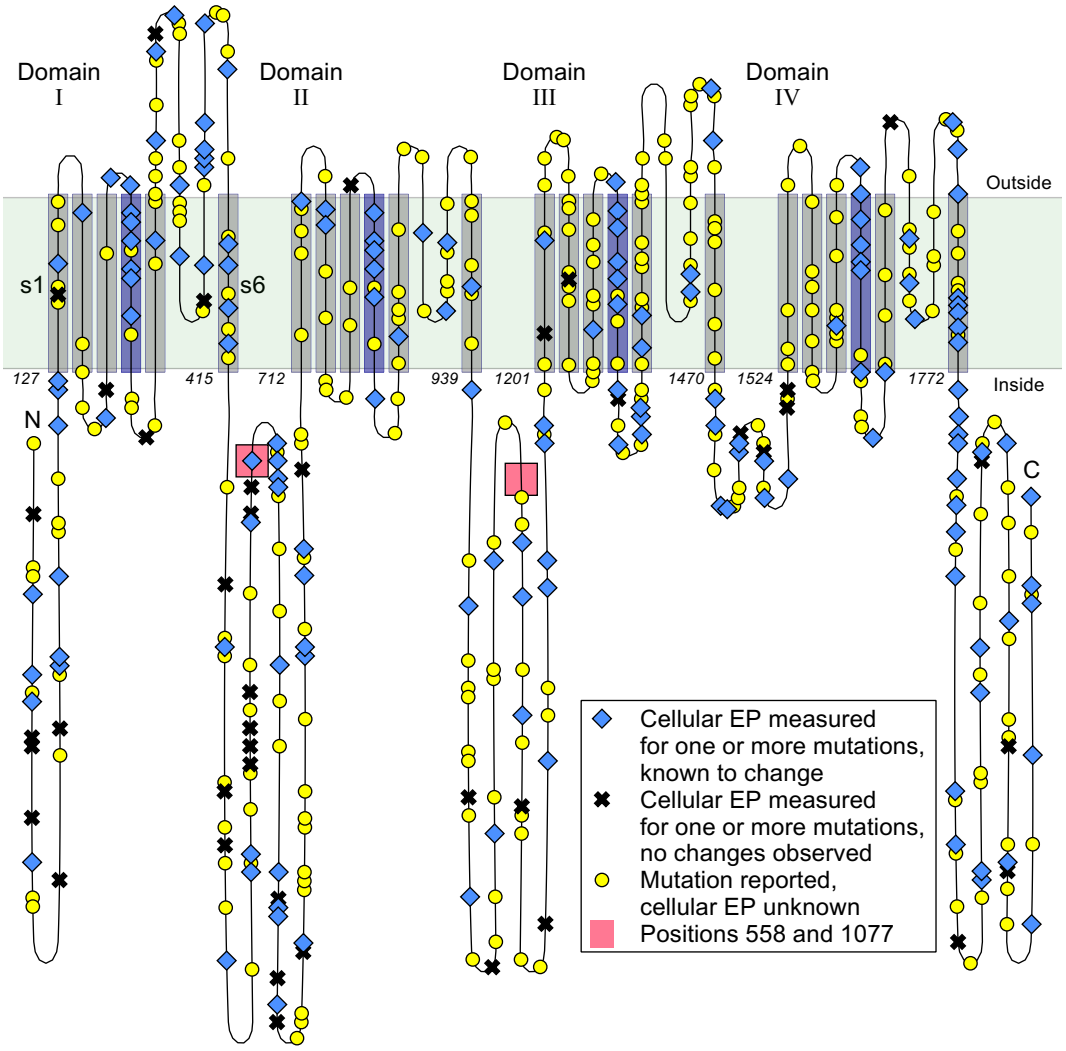

Figure 6.1: A schematic overview of $Na_V1.5$. The transmembrane segments are shown for all four domains (left to right). In each domain, the voltage-sensing 4th segment is colored dark blue. Positions at which a mutation was tested and found to change the cellular EP are marked with blue diamonds. Positions at which one or more mutations were tested but no changes to the cellular EP were observed are indicated with black crosses. All remaining positions where a mutation was observed or described in the literature (i.e., investigated in connection with altered heart rhythm) are indicated with yellow circles. The locations of the common polymorphisms H558R and del1077Q are indicated with red boxes. The diagram was constructed with near-equal spacing between positions, to indicate the relative size of the sections. The linker between segments 5 and 6 of each domain is known to fold back into the membrane, as is shown in the diagram. Note that the folding of segments 5 and 6 and the inter-domain linkers in this diagram is purely symbolic, and the exact location of mutations may differ. The division of *SCN5A* into domains, segments and linkers is based on the annotations given on http://www.ncbi.nlm.nih.gov.

Table 6.3: The number of mutations in our database for various categories. Because some data is available for different substitutions at the same position, we also provide the number of unique positions seen.

	mutations	**positions**
Total found	610 (5.1%)	482 (24%)
With EP-data	243 (2.0%)	199 (9.9%)
EP changed	175	143
EP unchanged	68	64
Activation changed	69	60
Inactivation changed	125	104
Late component changed	40	35
Zero current	30	27
Possible	11923	2016
Possible (with duplicates)	13357	2016

Fig. 6.1 shows a schematic overview of $Na_V1.5$ and its four domains, each featuring six transmembrane segments (shaded regions). The fourth segment in each domain is sensitive to changes in voltage, and the linker between segments 5 and 6 is known to fold back into the membrane to create the channel pore (Catterall, 2000). Both the C-terminus and the linker between domains III and IV have been associated with inactivation and the late component of the sodium current (Motoike et al., 2004). Many mutations outside of these sensitive areas have also been linked to arrhythmia.

A numerical view of the data is given in Table 6.3. It shows the number of mutations in our database, and the number of unique positions at which they occur. In addition to the total number gathered, the table shows the number for which EP-data is available, the number for which EP was altered, and the totals for each specific type of change. We gathered 378 reports of EP-data measurements, but as several studies investigated the same mutations (either confirming previous work or researching new aspects), we found cellular EP for only 243 missense mutations. The final row in the table gives the total number of possible missense mutations arising from a single nucleotide change in *SCN5A* before and after removing duplicate gene products. This was calculated by simply listing all nucleotide substitutions in the coding region of *SCN5A* and noting which ones resulted in an amino-acid switch (not including stop codons). From this we calculated that there are approximately $11923/2016 \approx 5.91$ possible mutations per position in the gene, so that while Fig. 6.1 accurately reflects the positions at which mutations are known, it should not be taken as an indication of the coverage of our mutation dataset, which it overstates by about six times. A list of mutations and the resulting changes in cellular EP is given in Section 6.A.5.

6.3.1 Positional properties

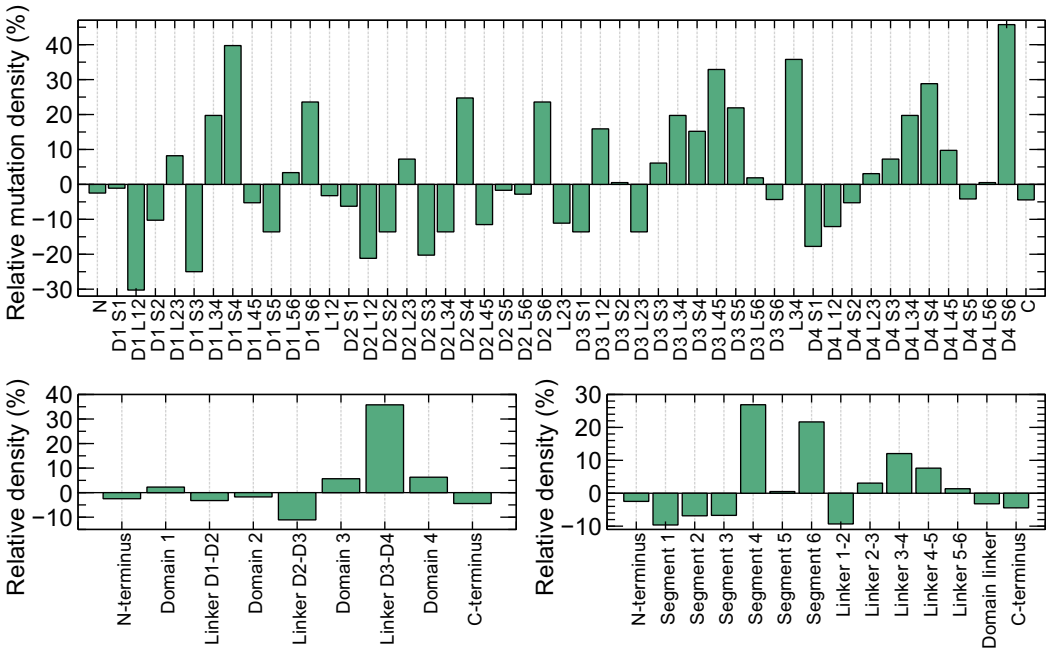

Figure 6.2: Relative mutation densities in different regions of *SCN5A*. Mutation densities were calculated as *number-of-mutations-in-region/length-of-region*. Relative densities were then obtained by subtracting the mutation density of the entire gene. The resulting measure indicates which regions of the protein have a higher or lower-than-average number of mutations per amino acid. The top panel shows the relative density for all regions of *SCN5A*, starting with the N-terminus (N), then segment 1 of domain 1 (D1S1), the linker between segments 1 and 2 in domain 1 (D1L12), etc. The linker between domains 1 and 2 is indicated as L12. The bottom left panel shows the relative mutation density in the four domains, the terminals and the domain linkers. The bottom right panel shows the density in the different types of region: first segment, second segment, linker between segments 1 and 2 and so on.

Fig. 6.2 shows the estimated *relative mutation densities* in all regions of the channel. The mutations used for this figure were all reported in the literature on cardiac arrhythmias (see Section 6.2.1). The voltage-sensing fourth segment was found to have the highest relative mutation density. Although many mutations were reported in the C- and N-terminus, their large size resulted in a low mutation *density*. Differences between the same regions in different domains were found. For example the linker between segments 3 and 4 was found to have a higher-than-average mutation density in domains 1, 3 and 4 but a lower-than-average density in domain 2. Looking at domains on the whole showed similar differences, with mutations in domain 2 being relatively uncommonly reported while domains 3 and 4 were most likely to contain mutations reported in the scientific literature. Due to its short length, and perhaps its role in inactivation, the linker between domains 3 and 4 was found to have a very high mutation density.

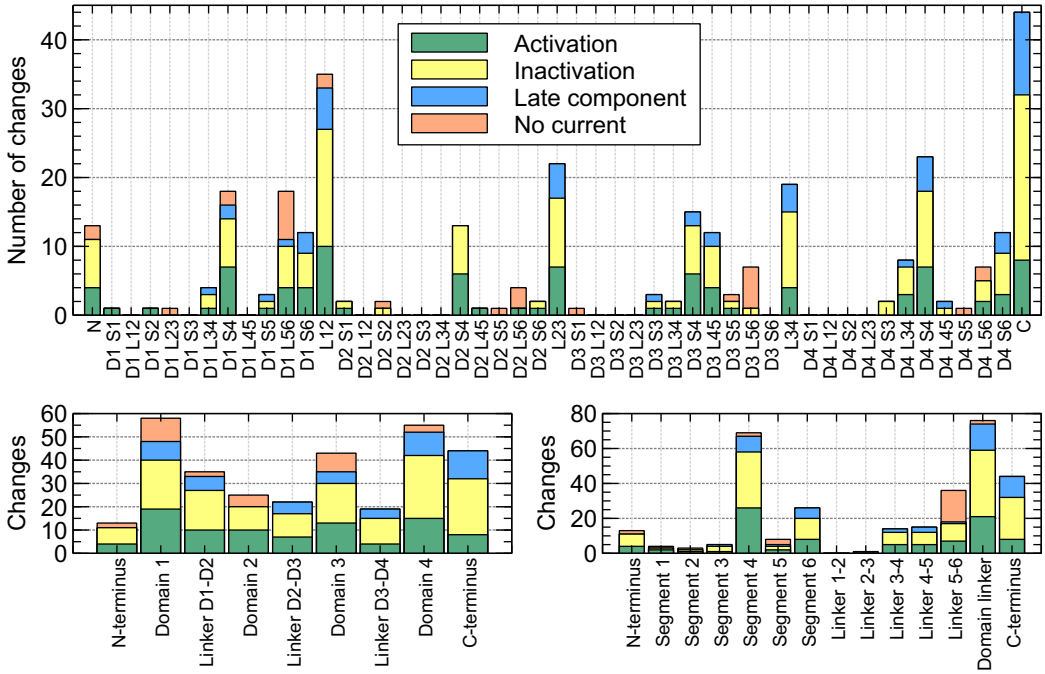

Figure 6.3: Number of times a significant change in cellular EP was reported due to mutations in different regions of *SCN5A*. This figure is based entirely on mutations for which cellular EP data is known. Mutations that induced multiple changes were counted twice, so if a mutation significantly influenced both activation and inactivation the counts for both were increased by one. Conflicts in EP data were resolved by tallying votes for and against significant change (see Section 6.2.6).

The number of changes induced by mutations in different regions of the gene are shown in Fig. 6.3. Mutations leading to a channel that failed to produce any current appeared to occur predominantly in the pore-forming linker between segments 5 and 6. This suggests changes to the pore were investigated more often than mutations abolishing current through some other mechanism (e.g., extreme changes in voltage dependence or trafficking and folding defects). Among the transmembrane segments, the voltage-sensing fourth segment was the main contributor of changes in activation, but surprisingly the domain linkers were almost equally prone. However, the number of changes in activation per amino acid was much higher in the fourth segment than anywhere else in the gene. Changes to inactivation were also common in the voltage-sensing segment, but also occurred frequently in the domain linkers and the C-terminus. Surprisingly, the linker between domains 3 and 4 showed very few mutations affecting inactivation, but this may be explained by its relatively small size. Most mutations affecting late I_{Na} were found in the domain linkers and C-terminus. In general, mutations affecting the late component of I_{Na} were found in regions also affecting inactivation, supporting the idea that late I_{Na} is connected to a failure to fully inactivate.

These results are consistent with earlier reports of I_{Na} structure-function relationships. For example, Kapa et al. (2009) investigated the predictive value of different *SCN5A* regions when predicting pathogenicity of long-QT syndrome. They found a strong link between long-QT pathogenicity and the transmembrane segments and the C-terminus, which agrees with our finding that these regions are linked to changes in the late component of I_{Na}. While Fig. 6.3 shows a connection between the domain linkers and the late component, no such link was established in the study by Kapa et al., but this may be explained by our larger dataset and *SCN5A*-specific approach. Motoike et al. (2004) showed that inactivation and late I_{Na} are associated with both the C-terminus and the linker between domains 3 and 4. Our results confirm the role of the C-terminus for both, but indicate that while the 3-4 linker has a very high mutation *density*, the absolute number of mutations affecting inactivation and late I_{Na} is similar to the other domain linkers. This may point to a novel role for the other domain linkers, but could also be explained if most mutations in the 3-4 linker are too severe to be compatible with life (see Section 6.4.2.2).

6.3.2 Amino-acid properties

In Fig. 6.4, a color-coded representation of the amino-acid substitutions in our database is shown. Each square in the central panel shows if a particular amino-acid substitution occurred more frequently or less frequently than expected (assuming all nucleotide substitutions are equally likely). The histograms at the top and side show the over/under-representation of amino acids in general. Replacements of arginine (R, positive charge) for histidine (H, positive charge) were seen most often, followed closely by R to glutamine (Q, no charge), and threonine (T, no charge) for methionine (M, no charge). R was 4 times more likely to be replaced than average, and tryptophan (W) was the most common substitute. Interestingly, the results were difficult to explain using amino-acid properties. For example, charge conservation was over-represented in some cases (R to H) and under-represented in others (aspartic acid, D to glutamic acid, E).

We next sought to relate the changes in EP to changes in amino-acid *properties* induced by each mutation. In Fig. 6.5, the distribution of property changes is plotted separately for different types of change of EP. Changes in charge were marginally more common in changes to activation and inactivation than in the unchanged case, and large changes to α-helix propensity were uncommon regardless of the associated EP-change. In some properties (for example volume) a slight bias against zero values could be seen, but this is explained by the fact that we did not include synonymous mutations so that near-zero property differences are statistically unlikely (and sometimes impossible). Taken together, the results indicate that changes in individual amino acids are unsuitable to accurately predict the effects of a mutation on I_{Na}.

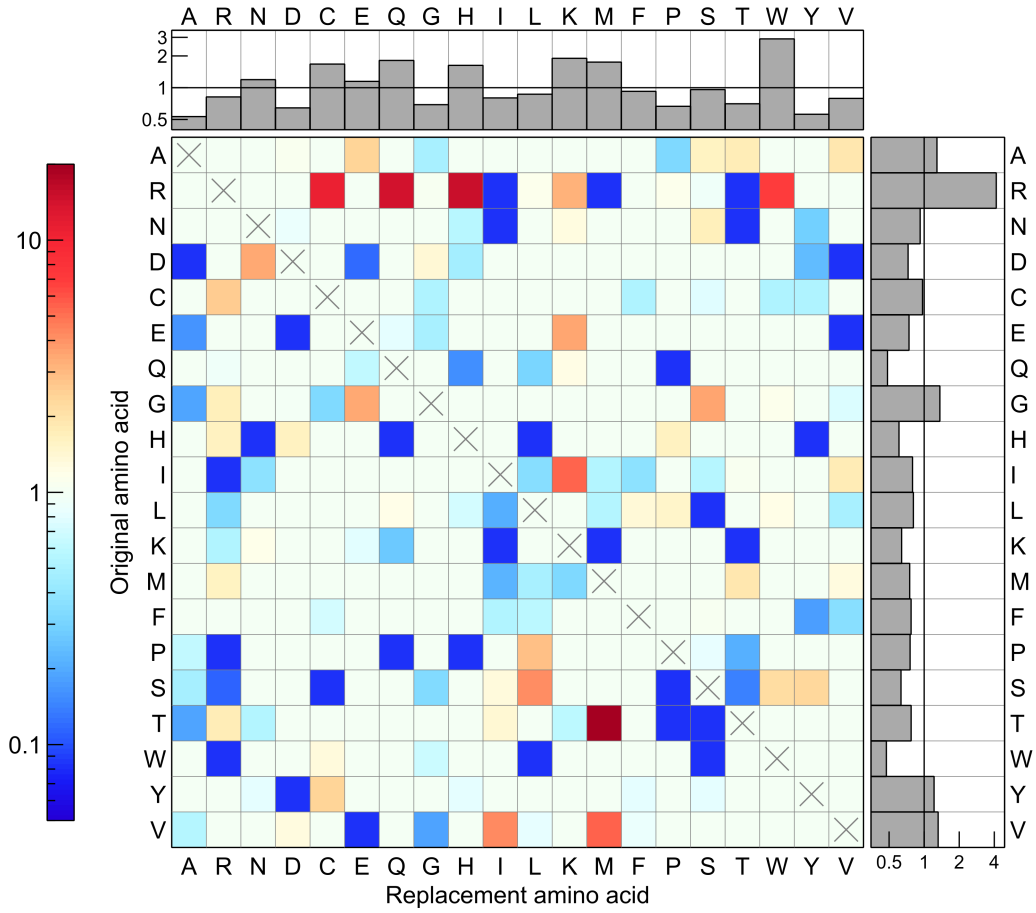

Figure 6.4: (*Central panel*) The ratio of found amino-acid substitution versus expected substitutions. Each row represents the original amino acid, while each column represents the residue it was replaced with. A dark red square indicates this substitution happened more often than expected, while a dark blue square shows that the substitution happened fewer times than was expected. Details of how the figure was constructed are given in Section 6.2.5. (*Top panel*) A histogram showing the cumulative ratios for the new amino acids. (*Right panel*) A histogram showing the cumulative ratios for the old amino acids.

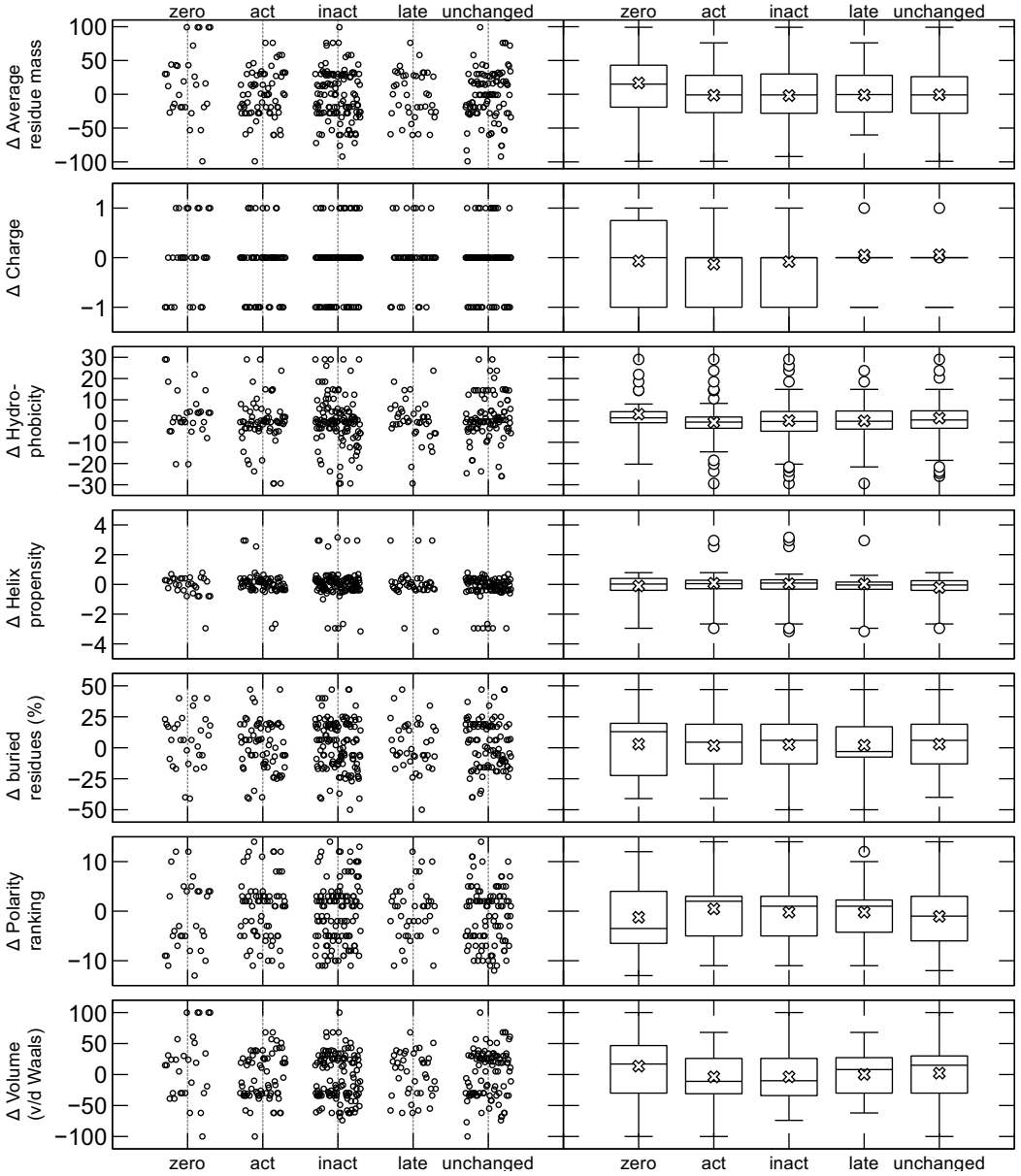

Figure 6.5: (*Left*) Changes in EP in relation to changes in amino-acid properties. We calculated the difference in several properties between the new and the old amino acid involved in the mutation. From left to right, the figure shows mutations that remove all current, affect activation, affect inactivation, affect the late component, or do not seem to affect the current at all. The left panel shows the raw data, plotted with a slight 'jitter' on the x-axis to better distinguish individual points. (*Right*) Box plots for the same data. The line inside the box represents the median, and the top and bottom of the box indicate the first and third quartiles. The whiskers indicate the data within 1.5IQR of the upper and lower bounds of the box, and a cross is drawn at the sample mean. A one-way ANOVA test found no significant differences between the group means.

6.3.3 Midpoints of (in)activation

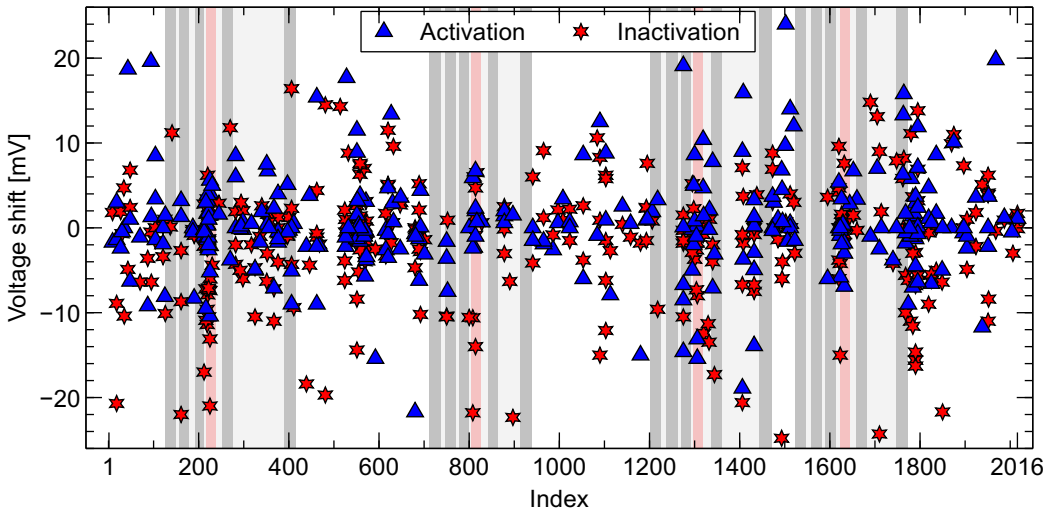

Figure 6.6: The measured shift in midpoint of activation and inactivation, plotted against the position of the mutation on the gene. This figure was constructed from all the available EP-data, and so may include the same mutation more than once. Midpoint shifts are incorporated without regards to the statistical significance of the shift. The positions corresponding to transmembrane segments are indicated using grey shading, and the voltage-sensing fourth segments are highlighted in red.

To determine if quantitative predictions could be made, we investigated the link between the site of the mutation, and size of the resulting shift in midpoint of (in)activation As Fig. 6.6 shows, large shifts in midpoints were observed throughout the gene. Compared to the other transmembrane segments, the fourth segment stood out due to the large number of mutations, and many large shifts could be seen. Yet large shifts were also frequently observed in other transmembrane segments, in the N- and C-terminus and in the domain linkers.

Table 6.4: Success in predicting presence of inactivation defects, expressed as accuracy (ACC), sensitivity, specificity, area under the curve (AUC), and the Matthews correlation coefficient (MCC).

Method	ACC (%)	Sens. (%)	Spec. (%)	AUC	MCC
Zero-R	61.0	100	0	0.490	0
Random forest	62.4	72.8	46.3	0.671	0.195
Naive Bayes	70.2	75.2	62.5	0.730	0.376
MLP classifier	68.3	68.8	67.5	0.695	0.356
Support-vector machine	60.5	99.2	0	0.496	-0.056
k-Nearest neighbor	62.0	70.4	48.8	0.590	0.193

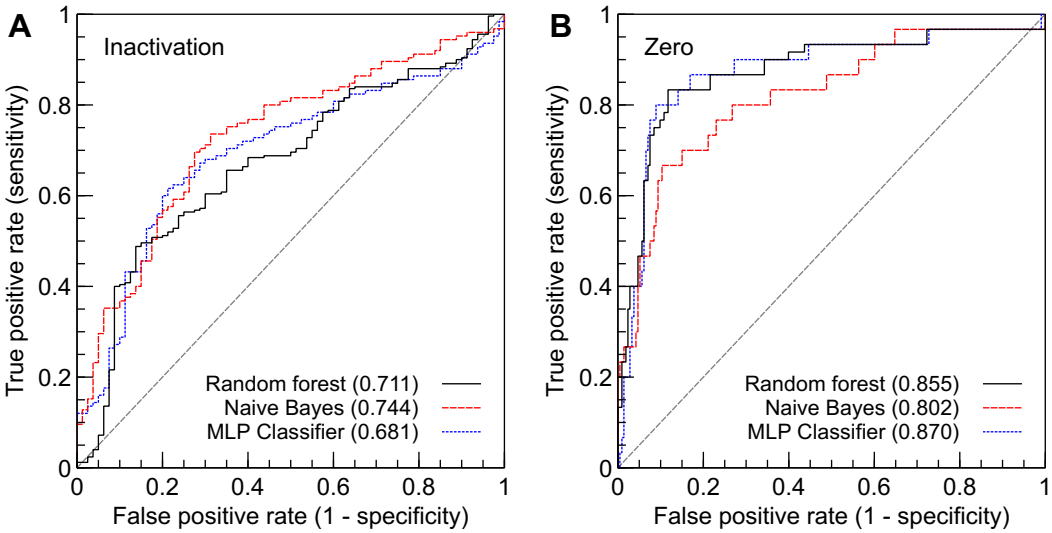

Figure 6.7: Receiver operating characteristics for the inactivation and zero-current classification problems, for the three methods that performed best. The corresponding areas (AUCs) are indicated in brackets.

6.3.4 Machine-learning results

Table 6.4 shows the success rate of a number of different methods applied 'out-of-the-box' to the problem of determining whether or not a mutation would affect inactivation. Compared to baseline (the Zero-R classifier), only modest improvements in accuracy could be seen, indicating that none of the tested methods performed well on accuracy. The Naive Bayes classifier scored highest, with correct guesses for 70% of mutations, just 9 percent points higher than Zero-R (statistically significant with $p \approx 0.04$ using Fisher's exact test). However, the method's specificity (true negative rate) could be improved considerably over Zero-R, leading to strong increases in both AUC and MCC. The AUC for the three best-performing classifiers for inactivation is visualized in Fig. 6.7.A.

Table 6.5 shows the best results when predicting which mutations changed inactivation, activation or the late component and which mutations resulted in no current at all. For both activation and inactivation, only a modest improvement on baseline accuracy was made, but AUC and MCC could be improved considerably. Predicting changes to the late

Table 6.5: Best results per problem. Zero-R classifier results are shown in brackets.

Outcome	Percent correct	AUC	MCC	Method
Inactivation	70.2% (61.0%)	0.730 (0.5)	0.376 (0)	Naive Bayes
Activation	66.8% (62.5%)	0.646 (0.5)	0.279 (0)	Random forest
Late component	69.2% (66.7%)	0.637 (0.5)	0.277 (0)	Random forest
Zero current	89.7% (87.7%)	0.873 (0.5)	0.531 (0)	MLP classifier

Table 6.6: Success rate for predicting discretized shifts in midpoint of inactivation.

Method	Percent correct	AUC
Zero-R	43.1%	0.479
Random forest	58.7%	0.725
Naive Bayes	51.4%	0.661
MLP classifier	48.1%	0.625
Support-vector machine	44.0%	0.508
k-Nearest neighbor	53.7%	0.643

component proved most difficult, with MLP, the best-performing classifier, showing only 2% improvement over baseline. Only a small number of mutations abolished I_{Na} completely, leading to a very high baseline (Zero-R) accuracy of 89.7%, which none of the methods could significantly improve. However, improvements on AUC were seen with a Random forest, Naive Bayes or MLP classifier.

We next ranked the different features (mutation properties) from the highest to the lowest information gain (see Section 6.2.8). For the inactivation problem, the most useful properties were region type (N-terminus, segment 1, linker 5-6, etc.), the distance (on the gene) to the pore-forming linker between segments 5 and 6, the distance to segment 5 and the distance to the linker between domains 3 and 4. Region type was the most useful feature for all four problems, and only the zero-current dataset assigned a non-zero information gain to any of the physical amino-acid properties. Even difference in charge resulted in a very small information gain in the voltage-dependent activation problem, which corresponds to the findings in Fig. 6.5. The information gain rankings for each problem are given in Section 6.A.4.

Finally, we assessed the performance of the same methods on the problem of predicting discretized shifts in activation and inactivation. The results for inactivation are shown in Table 6.6. Here, the Random forest method performed best, but overall accuracy was low. The results for activation were similar.

6.4 Discussion

We assembled a large dataset containing information about mutations reported in the literature on *SCN5A* channelopathies and the resulting changes to the cellular EP.

We found that missense mutations occur throughout the gene, but with a higher rate per

amino acid in transmembrane segments 4 and 6 than in any other segment. The linkers between domain 1-2 and 2-3 showed a lower than average mutation density, but a high density was seen in the linker between domains 3 and 4. Of the four domains, domain 2 had the lowest mutation density.

Changes in function correlated with the location of the mutation on the gene. Complete abolishment of current was often observed for mutations in the pore-forming linkers between segment 5 and 6. Effects on inactivation were mainly seen in the voltage-sensing 4th segment, the 6th segment, the domain linkers and the C-terminus. This is consistent with earlier findings by Brunklaus et al. (2014), who showed mutations in these regions were often implicated in LQT-3. Mutations influencing late I_{Na} often occurred in the C-terminus, and appeared mostly in areas also affecting inactivation.

The reported amino-acid substitutions did not occur with the frequencies that would be expected based on unbiased single nucleotide changes. Instead, arginine mutations were strongly overrepresented in our dataset, while tryptophan was the most common substitute residue. However, no strong relationship between the change in amino-acid properties and the mutation's effects could be seen.

We applied five different machine-learning techniques to the problems of predicting qualitative changes in EP. In terms of accuracy, no major improvements over baseline (i.e., the performance of a Zero-R classifier) were seen. However, using Naive Bayes and MLP classifiers we found a reasonable trade-off between specificity and sensitivity could be achieved, leading to better-than-chance AUCs and MCCs. The region type (see Section 6.2.7) was found to be the most informative feature of a mutation in all four problems examined. Again, the physical properties of the exchanged amino acids provided little information.

6.4.1 Comparison to previous work

To the best of our knowledge, this work is the first to try and predict changes to the current instead of predicting pathogenicity, so that a comparison with previous studies and alternative bioinformatics methods is difficult to make. However, Leong et al. (2015) tested the performance of different tools for predicting pathogenicity of channel mutations and found they all performed poorly on *SCN5A* compared to *KCNQ1* and *KCNH2*. The AUC and MCC of our current-phenotype predictions were higher than those listed by Leong et al. for commercially available tools to predict pathogenicity, which lends some support to our hypothesis that current phenotypes may be predicted more accurately than clinical ones. Our work also provides a novel and comprehensive compendium of *SCN5A* mutations, similar to, for example, (Kapplinger et al., 2015) but with a unique focus on I_{Na}-characteristics.

6.4.2 Future work: improving predictions

The predictive power of a dataset depends on three critical factors: it must contain enough information, it must be *unbiased*, representing equally plausible outcomes in equal measures, and it must be *internally consistent*. Once a dataset meeting these criteria is available, it must be reformatted in such a way that each mutation is represented by appropriate *features*. These are properties of the mutation that are indicative of some essential aspect of the mutation, such as its location in the protein or the associated change in electrical charge. In the following sections, each of these factors is addressed separately, and recommendations for the future are made.

6.4.2.1 Increasing dataset size

Considering the work that goes into measuring the cellular EP changes due to a mutation, the total number of 378 EP recordings of 243 unique mutations is an impressive achievement by the scientific community. However, as Table 6.3 shows this accounts for only 2.0% of the total number of amino-acid substitutions possible from a single nucleotide substitution. As shown in Section 6.A.1, the number of EP data reports for *SCN5A* mutations has steadily increased each year. One development that *could* lead to dramatic increases in data is the inclusion of *paralogues* (Walsh et al., 2014; Amarouch and Abriel, 2015). This entails aligning the sequence of *SCN5A* with that of highly similar sodium channel genes (i.e., *SCN1A*, *SCN2A*, *SCN3A*, etc) and using data about their mutations for similar (conserved) positions in *SCN5A*.

Besides increasing the size of the dataset, care must be taken to improve the manner in which experimental conditions are reported, perhaps using a scheme such as outlaid by Quinn et al. (2011). For example, Section 6.A.2 shows that the fraction of papers that did not explicitly state the α-subunit that was used has remained significant in the last decade, despite the availability of sequencing methods and unique IDs for clones.

6.4.2.2 Reducing dataset bias

Almost all of the mutations listed in our database were reported as a result of a clinical investigation of a patient with some pathological cardiac phenotype. As Table 6.3 shows, only 28% of EP-data results in our dataset showed no change. This bias is likely created by the process of identifying, investigating and publishing mutations: Why investigate a healthy patient, study a mutation not known to be relevant or publish a negative result? Indeed, the mutations we report as 'unchanged' were almost exclusively published in papers reporting that an effect *was* seen in the presence of a secondary factor (for example the common polymorphism H558R or drugs such as lidocaine). This suggests that the negative results in our database may be borderline positive, so that the actual bias problem is still greater. One area where our data does not suffer from reporting bias is the 'zero current'

predictions, for which there are many negative examples. As Table 6.5 shows, the classifiers for this task had the highest AUC and MCC of all tasks, which shows the importance of reducing this type of bias.

Another source of bias is introduced by compatibility of a mutation with life. The influence of this bias is more difficult to judge: Since extreme mutations (such as frameshift mutations or trafficking defects) are still commonly reported, it seems that if a heterozygous mutation renders a channel completely ineffective, the body can compensate by upregulating the overall production of cardiac sodium channels or downregulating others (Sarkar and Sobie, 2010). This means that truly catastrophic mutations are likely not at the extreme end of the cellular EP spectrum, but have a slightly less extreme effect, for example a strong increase in late sodium or a large shift in voltage-dependence of activation causing the channel to activate around the resting potential. There is also a chance that a non-functioning heterozygously expressed channel interferes with the unmutated channel via dominant-negative α-subunit interaction (Clatot et al., 2012b).

Addressing the problem of dataset bias requires a targeted approach. Using Fig. 6.2 and Fig. 6.4 as a guide, mutations in under-represented areas or with uncommon amino-acid substitutions could be identified and investigated. This would involve investing resources into mutations with no clear clinical significance, but would greatly increase the value of the combined EP data gathered so far. A cheaper alternative may be to put out a call to all labs harboring unpublished negative data to process and publish it, ideally in a freely accessible online database.

6.4.2.3 Improving internal consistency

In our dataset, more than one EP data report exists for 74 mutations, and some inconsistency can be seen for 43 of those (58%). Two examples of internal inconsistency are given in Section 6.A.3. For figures such as Fig. 6.3, which dealt with EP data *classes* (activation, inactivation, etc.) we used a voting system to resolve conflicts (see Section 6.2.3). For numerical data (midpoint shifts) we used a filtered version of the dataset in which conflicts were resolved by selecting the favored experimental conditions. In the future, when even more data is available, it may be possible to select only a subset of the data that conforms to a certain experimental set-up. This will resolve the issue of different experimental conditions, but the best way to deal with remaining conflicts remains an open issue.

6.4.2.4 Finding suitable features

In our current set-up, each mutation is described by two types of feature: positional properties (e.g., the index on the gene, the distance to the nearest voltage sensor, etc.) and properties derived from the amino-acid substitution (e.g., change in charge, change in hydrophobicity, etc.). Looking at Fig. 6.2 and Fig. 6.3 it can be seen that there is some

correlation between position on the gene and the change in EP. While it is not the position on the gene, but the position in the folded protein that determines function, nearness on the gene implies nearness in three-dimensional space. The amino-acids substituted by the mutation are much harder to link to changes in channel function (Fig. 6.4). To get closer to physical function, we added a number of commonly used amino acid properties, specifically the change in the property induced by the substitution. However, visual inspection showed no clear emergence of structure (Fig. 6.5).

Creating a workable predictor will require finding features that capture the difference in physical properties before and after an amino-acid substitution. One approach could be to build a full physical model and use molecular dynamics methods to compare channel structure before and after a mutation. However, such models are usually based on homology models which do not include the important domain linking segments and terminals, and molecular dynamics is computationally very expensive. An alternative approach may be to segment the gene, for example using the 'basic units of protein structure' proposed by Berezovsky et al. (2016), and then to inspect the amino-acid properties on a per-segment basis or via the calculation of three-dimensional 'moments' (Silverman, 2000).

Finally, it will also be important to take into account any post-translational modification of channel function via the interaction with various signaling mechanisms (Herren et al., 2013).

6.5 Conclusion

There is a surprisingly large amount of data on *SCN5A* missense mutations available in the literature and EP data is known for 243 mutations: 2% of the 11923 mutations that could theoretically result from single nucleotide changes. However, these data show a strong bias towards pathogenic mutations and show internal inconsistency in 58% of the 74 mutations investigated more than once. Prediction is further hampered by the lack of good quantitative measures of mutation similarity based on the physical properties of the substituted amino acids. In order to arrive at good genotype-phenotype predictions without resorting to costly molecular dynamics simulations, both these issues will have to be addressed directly by the scientific community.

Acknowledgments

The work of Paul G.A. Volders is supported by The Netherlands CardioVascular Research Initiative, CVON PREDICT. Jordi Heijman is supported by a Veni grant from the Netherlands Organization for Scientific Research (ZonMw 91616057). M.C. thanks Evgueni Smirnov for his help with machine-learning techniques and Georg Summer and Markos Xenakis for our valuable discussions.

6.A Supplementary results

6.A.1 Reported mutations over time

Fig. 6.8 shows that the number of publications mentioning mutations in *SCN5A* has been steadily increasing each year, while the number of newly reported mutations exhibits more fluctuation. The number of EP data reports has also seen a gradual increase over time.

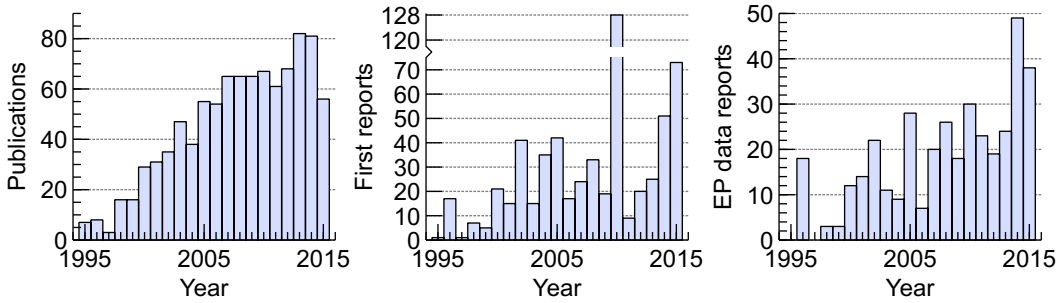

Figure 6.8: (*Left*) The number of publications on PubMed matching the query '*SCN5A* mutation', per year. (*Center*) The number of first reports of mutations in our database, per year. Note the broken y-axis to accommodate the large number of mutations reported in 2010. (*Right*) The number of EP data reports in our database, per year.

6.A.2 Reporting of experimental conditions

Fig. 6.9 shows that, despite the availability of sequencing and databases for genes and gene products, the number of publications not reporting the exact α-subunit used is high.

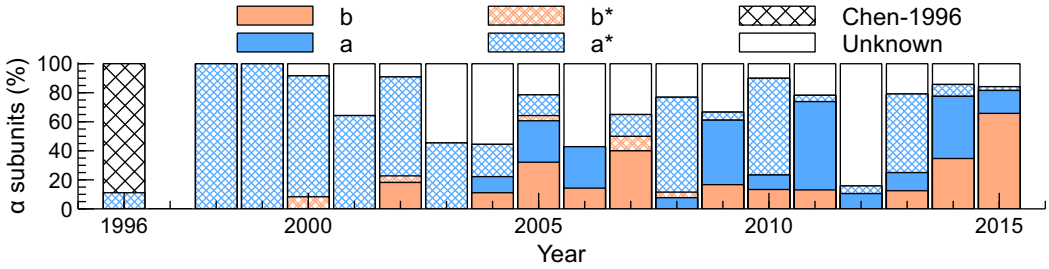

Figure 6.9: The different α-subunits used, in percentages per year. The fraction of subunits with some uncommon variant (a*, b*) can be seen to diminish over time, but the proportion of studies that do not report the variant they use is still significant.

6.A.3 Inconsistencies in the dataset

Two examples of mutations reported multiple times are given in Table 6.7. The first, R222Q, was investigated using different α-subunits, with and without β1-subunits and in different expression systems but all experimenters obtained similar results. The second, D1790G, was investigated under more similar conditions, but experimenters found different results.

Table 6.7: Consistent and inconsistent EP-change reports. Mutations can have an effect on activation (A), inactivation (I) and late I_{Na} (L) or they may lead to no measurable current (Z). Changes are characterized as yes/no or unmeasured, and the number of cells used to test the mutant are shown in brackets. In addition, the used expression system is shown, along with the α-subunit used, the co-expression of β1-subunits, and the original reference.

R222Q						
A	**I**	**L**	α	β**1**	**Cell**	**Reference**
yes (6)	yes (9)	no (8)	a	no	HEK	Cheng et al. (2010)
yes (13)	yes (13)	no (10)	b	no	HEK	Cheng et al. (2010)
yes (11)	yes (10)		a	yes	COS	Laurent et al. (2012)
yes (10)	yes (10)			yes	CHO	Mann et al. (2012)
yes (8)	yes (8)	no (-)	a	no	CHO	Nair et al. (2012)
yes (13)	yes (14)	no (7)		yes	HEK	Beckermann et al. (2014)
D1790G						
A	**I**	**L**	α	β**1**	**Cell**	**Reference**
no (-)	no (9)		a*	no	HEK	An et al. (1998)
no (6)	yes (20)	no (20)	a*	yes	HEK	An et al. (1998)
	yes (4)		a*	yes	HEK	Abriel et al. (2000)
yes (9)	yes (9)	yes (-)	a*	yes	HEK	Baroudi and Chahine (2000)
yes (6)	yes (13)	no (-)	a*	no	HEK	Wehrens et al. (2000)
no (6)	yes (6)		a*	yes	HEK	Liu et al. (2002)
yes (8)	yes (16)			no	HEK	Liu et al. (2003)

6.A.4 Information gain per feature

The following four tables show the *information gain* of each feature in the machine-learning datasets, for the problems of predicting changes to activation, changes to inactivation, changes to the late component, and complete absence of I_{Na}. Information gain is an entropy-based measure, see the Weka documentation (`http://www.cs.waikato.ac.nz/ml/weka/`) for details.

Table 6.8: Information gain: Activation

Gain	Feature	Gain	Feature
0.1048	Region type	0	Δ Volume (v/d Waals)
0.0959	Distance to any transmembrane segment	0	Δ Average residue mass
0.088	Segment type	0	Δ Charge
0.0814	Distance to segment 4 - segment 5 linker	0	Distance to C-terminus
0.0791	Conservedness score	0	Δ Helix-propensity
0.0777	Side	0	Distance to segment 5 - segment 6 linker
0.0771	Distance to segment 5	0	Distance to segment 6
0.0731	Distance to segment 4	0	Distance to linker domain III - domain IV
0	Δ Hydrophobicity	0	Substitution likelihood (Gonnet)
0	Δ % Buried residues	0	Amino-acid similarity (Grantham)
0	Δ Polarity ranking	0	Index on the gene

Table 6.9: Information gain: Inactivation

Gain	Feature	Gain	Feature
0.1829	Region type	0.0618	Distance to segment 4
0.1108	Distance to segment 5 - segment 6 linker	0	Δ Volume (v/d Waals)
0.0973	Distance to segment 5	0	Distance to segment 6
0.0927	Distance to linker domain III - domain IV	0	Δ Polarity ranking
0.0903	Conservedness score	0	Δ Average residue mass
0.0895	Distance to C-terminus	0	Δ % Buried residues
0.0895	Index on the gene	0	Δ Charge
0.0801	Segment type	0	Δ Hydrophobicity
0.079	Distance to any transmembrane segment	0	Substitution likelihood (Gonnet)
0.0697	Distance to segment 4 - segment 5 linker	0	Amino-acid similarity (Grantham)
0.0668	Side	0	Δ Helix-propensity

Table 6.10: Information gain: Late component

Gain	Feature	Gain	Feature
0.1154	Region type	0	Δ Helix-propensity
0.039	Side	0	Conservedness score
0.0357	Segment type	0	Amino-acid similarity (Grantham)
0	Distance to C-terminus	0	Distance to segment 5 - segment 6 linker
0	Substitution likelihood (Gonnet)	0	Distance to any transmembrane segment
0	Δ Hydrophobicity	0	Distance to segment 6
0	Δ Charge	0	Distance to segment 5
0	Δ Polarity ranking	0	Distance to linker domain III - domain IV
0	Δ Average residue mass	0	Distance to segment 4 - segment 5 linker
0	Δ % Buried residues	0	Distance to segment 4
0	Δ Volume (v/d Waals)	0	Index on the gene

Table 6.11: Information gain: Zero current

Gain	Feature	Gain	Feature
0.2139	Region type	0	Distance to C-terminus
0.1356	Distance to segment 5 - segment 6 linker	0	Δ % Buried residues
0.1163	Side	0	Δ Hydrophobicity
0.1116	Distance to segment 4	0	Δ Charge
0.0999	Segment type	0	Conservedness score
0.0753	Distance to segment 4 - segment 5 linker	0	Δ Helix-propensity
0.0601	Distance to segment 5	0	Substitution likelihood (Gonnet)
0.049	Δ Average residue mass	0	Distance to segment 6
0.049	Δ Volume (v/d Waals)	0	Distance to linker domain III - domain IV
0.0458	Distance to any transmembrane segment	0	Amino-acid similarity (Grantham)
0	Δ Polarity ranking	0	Index on the gene

6.A.5 EP-data overview

Table 6.12 shows the EP-data collected for this paper. The first columns show the EP-data reference and the mutation. The next four indicate whether the authors considered the mutation to change activation, inactivation, or the late component, and whether the mutation abolished current completely. The next two columns show any reported shifts in midpoint of activation (ΔV_a) and inactivation (ΔV_i). Finally, the cell type, α-subunit, and co-expression of β1-subunit are given. Cell types are HEK cells, CHO cells, Oocytes (Ooc.) or Mouse myocyte (MM). α-subunits are as defined in this paper (see Table 6.1), with the addition of a^{**} which indicates the alpha-subunit used in a study by Chen et al. A digital version of the same data can be obtained from the author.

Table 6.12: EP Data

Publication	Mutation	Act.	Inact.	Late	Zero	ΔV_a	ΔV_i	Cell	α	$\beta 1$
Gütter et al. (2013)	G9V	no	no	no		1.3	0.01	HEK	a*	no
Gütter et al. (2013)	R18Q	no	no			0.5	2.2	HEK	a*	no
Gütter et al. (2013)	R18W	no	yes	no		-0.2	1.3	HEK	a*	no
Gütter et al. (2013)	R27H	yes	yes			4	-0.4	HEK	a*	no
Kapplinger et al. (2015)	E30G	no	yes	no		-0.2	2.6	HEK	b	no
Tan et al. (2005)	R34C	no	no	no		-2	0	HEK	b	no
Tan et al. (2005)	R34C	no	no	no		3	2	HEK	a	no
Gütter et al. (2013)	G35S	no	no			-1.7	-1.8	HEK	a*	no
Lin et al. (2008)	R43Q	no	no	no		-0.29	-1.77	HEK	a*	yes
Kapplinger et al. (2015)	E48K	yes	no	no		3.9	-2.7	HEK	b	no
Kapplinger et al. (2015)	E48K	no	no	no		3.8	0.4	HEK	a	no
Hoshi et al. (2014)	N70K		no				-0.14	HEK	a	no
Kapplinger et al. (2015)	Y87C	no	no	no		0.6	-1.5	HEK	b	no
Beyder et al. (2014)	I94V	no	yes	no		-0.5	-1.3	HEK	b	no
Gütter et al. (2013)	V95I	yes	no			1.2	1	HEK	a*	no
Clatot et al. (2012a)	R104K	yes	no			8.6	0	HEK		no
Gütter et al. (2013)	R104Q	no	yes			-0.5	-1.6	HEK	a*	no
Clatot et al. (2012a)	R104W				yes			HEK		no
Clatot et al. (2012a)	R121W				yes			HEK		no
Holst et al. (2010)	R121W				yes			HEK		no
Gütter et al. (2013)	V125L	no	yes	no		0.7	3.1	HEK	a*	no
Gütter et al. (2013)	K126E	no	yes			2.8	3.4	HEK	a*	no
Swan et al. (2014)	I137V	no	no			-0.5	1.6	HEK	b	yes
Swan et al. (2014)	I141V	yes	no			-7	1.5	HEK	b	yes
Gui et al. (2010a)	E161K	yes	no			19.8	1.5	HEK	a*	no
Gui et al. (2010b)	E161K	yes	no			19.1	1.9	HEK	a*	no
Smits et al. (2005a)	E161K	yes	no			11.9	0.9	HEK	a*	no
Gui et al. (2010a)	T187I				yes			HEK	a*	no
Gui et al. (2010b)	T187I				yes			HEK	a*	no
Kapplinger et al. (2015)	R190Q	no	no	no		0.1	0.8	HEK	b	no
Gui et al. (2010a)	L212P	yes	yes			-15	-10.5	HEK	a*	no
Gui et al. (2010b)	L212P	yes	yes			-14.6	-10.4	HEK	a*	no
Makita et al. (2005)	L212P	yes	yes	no		-15.4	-9	HEK		yes
Kapplinger et al. (2015)	S216L	no	no	no		-2	0.3	HEK	b	no
Marangoni et al. (2011)	S216L	no	no	no		1	1	HEK	a*	yes
Wang et al. (2007a)	S216L	no	yes	yes		-0.2	4.7	HEK	b	yes
Abe et al. (2014)	R219H	yes	yes			1.7	-11.4	HEK	b	no
Chen et al. (1996)	R219H	yes	yes			-2.3	-9.6	Ooc.	a**	no
Gosselin-Badaroudine et al. (2012)	R219H	no	no			-1.7	3.67	Ooc.		yes
Chen et al. (1996)	R219Q	no	no			3.3	-0.8	Ooc.	a**	no
Beyder et al. (2014)	T220I	no	yes	no		-2.1	-7.4	HEK	b	no
Gui et al. (2010a)	T220I	yes	yes			-1	-5.6	HEK	a*	no
Gui et al. (2010b)	T220I	no	yes			-1.8	-6.4	HEK	a*	no
Beckermann et al. (2014)	R222Q	yes	yes	no		-13.9	-6.7	HEK		yes
Cheng et al. (2010)	R222Q	yes	yes	no		-15.4	-8	HEK	a	no
Cheng et al. (2010)	R222Q	yes	yes	no		-13.1	-4.2	HEK	b	no
Laurent et al. (2012)	R222Q	yes	yes			-11.7	-4	COS	a	yes
Mann et al. (2012)	R222Q	yes	yes			-6.3	-6.2	CHO		yes
Nair et al. (2012)	R222Q	yes	yes	no		-9	-7.3	CHO	a	no
Chen et al. (1996)	R225E				yes			Ooc.	a**	no
Beckermann et al. (2014)	R225P	yes	yes	yes		0.2	-0.8	HEK		yes
Beckermann et al. (2014)	R225Q	yes	yes	yes		-2.9	-4.2	HEK		yes
Chen et al. (1996)	R225Q	yes	yes			4.7	5.8	Ooc.	a**	no
Bezzina et al. (2003)	R225W	yes	yes	no		14	11.1	Ooc.	a*	yes
Hoshi et al. (2014)	R225W		no				-1.81	HEK	a	no
Watanabe et al. (2011a)	A226D				yes			HEK		yes
Neu et al. (2010)	I230T	yes	yes			15.4	-4.9	HEK	a*	yes
Kapplinger et al. (2015)	Q245K	no	no	no		-3.7	0.7	HEK	b	no
Calloe et al. (2011)	Q270K	yes	yes	yes		5.8	9.9	CHO	b	yes
Itoh et al. (2005a)	R282H				yes	5	5	HEK	a*	yes
Poelzing et al. (2006)	R282H				yes			HEK	a	no
Shinlapawittayatorn et al. (2011b)	R282H				yes			HEK	a	no
Shinlapawittayatorn et al. (2011b)	G292S		yes				7.3	HEK	a	no
Shinlapawittayatorn et al. (2011b)	V294M						4.1	HEK	a	no
Saito et al. (2009)	G298S	no	no					HEK	a	no
Saito et al. (2009)	G298S	no	no					HEK	b	no
Wang et al. (2002)	G298S	no	yes	no		3.6	7.4	HEK	a*	yes
Shinlapawittayatorn et al. (2011b)	K317N				yes			HEK	a	no
Keller et al. (2005)	L325R	yes	yes			10.4	4.4	HEK	b*	yes
Shinlapawittayatorn et al. (2011b)	L325R				yes			HEK	a	no
Cordeiro et al. (2006)	P336L	no	no			1.7	-1.5	HEK		yes
Olesen et al. (2012)	R340Q	yes	yes	no		-6.2	-5.5	HEK		no
Shinlapawittayatorn et al. (2011b)	G351V				yes			HEK	a	no
Vatta et al. (2002a)	G351V	no	no			0	2.1	Ooc.		no
Guo et al. (2016)	Y352C	no	yes			0		HEK	a	no
Pfahnl et al. (2007)	T353I	no	yes	yes		1	11	HEK	b*	no

Publication	Mutation	Act.	Inact.	Late	Zero	ΔV_a	ΔV_i	Cell	α	$\beta 1$
Zhang et al. (2015)	T353I	yes	yes	yes		-2.2	-6.32	HEK		no
Shinlapawittayatorn et al. (2011b)	D356N				yes			HEK	a	no
Hong et al. (2004)	R367H				yes			HEK	a*	no
Shinlapawittayatorn et al. (2011b)	R367H				yes			HEK	a	no
Vatta et al. (2002b)	R367H				yes			Ooc.	b	no
Watanabe et al. (2011a)	R367H				yes			HEK		yes
Detta et al. (2014)	R376C	yes	no			11.5	0	HEK	a*	yes
Detta et al. (2014)	R376H	no	no			1.5	0	HEK	a*	yes
Frustaci et al. (2005)	R376H				yes			HEK		yes
Rossenbacker et al. (2004)	R376H	no	no			0	0	HEK		yes
Kapplinger et al. (2015)	I397F	yes	yes	yes		-6.9	5.1	HEK	b	no
Kapplinger et al. (2015)	I397F	no	yes	yes		0.4	9.1	HEK	a	no
Hu et al. (2007)	G400A	no	yes	no		1.32	-6.39	HEK	b*	yes
Kato et al. (2014)	N406K	yes	yes	yes		8.6	2.9	CHO	a*	yes
Itoh et al. (2005b)	N406S	yes	yes			15.9	9.6	HEK	a*	yes
Itoh et al. (2007)	N406S		yes	no			2.7	HEK	a*	yes
Horne et al. (2011)	V411M	yes	yes	yes		-8.1	-7.9	HEK		no
Hoshi et al. (2014)	E439K		no				-0.52	HEK	a	no
Crotti et al. (2012)	E446K	no	yes			-0.7	-6.2	HEK		yes
Kapplinger et al. (2015)	E462A	no	no	no		-2.6	1.2	HEK	b	no
Kapplinger et al. (2015)	E462A	no	no	no		-2.2	0.9	HEK	a	no
Kapplinger et al. (2015)	E462K	no	no	no		-1.9	-3	HEK	b	no
Holst et al. (2009)	P468L	no	no			-1.4	2.8	HEK		no
Tan et al. (2005)	R481W	no	yes	no		1	-6	HEK	b	no
Tan et al. (2005)	R481W	no	yes	no		-6	-4	HEK	a	no
Viswanathan et al. (2003)	T512I	yes	yes			-7.5	-8.7	HEK	a*	yes
Tan et al. (2001)	G514C	yes	yes	no		10.1	6.9	HEK		no
Shuraih et al. (2007)	S524Y	no	no			-5	1.6	HEK	b	no
Tan et al. (2005)	S524Y	no	no	no		-1	-2	HEK	b	no
Tan et al. (2005)	S524Y	no	no	no		3	3	HEK	a	no
Aiba et al. (2014)	R526H	no	no			-0.2	-0.5	HEK		yes
Hoshi et al. (2014)	R526H		no				-1.81	HEK	a	no
Aiba et al. (2014)	S528A	no	no			-2.2	0.4	HEK		yes
Otagiri et al. (2008)	F532C	no	no	no		0	0	HEK		yes
Chiang et al. (2009)	A551E		no				0	HEK		yes
Chiang et al. (2009)	A551T	no	yes			0	-5	HEK		yes
Juang et al. (2014)	A551T	yes	no			-1.8	-1.4	HEK	a	yes
Chiang et al. (2009)	A551V		yes				-4.7	HEK		yes
Hoshi et al. (2014)	G552R		no				-1.75	HEK	a	no
Hoshi et al. (2014)	E555K		no				-2.68	HEK	a	no
Cheng et al. (2010)	H558R	no	no	no		-0.9	-1	HEK	a	no
Cheng et al. (2010)	H558R	no	no	no		-0.3	0.6	HEK	b	no
Gui et al. (2010b)	H558R	no	no			-1.7	-1.5	HEK	a*	no
Kauferstein et al. (2013)	H558R	no	no			2.55	-1	Ooc.		no
Murphy et al. (2012)	H558R	no	no			5.1	-0.8	HEK	a*	no
Surber et al. (2008)	H558R	no	no	no		0.6	-2.2	Ooc.	a*	no
Tan et al. (2005)	H558R	no	no	no		0	-6	HEK	b	no
Tan et al. (2005)	H558R				yes			HEK	a	no
Hoshi et al. (2014)	L567Q		no				-0.43	HEK	a	no
Wan et al. (2001b)	L567Q	yes	yes			7.1	-11.3	HEK		yes
Kapplinger et al. (2015)	R569G	yes	no	no		-7.1	0.7	HEK	b	no
Kapplinger et al. (2015)	R569W	no	no	no		-1.3	0.7	HEK	b	no
Glynn et al. (2015)	S571A		no	yes			0	MM		yes
Glynn et al. (2015)	S571E		no	yes			0	MM		yes
Albert et al. (2008)	A572D	no	yes			-2.5	0.8	Ooc.	a*	yes
Tester et al. (2010)	A572D	no	no	no		0	-3	HEK	b	no
Albert et al. (2008)	A572F	no	yes			-3.8	-2.4	Ooc.	a*	yes
Juang et al. (2014)	N592K	yes	no			3.2	1.2	HEK	a	yes
Albert et al. (2008)	G615E	no	yes			-3.4	1.7			yes
Beyder et al. (2014)	G615E	yes	yes	no		5.6	3.1	HEK	b	no
Yang et al. (2002)	G615E	no	no	no		0.5	2.4	HEK	a*	yes
Yang et al. (2002)	L618F	no	no	no		-4.9	3.9	HEK	a*	yes
Wehrens et al. (2003)	L619F	no	yes	yes		-0.1	5.8	HEK		yes
Hoshi et al. (2014)	R620C		no				-2.17	HEK	a	no
Kapplinger et al. (2015)	R620C	no	yes	no		0.5	2.3	HEK	b	no
Calloe et al. (2013)	R620H	no	no			0	0	CHO	b	no
Kapplinger et al. (2015)	P627L	no	no	no		-1.1	1	HEK	b	no
Beyder et al. (2014)	T630M	no	yes	no		1.5	1.3	HEK	b	no
Hoshi et al. (2014)	T632M		no				-2.33	HEK	a	no
Hoshi et al. (2014)	A647D		no				-1.06	HEK	a	no
Beyder et al. (2014)	P648L	no	yes	no		2	-0.5	HEK	b	no
Cheng et al. (2011)	R680H	no	no	yes		1.1	2.4	HEK	b	no
Cheng et al. (2011)	R680H	no	no	no		-2.6	-1.5	HEK	a	no
Wang et al. (2007a)	R680H	no	yes	no		-1.9	0.1	HEK	b	yes
Mok et al. (2003)	H681P	yes	yes			-9.5	-17.3	HEK		yes
Sottas et al. (2013)	R689C	no	no	yes		0.1	-0.2	HEK		yes
Hong et al. (2012)	R689H				yes					no
Kapplinger et al. (2015)	R689H	yes	yes	no		-5.2	-4.3	HEK	b	no

Publication	Mutation	Act.	Inact.	Late	Zero	ΔV_a	ΔV_i	Cell	α	$\beta 1$
Sottas et al. (2013)	R689H	no	no	yes		-0.7	-0.6	HEK		yes
Kapplinger et al. (2015)	Q692K	yes	no	no		-2.2	-4.3	HEK	b	no
Kapplinger et al. (2015)	Q692K	no	no	no		-1.1	2.3	HEK	a	no
Hoshi et al. (2014)	P701L		no				-3.04	HEK	a	no
Vatta et al. (2002b)	A735V	yes	yes			6.7	-0.1	Ooc.	b	no
Kapplinger et al. (2015)	Q750R	no	no	no		3.2	-1.6	HEK	b	no
Kapplinger et al. (2015)	Q750R	no	yes	no		0.3	-2.5	HEK	a	no
Potet et al. (2003)	G752R				yes			COS		no
Kapplinger et al. (2015)	R800L	no	no	no		-1	0.9	HEK	b	no
Chen et al. (1996)	R808H	yes	yes			6.3	0	Ooc.	a**	no
Chen et al. (1996)	R808Q	yes	yes			13.3	8.2	Ooc.	a**	no
Calloe et al. (2013)	R811H	no	yes			-0.6	-8.4	CHO	b	no
Wang et al. (2015)	L812Q	no	yes			-0.33	-19.7	HEK	a*	no
Chen et al. (1996)	R814E	yes	no			15.8	-2.4	Ooc.	a**	no
Chen et al. (1996)	R814Q	yes	yes			0.4	-9.6	Ooc.	a**	no
Beckermann et al. (2014)	R814W	yes	yes	no		-3.8	1.1	HEK		yes
Nguyen et al. (2008)	R814W	yes	yes			-5.7	-2.9	HEK	a*	yes
Kinoshita et al. (2016)	K817E	yes	yes			24	0.1	HEK	a	yes
David et al. (2012)	L828F	yes	no			-21.7	-8.4			no
Watanabe et al. (2011a)	L846R				yes			HEK		yes
Clatot et al. (2012a)	R878C				yes			HEK		no
Gui et al. (2010a)	R878C				yes			HEK	a*	no
Gui et al. (2010b)	R878C				yes			HEK	a*	no
Zhang et al. (2008)	R878C				yes			HEK	a*	yes
Zhang et al. (2008)	R878C				yes			HEK	a*	no
Zhang et al. (2008)	R878C				yes			Ooc.	a*	no
Zhang et al. (2008)	R878K				yes			HEK	a*	no
Tarradas et al. (2013)	I890T	yes	no	no		4.7	0.7	HEK	a*	no
Kapplinger et al. (2015)	G897E				yes			HEK	b	no
Wang et al. (2007b)	N927K	yes	yes			-7.1		HEK	a*	yes
Ruan et al. (2007)	S941N	no	no	yes		-0.6	-0.3	HEK		yes
Schwartz et al. (2000)	S941N			yes				Ooc.	b*	no
Hsueh et al. (2009)	R965C	no	yes			1.45	-9.4	HEK	a	yes
Hoshi et al. (2014)	R965H		no				-0.3	HEK	a	no
Hayashi et al. (2015)	R986Q	no	no			1.3	-0.2	CHO		yes
Beyder et al. (2014)	A997T	yes	yes	no		19.6	6.2	HEK	b	no
Hu et al. (2010)	P1008S	no	no				1.37	HEK		yes
Frustaci et al. (2005)	R1023H	no	yes			3.4	2.5	HEK		yes
Hoshi et al. (2014)	R1023H		no				2.25	HEK	a	no
Hoshi et al. (2014)	E1053K		no				3.71	HEK	a	no
Mohler et al. (2004)	E1053K	yes	yes			-8.3	-4.7	HEK	a*	yes
Otagiri et al. (2008)	G1084S	yes	yes	no		1.5	-5.5	HEK		yes
Juang et al. (2014)	P1090L	no	no			-0.5	-1.5	HEK	a	yes
Tan et al. (2005)	P1090L	yes	no	no		-5	-4	HEK	b	no
Tan et al. (2005)	P1090L	no	no	no		1	3	HEK	a	no
Cheng et al. (2011)	S1103Y	yes	no	no		1.8	6.3	HEK	b	no
Cheng et al. (2011)	S1103Y	no	yes	no		-1.6	-2.6	HEK	a	no
Splawski et al. (2002)	S1103Y	yes	no	yes		-4.5	0	HEK	b	no
Tan et al. (2005)	S1103Y	yes	yes	no		-3	-3	HEK	b	no
Tan et al. (2005)	S1103Y	yes	yes	no		5	6	HEK	a	no
Hoshi et al. (2014)	A1113V		no				-0.78	HEK	a	no
Hoshi et al. (2014)	S1140T		no				-3.05	HEK	a	no
Beyder et al. (2014)	G1158S	no	yes	no		3.2	-3.3	HEK	b	no
Winkel et al. (2012)	P1177L	no	no	yes		0.2	-1.5	HEK		no
Ge et al. (2008)	A1180V	no	yes	yes		1.4	-4.4	HEK	a	yes
Huang et al. (2006)	R1193Q	no	yes	yes		2	-5.2	HEK		no
Tan et al. (2005)	R1193Q	no	no	no		-1	-2	HEK	b	no
Tan et al. (2005)	R1193Q	yes	yes	no		-6	-5	HEK	a	no
Vatta et al. (2002b)	R1193Q	no	yes			0	3.9	Ooc.	b	no
Wang et al. (2004)	R1193Q	no	yes	yes		0	-6	HEK	a	no
Medeiros-Domingo et al. (2009)	R1195H	yes	yes	no		-9.2	-10	HEK	b	no
Albert et al. (2008)	W1206C	no	no			-2.6	0.8	Ooc.	a*	yes
Calloe et al. (2013)	S1218I				yes			CHO	b	no
Yang et al. (2002)	F1250L	no	no	no		7.5	6.2	HEK	a*	yes
Groenewegen et al. (2003b)	D1275N	no	no			3.36	-0.7	Ooc.	a*	yes
Groenewegen et al. (2003b)	D1275N	yes	yes			3.8	-4.05	Ooc.	a*	no
Gui et al. (2010a)	D1275N	yes	yes			3.1	1.8	HEK	a*	no
Gui et al. (2010b)	D1275N	yes	yes			3	1	HEK	a*	no
Hoshi et al. (2014)	D1275N		no				-0.84	HEK	a	no
Watanabe et al. (2011c)	D1275N	no	no			0.7	-3.9	CHO	a	no
Watanabe et al. (2011c)	D1275N	yes	no			12	1.4	HEK	a	yes
Watanabe et al. (2011c)	D1275N	no	yes	yes		-1.5	7.6	MM		no
Abriel et al. (2001)	E1295K	yes	yes			2.9	5.2	HEK	a*	yes
Liu et al. (2002)	E1295K	yes	yes			3.4	5.2	HEK	a*	yes
Gui et al. (2010a)	P1298L	no	yes			-0.5	-8.9	HEK	a*	no
Gui et al. (2010b)	P1298L	no	yes			-1.4	-10.1	HEK	a*	no
Chen et al. (1996)	K1300H	yes	yes			0.3	-13.1	Ooc.	a**	no
Chen et al. (1996)	K1300Q	yes	yes			-10.4	-21	Ooc.	a**	no

Publication	Mutation	Act.	Inact.	Late	Zero	ΔV_a	ΔV_i	Cell	α	$\beta 1$
Beyder et al. (2014)	T1304M	no	no	no		-0.3	0.6	HEK	b	no
Kapplinger et al. (2015)	T1304M	no	no	no		-3.5	-0.7	HEK	b	no
Wang et al. (2007a)	T1304M	yes	yes	yes		6.7	11.2	HEK	b	yes
Chen et al. (1996)	R1306E	yes	yes			-2.1	-21.8	Ooc.	a**	no
Chen et al. (1996)	R1306Q	yes	yes			5.9	-10.6	Ooc.	a**	no
Wang et al. (2016)	R1309H	yes	yes	yes		4.5	-6.2	HEK		yes
Casini et al. (2007)	G1319V	yes	yes	no		3.7	-6	HEK		yes
Hoshi et al. (2014)	G1319V		no				-1.92	HEK	a	no
Kapplinger et al. (2015)	M1320V	no	no	no		0.7	2.4	HEK	b	no
Wang et al. (1996)	N1325S	yes	yes	yes		-6.4	-2.5	HEK	a*	no
Yong et al. (2007)	N1325S	no	yes	yes		0	7.1			no
Wedekind et al. (2001)	A1330P	no	yes	no		-1.5	8.3	HEK	a*	yes
Smits et al. (2005b)	A1330T	no	yes	no		2.4	6.9	HEK	a*	yes
Ruan et al. (2007)	P1332L	yes	yes	no		-5	-6.4	HEK		yes
Huang et al. (2009)	S1333Y	yes	yes	yes		-8.5	7	HEK	a*	yes
Samani et al. (2009)	V1340I	no	no			-1.1	3.6	HEK	b	yes
Samani et al. (2009)	V1340I				yes			HEK	a	yes
Keller et al. (2006)	F1344S	yes	yes			9.7	-0.65	HEK		yes
Kyndt et al. (2001)	G1406R				yes			Ooc.	a*	no
Kyndt et al. (2001)	G1406R				yes			Ooc.	a*	yes
Tan et al. (2006)	G1406R	no	yes	no		1.9	-10.5	HEK	a	no
Tan et al. (2006)	G1406R	no	yes	no		3.4	-6.3	HEK	b	no
Gui et al. (2010a)	G1408R				yes			HEK	a*	no
Gui et al. (2010b)	G1408R				yes			HEK	a*	no
Baroudi et al. (2001)	R1432C				yes			HEK	a*	yes
Baroudi et al. (2001)	R1432G				yes			HEK	a*	yes
Baroudi et al. (2001)	R1432G	no	no			0	0	Ooc.	a*	yes
Deschênes et al. (2000)	R1432G				yes			HEK	a*	no
Baroudi et al. (2001)	R1432H				yes			HEK	a*	yes
Baroudi et al. (2001)	R1432K	no	no			-4.94	0.2	HEK	a*	yes
Six et al. (2008)	P1438L				yes			HEK		yes
Sarhan et al. (2009)	F1473A		yes				14.8	HEK	a	no
Bankston et al. (2007b)	F1473C	no	yes	yes		-2.4	8.8	HEK	a*	yes
Ruan et al. (2010)	F1473S	yes	yes	yes		-18.9	-4.4	HEK		yes
Moreau et al. (2013)	Q1476R	no	yes	yes		1.6	6.5	HEK	a*	yes
Kapplinger et al. (2015)	I1485V	no	yes	no		-2.5	6.8	HEK	b	no
Wang et al. (2007a)	F1486L	yes	yes	yes		3.7	14.3	HEK	b	yes
Li et al. (2009)	K1493R	no	yes	no		-1.58	5.13	HEK		no
Sarhan et al. (2009)	Y1494A		yes				7.9	HEK	a	no
Sarhan et al. (2009)	Y1495A		no				2.6	HEK	a	no
Hoshi et al. (2014)	L1501V		no				0.19	HEK	a	no
Hoshi et al. (2014)	G1502S		yes				-7.18	HEK	a	no
Saber et al. (2015)	P1506S	yes	yes			9	-14	HEK		yes
Beyder et al. (2014)	R1512Q	no	no	no		2.9	3	HEK	b	no
Deschênes et al. (2000)	R1512W	no	yes			0.9	2.6	HEK	a*	no
Rook et al. (1999)	R1512W	yes	yes			-5.1	-3.8	Ooc.	a*	no
Sarhan et al. (2009)	F1520A		no				1.1	HEK	a	no
Sarhan et al. (2009)	F1522A		no				-0.6	HEK	a	no
Nguyen et al. (2008)	D1595H	no	yes			-0.3	-6.8	HEK	a*	yes
Wang et al. (2002)	D1595N	no	yes	no		-1.3	4.2	HEK	a*	yes
Surber et al. (2008)	T1620H	no	yes			-0.03	1.26	Ooc.	a*	no
Surber et al. (2008)	T1620K	yes	yes	yes		-5.8	-4.14	Ooc.	a*	no
Baroudi et al. (2000)	T1620M	no	yes	no		0	0	HEK	a*	yes
Baroudi et al. (2000)	T1620M	no	yes	no		0	9.6	Ooc.	a*	yes
Shirai et al. (2002)	T1620M	yes	yes			6.8	13.1	HEK	a*	no
Wang et al. (2000)	T1620M	no	yes			0	6.2	HEK	a*	yes
Surber et al. (2008)	T1620R	yes	yes			-6.56	-13.5	Ooc.	a*	no
Chen et al. (1996)	R1623H	yes	yes			-2.4	-0.9	Ooc.	a**	no
Chen et al. (1996)	R1623Q	yes	yes			2.3	4.7	Ooc.	a**	no
Kambouris et al. (2000)	R1623Q		yes			0	-7.2	Ooc.		yes
Makita et al. (1998)	R1623Q	no	yes	yes			-1.4	Ooc.	a*	no
Tsurugi et al. (2009)	R1623Q	no	no	no		-0.9	-3.8	HEK		no
Olesen et al. (2012)	R1626H	yes	yes	yes		4.4	-5.6			no
Ruan et al. (2007)	R1626P	no	yes	yes		-3.1	-7.1	HEK		yes
Chen et al. (1996)	R1629E	yes	yes			6.7	-3.7	Ooc.	a**	no
Chen et al. (1996)	R1629Q	yes	yes			8.6	-57.5	Ooc.	a**	no
Zeng et al. (2013)	R1629Q	no	yes			2.3	-20.6	HEK		yes
Wang et al. (2008)	G1631D	yes	yes	yes		7.8	14.5	HEK	a*	yes
Nakajima et al. (2015)	R1632C	no	yes	no		-2.2	-24.8	HEK	b	yes
Gui et al. (2010a)	R1632H	no	yes			-1.4	-20.7	HEK	a*	no
Gui et al. (2010b)	R1632H	no	yes			-2.4	-22	HEK	a*	no
Frustaci et al. (2005)	R1644C	yes	yes			8.48	-1	HEK		yes
Wang et al. (1996)	R1644H	no	yes	yes		1.7	2.1	HEK	a*	no
Ruan et al. (2007)	M1652R	no	yes	yes		0.7	7.6	HEK		yes
Cordeiro et al. (2006)	I1660V				yes			HEK		yes
Núñez et al. (2013)	D1690N	no	no	no		4.7	3.2	CHO	a*	yes
Otagiri et al. (2008)	F1705S	yes	yes	no		-1	-17	HEK		yes
Akai et al. (2000)	S1710L	yes	yes			17.7	-24.3	HEK	a*	yes

Publication	Mutation	Act.	Inact.	Late	Zero	ΔV_a	ΔV_i	Cell	α	$\beta 1$
Shirai et al. (2002)	S1710L	yes	yes			18.7	-21.7	HEK	a*	no
Amin et al. (2005)	D1714G	no	yes			1.9	1.9	HEK		yes
Baroudi et al. (2004)	G1740R				yes			HEK		no
Valdivia et al. (2004)	G1743R				yes			HEK	b	no
Núñez et al. (2013)	G1748D	yes	yes	no		13.4	13.8	CHO	a*	yes
Chang et al. (2004)	I1762A	no	yes	no		4.1	11.8	HEK		yes
Chang et al. (2004)	V1763M	yes	yes	yes		-3.8	11.5	HEK		yes
Chang et al. (2004)	V1764M	no	yes	yes		-0.7	6	HEK		yes
Valdivia et al. (2002)	M1766L	no	yes	yes		7	9	HEK	b*	yes
Groenewegen et al. (2003a)	I1768V	no	yes	no		0.7	0.9	Ooc.	a*	no
Kauferstein et al. (2013)	I1768V	yes	yes			-6.7	-1.1	Ooc.		no
Rivolta et al. (2002)	I1768V	no	yes	no		0	7.6	HEK		yes
Kato et al. (2014)	N1774D	yes	yes	yes		-7.9	-0.9	CHO	a*	yes
Lupoglazoff et al. (2001)	V1777M	yes	yes	yes		-8.99	-12.4	HEK		yes
Kapplinger et al. (2015)	T1779M	no	yes	no		-3.1	-3.6	HEK	b	no
Beyder et al. (2014)	E1780G	no	yes	no		3.6	2.1	HEK	b	no
Deschênes et al. (2000)	E1784K	yes	yes	yes		8.8	-14.4	HEK	a*	no
Hu et al. (2014)	E1784K	no	yes	yes		0	-18.4	HEK	b	no
Makita et al. (2008)	E1784K	yes	yes	yes		12.5	-15	HEK		yes
Wei et al. (1999)	E1784K		yes	yes			-12.1	Ooc.	a*	yes
Hu et al. (2015)	S1787N	no	no	yes		-1	1	HEK	b	no
Hu et al. (2015)	S1787N	no	no	no		-1	-1	HEK	a	no
Abriel et al. (2000)	D1790G		yes				-15.6	HEK	a*	yes
An et al. (1998)	D1790G	no	no	no		0	-2.9	HEK	a*	no
An et al. (1998)	D1790G	no	yes	no		0	-16.3	HEK	a*	yes
Baroudi and Chahine (2000)	D1790G	yes	yes	yes		5.36	-14.6	HEK	a*	yes
Liu et al. (2002)	D1790G	no	yes			1.4	-10.2	HEK	a*	yes
Liu et al. (2003)	D1790G	yes	yes			8.49	-22.3	HEK		no
Wehrens et al. (2000)	D1790G	yes	yes	no		6	-15	HEK	a*	no
Liu et al. (2002)	Y1795C	no	yes			-1	-2.8	HEK	a*	yes
Rivolta et al. (2001)	Y1795C	no	yes	yes		-1	-10.5	HEK		yes
Tateyama et al. (2003)	Y1795C		yes	yes		0	-11	HEK		yes
Liu et al. (2002)	Y1795E	no	yes			1.7	-10.4	HEK	a*	yes
Liu et al. (2002)	Y1795H	no	yes			0.9	-10.5	HEK	a*	yes
Rivolta et al. (2001)	Y1795H	no	yes	yes		1.1	-10.9	HEK		yes
Tateyama et al. (2003)	Y1795H		yes	yes		0	-11	HEK		yes
Liu et al. (2002)	Y1795R	no	yes			2.1	-10.6	HEK	a*	yes
Kapplinger et al. (2015)	D1819N	no	no	no		-1.9	-0.9	HEK	b	no
Olesen et al. (2012)	D1819N	no	yes	yes		0.1	0.2	HEK		no
Liu et al. (2005)	L1825P	no	yes	yes		0	-7.3	CHO	b	no
Makita et al. (2002)	L1825P	yes	yes	yes		8.9	-11	HEK	a*	yes
Cheng et al. (2010)	I1836T	no	no	no		0.5	0.5	HEK	a	no
Cheng et al. (2010)	I1836T	no	no	no		0.4	1.7	HEK	b	no
Musa et al. (2015)	H1849R	no	yes			-0.5	-6.7	HEK		no
Petitprez et al. (2008)	C1850S	no	yes			1.4	-11.6	HEK	b*	yes
Beyder et al. (2014)	A1870D	no	yes	no		0.6	-1.1	HEK	b	no
Makiyama et al. (2008)	M1875T	no	yes	no		-0.48	16.4	HEK	a*	yes
Beyder et al. (2014)	L1896V	no	no	no		0.5	-2.6	HEK	b	no
Olesen et al. (2012)	R1897W	no	yes	no		-1.6	-6.2	HEK		no
Bankston et al. (2007a)	S1904L	no	yes	yes		-1.3	-4.9	HEK		yes
Glaaser et al. (2012)	S1904L		no	yes			0.6	HEK		no
Rook et al. (1999)	A1924T	yes	no			-9	-0.2	Ooc.	a*	no
Tan et al. (2002)	A1924T	no	yes					HEK	a*	no
Hoshi et al. (2014)	E1938K		no				-0.96	HEK	a	no
Shinlapawittayatorn et al. (2011a)	V1951L		yes	no			8.8	HEK	a	no
Tan et al. (2005)	V1951L	no	no	no		-1	3	HEK	b	no
Tan et al. (2005)	V1951L	no	no	no		0	-2	HEK	a	no
Wang et al. (2007a)	V1951L	no	yes	no		-1.6	1.8	HEK	b	yes
Olesen et al. (2012)	V1951M	no	no	no		-3.6	0	HEK		no
Beyder et al. (2014)	M1952T	no	no	no		0.2	4	HEK	b	no
Frustaci et al. (2005)	I1968S	no	yes			0	-0.3	HEK		yes
Ellinor et al. (2008)	N1987K	no	yes	no		-1.3	-3.4	Ooc.	a*	yes
Bébarová et al. (2008)	F2004L	yes	yes	yes		3.3	-7.5	CHO	a	no
Wang et al. (2007a)	F2004L	no	yes	yes		0.7	4.7	HEK	b	yes
Shinlapawittayatorn et al. (2011a)	P2006A		yes	yes			10.6	HEK	a	no
Wang et al. (2007a)	P2006A	no	yes	yes		-0.2	4.7	HEK	b	yes
Chen et al. (2016)	V2016M	yes	no	no		0.8	-1.8	HEK		yes
Shy et al. (2014)	V2016M	yes	no			3.7	1.9	HEK		no

CHAPTER 7

Using whole-ventricle simulations for physiology-based regularization in ECGI

This chapter is based on:

Matthijs J.M. Cluitmans*, Michael Clerx*, Nele Vandersickel, Ralf L.M. Peeters, Paul G.A. Volders, Ronald L. Westra (2016). Physiology-based Regularization of the Electrocardiographic Inverse Problem. In *Medical & Biological Engineering & Computing*.

The first two authors contributed equally to this publication: The PBR-method was developed and tested by Matthijs Cluitmans, who also collected the *in vivo* data. All AP simulations were created and run by Michael Clerx.

Abstract

The inverse problem of electrocardiography aims at noninvasively reconstructing electrical activity of the heart from recorded body-surface electrocardiograms. A crucial step is regularization, which deals with the ill-posedness of the problem by imposing constraints on the possible solutions. We developed a regularization method that includes electrophysiological input. Body-surface potentials are recorded and a computed tomography scan is performed to obtain the torso-heart geometry. Propagating waveforms originating from several positions at the heart are simulated and used to generate a set of basis vectors representing spatial distributions of potentials on the heart surface. The real heart-surface potentials are then reconstructed from the recorded body-surface potentials by finding a sparse representation in terms of this basis. This method, which we named 'physiology-based regularization' (PBR), was compared to traditional Tikhonov regularization and validated using *in vivo* recordings in dogs. PBR recovered details of heart-surface electrograms that were lost with traditional regularization, attained higher correlation coefficients and led to improved estimation of recovery times. The best results were obtained by including approximate knowledge about the beat origin in the PBR basis.

Contents

7.1 Introduction . . . 139
7.2 Methods . . . 140
7.2.1 *In vivo* recordings . . . 141
7.2.2 Torso-heart geometry . . . 142
7.2.3 Simulation of epicardial potentials . . . 142
7.2.4 Creation of a realistic basis . . . 144
7.2.5 Sparse reconstruction of epicardial potentials . . . 144
7.2.6 Post-processing . . . 145
7.2.7 Statistical evaluation . . . 146
7.3 Results . . . 146
7.4 Discussion . . . 151
7.4.1 Activation and recovery times . . . 151
7.4.2 Beat origin localization . . . 151
7.4.3 Using tuned bases . . . 152
7.4.4 Parameter dependency . . . 152
7.4.5 Limitations and future work . . . 153
7.4.6 Other approaches . . . 153
7.5 Conclusion . . . 154
7.A SVD Bases . . . 155

7.1 Introduction

Cardiac arrhythmias are amongst the leading causes of death worldwide. The 12-lead electrocardiogram (ECG) is a well-established, patient-friendly, quick, reproducible, and cheap tool to determine normal cardiac activation and recovery, to diagnose cardiac arrhythmias, altered activation, ischemia, infarction, primary electrical abnormalities of the heart, structural disease, metabolic disorders, electrolyte imbalance, and other conditions. It reflects the attenuated and dispersed result of propagated electrical activity and recovery in the heart on the body surface.

However, it lacks the capacity to directly assess electrical activity at the level of the heart muscle at high resolution. Electrocardiographic imaging (ECGI) aims at noninvasively reconstructing the electrical activity of the heart, based on body-surface potential measurements and a patient-specific torso-heart geometry (Rudy and Messinger-Rapport, 1987; Ramanathan et al., 2004; van Oosterom, 2012a,b; Cluitmans et al., 2015b). This is achieved by solving what is known as the inverse problem of electrocardiography. In the last decades much progress has been made in ECGI, and clinical applications are published with increasing frequency, yet the accuracy of the reconstructed electrical heart activity is still suboptimal. This is partly due to the ill-posedness of the inverse problem: small variations (noise) in the input data will yield unique but unrealistic variations in the reconstructions (Cluitmans, 2016). To cope with this problem, *regularization* is applied, i.e., additional knowledge is incorporated in the form of constraints on the possible solutions to attain more realistic results. Such constraints are often based on physical or mathematical properties of the problem (MacLeod and Brooks, 1998; Pullan et al., 2005), but the use of electrophysiological properties has also been proposed (He et al., 2003; Ghodrati et al., 2006; Wang et al., 2010; Lopez-Rincon et al., 2015).

In a previous study (Cluitmans et al., 2014), we have shown that it may be beneficial to also include *simulated* electrophysiological input in the reconstruction process, using a method we call *physiology-based regularization* (PBR). In this method, propagating waveforms originating from several positions on the heart are simulated and used to generate a set of basis vectors representing spatial distributions of potentials on the heart surface. The real heart-surface potentials are then reconstructed from the recorded body-surface potentials as a sparse linear combination of these 'building blocks' on the heart surface. In other words, this new method decomposes the simulated heart-surface potential patterns into basis vectors which span the space of heart-surface potentials, and then solves the inverse problem by pursuing a sparse representation of the heart-surface potentials in terms of this basis.

In this manuscript, we provide a detailed description of PBR and use *in vivo* recordings to assess its performance. We investigate whether PBR can improve reconstructions of epicardial ventricular potentials, specifically with the goals of detecting the origin of ectopic beats and imaging substrates for arrhythmias.

7.2 Methods

The potential-based formulation of the forward/inverse problems of electrocardiography is based on the assumption that there is a direct relation between potentials on a closed surface surrounding the heart, and the body surface (Pullan et al., 2005). The closed surface surrounding the heart is usually taken to be the epicardium, i.e., the outer myocardial layer. The forward problem can then be defined as:

$$\Phi_B(t) = A\Phi_H(t) \tag{7.1}$$

where $\Phi_B(t)$ are the potentials on the body surface at a specific time instant t, $\Phi_H(t)$ the potentials on the heart surface, and A is the transfer matrix that relates these vectors. The transfer matrix captures the geometry and conductivity relation between the surfaces. It is assumed that the problem is quasi-static, that the torso volume is source-free, and that the transfer matrix is therefore time-independent.

The goal of the inverse problem is to find the cardiac potentials $\Phi_H(t)$ from the recorded body-surface potentials $\Phi_B(t)$ and a patient-specific transfer matrix A, usually based on a computed tomography (CT) scan. However, small variations in the body-surface potentials (e.g. due to noise) will result in disproportionately large changes in the computed cardiac potentials. In other words, the computed solution of the inverse problem does not depend continuously on the data and the problem is, therefore, ill-posed. Additional constraints are needed to obtain a stable, regularized solution. For example, the well-known Tikhonov method obtains a stable solution by placing bounds on the amplitude of the reconstructed cardiac potentials (or derivatives thereof) with a least-squares minimization at time t:

$$\min_{\Phi_H(t)} \left\{ \|A\Phi_H(t) - \Phi_B(t)\|_2^2 + \lambda(t) \|R\Phi_H(t)\|_2^2 \right\} \tag{7.2}$$

where R is the regularization operator (the identity matrix for zeroth order, the gradient operator for first order, or the Laplacian for second order regularization). The regularization parameter $\lambda(t)$ balances the quality of fit with the amount of regularization and can be determined with methods such as the L-curve. Recent papers review these and other regularization methods (Pullan et al., 2005; Milanič et al., 2014).

PBR is a regularization method that constrains the solutions based on patient-specific electrophysiology simulations. It is illustrated schematically in Fig. 7.1.A. First, as in regular ECGI, body-surface potentials are recorded (Section 7.2.1) and a CT scan is performed from which both a digitization of the heart-surface geometry and the location of the body-surface electrodes are obtained (Section 7.2.2). Next, simulations of propagating action potentials (APs) originating from different points on the digitized epicardium are run (Section 7.2.3). Singular value decomposition (SVD) is applied to the combined simulated patterns of epicardial APs, and truncation is applied to arrive at a small set of basis vectors representing

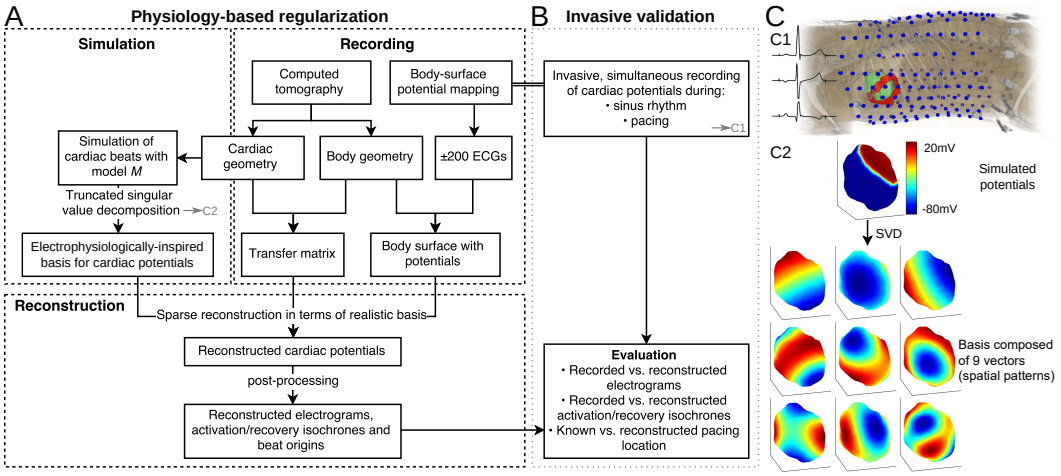

Figure 7.1: Schematic representation of physiology-based regularization (Panel A) and its validation in an *in vivo* canine model (panel B). Panel C1: Body-surface electrodes (blue), ventricular epicardium (green) and epicardial electrodes (red) in the canine experiment. Panel C2: Simulated potentials on the epicardium. Taking the singular value decomposition (SVD) of many (morphologically distinct) simulated beats yields a realistic basis of electrophysiologically relevant solutions that will be used to reconstruct epicardial potentials.

spatial distributions of potentials on the heart (Section 7.2.4). The real epicardial potentials are then reconstructed as sparse combinations of these vectors (Section 7.2.5).

By the nature of SVD, the resulting basis vectors span the space of simulated AP patterns on the heart surface. We assume that the simulated APs form a good surrogate for potential patterns that could be expected on a human heart, so that their basis vectors form a suitable basis for reconstruction of true heart-surface potentials. Furthermore, by aiming for a *sparse* representation in terms of this basis, we aim to further reduce the influence of ill-posedness. Crucially, although a basis might contain only a few vectors, the space they span contains all linear combinations of these vectors and so is vast. Therefore, we hypothesize that a limited number of simulated beats can already provide a basis from which a huge number of electrophysiologically realistic potential patterns can be reconstructed, including many patterns not encountered in any of the simulations. An example of a 9-vector basis is shown in Fig. 7.1.C.

To validate this method, we performed *in vivo* measurements of the epicardial potentials in three normal, anesthetized dogs, while simultaneously recording potentials at the body-surface. This is illustrated in Fig. 7.1.B and Fig. 7.1.C.

7.2.1 *In vivo* recordings

In vivo data was acquired in experiments with anesthetized dogs. This investigation conformed to the Guide for the Care and Use of Laboratory Animals published by the United

States National Institutes of Health (National Institutes of Health Publication 85-23, revised 1996). Animal handling was in accordance with the European Directive for the Protection of Vertebrate Animals Used for Experimental and Other Scientific Purposes (86/609/EU) and was approved by the institutional review committee for animal studies.

In three normal anesthetized dogs, two silicone bands with 99 electrodes were implanted around the basal and mid-basal epicardium after thoracotomy (Cluitmans et al., 2017). Each band consisted of two rows of electrodes, and an additional electrode was placed on the LV apical epicardium. After chest closure, body-surface electrodes (184 to 216, depending on torso size) were attached to the chest (ActiveTwo setup, BioSemi, Amsterdam, the Netherlands). This number of body-surface electrodes is more than sufficient to obtain a good reconstruction with traditional methods (Cluitmans et al., 2015a). Unipolar potential recordings were obtained simultaneously by the epicardial and body-surface electrodes. Beats were recorded during normal sinus rhythm or with epicardial pacing from electrodes on the left ventricle (LV) or right ventricle (RV).

7.2.2 Torso-heart geometry

A CT scan was performed and used to digitize a homogeneous geometry consisting of the body-surface electrodes and the epicardial surface. Segmentation of the surfaces from CT scans was performed manually with Seg3D (CIBC, 2015). The ventricular epicardium was digitized as a triangulated mesh with approximately 1700 nodes and the position of the 103 implanted electrodes was recorded. The septum was not included in this segmentation. The transfer matrix, relating the electrical activity on the cardiac surface to the body surface, was computed with methods available from the SCIrun software repository (Burton et al., 2011) and was based on a boundary-elements method. In one dog a three-dimensional digitization of the entire ventricular myocardium (including septum) was created in addition to that of the epicardial surface. This digitization had a much finer resolution, with grid points spaced 0.5mm apart in all three directions.

7.2.3 Simulation of epicardial potentials

Computational models of the AP were used to simulate waveform propagation over the digitized ventricular myocardium. To see the influence of the AP model used, we ran simulations with three different models: a neuronal model (FHN, FitzHugh, 1961), a mammalian ventricular model (LR92, Luo and Rudy, 1991), and a human ventricular model (TNNP, ten Tusscher and Panfilov, 2006).

Simplified simulations. For our main results, we used fast simulations on a coarse mesh representing the ventricular epicardial surface. The potential at each node in the mesh was modeled using one of the three single-cell AP models mentioned above. Currents between

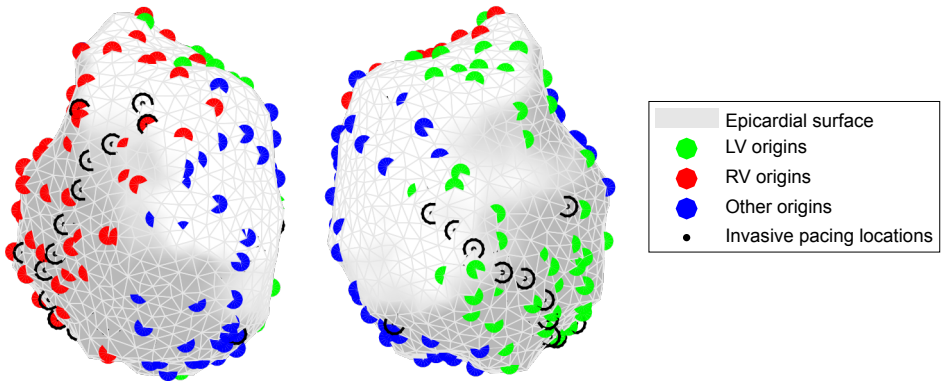

Figure 7.2: Example of the origins of 50 simulated beats on the LV (green), the RV (red), and other locations (blue); and invasive pacing locations (black). Note that the simulated origins generally don't match with the invasive pacing locations.

the nodes were introduced as $I = g\Delta V$ for every two nodes connected in the triangulation. The node-to-node conductance g was set as $g = \bar{g}/d^2$ where d is the distance between the nodes and $\bar{g}$ is a parameter that can be manipulated to adjust the speed of propagation. In this simplified approach, we assumed conduction was the same in all directions, and did not vary from node to node. Because PBR uses spatial but not temporal characteristics of the simulated waveforms, the exact timing of AP propagation is not important as long as the resulting data set contains realistic spatial patterns. To obtain these, we set $\bar{g}$ to a value that reproduced the main characteristics of ventricular activation and recovery, i.e., in chronological order: a propagating front of activation, fully activated ventricles, a wave of recovery, and fully recovered ventricles. These simulations were performed using Myokit, our toolkit for AP model development and simulation (see Chapter 3).

Beat origins. We performed simulations for each dog, with simulated beats originating from several, unique locations. Locations were chosen in three areas: (1) on the LV free wall, (2) on the RV free wall, and (3) at the base or apex of the ventricles (where no pacing was performed during the *in vivo* experiment). Origin locations within these areas were chosen pseudo-randomly, and inspected visually for a roughly uniform equidistant distribution. A single beat was simulated per origin. Where not stated otherwise, the reconstructions in this manuscript used beats from 50 origins per region. Fig. 7.2 shows an example of the origins of simulated beats.

Detailed simulations The method described above is a heuristic method, which is not guaranteed to provide the same accuracy as more advanced techniques such as finite-element methods using the monodomain or bidomain equations (although they are based on the same physical principles). In addition, the mesh used for these simulations was rather coarse com-

pared to the mesh size typically used for 'whole-heart' simulations. To validate the applicability of this simplified method for PBR, we performed additional detailed simulations for one of the dogs and compared the results. In these simulations, a fine-grained, regular, rectangular mesh was used, representing the entire ventricular myocardium, including the left, right, and septal walls. Propagation was then simulated by solving the monodomain equations using a finite-difference approximation and assuming zero-flux boundary conditions. Again, conduction in the myocardium was assumed to be homogeneous and isotropic, as no knowledge of the fiber direction was available. In these detailed monodomain simulations, 29 origins per region were used. For accurate comparison with the simplified simulations, regions were defined as before, with all beats originating from the epicardium of the free walls (never from the endocardium or septum). The simulations were performed using a parallelized monodomain solver (Vandersickel et al., 2016) and the TNNP model of the AP.

7.2.4 Creation of a realistic basis

For each dog and model, the heart-surface APs of all simulated beats were concatenated in a single potential matrix Φ_H. The number of rows in this matrix was equal to the number of heart-surface nodes, and the number of columns equaled the number of simulated beats (typically 50) times the number of time steps per beat (typically 550). This combined set of APs, reflecting a diversity of activation and recovery patterns, was then decomposed using singular value decomposition (SVD):

$$\Phi_H = UDV^T \tag{7.3}$$

Here the columns of U form a spatial basis for the simulated beats, the columns of V form a temporal basis, and the diagonal matrix D represents the corresponding singular values. The entries in D were ordered in non-increasing order, i.e., with the largest singular values first. Each singular value can be interpreted as a weight, where a small value indicates a small contribution of the corresponding spatial and temporal patterns to describing the overall data. A truncated spatial basis U_k was created by keeping only the k most influential elements. These capture the most prominent spatial patterns underlying the simulated potentials. Truncated bases can be beneficial as they leave fewer possibilities for ill-posed influences that could result in unrealistic solutions.

7.2.5 Sparse reconstruction of epicardial potentials

Assuming that U_k can be used as a basis for the epicardial potentials at any time t, there should be a vector $\beta(t)$ such that

$$\Phi_H(t) = U_k\beta(t) \tag{7.4}$$

and our forward problem becomes

$$\Phi_B(t) = AU_k\beta(t) \tag{7.5}$$

By using the truncated basis U_k instead of the full basis U, the reconstruction is constrained to only those elements of U that contain the most relevant physiological information. Reconstruction of epicardial potentials in terms of this new basis can then be achieved by Lasso regularization (Tibshirani, 1996). This is a form of least squares approximation that minimizes the least squares error of the direct solution $||AU_k\beta(t) - \Phi_B(t)||_2^2$ while at the same time requiring $||\beta||_1$ to be smaller than a given parameter $\lambda(t)$:

$$\min_{\beta(t)} \left\{ \|AU_k\beta - \Phi_B(t)\|_2^2 \right\} \text{ subject to } ||\beta(t)||_1 \leq \lambda(t) \tag{7.6}$$

This minimization can be solved for each time instant t independently. The resultant $\beta(t)$ can then be plugged into equation 7.4 to obtain the heart-surface potentials at time t.

L_1-norm penalties have previously been shown to give more accurate results than commonly used L_2-norms (Ghosh and Rudy, 2009). Constraining the L_1-norm of the parameter vector $\beta(t)$ tends to produce only a few nonzero coefficients in $\beta(t)$, leading to a sparse representation of the epicardial potentials. In other words, only the most important elements of the truncated basis will be used in the reconstruction of the epicardial potentials. As this basis consists only of well-defined spatial potential patterns, we expected that this approach would reduce the influence of ill-posedness. We used MATLAB to solve this Lasso problem, choosing $\lambda(t)$ such that the mean square error was minimized.

We reconstructed beats with bases generated from simulated beats originating from all regions of the heart for all three AP models (FHN_{all}, LR92_{all} and $\text{TNNPa}_{\text{all}}$). For beats paced at the LV or RV we compared these results to reconstructions based only on simulated beats originating from the appropriate region (FHN_{spec}, $\text{LR92}_{\text{spec}}$ and $\text{TNNPa}_{\text{spec}}$). In one dog, reconstructions were performed using a generic and a region-specific basis based on detailed monodomain simulations ($\text{TNNPb}_{\text{all}}$ and $\text{TNNPb}_{\text{spec}}$).

7.2.6 Post-processing

Activation and recovery times were determined from reconstructed electrograms with two different methods: a temporal-only method and a spatiotemporal method. The temporal-only approach defines the moment of activation as the moment of steepest voltage downslope (maximum $-d\Phi_H/dt$) during the QRS complex. Recovery times were defined as the moment of maximum $d\Phi_H/dt$ during the T wave. The spatiotemporal approach, proposed by Erem et al. (2011), takes advantage of the spatial relationship between neighboring nodes and their potentials, and could be better suited to estimate the activation time in noisy or fractionated electrograms. Erem et al. noted that not only the temporal signal (i.e., the local potential at a single node) changes quickly when an activation wavefront passes, but also the

spatial gradient of potentials between neighboring nodes. Their approach to activation-time estimation selects the moment at which the change in temporal derivative coincides with the change in spatial derivative. More formally, for each epicardial node, they define the activation time τ as:

$$\tau = \min_t \|D\Phi_H(t)\|_2 \cdot \frac{\partial \Phi_H(t)}{\partial t} \tag{7.7}$$

where $\Phi_H(t)$ is the potential at the epicardial node under consideration at time t, $D\Phi_H(t)$ is the approximated spatial gradient, and $\partial\Phi_H/\partial t$ the approximated temporal derivative.

7.2.7 Statistical evaluation

For each epicardial electrode, Pearson's correlation coefficient (CC) was computed between the recorded electrogram and the reconstructed electrogram at the corresponding (closest) virtual epicardial node. Linear correlation between recorded and reconstructed activation/recovery timings was assessed by means of Pearson's correlation coefficient. Results were statistically compared with Wilcoxon signed-rank tests (for paired measurements) or Wilcoxon rank-sum tests (for unpaired measurements).

Note that we only compare morphology, not absolute error, as the amplitude of the reconstructed potentials depends on the amount of regularization (especially with Tikhonov zeroth-order regularization, which constrains the amplitude explicitly). Moreover, morphology is usually of much more clinical significance, as it contains information about the order and timing of activation and recovery, and can indicate local tissue abnormalities (e.g., fractionation, ST segment deviation). We did not restrict our evaluation to comparing correlation coefficients of morphology, but also considered clinically relevant parameters such as activation timing, recovery timing, and beat-origin localization.

7.3 Results

Fig. 7.3 shows examples of recorded and reconstructed electrograms for a sinus beat and a paced beat in one dog. Electrograms were reconstructed with PBR using different AP models, and with traditional zeroth-order Tikhonov regularization for comparison. These examples show that, regardless of the AP model, all PBR-methods were able to recover some of the electrogram characteristics that were lost with Tikhonov regularization, for example the negative deflection in electrogram 1 and 2, and the positive deflection in electrogram 7. There were no significant changes between the different models used in PBR.

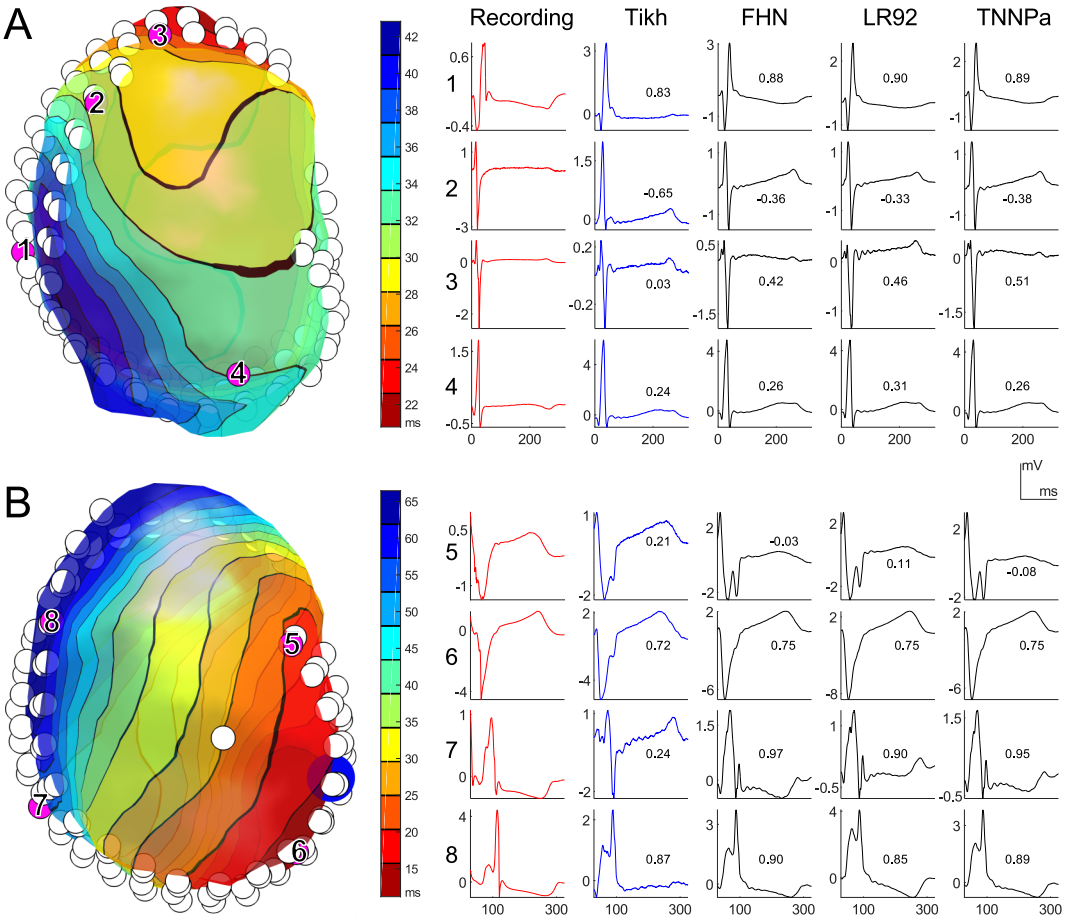

Figure 7.3: Ventricular epicardium (left, colored according to noninvasively reconstructed activation times) and recorded and reconstructed electrograms (right) during a sinus beat (panel A) and an LV paced beat (panel B, pacing location indicated by blue sphere). White circles represent the implanted epicardial electrodes. For selected electrodes (purple, numbered) the corresponding electrograms are shown: recorded (red), Tikhonov-reconstructed (blue) and electrograms reconstructed with PBR for three different basis types (FHN, LR92 or TNNPa). The numbers next to the electrograms indicate the correlation coefficient with the invasively recorded signal.

In Fig. 7.4, quality of reconstruction is shown for all beats. Data were analyzed for all three dogs, for 88 beats in total (of which 67 were epicardially paced, while 21 followed native sinus rhythm) and for 5203 epicardial electrogram pairs (recorded vs reconstructed). Results are shown for traditional regularization with Tikhonov, and for PBR using the full bases (FHN_{all}, LR92_{all} and $\text{TNNPa}_{\text{all}}$), and using region-specific bases (FHN_{spec}, $\text{LR92}_{\text{spec}}$ and $\text{TNNPa}_{\text{spec}}$). Fig. 7.4.A shows that the correlation between recorded and reconstructed electrograms increased significantly for 5 out of 6 PBR models. This indicates that more details were recovered by the PBR methods when compared to Tikhonov regularization, as expected from Fig. 7.3.

Table 7.1: Effect of More Complex AP Model.

Model	CC_{EGM}	R_{act}	R_{rec}	LE (mm)
Tikh	0.81	0.8	0.58	39
FHN_{all}	0.85*	0.77	0.62*	44*
$LR92_{all}$	0.83*	0.77	0.59	42
$TNNPa_{all}$	0.84*	0.77	0.60*	47*
$\mathbf{TNNPb_{all}}$	0.84*	0.77	0.62*	45
FHN_{spec}	0.87*	0.78	0.79*	39
$LR92_{spec}$	0.87*	0.78	0.69*	39
$TNNPa_{spec}$	0.87*	0.78	0.79*	39
$\mathbf{TNNPb_{spec}}$	0.87*	0.78	0.76*	40

Median accuracy metrics in one dog (39 recorded beats), investigating the added value of a detailed whole heart model (TNNPb). *, statistically significant difference with Tikhonov results. Activation and recovery times (and beat origins) determined from temporal-only criteria. LE: localization error, i.e., the distance between the known pacing location and reconstructed location of earliest activation.

In Fig. 7.4.B, activation and recovery times are shown as determined with the temporal-only method (top row) and the spatiotemporal method (bottom row). Spatiotemporal post-processing yielded more accurate timings than the temporal-only method. Activation times determined from PBR-based electrograms were no more accurate than those determined from Tikhonov-based electrograms. However, recovery times were significantly more accurate when PBR was used, especially with region-specific bases. Combining spatiotemporal post-processing with region-specific bases gave the most accurate results (with $R = 0.70$ to $R = 0.80$, $p < 0.05$).

Fig. 7.4.C shows that, in line with these results, localization error was improved by using spatiotemporal post-processing in all methods. Localization error did not further improve with PBR, although using region-specific PBR did remove one outlier.

Table 7.1 shows the results for a subset of the data (one dog, 39 recorded beats), where we also used the bases generated with the whole-heart model (TNNPb). From this table, it can be seen that a simple model of the AP combined with a simplified propagation model gives the same quality PBR reconstruction as a detailed three-dimensional monodomain model.

All previous results are based on PBR reconstructions using bases that consisted of components 2–10 of U, that is, the first ten components of the SVD of the simulated beats, not including the first component. The first component is a constant negative pattern, reflecting the -80 mV offset of the simulated APs. As we reconstruct electrograms (with a zero average), not APs, this offset component does not have a role for our purpose. Components 2–10 for a FHN-based set of simulated beats are shown in Fig. 7.1.C1. In Fig. 7.6, the basis components are shown for all AP models and beat origins in one dog. Reconstruction accuracy with different components of the SVD as basis is shown in Table 7.2 for components 2–5, 2–10, 2–15 and 2–25 for the full data set. For most metrics, using components 2–10 gave the best result.

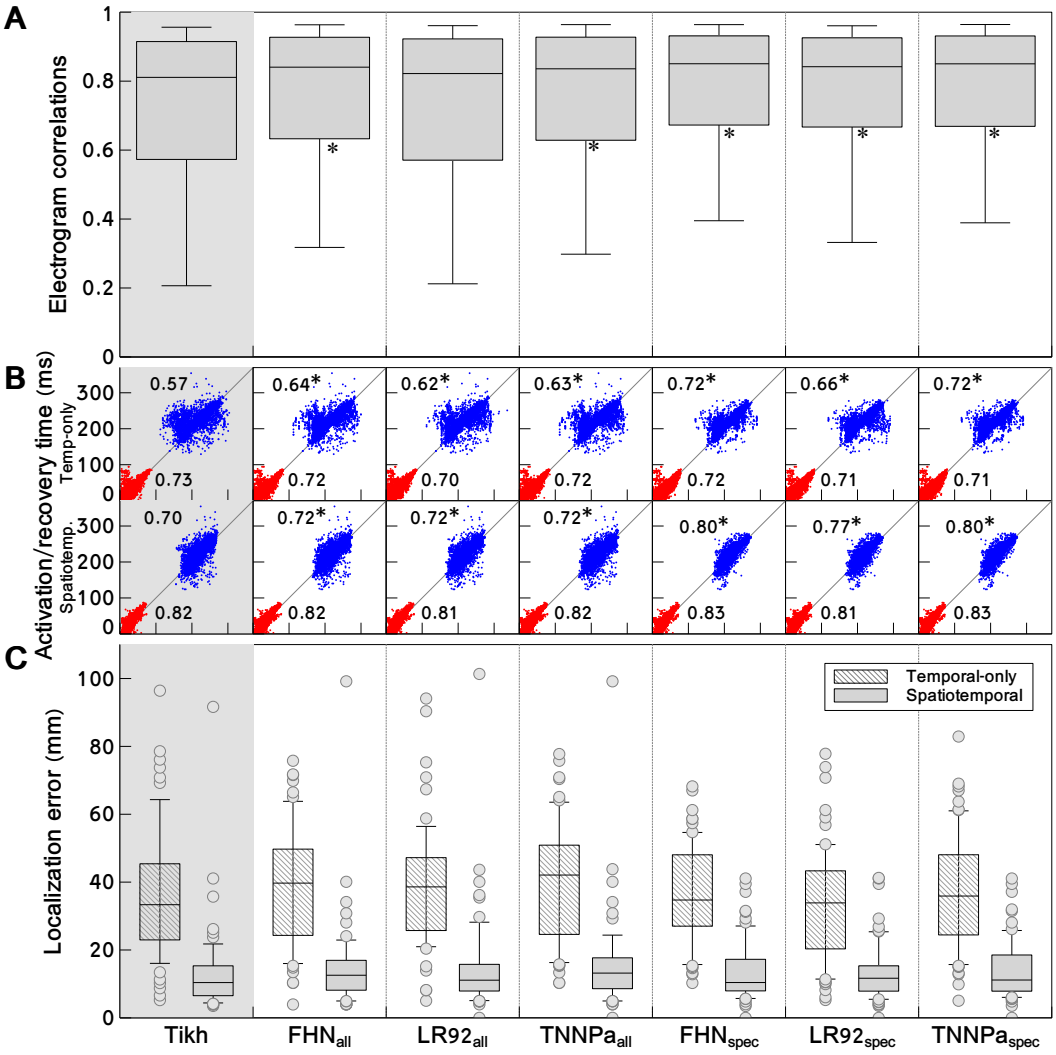

Figure 7.4: Results for the full data set. Columns show the result for the different reconstruction methods: traditional Tikhonov (Tikh) regularization, or regularization by a physiology-based method without (FHN_{all}, $LR92_{all}$ and $TNNPa_{all}$) and with (FHN_{spec}, $LR92_{spec}$ and $TNNPa_{spec}$) region-specific bases. Panel A: box plots of correlation coefficients between recorded and reconstructed electrograms. Box spans the interquartile range (IQR), i.e., the 25-75% range; median indicated by horizontal line; whiskers at 9-91% range. Overall, PBR improves reconstruction quality, especially using region-specific bases. Panel B: Activation times (red) and recovery times (blue) as reconstructed (horizontal axes) vs. recorded (vertical axes). Top row shows these timings as directly determined from the electrograms, i.e. with temporal-only criteria. Bottom row shows timings as determined with a spatiotemporal method. Recovery times, especially, are improved by PBR. Additional improvement is achieved when spatiotemporal post-processing is used. Panel C: Localization error between detected and known origins of pacing, as determined with temporal-only methods (hatched box plots) and with spatiotemporal methods (gray box plots). A combined use of spatiotemporal post-processing and PBR gives most accurate results. An asterisk (*) indicates significant improvement compared to Tikhonov results.

Table 7.2: Dependency on Basis Size.

Basis size	Tikh	FHN_{all}	$LR92_{all}$	$TNNPa_{all}$	FHN_{spec}	$LR92_{spec}$	$TNNPa_{spec}$
Correlation coefficients for electrograms (CC)							
5	0.81	0.80*	0.79*	0.80*	0.83*	0.83*	0.83*
10	”	**0.84***	**0.82**	**0.84***	**0.85***	**0.84***	**0.85***
15	”	0.81	0.81	0.81	0.82	0.81	0.82*
25	”	0.74*	0.73*	0.73*	0.72*	0.74*	0.71*
Activation time correlation (R)							
5	0.73	0.68	0.66	0.68	0.65	0.65	0.64
10	”	**0.72**	0.70	**0.72**	**0.72**	**0.71**	**0.71**
15	”	**0.72**	**0.71**	**0.72**	0.70	0.67	0.69
25	”	0.62	0.57	0.62	0.51	0.58	0.49
Recovery time correlation (R)							
5	0.57	0.62*	0.60	0.62*	0.69*	0.67*	0.69*
10	”	**0.64***	**0.62***	**0.63***	**0.72***	**0.66***	**0.72***
15	”	0.58	0.57	0.58	0.61*	0.62*	0.61*
25	”	0.41	0.39	0.42	0.37	0.36	0.35
Localization error (mm)							
5	33	48*	45*	48*	46*	41*	45*
10	”	40	39	42*	**35**	**34**	36
15	”	**34**	**30**	**33**	**35**	36	**34**
25	”	37	45*	37	41*	38	36*

Median accuracy metrics for the full data set for different number of components of the realistic basis (basis size k). *, statistically significant difference with Tikhonov results. Activation and recovery times (and beat origins) determined from temporal-only criteria.

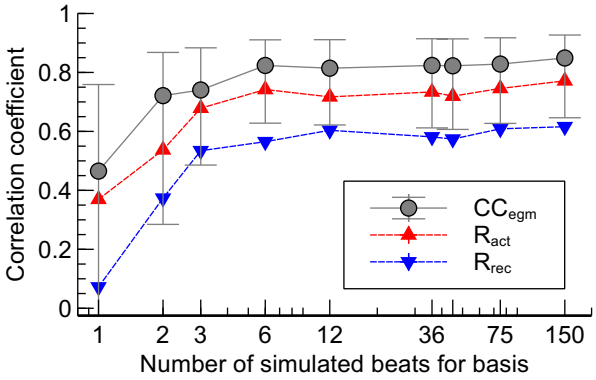

Figure 7.5: Dependency of the accuracy of PBR on the number of (unique) simulated beats that are used for the basis. Results for one dog (39 recorded beats), reconstructed with AP model FHN_{all}. Correlation coefficients between recorded and reconstructed electrograms (CC_{egm}) are maximal and stable when approximately 6 or more beats are simulated. Similarly, activation times (R_{act}) and recovery times (R_{rec}) are reconstructed with highest accuracy for 6 or more simulated beats.

Not only the basis size k is important, but also the number of morphologically-distinct beats that was used to create that basis. In Fig. 7.5, the dependency of PBR-accuracy on the number of simulated unique beats is explored in a subset of the data (one dog, 39 recorded beats) with the FHN_{all} basis. Both correlation between recorded and reconstructed electrograms, and the accuracy of activation and recovery times are maximal when data from 6 or more simulated beats is included in the basis U_k.

7.4 Discussion

We have shown in an *in vivo* experiment that PBR increases the accuracy of reconstruction of electrograms and recovery times, compared to traditional Tikhonov regularization, and was able to recover electrogram characteristics that were lost with Tikhonov regularization. This indicates that PBR yields more information in the reconstructed electrograms than traditional methods.

7.4.1 Activation and recovery times

PBR did not improve accuracy of activation times, which were already determined with reasonable accuracy using Tikhonov regularization. Activation times were most accurate when the spatiotemporal method for activation time estimation was used. In contrast, recovery times were determined more accurately with PBR than with Tikhonov regularization, and therefore profited less from spatiotemporal post-processing. However, a combination of PBR with spatiotemporal post-processing yielded the highest accuracy for recovery times.

Abnormalities in recovery patterns can be an important substrate for cardiac arrhythmia and they are often difficult to diagnose from the 12-lead ECG due to its limited spatial resolution. Noninvasive imaging of recovery abnormalities could therefore be very beneficial for risk assessment and to deepen our understanding of the role of recovery abnormlities in arrhythmia.

7.4.2 Beat origin localization

Beat origin localization is performed by finding the location with the earliest activation time. Since the accuracy of the estimated activation times did not improve significantly with PBR, beat origin locations were not significantly improved. However, some outliers were removed when region-specific bases were used. This is relevant for clinical practice, where the origin of a ventricular ectopic beat is often a target for invasive ablation therapy. More accurate localization of ectopic beats could help guide therapy, thereby reducing procedural time and improving success rates.

7.4.3 Using tuned bases

One interesting feature of PBR is that its bases can be tuned to a specific clinical question. From a 12-lead ECG, the LV or RV origin of an ectopic beat can often be determined without issues. In this study we have shown that, by using a basis specific to the LV or RV, a higher accuracy of electrogram reconstruction is achieved, along with a reduction of origin-localization outliers. One could argue that a more localized basis might be even more beneficial. However, according to a study investigating the accuracy of human interpretation of 12-lead ECG, an experienced cardiologist can correctly identify the ventricle of origin (LV vs RV) in 76.6% of the cases based on the 12-lead ECG, but further sublocalization within the ventricles is accurate in only 38.1%. Thus, one should be careful not to limite the basis to very specific regions, as this may result in the reconstruction of that beat (Erkapic et al., 2015).

Interestingly, the AP model used did not affect reconstruction quality, and a simplified model of AP propagation was found to perform as well as a fine-grained monodomain simulation. This may be explained by the fact that the truncated basis elements reflect the *spatial* potential patterns, mainly reflecting the order of activation. Consequently, as demonstrated in Section 7.A, the basis patterns obtained with SVD using different models are very similar.

PBR leaves temporal aspects largely unconstrained and it is unlikely that incorporating *temporal* patient-specific characteristics will benefit the results. However, including *spatial* information such as infarcted regions could directly influence reconstruction quality: these characteristics will have a large impact on simulated beat propagation and will therefore be incorporated in the truncated spatial basis. Similarly, incorporating *spatio-temporal* information such as abnormal regional changes to the AP may lead to improved reconstructions. These results suggest that even simpler methods for simulating propagating waves, for example using the eikonal equations (Wallman et al., 2012), may be applicable to PBR in its basic form. However, such methods do not offer as clear a road to integrating patient-specific spatio-temporal characteristics such as local changes in the ionic balances. As the dogs used in this study had normal hearts, we were not able to investigate these hypotheses.

7.4.4 Parameter dependency

PBR is able to reconstruct electrophysiologically relevant patterns using a limited number of basis elements (typically 9) generated from only a few simulated beats (6 or more). This is possible because a linear combination of these basis elements still spans a large enough solution space. The Lasso method allows any linear combination, but gives preference to sparse solutions, thereby reducing the influence of ill-posedness. The combination of a truncated realistic basis with Lasso optimization will result in solutions based on a small number of electrophysiologically relevant 'building blocks'.

An open question is how to automatically determine the number of elements needed in the truncated basis. With too few elements, the basis will not span the full range of possible potential patterns and the method will be unable to reconstruct all physiologically relevant cases. If too many elements are used, the ill-posedness of the inverse problem will dominate and allow noise-like influence of the 'less important' basis elements to obscure the real solution. In this study, we found that the optimal basis size was close to 9. For clinical applications, where no invasively measured potentials are available, methods are needed that automatically determine the optimal basis size. These should aim to find a balance where ill-posedness is reduced without overly constraining the solution space.

We have not investigated the dependency of PBR on the number of body-surface electrodes. Earlier work by our group shows that ECGI in general needs at least 80 electrodes on the body surface for accurate reconstruction of heart-surface potentials (Cluitmans et al., 2015a). However, PBR's lower dimensionality due to the sparse basis might warrant a lower number of body-surface electrodes. Especially in a clinical setting, where the 12-lead ECG is a commonly used tool, its reduced set of only 9 electrodes would make a practical alternative. Future studies should investigate whether this low number of electrodes in combination with PBR does indeed provide accurate results.

7.4.5 Limitations and future work

One important limitation of our current PBR implementation is that the basis is created from cellular AP simulations, whereas the actual inverse reconstruction is in terms of local electrograms. The cellular AP reflects potential differences over the cell membrane, whereas local electrograms reflect extracellular potential differences over larger regions of tissue. It is possible PBR results could be improved by using simulated local electrograms instead of cellular APs.

In the validation part of this study, we were limited by the healthy status of the animals and could not investigate the effect of (local) tissue abnormalities (e.g., myocardial infarction).

We had no information about anisotropy of the tissue, so this was not included in the simulations. However, we expect that the more complicated spatial patterns resulting from anisotropy can already be reconstructed using our current basis vectors. Future work may be needed to show if this is true.

7.4.6 Other approaches

We have presented a method to include electrophysiological data in the potential-based formulation of the inverse problem, but this was not the first attempt to achieve this. For example, He et al. (2003) proposed to solve the forward problem based on potentials from an anistropic heart model, and then compare the resulting body-surface potentials to recordings.

By optimizing the computed body-surface potentials, they obtained an estimate for the heart-surface potentials. Wang et al. (2010) employed a statistical framework to constrain inverse solutions to realistic transmembrane potential dynamics.

In a study by van Oosterom (1999), a method was presented to reconstruct the heart-surface potentials based on a-priori knowledge about their spatial covariance. This knowledge is usually not available and this method therefore cannot be applied in practice. However, with methods similar to those presented in the present paper, knowledge about the spatial covariance could be simulated, making it worthwhile to re-investigate this approach.

In a recent study by Lopez-Rincon et al. (2015), heart-surface potentials were reconstructed with the help of a simulation based on the bidomain equations, similar to the TNNPb monodomain simulations performed in this manuscript. We have shown that, in our implementation, such a detailed cellular implementation does not contribute to the accuracy of reconstructions.

Some implementations of the inverse problem of electrocardiography are not based on a potential-based formulation, as in this study, but define cardiac activity in terms of activation wavefronts or other equivalent sources. In the wavefront-based formulation of the inverse problem, (cellular) electrophysiology models have always been part of the reconstruction process, e.g., by including a model of the expected transmembrane potentials (van Dam et al., 2009) or modeling the activation wavefront as a physiologically-inspired propagating curve (Ghodrati et al., 2006).

Although our method was not the first to include electrophysiological data to improve the inverse reconstruction of electrical activity on the heart, to the best of our knowledge it is the first to apply it to obtain both activation and recovery patterns and validate these *in vivo*.

7.5 Conclusion

We have introduced and validated PBR, a novel method to noninvasively reconstruct epicardial potentials from body-surface potentials. By incorporating simulated electrophysiological input in the regularization of the inverse problem of electrocardiography, more information is recovered in the reconstructed epicardial electrograms. Reconstruction of recovery time, in particular, is improved with this method. While we found that the level of temporal detail in the simulations did not affect the results, the inclusion of spatial characteristics (i.e., suspected LV or RV origin) did improve accuracy. Noninvasive imaging of recovery abnormalities with PBR can greatly benefit risk assessment and improve understanding of their role in arrhythmias. This may help to answer clinical questions with improved accuracy.

Acknowledgments

The authors would like to thank Roel L.H.M.G. Spätjens for help with the figures, and Joël M.H. Karel and Pietro Bonizzi for technical discussions. Furthermore, the authors would like to thank Dana Brooks, Jaume Coll-Font, (Northeastern University, Boston, MA, USA), and Burak Erem (Harvard Medical School and Boston Children's Hospital, MA, USA), for kindly sharing their algorithm for spatiotemporal activation-time approximation. The work of P.G.A. Volders was supported by the Netherlands Heart Foundation (NHS2007T51) and a Vidi grant from the Netherlands Organization for Scientific Research (ZonMw 91710365).

7.A SVD Bases

A comparison of bases generated from different AP models is shown in Fig. 7.6. Each row shows bases elements 2–10 as created with a specific AP model (FHN, LR92, TNNPa or TNNPb) and a specific region of simulated origins: full epicardial surface (*all*), only the LV (*left*), or only the RV (*right*). The elements are shown in descending order (left-to-right) of contribution to the simulated potentials. Regardless of AP method and beat origins, the first basis elements capture simple patterns and later elements capture more complex patterns. There is a clear difference between basis elements of different beat origins (all versus left versus right), but less difference between basis elements of different AP models.

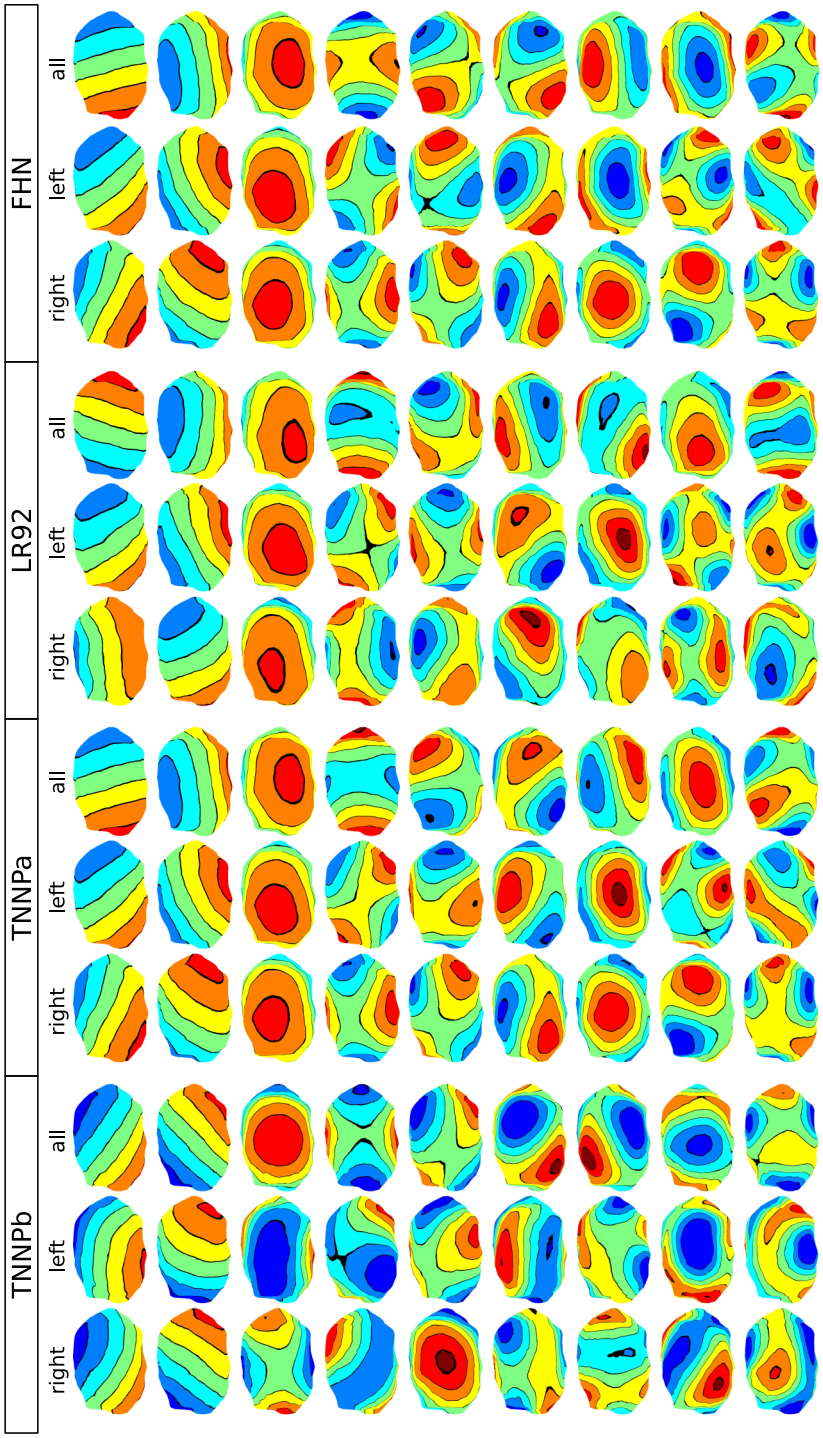

Figure 7.6: Bases created with PBR for different AP models and simulated beat origins, in one dog.

CHAPTER 8

Discussion

Contents

8.1 Introduction . . . 159
8.2 Multi-scale modeling and simulation . . . 162
8.2.1 Linking genes to channels and currents . . . 162
8.2.1.1 Simulation and fitting models of ionic currents . . . 163
8.2.2 Cells, coupled cells and tissue . . . 165
8.2.3 Towards whole-heart simulations . . . 168
8.3 Reliability and reproducibility . . . 169
8.3.1 Multi-model testing and model comparison . . . 170
8.3.2 Automated validation . . . 171
8.3.3 Free parameters and variability . . . 172
8.3.4 Data sharing and reporting standards . . . 172
8.4 Variability in multi-scale models of the AP . . . 173
8.4.1 Measuring variability . . . 174
8.4.2 Modeling and simulating variability . . . 175
8.4.3 Personalized modeling . . . 175
8.5 Conclusion . . . 176

8.1 Introduction

Diagnosis and treatment of cardiac arrhythmias can benefit greatly from a deeper understanding of the mechanisms by which they arise. A wealth of information has been gathered about the fundamental processes involved on the genetic, molecular, cell, tissue, organ, and whole-body levels, and modern clinicians have access to diagnostic methods on each of these scales. Yet to make full use of this information, an *integrative* or *systems approach* is required that combines information from the different levels, and adds information about how processes at the different scales interact (Rudy et al., 2008; Kohl et al., 2010; Noble, 2017). Computational methods, particularly *multi-scale modeling* and *simulation*, have been very useful in this respect. Chapters 3-7 of this thesis each address a different topic, combining information from different scales or developing methods to integrate them (see Fig. 1.1). In Chapter 3 we presented *Myokit*, our newly developed toolkit for action potential (AP) model simulation and development. Myokit can be used to create models of ion currents, integrate them into models of the cellular AP, and combine AP models into models of tissue. Chapter 4 then investigated a technique to speed up AP simulations. In Chapter 5 we measured *variability* in the kinetics of the fast sodium current I_{Na} and showed how it could affect the cellular AP. Chapter 6 then described our efforts to establish an *in silico* link from genetic mutations (in *SCN5A*) to current-level changes (in I_{Na}). Finally, in Chapter 7 we used Myokit to perform simplified whole-heart simulations that were used in the *regularization* problem of electrocardiographic imaging (ECGI), thereby making a connection to the whole-body scale. In this chapter, these topics are discussed in the broader context of using a systems approach to understand cardiac electrophysiology and arrhythmogenesis.

By combining multi-scale modeling with experiments, it is possible to link observations at the genetic or molecular scale to higher-level features of the physiology and pathophysiology of the heart. For example, Bébarová et al. (2008) measured I_{Na} through channels encoded by wild-type (WT) and mutated *SCN5A* and used modeling to extrapolate to the single-cell level, transmural myocardium, and the pseudo-ECG. Benson et al. (2008) studied the effects of channel-blocking drugs in simulations of single cells, fibers and 3-dimensional wedges of tissue. These studies investigated hypothesized disease mechanisms, and showed by simulation that certain molecular changes *could* be the cause of observed higher-level effects (e.g., changes to the ECG). Besides this use in evaluating mechanistic hypotheses, modeling also has direct predictive power, as was shown in recent studies into drug-development (Cummins Lancaster and Sobie, 2016) and clinical risk assessment (Hoefen et al., 2012; Arevalo et al., 2016). A schematic 'pipeline' illustrating a common pattern in these studies is shown in Fig. 8.1.

Many other set-ups are possible, for example including single channel function (Clancy and Rudy, 1999; Silva et al., 2009), subcellular detail (Greenstein and Winslow, 2002; Nivala et al., 2012), signaling (Saucerman et al., 2004; Heijman et al., 2011), contraction (Matsuoka

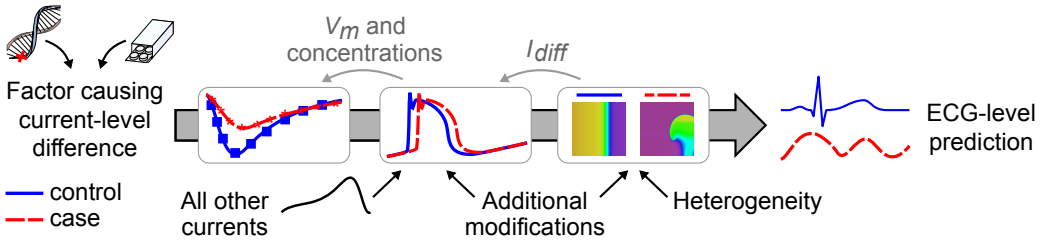

Figure 8.1: A common pattern in multi-scale modeling of cardiac electrophysiology, starting from effects at the ion-current level and building up to the levels of cell, tissue and pseudo-ECG. In the first step, the effect of a mutation, drug or other factor on an ion current is quantified experimentally. This leads to an updated model of the current that is integrated into a model of the cellular AP. At this stage, additional modifications can be made, for example to make the model more specific (e.g., cell type, gender) or to include disease or drug-induced changes (e.g., altered current densities and ionic concentrations). Next, a tissue-level model is constructed. At this level, heterogeneity in cell properties or tissue geometry can be added. Information travels from the lower to the higher scales, but there is also feedback in the form of the membrane potential (V_m), the ionic concentrations, and the diffusion current between cells (I_{diff}). Finally, a pseudo-ECG is calculated from the simulated tissue-level results.

et al., 2003; Cortassa et al., 2006), and 3-dimensional geometries (Panfilov and Holden, 1993; Gharaviri et al., 2012; Gurev et al., 2015). However, there are several challenges that need to be overcome before we can fully exploit the potential of these techniques.

Firstly, the relationship between diseases and molecular factors (such as ion channel subunits, channel-blocking drugs or compounds involved in signaling) is complex. While the successes of genetics and the advent of highly specific targeted drugs have occasionally led people to view (patho)physiology in terms of molecular factors, diseases themselves "represent emergent properties at the scale of the organism that result from dynamic interactions between multiple constantly changing molecular factors" (Weiss et al., 2015). In terms of Fig. 8.1, the exact change seen on the left is less important than how the altered current interacts with the other currents to form the AP, and arrhythmogenesis is best described in terms of higher-level emergent properties such as elongation of the AP or repolarization reserve[1] (Roden, 2008). A good example of this complexity is I_{Na}, where a single mutation in *SCN5A* (resulting in a single molecular-level change) can cause several distinct clinical phenotypes (Remme, 2013), where drugs targeting the channel are powerful but unpredictable (Remme and Wilde, 2014), and where pathogenicity predictions are still unreliable (see Leong et al., 2015, and Chapter 6 of this thesis).

Secondly, and related strongly to the previous point, is the fact that arrhythmias typically do not have a *single* cause. Instead, they require both a *vulnerable substrate*, (a specific set of potentially dangerous conditions) and a *trigger* (some spontaneous internal or external event that sets the arrhythmia off). The substrate is likely to be a combination of factors such as mutations, changes in ionic concentrations, or structural and electrical remodeling.

[1] A possible analogy is trying to study a conflict by focusing on the individual sides, despite the fact that crucial concepts like 'disagreement' and 'escalation' do not exist at the single-person level.

This need for multiple coacting factors to create the conditions for an arrhythmic event complicates diagnosis (top-down prediction) and risk-assessment (bottom-up prediction). For example, recreating the trigger in a clinical setting might not recreate the arrhythmia if the right substrate is not present (so that stress testing may be necessary). The trigger itself can even be an otherwise innocuous and common occurrence (even the sudden ringing of an alarm clock, see Wellens et al., 1972). Conversely, individual aspects of a vulnerable substrate, including rare mutations in ion-channel genes, can occur in otherwise healthy individuals without causing an arrhythmia. In Fig. 8.1 this is shown by the necessary introduction of additional modifications and heterogeneity at the cell and tissue levels.

The third and final complication discussed here, is the existence of variability between subjects, variability in a single subject over time, and even cell-to-cell variability within a single subject. Well-known examples of biological variability are outward appearance, the shape of the heart, and even the shape and size of individual myocytes. But variability extends beyond structural differences, and is also evident in the electrical properties of the heart (see also Chapter 5). A review by Marder and Goaillard (2006) presented strong evidence showing that major variability occurs in expression levels of neuronal ion channels, which correlate directly with the densities of the associated ion currents (Schulz et al., 2006). This level of variability is remarkable, as even small changes in the strength of ionic currents can have severe consequences in both neurons and myocytes. At the same time, some variation is inevitable as cells are not static entities but rebuild themselves constantly. For example, the channels carrying I_{Na} and I_{Kr} are replaced every 35 hours and 10 hours respectively (Maltsev et al., 2008; Vandenberg et al., 2012). A cardiac modeling study by Sarkar and Sobie (2010) showed that, despite a cardiomyocyte's sensitivity to changes in ion channel expression, a large degree of variability in expression is possible, provided it is *compensated* by changes to the other currents. As Marder and Goaillard explain, the ability of a cell to regulate its electrical function leads to a situation where parameters sensitive to sudden small changes can drift slowly but dramatically with time. In other words, as long as the cell can keep compensating, even 'sensitive parameters' can show large variation without apparent consequence. Weiss et al. (2012) pointed out the impact this has on understanding arrhythmogenesis: if, for example, repolarization in one patient's myocytes depends strongly on I_{Kr} while the same current plays only a small part in another, the two patients will have very different risks of arrhythmogenesis when administered I_{Kr}-blocking drugs. As a result, clinical treatment should not focus on 'fixing' specific currents, but on restoring dynamical phenomena such as repolarization (Weiss et al., 2015). In terms of trigger and substrate, the existence of strong variability in the mechanisms underlying the cellular AP implies that the substrate of patients with similar histories and genetic backgrounds can still be very different, and may even change over time.[2] In Fig. 8.1 variability can be *eliminated* by

[2] Besides complicating the analysis of arrhythmias, variability may confer an evolutionary advantage by allowing individuals to adapt (if changes are slow) or parts of the population to survive (if changes are fast). In other words, the idea that myocytes can function in different configurations is consistent with the idea of

adding modifications to create a patient-specific model, or it can be *included in the models* using techniques discussed in Section 8.4.

With these issues in mind, we now discuss multi-scale modeling of the cardiac AP, show where the work presented in this thesis can help increase the utility of multi-scale modeling for cardiology, and highlight future challenges.

8.2 Multi-scale modeling and simulation

Simulation with multi-scale models allows the interaction between dynamical processes in the heart to be explored. This means it can be used to study the cell-level properties that emerge when ion channels are coupled by a cell membrane, but also the tissue-level properties that emerge when cells are coupled by gap junctions and extracellular conduction. The view that diseases themselves represent such emergent properties implies that simulation is a crucial tool for the study of arrhythmogenesis. In contrast to experimental studies, computational studies allow complex arrhythmogenic substrates to be modeled and perfectly controlled (but see Section 8.3 for important caveats). Current applications of AP-model based simulation range from theoretical and fundamental ('basic') research to drug discovery and risk prediction in a clinical setting. Understanding and incorporating variability into these models is a challenge for the future (see Section 8.4). In this section, simulation and modeling at the different scales encountered in this thesis are discussed.

8.2.1 Linking genes to channels and currents

Multi-scale investigations of genetic defects in ion-channel genes commonly start with electrophysiological experiments to quantify the mutation's effects on the whole-cell current, after which the investigation continues *in silico*. Experiments can focus on the pore-forming α-subunit, but also on auxiliary β-subunits or genes for the many gene-products that bind to and interact with the macromolecular complex that forms the ion channel. Replacing this laborious experimental step with a computational approach could be both cost-effective and greatly increase the scale at which such work could take place.

In Chapter 6, we attempted to predict the change in I_{Na} due to a mutation in *SCN5A*, the gene encoding its pore-forming α-subunit. Using machine-learning techniques and a database of mutations with known effects, we showed that the absence or presence of particular changes could be predicted with better-than-chance accuracy. While we showed that the out-of-the-box accuracy of machine-learning methods on this database surpassed that of commercially available direct pathogenicity predictors, the accuracy was still low. For example, while presence of inactivation defects could be predicted with 70% accuracy, this was only slightly better than the 64% accuracy obtained by simply always guessing the most

using *redundancy* to create robustness.

common outcome. However, other measures such as the area under the curve (AUC) were improved considerably, suggesting the method may still hold promise for the future. More work in this area is required, particularly into decreasing bias in the data set by adding mutations with very small or very large effects (i.e., mutations that can easily go unnoticed and mutations incompatible with life, see Section 6.4.2.2). Another application of this idea would be to create a similar database for a different gene such as *KCNQ1*, for which clinical-phenotype predictions are known to be more accurate (Leong et al., 2015), which suggests that current-level predictions may be more accurate too.

An alternative approach is to model the channel behavior directly, using molecular dynamics (MD) simulations. With MD, all atoms in an ion channel can be modeled, along with considerable stretches of nearby membrane. Such simulations are well-developed, and have been the subject of much research: a very extensive review was given by Roux et al. (2004). However, these simulations cannot determine the 3-dimensional structure of the folded channel, which must instead be determined using crystallization of isolated channels. Once the structure for one channel is known, estimates for similar channels can be obtained with *homology modeling*. This technique can also be used to introduce mutations into the model, but as it starts from a fully formed channel it can not predict issues with transport or folding. Due to their computational complexity, MD simulations are limited to very short time scales i.e., 'tens of nanoseconds' rather than the milliseconds, seconds, and minutes typical in AP modeling (Southern et al., 2008). This means that, even with the expected increase in computing power, determining the effects of mutations on channel function *ab initio* is still a distant prospect (Silva and Rudy, 2010).

As a result, building models of ion currents based on whole-cell patch-clamp data remains a highly relevant and challenging task for the foreseeable future. Two recent developments worth mentioning in this context are automated patch-clamping and human induced pluripotent stem cells (hiPSC). With hiPSC, it is possible to culture a line of cells that can be made to *differentiate* into myocyte-like cells that can be clamped and measured (possibly with the addition of 'artificial' currents using *dynamic clamp*, see Meijer van Putten et al., 2014). Ma et al. (2013) have even obtained stem-cells from a patient and a sibling, and used these to study a mutation in a patient-specific setting. The benefit over cardiomyocytes is that these cells can be cultured, so that experimental work does not necessarily require the highly invasive clinical procedures needed to obtain cardiomyocytes from patients.

In the past decade, automated patch-clamp systems have been developed and used in safety testing and drug discovery (Stoelzle et al., 2011). With such systems, 'basic' patch-clamp protocols can be run on larger numbers of cells than with a traditional patch-clamp system (although expertise is still needed from the experimenter), but they can also be used to perform more complicated measurements such as recording late I_{Na} (Chevalier et al., 2014). An interesting future prospect is to improve the throughput and success rate of such devices

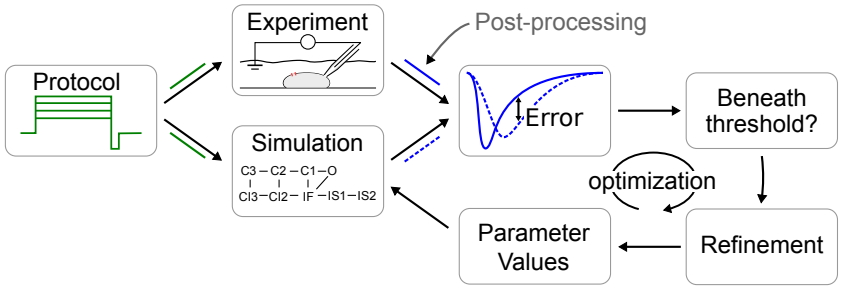

Figure 8.2: Fitting an ion current model to patch-clamp data using the whole-trace method. A single protocol is applied to a real cell and a simulated cell and (after post-processing of the experimental data) the results are compared. An optimization method is used to iteratively refine the parameter values and re-run the simulation until the error is below a preset threshold.

by using optimized protocols such as described in Clerx et al. (2015) and Fink and Noble (2009), followed by a robust model fitting routine (Loewe et al., 2016). Conventional electrophysiological values such as time constants and midpoints of (in)activation could then be obtained from the fitted models using simulation.

8.2.1.1 Simulation and fitting models of ionic currents

Traditional analysis of voltage-clamp and patch-clamp involves measuring quantities such as peak magnitude and time-to-peak, and using these to derive measures such as midpoint of activation. Several studies have pointed out that this does not use all the information in the measured signals and is more prone to errors than using *whole-trace fitting* (Hafner et al., 1981; Willms et al., 1999; Lee et al., 2006; Buhry et al., 2011). A schematic overview of a whole-trace model-fitting routine is shown in Fig. 8.2. A protocol is created and applied to a cell. Next, the same protocol is used in a simulation based on some model of the current, and the results are compared, resulting in some measure of the error, or 'score'. Finally, an optimization method is used that iteratively refines the model's parameter values and re-runs the simulation until the error is below some preset minimum.

With the exception of the experiment, all these steps can be handled within Myokit. The simulation step can be performed using any of its simulation engines (see Chapter 3). For very fast simulations with Markov models, the simulation engine based on eigenvalue decomposition can be used, but if non-linear effects need to be included the CVODE engine can be used instead (as was done in Chapter 5 to incorporate membrane charging time). As a future step, it may be possible to integrate Myokit's multi-cell GPU simulation engine with the parameter estimation routine, allowing large numbers of simulations to be run in parallel and potentially speeding up the parameter estimation process.

In addition to the standard simulation classes, Myokit contains an advanced simulation engine that uses automatic differentiation to calculate partial derivatives of the state and

other variables with respect to one or more parameters. This can be used to run *local identifiability checks* (Cobelli and DiStefano, 1980; Fink et al., 2008a). Using such checks, we can provide a partial[3] answer to the question 'does applying this patch-clamp protocol give us the information we need to find a unique set of parameter values that provide the best fit?' This can be used to check the validity of patch-clamp protocols. When investigating variability, such a protocol-checking method is vital to ensure the observed variability is not a result of the experimental set-up (see also Chapter 5).

In addition, identifiability checking can be used to *optimize* protocols, reducing their runtime while ensuring they provide the necessary information (Fink and Noble, 2009). In Clerx et al. (2015) we use this method to create a very short (260ms) protocol to extract all the information needed to fit the I_{Na} model by Clancy and Rudy (2002). While more work is needed to refine these methods, such optimized protocols hold great promise for the study of ion-channel behavior using whole-cell patch-clamp experiments. For example, when studying mutations, the method could be used to quickly train a model to a mutated current, and then remaining experiments could be run *in silico*. Alternatively, if the protocol is constantly re-run while a channel-blocking drug is applied, it could be used to study the mechanism by which the drug affects the channel (by inspecting which parameters change at which time). However, as shown in Clerx et al. (2015), this may first require improvements in our models of cardiac I_{Na}. Another area where improvements can be made is in the development or refinement of optimization methods that deal well with ion-current fitting problems. Such methods should accept a score function without derivatives, be fast, robust and capable of dealing with noise.

8.2.2 Cells, coupled cells and tissue

Once ion-current models have been defined, they can be grouped into cell models, and cell models can then be coupled to create tissue models (see Chapter 2). This has a wide range of well-established applications, including single-cell simulation, small and large-scale simulation of (heterogeneous) tissue (see Chapter 3), and whole-heart modeling (see Chapter 7). More recent applications include simulation of cell-to-cell variability (see Chapter 5) and detailed modeling of subcellular ionic concentrations. In this section, these applications are briefly discussed and Myokit's established and unexplored capabilities are reviewed.

Myokit includes a GPU-accelerated ODE solver for multi-cellular simulations (Chapter 3 and Chapter 4). By default, this simulation engine assumes homogeneous cells, connected in a rectangular grid as shown in Fig. 8.3.A. Such simulations can be used to study (altered) conduction velocities or spiral waves on homogeneous tissue (Fenton et al., 2002). In Myokit, any model parameter can be varied between cells (limited only by the amount of memory

[3] Because the method uses first-order derivatives evaluated at an initial set of parameter values, a positive result is only valid for nearby points in the parameter space. A negative result does imply the model is not globally identifiable.

in the hardware) and the connection strength between any two cells can be specified individually. This allows the same engine to be used to model heterogeneous networks of cells or patches of tissue in 1, 2 or 3 dimensions, as shown in Fig. 8.3.B. Allowing heterogeneity opens up a wide range of possibilities, including transmural strands (Bébarová et al., 2008), heterogeneous tissue (Panfilov and Vasiev, 1991; Ten Tusscher and Panfilov, 2003), irregular, three-dimensional geometries (Chapter 7), and models including fibrosis and structural or functional reentry. If *no* connections are specified, the engine can be used to simulate large numbers of cells in parallel, as shown in Fig. 8.3.C. This can be useful to explore the influence of a parameter over a wide range, which can be more informative than looking at derivatives especially when large changes or strong non-linear behavior is involved. By varying multiple parameters at once, this method could also be used to perform 'population of models' studies (Muszkiewicz et al., 2016) (although it is possible that multiple runs of the faster single-cell simulation engine may still provide better performance, especially when long pre-pacing periods are required). Another feasible use that we have yet to explore in detail, is the modeling of heterogeneously coupled networks of cells as shown in Fig. 8.3.D. Such studies can provide insights into the role of heterogeneous gap-junction expression in arrhythmogenesis (Prudat and Kucera, 2014). From a computational point of view, this is essentially the same situation as in Fig. 8.3.B. A relatively new development in cellular AP modeling is the use of models with large numbers of subcellular elements, as shown in Fig. 8.3.E. These simulations are typically aimed at exploring intracellular calcium waves or sparks, which can cause spontaneous contraction (Nivala et al., 2012; Voigt et al., 2014). It may be possible to use Myokit's multi-cell simulation by replacing the cell models with subcellular compartment models, and reinterpreting the variables used to represent gap-junction currents as intracellular diffusion. A further extension on this scheme would be to couple multiple, subcellularly detailed, cell models together into a system for studying the propagation (or lack of propagation) of spontaneously induced calcium waves. This is visualized in Fig. 8.3.F. Both types of simulation form a viable target for further Myokit development, but may require the introduction of stochastic variables in cell models (which are currently not supported) and the use of multiple models within the same simulation.

Some preliminary work towards *mixed-model* simulation in Myokit has been performed. Fig. 8.4 shows a simulation of propagation across the Purkinje-ventricular junction, modeled using a Purkinje cell model and a ventricular cell model. Such simulations have been used to study the conditions under which slowed conduction or conduction-block can arise which can play a part in arrhythmogenesis (Aslanidi et al., 2009b). In Myokit, this is implemented using a specialized simulation type which does not yet support heterogeneous cell parameters, customized connection strengths etc. An open question for the future is whether it is possible to adapt the standard multi-cell simulation to allow multiple model types without a loss of performance or an excessive increase in code complexity.

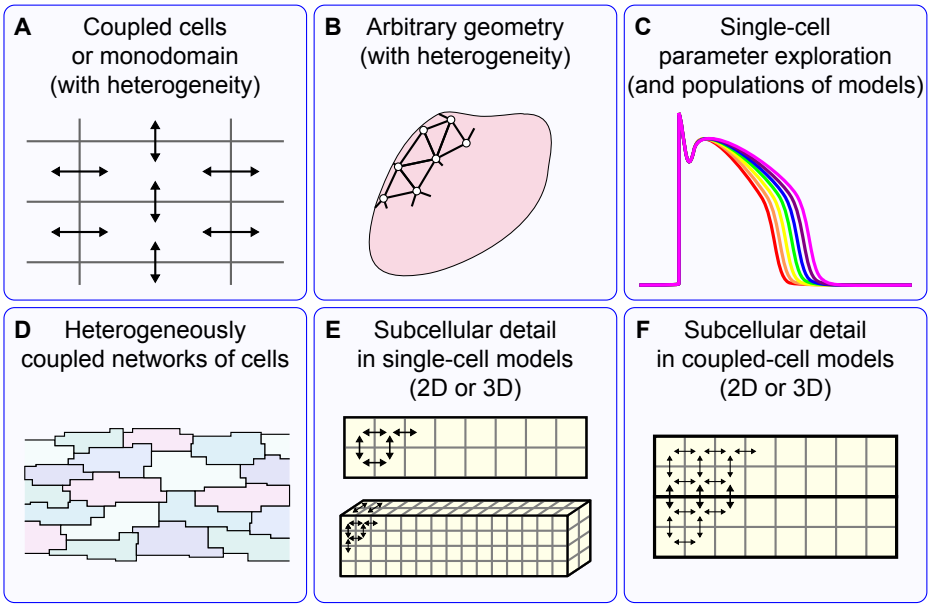

Figure 8.3: Multiple uses of Myokit's multi-cell simulation engine, including realized uses (top row) and potential ones (bottom row). (A) Rectangular grids of coupled cells or a rectangularly discretized space simulated with the monodomain equations. Model parameters and cell-to-cell conduction may be varied between cells. (B) Arbitrarily complex geometries, created by specifying each cell or node's connections manually. (C) Multiple single-cell simulations running in parallel, with different parameters for each cell. Future uses: (D) A network (E) Simulation of a single cell with a sub-cellular resolution, for example to investigate calcium sparks. (F) Like E but with multiple cells connected by gap junctions.

Figure 8.4: A simulation of the Purkinje-ventricular junction at $t = 3$ms, $t = 6.5$ms and $t = 18$ms. The Purkinje fiber is formed by 64×32 cells simulated using the model by DiFrancesco and Noble (1985). The ventricular tissue consists of 96×96 cells simulated using the model by Luo and Rudy (1991).

8.2.3 Towards whole-heart simulations

Despite impressive recent examples (Sugiura et al., 2012; Gurev et al., 2015), simulating ever larger parts of the heart is limited by computational power. For this reason, large-scale simulation projects often have a strong focus on performance, rather than versatility. Such projects typically require the model code to be written using the same language as the simulation engine, and may 'tweak' and optimize the model code in many ways (see for example the simulations by Mirin et al. (2012) or the highly efficient CARP simulation engine by Vigmond et al. (2003)). This sacrifice of versatility for performance may be partially circumvented by including an automatic model code generator, as is done in Chaste (Mirams et al., 2013), or even re-generating the model code for every simulation (as is done in Myokit).

One of the core ideas behind Myokit is that models are specified in an easy-to-use model language, and then automatically translated to faster 'low-level' code. This means that, at current, Myokit is unable to use optimizations that require the model equations to be written in a special form, such as the method proposed by Rush and Larsen (1978). However, since Myokit creates a symbolic form of the equations when parsing a model file, it may be possible to implement such optimizations automatically when generating code for large-scale multi-cellular simulations (similar to what was shown in Chapter 4). Similarly, other ways of automated model adaption could be investigated, for example using model order reduction to simplify Markov models of ion currents. Future work will need to determine if this is a worthwhile investment of resources or if it is more efficient to use Myokit up to a point, and then export the model to a format usable with existing high-performance software.

A different method to scale up simulations is by working towards better *model integration*: instead of simply linking smaller models together, models can be created that contain part of, but not all of, smaller models. In a way, this implies model simplification: deciding which details are absolutely necessary and which can be omitted for a particular simulation. Examples of details that can and have been modeled but may often be omitted include stochastic channel behavior (Heijman et al., 2013), subcellular calcium gradients (Greenstein and Winslow, 2002) and voltage-sensitivity of gap junctions (Gros and Jongsma, 1996). Some models have gone even further, and grouped currents together or omitted them completely (Courtemanche et al., 1990; Fenton and Karma, 1998; Bernus et al., 2002). By omitting detail from the AP, it becomes possible to build models of much larger spatial structures that incorporate new details such as fiber orientation, geometrical structure or communication between sub-models (for example propagation from the AV node to the atrium). For example, Fenton and Karma (1998) found that simplified AP models allowed them to study propagation through 3D anisotropic tissue. The model of the human right atrium by Podziemski and Żebrowski (2013) also uses simplified cell models, but this allows it to include models for both the SA and AV node. Balakrishnan et al. (2015) used simplified

AP models to create a whole-heart model that included the SA node, AV node, bundle of His, Purkinje, atrium and ventricles and that could recreate various arrhythmias. The low computational cost of such models also means they can be used to simulate behavior over longer periods of time, which opens up a road towards modeling long-term processes such as electrical remodeling. At the same time, these models are often (partly) phenomenological, rather than mechanistic, which can make it harder to relate them to experimental data. They also run the risk of missing subtle effects, in situations where the system is highly sensitive to small changes. Nevertheless, if care is taken to avoid these issues, simplified models form an attractive alternative to detailed mechanistic ones.

In Chapter 7, we used AP models connected in a simplified mesh representing the human ventricles to run simulations used in physiology-based regularization (PBR), a novel method for a crucial step in calculating heart-surface potentials from recorded body-surface potential mappings (ECGI). These simulations used detailed AP models and a patient-specific geometry, but also omitted details, notably the atria and conductive system. In addition, we used a simplified geometry with a small number of nodes. However, by comparing it to a more detailed simulation (again, only ventricles, but this time with a 3-dimensional geometry and a much higher number of nodes) we showed that this omission of detail had no consequence for the simulation's use in PBR. In part, this is likely due to the way PBR uses the simulations to generate spatial patterns of activation, which are then used as a basis for reconstructions. This implies that (1) any pattern that can be recreated as a combination of patterns present in the basis does not need to occur in the simulation, and (2) temporal information is mostly lost, so that details of timing in the AP models are not used. Further work is needed to see if simpler methods such as eikonal or graph-based activation models (Wallman et al., 2012) can be used, or if detailed AP models have benefits in more complex situations than studied in Chapter 7.

8.3 Reliability and reproducibility

A vulnerable substrate for an arrhythmia is composed of multiple factors. This presents an opportunity for modelers: making a change to a model's parameters is a straightforward task, while controlling variables experimentally can be costly, difficult, time-consuming, or physically impossible. At the same time, making multiple changes to a model, often based on imperfect or qualitative information about the substrate, presents a risk for the reliability of the results. Firstly, every changed parameter drives the model further from the healthy-cell situation for which it was parametrized. How can we be confident that the predictions of a model are still valid when using it to *extrapolate* outside of its validated range? Secondly, when changing multiple parameters at once, how can we make sure that other features of the model are not inadvertently lost? And if changes *can* be made without invalidating the model, doesn't that suggest the model is underconstrained so that there is a

danger of *overfitting*?[4] Closely related to the issue of reliability, is that of *reproducibility* of modeling and simulation results. For example, do papers provide all the information needed to recreate the described model validation, or to re-run simulation experiments? And will models by different groups provide the same results? If cardiac modeling is to be used for risk-prediction (such as in the studies by Hoefen et al. (2012); Arevalo et al. (2016) and Cummins Lancaster and Sobie (2016)), these questions of *reliability* need to be addressed.

These concerns are shared by the United States Food and Drug Administration, (FDA) which is now investigating the use of *in silico* prediction of drug arrhythmogenicity (in particular model-based prediction of QT prolongation, see Parekh et al., 2015). Their "Cardiac Modeling" research project[5] focuses almost entirely on VVUQ: *verification* (are the simulation methods mathematically correct and accurate?), *validation* (is the model realistic for the situation being investigated?), and *uncertainty quantification* (what is the error in the input and how will it affect the predictions?). The questions raised above mostly concern validation, although methods for dealing with variability are strongly related to those used in uncertainty quantification (see Pathmanathan et al., 2015; Mirams et al., 2016).

The following subsections each discuss an aspect of validating simulation results, and highlight some approaches taken by the cardiac modeling community to tackle the questions raised above.

8.3.1 Multi-model testing and model comparison

One way of assessing the reliability of a simulation result is by repeating the experiment using a different model and comparing the results (see for example Mann et al. (2016) and the editorial by Gong et al. (2017)). If there is a clear overlap between results from different models, this supports the idea that the changes are physiologically realistic, and do not push the models too far from their validated state. Conversely, a lack of any consensus would indicate that this is an area where models react sensitively to change. If some models *do* produce the intended result, careful work would need to be done to find out if this is due to their greater predictive power, due to the data the models were parametrized with[6], or simply due to chance. Additionally, it may be possible to combine the predictions of multiple models into probability estimates, for example to estimate arrhythmogenicity of a particular situation.

The most straightforward way to perform multi-model investigations is to perform all initial experimentation in a single model, establish a test-case, and then double-check by imple-

[4] A saying often quoted in this context, attributed to the physicist John von Neumann, is "With four parameters I can fit an elephant, with five I can make him wiggle his trunk." (Dyson, 2004). This was shown to be true half a century later by Mayer et al. (2010), who cheated slightly by using complex parameters. Perhaps typically, their efforts produce an abstraction that does little justice to elephant physiology.

[5] See http://www.fda.gov/MedicalDevices/ScienceandResearch/ResearchPrograms/ucm477370.htm

[6] In fact, another area where little work has been done is in comparing how well different AP models fit *the same data set*.

menting similar changes in other models. With custom written code, this is an arduous task as it involves the implementation of multiple models, possibly written in different programming languages. But by using tools that can import models from exchange formats such as CellML (Cuellar et al., 2003) this can be done with relative ease. A more extensible way is to use a library of models, all written in a standard form or *annotated* in a manner that allows simulation software to automatically identify and modify model variables. Myokit can be used for both manual and automated model comparison, as is shown in the example in Section 3.3. The most extensive tool for model comparison to date is the 'Cardiac Electrophysiology Web Lab' (Cooper et al., 2015a), which is available at `http://chaste.cs.ox.ac.uk/WebLab`. This tool contains a library of annotated CellML models and a set of experiments (written in a custom experiment description language), and allows users to run each experiment on each model and compare the results. A useful next step would be to standardize the annotations used in the Web Lab, and to set up an interface to let other tools interact with it directly.

8.3.2 Automated validation

A large part of model development consists of validating the model's predictions against several experimental data sets. As this is a labor-intensive process, it would make sense to automate this task. This would also allow automated (re-)validation to be performed after any change to the model (provided the validation experiments and data are publicly available, see Section 8.3.4). With such an approach, the complex changes needed to recreate an arrhythmic substrate could be carried out with greater confidence. Since many of the outputs a model should be validated against are emergent properties (e.g., the APD, APD restitution, conduction velocity), single and multi-cell simulation is a vital part of model-data comparisons.

Automated validation is similar to model comparison, so it would be useful to combine the two tasks. Tools like the aforementioned 'Web Lab' can compare models written in CellML with each other, but as of yet no system has been created that can also incorporate experimental data or multi-cellular simulations. Myokit can provide a partial solution due to its multi-cell capabilities and patch-clamp data import, but a greater effort, both technical and organizational, will be required to deal with this issue in a systematic manner. An overview of the remaining challenges as well as the future perspectives for systematic model-model and model-data comparisons is given by Cooper et al. (2015b).

Once the technical issues have been dealt with, more work is needed to learn how to interpret differences seen in such comparisons. In the light of variability (as well as noise), how different do two model outputs need to be before the models can be said to disagree? Can we update our models to not only match experimental averaged data, but also accurately predict output *ranges*? And can we validate different model outputs independently, or do

relationships between all used outputs need to be considered? Such questions will need to be addressed in order to fully make use of automated model comparison and validation tools and understand the role of variability in modeling of the cardiac cellular AP.

8.3.3 Free parameters and variability

Since their introduction, the number of parameters in models of the cardiac AP has increased steadily: from 5 named and 41 unnamed parameters in Noble (1962) to 222 named and 938 unnamed parameters in Heijman et al. (2011). Not all of these parameters can be measured directly, and as a result many of them are set by inspecting the model's output and tuning the parameters until the output matches the modeler's expectations (either manually, or using the method outlined in Section 8.2.1.1). However, given the size of modern models, it is likely they are still underconstrained. A study by Sarkar and Sobie (2010) addressed this issue directly, and showed how adding more model outputs (i.e., validating against a bigger data set) and applying sensitivity analysis can be used to reduce the number of free parameters in models of the AP. However, since their results regarding the different maximum conductances mirrored those of Marder and Goaillard (2006), the work by Sarkar and Sobie also became a seminal work in the study of variability in models of the cardiac AP (Sarkar et al., 2012; Weiss et al., 2012). If we take biological variability into account, the question arises which parameters can vary because the model is underconstrained (i.e., where we don't have enough data) and which can vary because this accurately reflects the underlying biology. This is a question that can only be answered with more quantitative experimental data on variability in the processes underlying the cardiac AP, such as provided in Chapter 5. Gathering such knowledge is critical if we want to be able to compare different models (e.g., to know when a model can be rejected). Cherry and Fenton (2007) ran simulations using two different models of the canine AP and found several differences. They too argued that this showed the need to validate against multiple outputs, but also suggested detail in models should be reduced when such validation data is unavailable. A recent overview of the issues with parameter tuning in models of the cardiac AP, and the challenges of variability and personalization, was given by Krogh-Madsen et al. (2016).

8.3.4 Data sharing and reporting standards

Sharing of models, methods, simulation details and experimental data is required for model validation and simulation experiment reproducibility. Model code is frequently shared online, and projects such as CellML (Cuellar et al., 2003) and the Physiome model repository (Yu et al., 2011) have been set up to standardize and promote this procedure. Sharing of methods is also common, with projects such as OpenCOR (Garny and Hunter, 2015), Chaste (Mirams et al., 2013) and Myokit all freely available online. However, to re-validate a model after downloading and making changes, users will also need access to the original (experimental) validation data and the simulation experiment code needed to (computationally) reproduce

it.

Projects such as MIASE (Waltemath et al., 2011a) and SED-ML (Waltemath et al., 2011b) have been set up to promote and standardize sharing of simulation code and improve reproducibility of biophysical simulation experiments. However, at the time of writing tools implementing SED-ML are scarce (with the notable exception of OpenCOR), and the language does not yet have the features required to describe realistic, complex computational-electrophysiology experiments (Cooper et al., 2015a). In this respect, tools like Myokit, which are intermediate between custom, free-form code and a fully standards-based approach, can perform a valuable transitional function.

For experimental data, the MICEE draft standard and website exist to aid in reporting (Quinn et al., 2011, see also `http://micee.org`), but a major effort for online sharing of electrophysiological data has yet to be made, and obtaining the data to (re)validate a model is a challenging task. In part, this is because the amount of data needed to create an AP model is so large, it almost inevitably contains data from multiple experiments from independent labs. The issue is further complicated by the fact that large parts of models are often 'inherited' from older ones, which complicates determining the full data set needed for validation (Niederer et al., 2009; Bueno-Orovio et al., 2014).[7] In addition, existing formats will need to be updated to incorporate the possibility of natural variability in models and experimental data, as well as relationships between the variability in different parameters (see Chapter 5). Nevertheless, to create reliable predictions, both the infrastructure and the willingness to share and compare experimental data and simulation results still need to be generated in the upcoming years.

8.4 Variability in multi-scale models of the AP

Conventional AP models are based on averaged data. For example, when creating a model of an ionic current an experimenter may record it in a number of cells, determine some physiological parameters (for example time constants and midpoints of activation) in each of them, and then calculate the average value of each parameter and pass it to a modeler. This is a valid approach if all variability in the parameters is due to measurement error. However, given the findings of Marder and Goaillard (2006) and the results presented in Chapter 5, it is clear this approach misses a great deal of the biological complexity of real myocytes by replacing a diverse population with a single, idealized, cell. Furthermore, it is not at all guaranteed that using the mean for each parameter will result in a physiologically viable model. Instead, a future challenge for AP models will be to (1) obtain measurements of the natural

[7] This complicated heritage, combined with the experimental difficulty and cost of obtaining data, has led to the situation where models include data gathered in different species, in different cell types, and using different procedures. Besides complicating the practicality of gathering and incorporating all the relevant data, this has a negative effect on the *applicability* of the resulting validation.

variability in all relevant parameters, (2) where possible, to record any relationships between the parameters (for example the relationship between midpoint of activation and inactivation seen in Chapter 5), (3) to update reporting standards and model languages to include variability and parameter interdependencies, (4) to further develop simulation methods that incorporate variability, and (5) to interpret what the existence of such variability means for the use and development of multi-scale models. These challenges are not independent. For example, deciding where to start measuring variability requires some estimate of where variability is most likely to be found and where it will have the most prominent effects on the AP or AP propagation. Despite these challenges, work in simulating variability has already shown promising results. For example, including hypothesized variability in conductance levels can predict variability in drug-induced APD prolongation (Britton et al., 2013) and improves predictions for the risk of drug-induced Torsades de Pointes (Cummins Lancaster and Sobie, 2016). We briefly discuss the challenges of measuring and simulating variability below.

8.4.1 Measuring variability

Most work on variability in AP model parameters so far has focused on variability in the expression levels of ion channel alpha-subunit genes, which correlates strongly with ion current maximum conductance. This type of variability can be measured by collecting several cells and measuring expression levels using techniques such as PCR. An advantage of PCR is that it can measure the transcription levels of multiple channel proteins in a single cell, allowing the relationship between them to be studied. As Schulz et al. (2006) showed, it is also possible to combine PCR and voltage-clamping to study channel expression levels and current characteristics in the same cell. An advantage of studying variability in maximum conductances is that the number of variables to consider is limited by the number of currents, and so is in the order of 10-20.

In Chapter 5 we investigated measuring variability in the *kinetical parameters* of an ion current (I_{Na}). We found this required careful consideration of (1) noise and artefacts in the recorded currents, (2) imperfect control of the membrane potential, (3) the methods used to analyze the recordings. Taking these three factors into account, we performed measurements of the time constants of inactivation in I_{Na} and found they varied considerably, with what appears to be a skewed distribution. Importantly, kinetics of fast and slow inactivation were not independent, but showed a moderate linear correlation. Another study by Pathmanathan et al. (2015) investigated the steady states (i.e., midpoints and slopes of (in)activation) of I_{Na}, and found these too varied between cells. Their study used existing data, and focused mainly on the mathematical aspects of quantifying variability instead of investigating the experimental side. Interestingly, they studied the same problem using two different data sets from the same laboratory, and discovered that the variability *between* the data sets exceeded that within the data sets, which matches with our observations about

the midpoints of (in)activation in Chapter 5. Our own literature review data of midpoints of activation and inactivation is consistent with the above results, but also shows a strong linear correlation between the midpoints of activation and inactivation.

To the best of our knowledge, this work provided the first direct investigation of variability in ion current model parameters. An important conclusion for AP model development is that parameters do not vary independently, but are correlated. This means studies using cell-to-cell variance cannot sample all parameters from independent probability distributions but should take care to incorporate parameter covariance. Similar studies for the other major currents are needed, preferably with very large numbers of cells, to gather the data needed to work towards variability-aware modeling.

8.4.2 Modeling and simulating variability

Incorporating (known or hypothesized) variability into models of the AP presents several challenges. First, model definition languages (such as CellML and Myokit's `mmt` format) need to be updated to allow parameter variability to be specified. Unofficial CellML extensions to allow this have already been proposed and used (Walmsley et al., 2013), but may need to be extended to allow parameter dependencies to be included. Next, simulation methods will need to be updated to allow the incorporation of variability. One way to do this is to simply re-run simulations many times with different parameter values, drawn from the appropriate distributions (Romero et al., 2009; Walmsley et al., 2013). Linear regression-analysis has been proposed as a way of interpreting the results, by quantifying the impact of each varied parameter on the simulation results (Sarkar and Sobie, 2010, 2011). To deal with the exponentially growing number of possible models when varying multiple parameters, a technique known as *Latin hypercube sampling* has been used (McKay et al., 1979; Britton et al., 2013). The required number of simulations can be reduced even further by training *Gaussian process emulators* to the output of simulations (Chang et al., 2015; Johnstone et al., 2016). These also provide a way of investigating the model's sensitivity to different parameters. An interesting extra step when working with populations of models, is to *calibrate* the population by accepting or rejecting models based on higher-level characteristics, such as the shape of the AP (Britton et al., 2013; Muszkiewicz et al., 2016). This method allows variability to be used in simulations even when the true underlying parameter distributions are not known. A good overview of methods to incorporate variability into cardiac AP models can be found in Walmsley (2013).

8.4.3 Personalized modeling

A different way of dealing with variability is by *personalizing* models. For example, whole-heart (or more commonly whole-ventricle) simulations, often already use patient-specific geometries (Aguado-Sierra et al., 2011; McDowell et al., 2012; Arevalo et al., 2016) and this

approach was also used in Chapter 7. However, electrophysiological properties can also be personalized using either knowledge of disease-induced changes (Reumann et al., 2009) or direct measurements of clinical data (Lombardo et al., 2016; Mann et al., 2016). Again, knowledge of variability in AP model parameters will be highly valuable here, as it can indicate where variability is expected and measurements need to be done. However, while modern techniques such as hiPSC may enable a wealth of data about individual patients to be obtained, the large number of parameters in multi-scale AP models suggests that a combined approach of personalization and variability-including modeling may be the most appropriate tool for patient-specific investigations.

8.5 Conclusion

Multi-scale models are used to integrate experimental data from different sources and help us gain a deeper understanding of cardiac electrophysiology. Simulation is an important part of this systems approach to biology, as it enables the study of phenomena that emergene from the interaction of biological processes at the different scales. Models of the cellular AP form the back-bone of these simulations. They are created by combining models of the ions, channels, and transporters they contain, and cell models in turn can be combined into tissue models. Exploring smaller and larger scales is limited by computational power, but good results can be obtained by carefully chosen trade-offs between detail and simplicity. As the substrate to develop an arrhythmia is typically complex, recreating substrates requires making several changes to models of the healthy cell. The issues this creates for the reliability of multi-scale models can be partially addressed by software tools for multi-model testing and automated validation. However, major data-sharing (and simulation sharing) efforts are required to make validation of models a routine activity for model users as well as developers. Incorporating biological variability into multi-scale models is challenging computationally, but the recognition of biological variability also raises new questions about how to interpret model comparisons and validation. In addition, much new experimental work is needed to characterize the variability in the electrophysiological properties of cardiomyocytes. Many of these issues are interrelated, for example the recognition of widespread biological variability has a profound impact on genotype-phenotype relations, model validation and development and will impact the way experimental results are reported. Conversely, investigations into variability rely on excellent experimental work, as well as theoretical work into parameter estimation, identifiability, stochastic simulation and constraining of free model parameters. As a result, computational tools can play a major part in the ongoing study of cardiac arrhythmia, not just through the development of new state-of-the-art technologies, but also through standardization and sharing of existing work. Indeed, sharing is a key point for the future, as none of the abovementioned problems can be tackled in isolation. Instead, future theoretical and experimental work should continue the fruitful interplay of model

and experiment, and proceed in a manner strongly informed by the complexities of cardiac electrophysiology.

APPENDIX A

Summary

The rhythm of the heart is regulated by processes at the genetic, molecular, cell, tissue, and organism scales. Computational models of the cardiac cellular action potential (AP) can be used as the basis for multi-scale models that connect these scales. This has made them essential tools in the study of cardiac arrhythmias. Far from existing in theoretical isolation, these models are widely used to interpret experimental data, design new experiments and make predictions about the results. Indeed, the complex and multi-faceted nature of arrhythmogenesis requires an ever-increasing level of cooperation between modelers and experimenters and the integration of knowledge from several fields in a *systems approach* to physiology. In this thesis, we show how software tools can aid in this process, we use simulations with AP models to connect processes at different scales, and we investigate the complexity seen even at the level of ionic currents.

In **Chapter 1**, the topic of this thesis is briefly introduced and an overview of the various chapters is given. **Chapter 2** then introduces the physiology and modeling of ion currents, the cellular AP, and electrical propagation from cell to cell.

Chapter 3 describes *Myokit*, our novel tool for AP model development, multi-scale simulation, and analysis. Myokit's ease of use and straightforward modeling language facilitate model sharing and re-use, while its graphical user interface and extensive toolbox allow simulation and analysis methods to be shared with a wide audience. Import and export facilities allow model exchange with various formats, and methods to import patch-clamp data and export patch-clamp protocols are provided. Fast single-cell simulation is implemented using CVODE, and a versatile multi-cell engine is provided that can run on the GPU using OpenCL. In addition, Myokit contains advanced simulation engines that can calculate partial derivatives, evaluate system stability or run fast simulations with Markov models. Three examples are provided that illustrate Myokit's use in single and multi-cellular investigations of Brugada syndrome, its use in model comparison, and its capabilities for fitting ion-channel models to patch-clamp data.

Chapter 4 examines the prospect of speeding-up simulations by replacing slow-to-evaluate mathematical expressions with less computationally expensive ones, and for this we focus on *splines*. We find spline approximations can be used to speed up equations commonly found in AP models, but that the relative number of such equations is lower for the larger published models. In addition, we find that GPU-parallelized simulations, which are increasingly used for large multi-cellular work, do not benefit from the technique. So while the principle of the method appears sound, its applicability to AP simulations is limited and other fields may benefit more from this technique.

Chapter 5 examines *variability* in the kinetics of the fast sodium current I_{Na}using CHO cells expressing human *SCN5A*. We show that a simple voltage-step experiment, performed under controlled conditions, elicits a current response that varies in shape and size from cell to cell. The time constants of inactivation vary with a skewed distribution, and a moderate linear correlation between the two constants can be seen. Through a careful analysis of our experimental setup we show that this variability is larger than expected from experimental error alone. By comparing the calculated standard deviations with those seen in myocyte experiments we show that in this case CHO cells are a good match for human myocytes. Next, we perform a literature review and see that the midpoints of activation and inactivation show a similar wide spread in all reported experiments and that there exists a strong linear correlation between midpoint of activation and midpoint of inactivation. Finally, we show how the observed variability can affect the cellular AP, and argue it should be reported as a feature of the ionic currents rather than a weakness of the experiments.

Chapter 6 contains an extensive review of published nonsynonymous missense mutations in *SCN5A*and their effect on I_{Na}. Using this data, we investigate if *machine-learning* techniques can be used to predict mutation-induced changes in I_{Na}. We find that 610 out of 11923 (5.1%) of possible missense mutations have been studied, and that in many cases the location of mutations on the gene correlates with a specific change in function. However, the effects of the amino acid substitutions do not show any immediately useful patterns. Using machine learning techniques on this data set, we can create better-than-chance predictions of an *SCN5A* mutation's effects, but the general accuracy is low (around 70%). By carefully examining the results we show that this is mainly due to a strong bias in the dataset, combined with inconsistencies and a lack of suitable *features* to describe mutations in a meaningful manner.

Chapter 7 investigates the use of AP models in reconstructing heart-surface potentials from noninvasive measurements of body-surface potentials in a technique we call *physiology-based regularization* (PBR). We use AP models to simulate wave propagation over the heart and then perform singular-value decomposition to create a small set of base patterns from which the more complicated patterns can be constructed. By restricting the heart-surface potential patterns to ones composed from this basis, more accurate reconstructions can be

made. We show that our method recovers more details of heart-surface electrograms than traditional regularization methods, obtains higher correlation coefficients with invasively measured signals, and leads to improved estimates of recovery times. By using different models and simulation methods, we show that adding *temporal* detail to the used AP models does not improve the results, and that simplified propagation models are adequate for this purpose.

Finally, **Chapter 8** discusses the use of multi-scale models to link ion-channel function to arrhythmogenesis and body-level observations, in a systems approach to electrophysiology. We argue that the complex relationship between molecular-level effects and diseases requires simulation, so that the development of tools like Myokit is a worthwhile investment for years to come. At the same time, the multifactorial nature of arrhythmogenesis implies that modelers will necessarily push models far from the situations for which they were created, which increases the scope for errors. We discuss the role of model comparison, automated validation, and data sharing in addressing this problem. The existence of natural variability increases these difficulties, and changes the way comparisons of models to other models or experimental data should be interpreted. Yet it also has the potential to explain observed differences in drug-response or the clinical manifestation of ion-channel mutations, so that a deeper understanding of variability is vital for future investigations. We conclude that problems in cardiac cellular electrophysiology can best be tackled with a combined experimental/theoretical approach.

APPENDIX B

Valorization

Since 2013, Maastricht University requires its doctoral theses to come equipped with a "Valorization Addendum", with the intended goal of increasing the "visibility and societal impact" of its research. Among the examples of such "value creation" are open source tools, software and the process of "making models and systems available" (Maastricht University Board of Deans, 2013). This chapter is submitted to comply with this requirement.

Computational models of the cardiac action potential (AP) can form the basis of *multi-scale models* of cardiac physiology and pathophysiology (Southern et al., 2008). In the past decades, several studies have shown how such models can be modified to include the molecular changes caused by genetic defects or drugs, so that their effects on the cell, tissue, and organ levels can be predicted (Chapter 8). The mechanistic insights and predictive power these models provide is badly needed, as the link between such molecular changes and arrhythmias is complex and still incompletely understood (Weiss et al., 2015).

Setting up multi-scale simulations can be a time consuming process and, even for cutting-edge science, often involves reimplementing existing techniques. Having *re-usable*, model-independent software tools can save time and effort, can make numerical methods available to a wide audience, and can help to shift the focus of the experimenter from computational aspects to biology. Chapter 3 of this thesis introduced *Myokit*, a tool for (multi-scale) modeling of the cardiac AP. Myokit contains methods to create models of ionic currents (possibly altered by drugs or mutations), to integrate them into models of the cellular AP, and to use them in simulations of cardiac tissue. In addition, Myokit has support for model import and export, removing the need for manual model (re-)implementation. Chapters 3, 5, and 7 contain examples of Myokit's scientific use.

In this valorization addendum, we highlight examples of non-academic use of AP-model based simulations. We then discuss how we have made Myokit, our tool for such work, available to the community. Finally, we look at the first, promising, signs of early adoption of Myokit outside of Maastricht University.

AP-models have applications beyond academia

Simulations of the cardiac cellular AP have a long history in science, where they have been used to investigate the basic principles of cardiac electrophysiology (see Chapter 2 and Chapter 8). Sharing and promoting Myokit among an academic audience has an impact on society, as it has the potential to accelerate scientific work via the sharing of methods (included in Myokit) and models (using Myokit's support for exchange languages such as CellML, see Hedley et al., 2001). This type of knowledge dissemination is discussed in detail in the introduction to Chapter 3. Outside of science, the predictive power of AP-model based simulation is increasingly being recognized. The examples listed below show how simulations can be used in risk stratification (clinical use), drug development (industrial use), and regulation (governmental use).

Hoefen et al. (2012) showed that simulations of transmural repolarization prolongation can be used to distinguish low-risk and high-risk mutations in *LQT1-syndrome* with increased specificity and sensitivity. This provides a direct use of simulation in the optimization of clinical treatment. Similar transmural simulations were used as the first example in Chapter 3. Risk of inducing *torsades de points* is a common reason to reject drugs during development. Cummins Lancaster and Sobie (2016) simulated the effect of several drugs on the human cellular AP, and found that this provided more reliable predictions of their arrhythmogenicity than existing *in vitro* assays. To increase the reliability of their predictions, they repeated their simulations in multiple models of the AP, much like in the third example shown in Chapter 3. The increasing interest of regulatory bodies to use mechanistic cardiac modeling in drug safety testing is discussed in depth in a review by Davies et al. (2016). While Myokit is aimed primarily at scientific users, it could easily be used outside of academia in pilot projects, exploratory studies, prototyping, or as the inspiration for specialized commercial software.

Myokit is available to the community

Since the start of its development, Myokit has been made available online. This has allowed scientists outside of Maastricht to use it, has generated valuable feedback for its development, and has promoted the visibility of multi-disciplinary biomedical research at Maastricht University.

We have taken care to provide adequate documentation to enable external use. A PDF version of Myokit's documentation currently runs to 277 pages (although the same information is more easily accessed via the Myokit website). In addition, the Myokit website contains several examples of its use and further examples were provided with our recent publication about the tool (Clerx et al., 2016). In 2014, we organized a workshop to introduce Myokit to scientific users, which attracted more than 30 international participants.

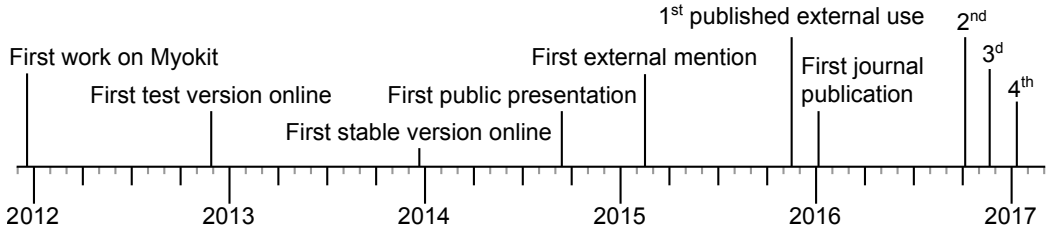

Figure B.1: Myokit development, publications and early adoption. Recent events include its first public presentation (Clerx et al., 2014), the first time Myokit was mentioned in a peer-reviewed article by an external group (Garny and Hunter, 2015), the first time it was *used* in a peer-reviewed article by an external group, (Law and Levin, 2015) and publication of the article that formed the base of Chapter 3 (Clerx et al., 2016).

Myokit is fully open-source and can be downloaded and used free-of-charge under the GNU General Public License (GPL, see also http://myokit.org). In addition, Myokit itself is based entirely on open-source components such as Python, NumPy/SciPy (Jones et al., 2001), Matplotlib (Hunter, 2007) and Sundials (Hindmarsh et al., 2005). Combined with an operating system such as GNU/Linux, this creates an entirely open-source environment, available free of charge. In addition, Myokit can be run on Windows or OS/X (Apple).

Myokit is already being used outside of Maastricht

Myokit development started in December 2011 and it was first presented publicly in September 2014. The first peer-reviewed article discussing it in detail was published in January 2016. A brief timeline of its development and publication is provided in Fig. B.1 and an extended version can be found on the Myokit website (http://myokit.org/changelog). Given the time it takes to adopt a new work flow, perform research, and have it published, it will take some time before Myokit's success in the (scientific) community can be assessed. Some preliminary data is presented below. First, Myokit has been downloaded over 600 times as of July 2016. But while some effort[1] has been made to filter real users from automated downloads, this may not be an accurate statistic. Secondly, a mailing list was started in January 2016 where users can receive updates and ask questions about Myokit, so far this has 15 subscribed users (which is similar to older, more established tools like OpenCOR). Another measure of Myokit's visibility came in 2016, when its principal developer was elected for a three-year term on the CellML editorial board[2]. However, the best feedback has come in the form of personal communication and citations. Based on such feedback, we know of at least three instances where Myokit has been used for teaching outside of Maastricht (at both Bachelor and Master level, see http://myokit.org/publications). The first study (by scientists other than the Myokit developers) using Myokit for simulations came in 2015,

[1] Filtering was applied by excluding any IP address with 20 or more downloads, excluding any downloads with a 'user-agent' indicating an automated search rather than a human user and by requesting that search engines do not download the tracked files.

[2] See https://www.cellml.org/about/news/cellml-editor-election-results-2016

Figure B.2: The blue dots show locations where papers were published using Myokit. Green dots indicate known Myokit users. Red dots indicate mentions of Myokit in papers about related software, while yellow dots indicate universities where Myokit was used for teaching. Finally, the grey dot indicates Maastricht, where Myokit was developed.

just before the first journal article describing Myokit was published (Law and Levin, 2015). Three further publications, including two in high-ranking journals, emerged in 2016 and early 2017 (Park et al., 2016; Boukhabza et al., 2016; Schmidt et al., 2017). Three more publications refer to Myokit when comparing electrophysiology software, which further adds to the visibility of Maastricht University in this field (Garny and Hunter, 2015; Castro et al., 2016; Onal et al., 2016). Fig. B.2 shows the geographic locations of known early Myokit usage and citations.

Conclusion

Multi-scale simulations based on models of the cardiac cellular AP are increasingly being used outside of academia. We have developed Myokit, a tool for such simulations and made it available online with a permissive license and extensive documentation. This has resulted in early adoption and helped (1) to disseminate research done at Maastricht University to a wider community and (2) to increase the world-wide visibility of Maastricht University's computational electrophysiological research.

APPENDIX C

Acknowledgments

Doing research has been an interesting, fun, and rewarding experience. The final product of these last five years, this thesis, contains ideas and textual input from so many people that I sometimes feel more like an editor than an author. Having said that, I want to thank my supervisory team for giving me an incredible amount of freedom, without which a stubborn person like me probably couldn't have done this.

Pieter, thank you for guiding me from the start of a master's project to the end of a PhD.[1] Over the years, my focus shifted from computation to physiology, but I think together we found a lot of overlap. None of the mathematical work in my thesis (or Myokit) would have been possible without you, but much more important than that, you were always the first to recognise the days when I just needed someone to say "Well done". Thank you! **Paul**, bedankt voor je kritisch inzicht, je steun en vertrouwen (ook naar buiten toe), en voor je niet-aflatende sturing naar de fysiologisch relevante kant. Vooral ook bedankt voor je geduld om buitenstaanders zoals mij te laten leren, en voor je inspanningen om van een multidiscplinaire groep een hecht team te vormen. Ik hoop dat ik dit in de toekomst weer door kan geven. **Ralf**, bedankt voor je rust en je inzicht, waarmee je niet alleen wetenschappelijk werk maar ook menige vergadering hebt gered. Ik heb me altijd thuis gevoeld bij DKE (de laatste tien jaar!), en dat ligt voor een groot deel aan jou en Ronald. Ik ben ondertussen ook begonnen aan het boek van Dirk Struik. Bedankt! **Enno**, mijn onofficiële begeleider, bedankt voor alle goede ideeën, voor alle gezellige avonden en voor de inspiratie om groot te denken. De tijd en de moeite die je geïnvesteerd hebt om Myokit te promoten blijft nog steeds nieuwe verassingen opleveren. **Ronald**, ontzettend bedankt dat je mij aan Pieter en Paul hebt voorgesteld en het hele proces in gang hebt gezet. Ook je advies in die eerste dagen waardeer ik nog steeds enorm. **Jordi**, bedankt voor al je hulp aan het begin en het eind van mijn thesis (als een soort inverse Enno!). Ik hoop dat we onze goede samenwerking nog lang kunnen doorzetten!

And a very special thanks to all **the members of the assessment committee and corona**. Thank you all for being part of this special day.

[1] And thank you **Steven** for enduring six years of our conversations!

Choosing paranymphs was one of my favourite pastimes during the early phases of my project, with the choices ranging from various celebrities to Ronald and Paul (nothing in the rules says you can't). After approaching the problem from many different angles, I realised the question was who I'd most like to ask for help, and so I've asked the two people who've helped me the most. **Matthijs** & **John**, choosing you was not very funny but I'll never regret it. Thanks!

Special thanks to everyone at CARIM, and 'Team Volders' in particular. **Roel** won the university-wide employee of the year award while I worked in his[2] lab. In addition to the many qualities that were listed by the awarding committee, I would like to mention his ability to stay perfectly calm while a novice experimenter rips out every cable in the lab and covers the furniture in tin-foil. Bedankt Roel! Thanks **Sandrine** for the cells, the photographs and the vlaai! **Beatrice**, **Cristina**, **Cristina**, **Henk**, **Pieter**, **Rachel**, **Annerie**, **Bart**, **Chiara**, **Dan**, **Gabriele**, **Henry**, **Lucien**, **Mylène**, and honorary members **Antonio** and **Gudrun**, thanks for all the help and the good times! Thanks **Miren** for teaching me the basics of patch-clamping and how to hold a pipette! Bedankt **Helma** voor de prettige samenwerking. **Monique**, bedankt voor alle fijne gesprekken en al je hulp en kennis, wat mij betreft ben jij de onderdirecteur van de UM en absoluut geen 'meubilair'! **Ajay**, thanks for all the great conversations, for your optimistic cookery tips, and for all the fun!

Thanks to all the people at DKE, and the members of the BMI group in particular. **Pietro**, thanks for all the coffee breaks and your insights into life, science, and how to enjoy both at the same time. Thanks **Evgueni** for all the help with machine-learning. If I ever do another PhD... Thanks **Joel** and **Stef**, for being part of Team CINC, I had a great time! **Markos**, thanks for all the insightful conversations, I love your hardcore physics approach to physiology and hope we can collaborate on it in the future! Thanks also to **Nasser**, **Firat**, **Maryam**, **Rachel**, **Zita** and all the others at BMI, Systems Biology, at the Swarm lab, and at DKE!

Besides the occasional triumph of doing something that works, the best part of science to me has been the conferences, where you meet new people who then quickly become old friends. Bedankt **Nele** voor alle gesprekken binnen en buiten werk. Ik geniet er elke keer van! Bedankt ook **Ronald Wilders** en **Antoni van Ginneken** voor de leuke tijd op conferenties en de ontzettend leerzame middag in jullie lab. Special thanks to **Gary Mirams**, **Jonathan Cooper**, **Alan Garny**, **Eugene Chang**, **Anna Muszkiewicz** and all the other brilliant people I met in the first part of my career!

Heel erg bedankt ook **Tom**, en alle **vrienden en collega's** bij Floraccess!

Of course I'd like to thank all my friends in Maastricht and beyond for all the support and fun! **Daan**, bedankt voor alle biertjes, goeie gesprekken en jazz met **Hendrik**, **Antoine** en

[2]Sorry Paul.

de forum club. Thanks **Masa** for all the games, bedankt **Jan** voor alle lessen, and thanks (Mr) **Gary** for all the fun throughout the years! **Lauren**, you're pretty Skye for a white guy[3]. **Rens** en **Elke** en **Linus** bedankt voor alles! Bedankt voor alle hulp! **René** and **Sandra**, I love you both. **Koen**, **Matthijs** en **Sergio**, **Linda**, **Eva** en **Susan** (maar ook MWM2! **Eefje**, **Thijmen**, **Pelle**, **Lieke**, **Quinten** en **Tim**) ik heb nu al zin in de komende repetities. En **Saskia** bedankt voor alles door de jaren heen!

Jennifer, you came home from priceless old masters, Dalí, and Warhol, only to hear me blether about patch-clamping and derivative-free optimization. I can only apologise. Thank you so much for putting up with me and my erratic work habits, for being incredibly supportive, and for being the love of my life. I look forward to spending the rest of our days together.

Dan nog bedankt aan iedereen in mijn enorme familie in Nederland, my family in Ireland, and now even my family in Scotland! Thanks **Debbie**, **Julie**, **Joseph**, **Christine** and **Steve** for the fun times in Glasgow and beyond.

Finally, **Connor**, **Ciara**, **Mam** and **Dad**. I've tried really hard to write something here but, well, I hope you already know.
Thanks.

[3] I can't believe I'm printing that.

APPENDIX D

Curriculum vitae and publications

Michael Clerx was born in Roermond, on May 26th 1983, to a Dutch father and an Irish mother. In 2002 he began studying Applied Physics at Eindhoven University of Technology but quickly switched to Mechanical Engineering, hoping they'd let him use a hammer. After several years of equations, side jobs, playing in bands and running his own web-development business, he moved to Maastricht where he obtained a BSc in Knowledge Engineering from Maastricht Engineering in 2009, followed by an MSc in Artificial Intelligence (cum laude) in 2011. In November 2011 he began working on an interdisciplinary PhD-project at Maastricht University, working for the Department of Data Science and Knowledge Engineering (DKE) and the CARIM School for Cardiovascular Diseases.

Peer-reviewed publications

1. Michael Clerx, Pieter Collins, Enno de Lange and Paul G.A. Volders (2016). *Myokit: A simple interface to cardiac cellular electrophysiology.* Progress in Biophysics and Molecular Biology. Volume 120, issues 1–3, pages 100–114.
2. Matthijs J.M. Cluitmans*, Michael Clerx*, Nele Vandersickel, Ralf L.M. Peeters, Paul G.A. Volders, Ronald L. Westra (2016). *Physiology-based Regularization of the Electrocardiographic Inverse Problem.* Medical & Biological Engineering & Computing.
3. Michael Clerx, Roel L.H.M.G. Spätjens, Cristina Altrocchi, Sandrine R.M. Seyen, Pieter Collins, Enno de Lange, Ralf L.M. Peeters, Paul G.A. Volders (2016). *Variability in the dynamical properties of human cardiac I_{Na}.* Manuscript in preparation.
4. Michael Clerx, Pieter Collins (2014). *Reducing run-times of excitable cell models by replacing computationally expensive functions with splines.* Mathematical Theory of Networks and Systems, Groningen 2014. Volume 21, pages 84–89.

   *The first two authors contributed equally to this publication.

Conference proceedings

1. Michael Clerx, Pieter Collins, Paul G.A. Volders (2015). *Applying novel identification protocols to Markov models of I_{Na}.* Computing in Cardiology, Nice 2015. Volume 42, pages 889–892.
2. Michael Clerx, Paul G.A. Volders and Pieter Collins (2014). *Myokit: A Framework for Computational Cellular Electrophysiology.* Computing in Cardiology, Boston 2014. Volume 41, pages 229–232.

Abstracts

1. Michael Clerx, Roel L.H.M.G. Spätjens, Cristina Altrocchi, Sandrine R.M. Seyen, Pieter Collins, Enno de Lange, Ralf L.M. Peeters, Paul G.A. Volders. *Variability in the kinetics of cardiac I_{Na}.*
   Plenary presentation, Travel award winner, 40th Official Meeting of the European Working Group on Cardiac Cellular Electrophysiology, Glasgow, September 2-4 2016.
2. Michael Clerx. *Myokit: A Toolkit for Computational Cellular Electrophysiology*
   Oral presentation, Winner of the 'Application Showcase', byteMAL: Bioinformatics for Young inTernational researcher Expo, Maastricht, March 9th 2016.
3. Michael Clerx. *Multi-scale computational approaches to cardiac arrhythmia.*
   Oral presentation, Second International Exploratory Workshop Computational Tools to Investigate Genetic Channelopathies. Beatenberg, January 10-12 2016.
4. Michael Clerx, Pieter Collins, Paul G.A. Volders. *Quantification of I_{Na} Variability.*
   Poster presentation, 39th Official Meeting of the European Working Group on Cardiac Cellular Electrophysiology, Milan, June 21-22 2015.
5. Michael Clerx , Błażej Chmielarz, Enno de Lange. *Good enough solutions in Markov models: Bad news for modeling?*
   Poster presentation, 38th Official Meeting of the European Working Group on Cardiac Cellular Electrophysiology, Maastricht, September 20-22 2014.
6. Michael Clerx, Ronald L. Westra, Paul G.A. Volders. *From Genotype to Cellular Phenotype: A Markov Model of SCN5A offers insights into understanding channelopathies.*
   Poster presentation, 38th Official Meeting of the European Working Group on Cardiac Cellular Electrophysiology, Maastricht, September 20-22 2014.
7. Michael Clerx, Ronald L. Westra, Paul G.A. Volders. *Validation of Sodium channel models through simulated experiment.*
   Poster presentation, PhD-training courses, Dutch Heart Foundation, Arnhem, September 30 - October 4th 2013.

Other scientific activities

1. Elected onto the CellML Editorial Board for the term 2016-2019, and co-authored the first CellML 2.0 draft specification in 2017.
2. Developed the open-source tool *Myokit*, now used by several teams internationally. Efforts to promote Myokit use include a website (`http://myokit.org`), extensive documentation (`http://docs.myokit.org`), and the organization of a workshop "In-Silico Cellular Electrophysiology with Myokit" in 2014, with over 30 international attendees.

Awards

1. Awarded a travel grant (for one of the ten best abstracts) to attend and present at the 40th Official Meeting of the European Working Group on Cardiac Cellular Electrophysiology, Glasgow, September 2-4 2016.
2. Winner of the Application Showcase at byteMAL: Bioinformatics for Young International Researchers Expo, Maastricht, March 9th.

References

Abe, K., Machida, T., Sumitomo, N., Yamamoto, H., Ohkubo, K., Watanabe, I., Makiyama, T., Fukae, S., Kohno, M., Harrell, D.T., et al., 2014. Sodium channelopathy underlying familial sick sinus syndrome with early onset and predominantly male characteristics. Circulation: Arrhythmia and Electrophysiology 7, 511–517.

Abriel, H., Cabo, C., Wehrens, X.H., Rivolta, I., Motoike, H.K., Memmi, M., Napolitano, C., Priori, S.G., Kass, R.S., 2001. Novel arrhythmogenic mechanism revealed by a long-QT syndrome mutation in the cardiac Na+ channel. Circulation Research 88, 740–745.

Abriel, H., De Lange, E., Kucera, J.P., Loussouarn, G., Tarek, M., 2013. Computational tools to investigate genetic cardiac channelopathies. Frontiers in Physiology 4, 390.

Abriel, H., Wehrens, X., Benhorin, J., Kerem, B., Kass, R., 2000. Molecular pharmacology of the sodium channel mutation D1790G linked to the long-QT syndrome. Circulation 102, 921–925.

Ackerman, M.J., Splawski, I., Makielski, J.C., Tester, D.J., Will, M.L., Timothy, K.W., Keating, M.T., Jones, G., Chadha, M., Burrow, C.R., et al., 2004. Spectrum and prevalence of cardiac sodium channel variants among black, white, Asian, and Hispanic individuals: implications for arrhythmogenic susceptibility and Brugada/long QT syndrome genetic testing. Heart Rhythm 1, 600–607.

Aguado-Sierra, J., Krishnamurthy, A., Villongco, C., Chuang, J., Howard, E., Gonzales, M.J., Omens, J., Krummen, D.E., Narayan, S., Kerckhoffs, R.C., et al., 2011. Patient-specific modeling of dyssynchronous heart failure: a case study. Progress in Biophysics and Molecular Biology 107, 147–155.

Aha, D.W., Kibler, D., Albert, M.K., 1991. Instance-based learning algorithms. Machine Learning 6, 37–66.

Aiba, T., Farinelli, F., Kostecki, G., Hesketh, G.G., Edwards, D., Biswas, S., Tung, L., Tomaselli, G.F., 2014. A mutation causing Brugada syndrome identifies a mechanism for altered autonomic and oxidant regulation of cardiac sodium currents. Circulation: Cardiovascular Genetics 7, 249–256.

Akai, J., Makita, N., Sakurada, H., Shirai, N., Ueda, K., Kitabatake, A., Nakazawa, K., Kimura, A., Hiraoka, M., 2000. A novel SCN5A mutation associated with idiopathic ventricular fibrillation without typical ECG findings of Brugada syndrome. FEBS Letters 479, 29–34.

Albert, C.M., Nam, E.G., Rimm, E.B., Jin, H.W., Hajjar, R.J., Hunter, D.J., MacRae, C.A., Ellinor, P.T., 2008. Cardiac sodium channel gene variants and sudden cardiac death in women. Circulation 117, 16–23.

Amarouch, M.Y., Abriel, H., 2015. Cellular hyper-excitability caused by mutations that alter the

activation process of voltage-gated sodium channels. Frontiers in Physiology 6.

Amin, A., Verkerk, A., Bhuiyan, Z., Wilde, A., Tan, H., 2005. Novel Brugada syndrome-causing mutation in ion-conducting pore of cardiac Na+ channel does not affect ion selectivity properties. Acta Physiologica Scandinavica 185, 291–301.

Amin, A.S., Asghari-Roodsari, A., Tan, H.L., 2010. Cardiac sodium channelopathies. Pflügers Archiv-European Journal of Physiology 460, 223–237.

Amorim, R.M., Rocha, B.M., Campos, F.O., Dos Santos, R.W., 2010. Automatic code generation for solvers of cardiac cellular membrane dynamics in GPUs, in: Engineering in Medicine and Biology Society (EMBC), 2010 Annual International Conference of the IEEE, IEEE. pp. 2666–2669.

An, R., Wang, X., Kerem, B., Benhorin, J., Medina, A., Goldmit, M., Kass, R., 1998. Novel LQT-3 mutation affects Na+ channel activity through interactions between α-and β1-subunits. Circulation Research 83, 141–146.

Antzelevitch, C., Pollevick, G.D., Cordeiro, J.M., Casis, O., Sanguinetti, M.C., Aizawa, Y., Guerchicoff, A., Pfeiffer, R., Oliva, A., Wollnik, B., et al., 2007. Loss-of-function mutations in the cardiac calcium channel underlie a new clinical entity characterized by ST-segment elevation, short QT intervals, and sudden cardiac death. Circulation 115, 442–449.

Arevalo, H.J., Vadakkumpadan, F., Guallar, E., Jebb, A., Malamas, P., Wu, K.C., Trayanova, N.A., 2016. Arrhythmia risk stratification of patients after myocardial infarction using personalized heart models. Nature Communications 7.

Armstrong, C.M., 2006. Na channel inactivation from open and closed states. Proceedings of the National Academy of Sciences 103, 17991–17996.

Armstrong, C.M., Bezanilla, F., 1977. Inactivation of the sodium channel. II. Gating current experiments. The Journal of General Physiology 70, 567–590.

Aslanidi, O.V., Al-Owais, M., Benson, A.P., Colman, M., Garratt, C.J., Gilbert, S.H., Greenwood, J.P., Holden, A.V., Kharche, S., Kinnell, E., et al., 2012. Virtual tissue engineering of the human atrium: modelling pharmacological actions on atrial arrhythmogenesis. European Journal of Pharmaceutical Sciences 46, 209–221.

Aslanidi, O.V., Boyett, M.R., Dobrzynski, H., Li, J., Zhang, H., 2009a. Mechanisms of transition from normal to reentrant electrical activity in a model of rabbit atrial tissue: interaction of tissue heterogeneity and anisotropy. Biophysical Journal 96, 798–817.

Aslanidi, O.V., Stewart, P., Boyett, M.R., Zhang, H., 2009b. Optimal velocity and safety of discontinuous conduction through the heterogeneous Purkinje-ventricular junction. Biophysical Journal 97, 20–39.

Balakrishnan, M., Chakravarthy, V.S., Guhathakurta, S., 2015. Simulation of cardiac arrhythmias using a 2D heterogeneous whole heart model. Frontiers in Physiology 6.

Bankston, J.R., Sampson, K.J., Kateriya, S., Glaaser, I.W., Malito, D.L., Chung, W.K., Kass, R.S., 2007a. A novel LQT-3 mutation disrupts an inactivation gate complex with distinct rate-dependent phenotypic consequences. Channels 1, 273–280.

Bankston, J.R., Yue, M., Chung, W., Spyres, M., Pass, R.H., Silver, E., Sampson, K.J., Kass, R.S., 2007b. A novel and lethal de novo LQT-3 mutation in a newborn with distinct molecular pharmacology and therapeutic response. PLOS ONE 2, e1258.

Barbosa, C.B., dos Santos, R.W., Amorim, R.M., Ciuffo, L.N., Manfroi, F., Oliveira, R.S., Campos, F.O., 2006. A transformation tool for ODE based models., in: International Conference on Computational Science (1), pp. 68–75.

Baroudi, G., Carbonneau, E., Pouliot, V., Chahine, M., 2000. SCN5A mutation (T1620M) causing Brugada syndrome exhibits different phenotypes when expressed in Xenopus oocytes and mammalian cells. FEBS Letters 467, 12–16.

Baroudi, G., Chahine, M., 2000. Biophysical phenotypes of SCN5A mutations causing long QT and Brugada syndromes. FEBS Letters 487, 224–228.

Baroudi, G., Napolitano, C., Priori, S.G., Del Bufalo, A., Chahine, M., 2004. Loss of function associated with novel mutations of the SCN5A gene in patients with Brugada syndrome. Canadian Journal of Cardiology 20, 425–430.

Baroudi, G., Pouliot, V., Denjoy, I., Guicheney, P., Shrier, A., Chahine, M., 2001. Novel mechanism for Brugada syndrome defective surface localization of an SCN5A mutant (R1432G). Circulation Research 88, e78–e83.

Bassingthwaighte, J.B., 2000. Strategies for the Physiome project. Annals of Biomedical Engineering 28, 1043–1058.

Bébarová, M., O'Hara, T., Geelen, J.L., Jongbloed, R.J., Timmermans, C., Arens, Y.H., Rodriguez, L.M., Rudy, Y., Volders, P.G., 2008. Subepicardial phase 0 block and discontinuous transmural conduction underlie right precordial ST-segment elevation by a SCN5A loss-of-function mutation. American Journal of Physiology – Heart and Circulatory Physiology 295, H48–H58.

Beckermann, T.M., McLeod, K., Murday, V., Potet, F., George, A.L., 2014. Novel SCN5A mutation in amiodarone-responsive multifocal ventricular ectopy-associated cardiomyopathy. Heart Rhythm 11, 1446–1453.

Beeler, G.W., Reuter, H., 1977. Reconstruction of the action potential of ventricular myocardial fibres. The Journal of Physiology 268, 177–210.

Benson, A.P., Aslanidi, O.V., Zhang, H., Holden, A.V., 2008. The canine virtual ventricular wall: a platform for dissecting pharmacological effects on propagation and arrhythmogenesis. Progress in Biophysics and Molecular Biology 96, 187–208.

Berezovsky, I.N., Guarnera, E., Zheng, Z., 2016. Basic units of protein structure, folding, and function. Progress in Biophysics and Molecular Biology .

Bernus, O., Wilders, R., Zemlin, C.W., Verschelde, H., Panfilov, A.V., 2002. A computationally efficient electrophysiological model of human ventricular cells. American Journal of Physiology – Heart and Circulatory Physiology 282, H2296–H2308.

Bers, D., 2001. Excitation-contraction coupling and cardiac contractile force. volume 237. Springer Science & Business Media.

Beyder, A., Mazzone, A., Strege, P.R., Tester, D.J., Saito, Y.A., Bernard, C.E., Enders, F.T., Ek, W.E., Schmidt, P.T., Dlugosz, A., et al., 2014. Loss-of-function of the voltage-gated sodium channel NaV1.5 (channelopathies) in patients with irritable bowel syndrome. Gastroenterology 146, 1659–1668.

Beyder, A., Rae, J.L., Bernard, C., Strege, P.R., Sachs, F., Farrugia, G., 2010. Mechanosensitivity of NaV1.5, a voltage-sensitive sodium channel. The Journal of Physiology 588, 4969–4985.

Bezzina, C.R., Rook, M.B., Groenewegen, W.A., Herfst, L.J., van der Wal, A.C., Lam, J., Jongsma, H.J., Wilde, A.A., Mannens, M.M., 2003. Compound heterozygosity for mutations (W156X and R225W) in SCN5A associated with severe cardiac conduction disturbances and degenerative changes in the conduction system. Circulation Research 92, 159–168.

Black, H.S., 1937. Wave translation system. US Patent 2,102,671.

Bondarenko, V.E., Szigeti, G.P., Bett, G.C., Kim, S.J., Rasmusson, R.L., 2004. Computer model of action potential of mouse ventricular myocytes. American Journal of Physiology – Heart and Circulatory Physiology 287, H1378–H1403.

Boukhabza, M., El Hilaly, J., Attiya, N., El-Haidani, A., Filali-Zegzouti, Y., Mazouzi, D., Amarouch, M.Y., 2016. In silico evaluation of the potential antiarrhythmic effect of epigallocatechin-3-gallate on cardiac channelopathies. Computational and Mathematical Methods in Medicine .

Breiman, L., 2001. Random forests. Machine Learning 45, 5–32.

Britton, O.J., Bueno-Orovio, A., Van Ammel, K., Lu, H.R., Towart, R., Gallacher, D.J., Rodriguez, B., 2013. Experimentally calibrated population of models predicts and explains intersubject variability in cardiac cellular electrophysiology. Proceedings of the National Academy of Sciences 110, E2098–E2105.

Brunklaus, A., Ellis, R., Reavey, E., Semsarian, C., Zuberi, S.M., 2014. Genotype phenotype associations across the voltage-gated sodium channel family. Journal of Medical Genetics 51, 650–658.

Buddeke, J., van Dis, I., Vaartjes, I., Visseren, F., Bots, M., 2015. Sterfte aan hart- en vaatziekten in nederland, in: Van Dis, I., Buddeke, J., Vaartjes, I., Visseren, F., Bots, M. (Eds.), Hart- en vaatziekten in Nederland 2015, cijfers over heden, verleden en toekomst. Hartstichting, Den Haag. chapter 1, pp. 7–20.

Bueno-Orovio, A., Cherry, E.M., Fenton, F.H., 2008. Minimal model for human ventricular action potentials in tissue. Journal of Theoretical Biology 253, 544–560.

Bueno-Orovio, A., Sánchez, C., Pueyo, E., Rodriguez, B., 2014. Na/K pump regulation of cardiac repolarization: insights from a systems biology approach. Pflügers Archiv-European Journal of Physiology 466, 183–193.

Buhry, L., Grassia, F., Giremus, A., Grivel, E., Renaud, S., Saïghi, S., 2011. Automated parameter estimation of the Hodgkin-Huxley model using the differential evolution algorithm: application to neuromimetic analog integrated circuits. Neural Computation 23, 2599–2625.

Burton, B.M., Tate, J.D., Erem, B., Swenson, D.J., Wang, D.F., Steffen, M., Brooks, D.H.,

Van Dam, P.M., Macleod, R.S., 2011. A toolkit for forward/inverse problems in electrocardiography within the SCIRun problem solving environment, in: Engineering in Medicine and Biology Society, EMBC, 2011 Annual International Conference of the IEEE, IEEE. pp. 267–270.

Butterworth, E., Jardine, B.E., Raymond, G.M., Neal, M.L., Bassingthwaighte, J.B., 2013. JSim, an open-source modeling system for data analysis. F1000Research 2.

Cabo, C., Boyden, P.A., 2003. Electrical remodeling of the epicardial border zone in the canine infarcted heart: a computational analysis. American Journal of Physiology – Heart and Circulatory Physiology 284, H372–H384.

Calloe, K., Refaat, M.M., Grubb, S., Wojciak, J., Campagna, J., Thomsen, N.M., Nussbaum, R.L., Scheinman, M.M., Schmitt, N., 2013. Characterization and mechanisms of action of novel NaV1.5 channel mutations associated with Brugada syndrome. Circulation: Arrhythmia and Electrophysiology 6, 177–184.

Calloe, K., Schmitt, N., Grubb, S., Pfeiffer, R., David, J.P., Kanter, R., Cordeiro, J.M., Antzelevitch, C., 2011. Multiple arrhythmic syndromes in a newborn, owing to a novel mutation in SCN5A. Canadian Journal of Physiology and Pharmacology 89, 723–736.

Carbonell-Pascual, B., Godoy, E., Ferrer, A., Romero, L., Ferrero, J.M., 2016. Comparison between Hodgkin–Huxley and Markov formulations of cardiac ion channels. Journal of Theoretical Biology 399, 92–102.

Carro, J., Rodríguez, J.F., Laguna, P., Pueyo, E., 2011. A human ventricular cell model for investigation of cardiac arrhythmias under hyperkalaemic conditions. Philosophical Transactions of the Royal Society of London A: Mathematical, Physical and Engineering Sciences 369, 4205–4232.

Carusi, A., Burrage, K., Rodriguez, B., 2012. Bridging experiments, models and simulations: an integrative approach to validation in computational cardiac electrophysiology. American Journal of Physiology – Heart and Circulatory Physiology 303, H144–H155.

Casini, S., Tan, H.L., Bhuiyan, Z.A., Bezzina, C.R., Barnett, P., Cerbai, E., Mugelli, A., Wilde, A.A., Veldkamp, M.W., 2007. Characterization of a novel SCN5A mutation associated with Brugada syndrome reveals involvement of DIIIS4–S5 linker in slow inactivation. Cardiovascular Research 76, 418–429.

Castro, J., Monasterio, V., Carro, J., 2016. Volunteer computing approach for the collaborative simulation of electrophysiological models, in: 25th IEEE International Conference on Enabling Technologies: Infrastructure for Collaborative Enterprises, IEEE. pp. 118–123.

Catterall, W.A., 2000. From ionic currents to molecular mechanisms: the structure and function of voltage-gated sodium channels. Neuron 26, 13–25.

Chang, C.C., Acharfi, S., Wu, M.H., Chiang, F.T., Wang, J.K., Sung, T.C., Chahine, M., 2004. A novel SCN5A mutation manifests as a malignant form of long QT syndrome with perinatal onset of tachycardia/bradycardia. Cardiovascular Research 64, 268–278.

Chang, C.C., Lin, C.J., 2011. LIBSVM: a library for support vector machines. ACM Transactions on Intelligent Systems and Technology (TIST) 2, 27.

Chang, E.T., Strong, M., Clayton, R.H., 2015. Bayesian sensitivity analysis of a cardiac cell model using a Gaussian process emulator. PLOS ONE 10, e0130252.

Chen, J., Makiyama, T., Wuriyanghai, Y., Ohno, S., Sasaki, K., Hayano, M., Harita, T., Nishiuchi, S., Yamamoto, Y., Ueyama, T., et al., 2016. Cardiac sodium channel mutation associated with epinephrine-induced QT prolongation and sinus node dysfunction. Heart Rhythm 13, 289–298.

Chen, L., Santarelli, V., Horn, R., Kallen, R., 1996. A unique role for the S4 segment of domain 4 in the inactivation of sodium channels. The Journal of General Physiology 108, 549–556.

Cheng, J., Morales, A., Siegfried, J.D., Li, D., Norton, N., Song, J., Gonzalez-Quintana, J., Makielski, J.C., Hershberger, R.E., 2010. SCN5A rare variants in familial dilated cardiomyopathy decrease peak sodium current depending on the common polymorphism H558R and common splice variant Q1077del. Clinical and Translational Science 3, 287–294.

Cheng, J., Tester, D.J., Tan, B.H., Valdivia, C.R., Kroboth, S., Ye, B., January, C.T., Ackerman, M.J., Makielski, J.C., 2011. The common African American polymorphism SCN5A-S1103Y interacts with mutation SCN5A-R680H to increase late Na current. Physiological Genomics 43, 461–466.

Cherry, E.M., Ehrlich, J.R., Nattel, S., Fenton, F.H., 2007. Pulmonary vein reentry-properties and size matter: insights from a computational analysis. Heart Rhythm 4, 1553–1562.

Cherry, E.M., Fenton, F.H., 2007. A tale of two dogs: analyzing two models of canine ventricular electrophysiology. American Journal of Physiology - Heart and Circulatory Physiology 292, H43–H55.

Chevalier, M., Amuzescu, B., Gawali, V., Todt, H., Knott, T., Scheel, O., Abriel, H., 2014. Late cardiac sodium current can be assessed using automated patch-clamp. F1000Research 3.

Chiang, K.C., Lai, L.P., Shieh, R.C., 2009. Characterization of a novel NaV1.5 channel mutation, A551T, associated with Brugada syndrome. Journal of Biomedical Science 16, 1.

CIBC, 2015. Seg3D: Volumetric Image Segmentation and Visualization. Scientific Computing and Imaging Institute (SCI).

Clancy, C.E., Rudy, Y., 1999. Linking a genetic defect to its cellular phenotype in a cardiac arrhythmia. Nature 400, 566–569.

Clancy, C.E., Rudy, Y., 2002. Na^+ channel mutation that causes both Brugada and long-QT syndrome phenotypes: a simulation study of mechanism. Circulation 105, 1208–1213.

Clancy, C.E., Zhu, Z.I., Rudy, Y., 2007. Pharmacogenetics and anti-arrhythmic drug therapy: a theoretical investigation. American Journal of Physiology – Heart and Circulatory Physiology 292, H66–H75.

Clatot, J., Ziyadeh-Isleem, A., Maugenre, S., Denjoy, I., Liu, H., Dilanian, G., Hatem, S.N., Deschênes, I., Coulombe, A., Guicheney, P., et al., 2012a. Dominant-negative effect of SCN5A N-terminal mutations through the interaction of NaV1.5 α-subunits. Cardiovascular Research 96, 53–63.

Clatot, J., Ziyadeh-Isleem, A., Maugenre, S., Denjoy, I., Liu, H., Dilanian, G., Hatem, S.N., De-

schênes, I., Coulombe, A., Guicheney, P., et al., 2012b. Dominant-negative effect of SCN5A N-terminal mutations through the interaction of NaV1.5 α-subunits. Cardiovascular Research 96, 53–63.

Clayton, R., Panfilov, A., 2008. A guide to modelling cardiac electrical activity in anatomically detailed ventricles. Progress in Biophysics and Molecular Biology 96, 19–43.

Clerx, M., Collins, P., de Lange, E., Volders, P.G.A., 2016. Myokit: A simple interface to cardiac cellular electrophysiology. Progress in Biophysics and Molecular Biology 120, 100–114.

Clerx, M., Collins, P., Volders, P.G.A., 2015. Applying novel identification protocols to Markov models of INa, in: Computing in Cardiology, CINC. pp. 889–892.

Clerx, M., Volders, P.G.A., Collins, P., 2014. Myokit: A framework for computational cellular electrophysiology, in: Computing in Cardiology, CINC. pp. 229–232.

Cluitmans, M., 2016. Noninvasive reconstruction of cardiac electrical activity: Mathematical innovation, in vivo validation and human application. Ph.D. thesis. Maastricht University.

Cluitmans, M.J., Bonizzi, P., Karel, J.M., Das, M., Kietselaer, B.L., de Jong, M.M., Prinzen, F.W., Peeters, R.L., Westra, R.L., Volders, P.G., 2017. In vivo validation of electrocardiographic imaging. Journal of the American College of Cardiology: Clinical Electrophysiology .

Cluitmans, M.J., de Jong, M.M., Volders, P.G., Peeters, R.L., Westra, R.L., 2014. Physiology-based regularization improves noninvasive reconstruction and localization of cardiac electrical activity, in: Computing in Cardiology, CINC. pp. 1–4.

Cluitmans, M.J., Karel, J., Bonizzi, P., de Jong, M.M., Volders, P.G., Peeters, R.L., Westra, R.L., 2015a. In-vivo evaluation of reduced-lead-systems in noninvasive reconstruction and localization of cardiac electrical activity, in: Computing in Cardiology, CINC. pp. 221–224.

Cluitmans, M.J., Peeters, R.L., Westra, R.L., Volders, P.G., 2015b. Noninvasive reconstruction of cardiac electrical activity: update on current methods, applications and challenges. Netherlands Heart Journal 23, 301–311.

Cobelli, C., DiStefano, J., 1980. Parameter and structural identifiability concepts and ambiguities: a critical review and analysis. American Journal of Physiology-Regulatory, Integrative and Comparative Physiology 239, R7–R24.

Cole, K.S., 1968. Membranes, ions, and impulses: a chapter of classical biophysics. Univ of California Press.

Cooper, J., Mirams, G.R., Niederer, S.A., 2011. High-throughput functional curation of cellular electrophysiology models. Progress in Biophysics and Molecular Biology 107, 11–20.

Cooper, J., Scharm, M., Mirams, G.R., 2015a. The cardiac electrophysiology web lab. PeerJ PrePrints 3, e1652.

Cooper, J., Spiteri, R.J., Mirams, G.R., 2014. Cellular cardiac electrophysiology modelling with Chaste and CellML. Frontiers in Physiology 5, 511.

Cooper, J., Vik, J.O., Waltemath, D., 2015b. A call for virtual experiments: accelerating the scientific process. Progress in Biophysics and Molecular Biology 117, 99–106.

Cooper, J., Whiteley, J.P., Gavaghan, D.J., 2010. A posteriori error analysis for the use of lookup tables in cardiac electrophysiology simulations. SIAM Journal on Scientific Computing 32, 2167–2189.

Coraboeuf, E., Weidmann, S., 1949. Potentiel de repos et potentiels d'action du muscle cardiaque, mesures a l'aide d'electrodes intracellulaires. Comptes Rendus Des Seances De La Societe De Biologie Et De Ses Filiales 143, 1329–1331.

Cordeiro, J.M., Barajas-Martinez, H., Hong, K., Burashnikov, E., Pfeiffer, R., Orsino, A.M., Wu, Y.S., Hu, D., Brugada, J., Brugada, P., et al., 2006. Compound heterozygous mutations P336L and I1660V in the human cardiac sodium channel associated with the Brugada syndrome. Circulation 114, 2026–2033.

Corrias, A., Giles, W., Rodriguez, B., 2011. Ionic mechanisms of electrophysiological properties and repolarization abnormalities in rabbit Purkinje fibers. American Journal of Physiology – Heart and Circulatory Physiology 300, H1806–H1813.

Cortassa, S., Aon, M.A., O'Rourke, B., Jacques, R., Tseng, H.J., Marbán, E., Winslow, R.L., 2006. A computational model integrating electrophysiology, contraction, and mitochondrial bioenergetics in the ventricular myocyte. Biophysical Journal 91, 1564–1589.

Courtemanche, M., Ramirez, R.J., Nattel, S., 1998. Ionic mechanisms underlying human atrial action potential properties: insights from a mathematical model. American Journal of Physiology – Heart and Circulatory Physiology 275, H301–H321.

Courtemanche, M., Skaggs, W., Winfree, A.T., 1990. Stable three-dimensional action potential circulation in the Fitzhugh-Nagumo model. Physica D: Nonlinear Phenomena 41, 173–182.

Coutu, P., Metzger, J.M., 2005. Genetic manipulation of calcium-handling proteins in cardiac myocytes. II. mathematical modeling studies. American Journal of Physiology – Heart and Circulatory Physiology 288, H613–H631.

Crotti, L., Hu, D., Barajas-Martinez, H., De Ferrari, G.M., Oliva, A., Insolia, R., Pollevick, G.D., Dagradi, F., Guerchicoff, A., Greco, F., et al., 2012. Torsades de pointes following acute myocardial infarction: evidence for a deadly link with a common genetic variant. Heart Rhythm 9, 1104–1112.

Cuellar, A.A., Lloyd, C.M., Nielsen, P.F., Bullivant, D.P., Nickerson, D.P., Hunter, P.J., 2003. An overview of CellML 1.1, a biological model description language. SIMULATION 79, 740–747.

Cummins Lancaster, M., Sobie, E.A., 2016. Improved prediction of drug-induced torsades de pointes through simulations of dynamics and machine learning algorithms. Clinical Pharmacology & Therapeutics .

van Dam, P.M., Oostendorp, T.F., Linnenbank, A.C., van Oosterom, A., 2009. Non-invasive imaging of cardiac activation and recovery. Annals of Biomedical Engineering 37, 1739–1756.

David, M., Ter Bekke, R., Seyen, S., Krapels, I., Van den Wijngaard, A., Spätjens, R., Volders, P., 2012. Augmented window INa by the novel SCN5A mutation L828F: Implications for abnormal ventricular impulse formation and treatment, in: Heart Rhythm Society, pp. AB04–02.

Davies, M.R., Mistry, H.B., Hussein, L., Pollard, C.E., Valentin, J.P., Swinton, J., Abi-Gerges, N.,

2012. An in silico canine cardiac midmyocardial action potential duration model as a tool for early drug safety assessment. American Journal of Physiology – Heart and Circulatory Physiology 302, H1466–H1480.

Davies, M.R., Wang, K., Mirams, G.R., Caruso, A., Noble, D., Walz, A., Lavé, T., Schuler, F., Singer, T., Polonchuk, L., 2016. Recent developments in using mechanistic cardiac modelling for drug safety evaluation. Drug discovery today 21, 924–938.

Decker, K.F., Heijman, J., Silva, J.R., Hund, T.J., Rudy, Y., 2009. Properties and ionic mechanisms of action potential adaptation, restitution, and accommodation in canine epicardium. American Journal of Physiology – Heart and Circulatory Physiology 296, H1017–H1026.

Demir, S.S., Clark, J.W., Giles, W.R., 1999. Parasympathetic modulation of sinoatrial node pacemaker activity in rabbit heart: a unifying model. American Journal of Physiology – Heart and Circulatory Physiology 276, H2221–H2244.

Deo, R.C., 2015. Machine learning in medicine. Circulation 132, 1920–1930.

Deschênes, I., Baroudi, G., Berthet, M., Barde, I., Chalvidan, T., Denjoy, I., Guicheney, P., Chahine, M., 2000. Electrophysiological characterization of SCN5A mutations causing long QT (E1784K) and Brugada (R1512W and R1432G) syndromes. Cardiovascular Research 46, 55–65.

Detta, N., Frisso, G., Limongelli, G., Marzullo, M., Calabrò, R., Salvatore, F., 2014. Genetic analysis in a family affected by sick sinus syndrome may reduce the sudden death risk in a young aspiring competitive athlete. International Journal of Cardiology 170, e63–e65.

Devenyi, R.A., Sobie, E.A., 2016. There and back again: Iterating between population-based modeling and experiments reveals surprising regulation of calcium transients in rat cardiac myocytes. Journal of Molecular and Cellular Cardiology 96, 38–48.

DiFrancesco, D., Noble, D., 1985. A model of cardiac electrical activity incorporating ionic pumps and concentration changes. Philosophical Transactions of the Royal Society of London B: Biological Sciences 307, 353–398.

Drummond, G., Vowler, S., 2011. Show the data, don't conceal them. The Journal of Physiology 589, 1861.

Dumaine, R., Towbin, J.A., Brugada, P., Vatta, M., Nesterenko, D.V., Nesterenko, V.V., Brugada, J., Brugada, R., Antzelevitch, C., 1999. Ionic mechanisms responsible for the electrocardiographic phenotype of the Brugada syndrome are temperature dependent. Circulation Research 85, 803–809.

Dyson, F., 2004. A meeting with Enrico Fermi. Nature 427, 297–297.

Eberhart, R.C., Kennedy, J., 1995. A new optimizer using particle swarm theory, in: Proceedings of the Sixth International Symposium on Micro Machine and Human Science, New York, NY. pp. 39–43.

Ellinor, P.T., Nam, E.G., Shea, M.A., Milan, D.J., Ruskin, J.N., MacRae, C.A., 2008. Cardiac sodium channel mutation in atrial fibrillation. Heart Rhythm 5, 99–105.

Erem, B., Brooks, D.H., Van Dam, P.M., Stinstra, J.G., MacLeod, R.S., 2011. Spatiotemporal

estimation of activation times of fractionated ECGs on complex heart surfaces, in: Engineering in Medicine and Biology Society, EMBC, 2011 Annual International Conference of the IEEE, IEEE. pp. 5884–5887.

Erkapic, D., Greiss, H., Pajitnev, D., Zaltsberg, S., Deubner, N., Berkowitsch, A., Möllman, S., Sperzel, J., Rolf, A., Schmitt, J., et al., 2015. Clinical impact of a novel three-dimensional electrocardiographic imaging for non-invasive mapping of ventricular arrhythmias – a prospective randomized trial. Europace 17, 591–597.

Feng, J., Li, G.r., Fermini, B., Nattel, S., 1996. Properties of sodium and potassium currents of cultured adult human atrial myocytes. American Journal of Physiology – Heart and Circulatory Physiology 270, H1676–H1686.

Fenton, F., Karma, A., 1998. Vortex dynamics in three-dimensional continuous myocardium with fiber rotation: filament instability and fibrillation. Chaos: An Interdisciplinary Journal of Nonlinear Science 8, 20–47.

Fenton, F.H., Cherry, E.M., Hastings, H.M., Evans, S.J., 2002. Multiple mechanisms of spiral wave breakup in a model of cardiac electrical activity. Chaos: An Interdisciplinary Journal of Nonlinear Science 12, 852–892.

Fernandez, F.R., Morales, E., Rashid, A.J., Dunn, R.J., Turner, R.W., 2003. Inactivation of Kv3.3 potassium channels in heterologous expression systems. Journal of Biological Chemistry 278, 40890–40898.

Fink, M., Batzel, J.J., Tran, H., 2008a. A respiratory system model: parameter estimation and sensitivity analysis. Cardiovascular Engineering 8, 120–134.

Fink, M., Giles, W.R., Noble, D., 2006. Contributions of inwardly rectifying K+ currents to repolarization assessed using mathematical models of human ventricular myocytes. Philosophical Transactions of the Royal Society of London A: Mathematical, Physical and Engineering Sciences 364, 1207–1222.

Fink, M., Noble, D., 2009. Markov models for ion channels: versatility versus identifiability and speed. Philosophical Transactions of the Royal Society of London A: Mathematical, Physical and Engineering Sciences 367, 2161–2179.

Fink, M., Noble, D., Virag, L., Varro, A., Giles, W.R., 2008b. Contributions of HERG K+ current to repolarization of the human ventricular action potential. Progress in Biophysics and Molecular Biology 96, 357–376.

Fitzhugh, R., 1960. Thresholds and plateaus in the Hodgkin-Huxley nerve equations. The Journal of General Physiology 43, 867–896.

FitzHugh, R., 1961. Impulses and physiological states in theoretical models of nerve membrane. Biophysical Journal 1, 445.

FitzHugh, R., 1969. Biological engineering. volume 9. McGraw-Hill Companies.

Flaim, S.N., Giles, W.R., McCulloch, A.D., 2006. Contributions of sustained INa and IKv43 to transmural heterogeneity of early repolarization and arrhythmogenesis in canine left ventricular myocytes. American Journal of Physiology – Heart and Circulatory Physiology 291, H2617–

H2629.

Fox, J.J., McHarg, J.L., Gilmour, R.F., 2002. Ionic mechanism of electrical alternans. American Journal of Physiology – Heart and Circulatory Physiology 282, H516–H530.

Frustaci, A., Priori, S.G., Pieroni, M., Chimenti, C., Napolitano, C., Rivolta, I., Sanna, T., Bellocci, F., Russo, M.A., 2005. Cardiac histological substrate in patients with clinical phenotype of Brugada syndrome. Circulation 112, 3680–3687.

Garcia, V.M., Liberos, A., Climent, A.M., Vidal, A., Millet, J., Gonzalez, A., 2011. An adaptive step size GPU ODE solver for simulating the electric cardiac activity, in: Computing in Cardiology, CINC. pp. 233–236.

Garny, A., Hunter, P.J., 2015. OpenCOR: a modular and interoperable approach to computational biology. Frontiers in Physiology 6, 26.

Garny, A., Kohl, P., Hunter, P.J., Boyett, M.R., Noble, D., 2003. One-dimensional rabbit sinoatrial node models. Journal of Cardiovascular Electrophysiology 14, S121–S132.

Ge, J., Sun, A., Paajanen, V., Wang, S., Su, C., Yang, Z., Li, Y., Wang, S., Jia, J., Wang, K., et al., 2008. Molecular and clinical characterization of a novel SCN5A mutation associated with atrioventricular block and dilated cardiomyopathy. Circulation: Arrhythmia and Electrophysiology 1, 83–92.

Gharaviri, A., Verheule, S., Eckstein, J., Potse, M., Kuijpers, N.H., Schotten, U., 2012. A computer model of endo-epicardial electrical dissociation and transmural conduction during atrial fibrillation. Europace 14, v10–v16.

Ghodrati, A., Brooks, D.H., Tadmor, G., MacLeod, R.S., 2006. Wavefront-based models for inverse electrocardiography. IEEE Transactions on Biomedical Engineering 53, 1821–1831.

Ghosh, S., Rudy, Y., 2009. Application of L1-norm regularization to epicardial potential solution of the inverse electrocardiography problem. Annals of Biomedical Engineering 37, 902–912.

Gillespie, D.T., 1976. A general method for numerically simulating the stochastic time evolution of coupled chemical reactions. Journal of Computational Physics 22, 403–434.

Glaaser, I.W., Osteen, J.D., Puckerin, A., Sampson, K.J., Jin, X., Kass, R.S., 2012. Perturbation of sodium channel structure by an inherited long QT syndrome mutation. Nature Communications 3, 706.

Gleeson, P., Crook, S., Cannon, R.C., Hines, M.L., Billings, G.O., Farinella, M., Morse, T.M., Davison, A.P., Ray, S., Bhalla, U.S., et al., 2010. NeuroML: A language for describing data driven models of neurons and networks with a high degree of biological detail. PLOS Computational Biology 6, e1000815.

Glynn, P., Musa, H., Wu, X., Unudurthi, S.D., Little, S., Qian, L., Wright, P.J., Radwanski, P.B., Gyorke, S., Mohler, P.J., et al., 2015. Voltage-gated sodium channel phosphorylation at ser571 regulates late current, arrhythmia, and cardiac function in vivo. Circulation 132, 567–577.

Gong, J.Q., Shim, J.V., Núñez-Acosta, E., Sobie, E.A., 2017. I love it when a plan comes together: Insight gained through convergence of competing mathematical models. Journal of Molecular

and Cellular Cardiology 102, 31–33.

Gonnet, G.H., Cohen, M.A., Benner, S.A., 1992. Exhaustive matching of the entire protein sequence database. Science 256, 1443–1445.

Gosselin-Badaroudine, P., Keller, D.I., Huang, H., Pouliot, V., Chatelier, A., Osswald, S., Brink, M., Chahine, M., 2012. A proton leak current through the cardiac sodium channel is linked to mixed arrhythmia and the dilated cardiomyopathy phenotype. PLOS ONE 7, e38331.

Graham, J., Gerard, R., 1946. Membrane potentials and excitation of impaled single muscle fibers. Journal of Cellular and Comparative Physiology 28, 99–117.

Grandi, E., Pandit, S.V., Voigt, N., Workman, A.J., Dobrev, D., Jalife, J., Bers, D.M., 2011. Human atrial action potential and Ca2+ model sinus rhythm and chronic atrial fibrillation. Circulation Research 109, 1055–1066.

Grandi, E., Pasqualini, F.S., Bers, D.M., 2010. A novel computational model of the human ventricular action potential and Ca transient. Journal of Molecular and Cellular Cardiology 48, 112–121.

Grantham, R., 1974. Amino acid difference formula to help explain protein evolution. Science 185, 862–864.

Greenstein, J.L., Hinch, R., Winslow, R.L., 2006. Mechanisms of excitation-contraction coupling in an integrative model of the cardiac ventricular myocyte. Biophysical Journal 90, 77–91.

Greenstein, J.L., Winslow, R.L., 2002. An integrative model of the cardiac ventricular myocyte incorporating local control of Ca2+ release. Biophysical Journal 83, 2918–2945.

Griewank, A., Corliss, G., 1991. Automatic differentiation of algorithms: theory, implementation and application. SIAM, Philadelphia, PA, USA.

Groenewegen, W.A., Bezzina, C.R., van Tintelen, J.P., Hoorntje, T.M., Mannens, M.M., Wilde, A.A., Jongsma, H.J., Rook, M.B., 2003a. A novel LQT3 mutation implicates the human cardiac sodium channel domain IVS6 in inactivation kinetics. Cardiovascular Research 57, 1072–1078.

Groenewegen, W.A., Firouzi, M., Bezzina, C.R., Vliex, S., van Langen, I.M., Sandkuijl, L., Smits, J.P., Hulsbeek, M., Rook, M.B., Jongsma, H.J., et al., 2003b. A cardiac sodium channel mutation cosegregates with a rare connexin 40 genotype in familial atrial standstill. Circulation Research 92, 14–22.

Gros, D.B., Jongsma, H.J., 1996. Connexins in mammalian heart function. Bioessays 18, 719–730.

Gui, J., Wang, T., Jones, R.P., Trump, D., Zimmer, T., Lei, M., 2010a. Multiple loss-of-function mechanisms contribute to SCN5A-related familial sick sinus syndrome. PLOS ONE 5, e10985.

Gui, J., Wang, T., Trump, D., Zimmer, T., Lei, M., 2010b. Mutation-specific effects of polymorphism H558R in SCN5A-related sick sinus syndrome. Journal of Cardiovascular Electrophysiology 21, 564–573.

Guo, Q., Ren, L., Chen, X., Hou, C., Chu, J., Pu, J., Zhang, S., 2016. A novel mutation in the SCN5A gene contributes to arrhythmogenic characteristics of early repolarization syndrome. International Journal of Molecular Medicine 37, 727–733.

Gurev, V., Pathmanathan, P., Fattebert, J.L., Wen, H.F., Magerlein, J., Gray, R.A., Richards, D.F., Rice, J.J., 2015. A high-resolution computational model of the deforming human heart. Biomechanics and Modeling in Mechanobiology 14, 829–849.

Gütter, C., Benndorf, K., Zimmer, T., 2013. Characterization of N-terminally mutated cardiac Na+ channels associated with long QT syndrome 3 and Brugada syndrome. Sudden arrhythmic death: from basic science to clinical practice , 41.

Hafner, D., Borchard, U., Richter, O., Neugebauer, M., 1981. Parameter estimation in Hodgkin-Huxley-type equations for membrane action potentials in nerve and heart muscle. Journal of Theoretical Biology 91, 321–345.

Hall, M., Frank, E., Holmes, G., Pfahringer, B., Reutemann, P., Witten, I.H., 2009. The WEKA data mining software: an update. ACM SIGKDD Explorations Newsletter 11, 10–18.

Hanck, D.A., Sheets, M.F., 1992. Time-dependent changes in kinetics of Na^+ current in single canine cardiac Purkinje cells. American Journal of Physiology – Heart and Circulatory Physiology 262, H1197–H1207.

Hayashi, K., Konno, T., Tada, H., Tani, S., Liu, L., Fujino, N., Nohara, A., Hodatsu, A., Tsuda, T., Tanaka, Y., et al., 2015. Functional characterization of rare variants implicated in susceptibility to lone atrial fibrillation. Circulation: Arrhythmia and Electrophysiology 8, 1095–1104.

He, B., Li, G., Zhang, X., 2003. Noninvasive imaging of cardiac transmembrane potentials within three-dimensional myocardium by means of a realistic geometry anisotropic heart model. IEEE Transactions on Biomedical Engineering 50, 1190–1202.

Hedley, P.L., Jørgensen, P., Schlamowitz, S., Moolman-Smook, J., Kanters, J.K., Corfield, V.A., Christiansen, M., 2009. The genetic basis of Brugada syndrome: a mutation update. Human Mutation 30, 1256–1266.

Hedley, W.J., Nelson, M.R., Bellivant, D., Nielsen, P.F., 2001. A short introduction to CellML. Philosophical Transactions of the Royal Society of London A: Mathematical, Physical and Engineering Sciences 359, 1073–1089.

Heijman, J., 2012. General discussion chapter, in: Computational analysis of β-adrenergic stimulation and its effects on cardiac ventricular electrophysiology. Ph.D. thesis. Maastricht University, pp. 201–222.

Heijman, J., Erfanian Abdoust, P., Voigt, N., Nattel, S., Dobrev, D., 2015. Computational models of atrial cellular electrophysiology and calcium handling, and their role in atrial fibrillation. The Journal of Physiology .

Heijman, J., Volders, P.G., Westra, R.L., Rudy, Y., 2011. Local control of β-adrenergic stimulation: Effects on ventricular myocyte electrophysiology and Ca(2+)-transient. Journal of Molecular and Cellular Cardiology 50, 863–871.

Heijman, J., Zaza, A., Johnson, D.M., Rudy, Y., Peeters, R.L.M., Volders, P.G.A., Westra, R.L., 2013. Determinants of beat-to-beat variability of repolarization duration in the canine ventricular myocyte: A computational analysis. PLOS Computational Biology 9, 1–14.

Herren, A.W., Bers, D.M., Grandi, E., 2013. Post-translational modifications of the cardiac Na

channel: contribution of CaMKII-dependent phosphorylation to acquired arrhythmias. American Journal of Physiology – Heart and Circulatory Physiology 305, H431–H445.

Hille, B., 1970. Ionic channels in nerve membranes. Progress in Biophysics and Molecular Biology 21, 1–32.

Hille, B., 2001. Ion Channels of Excitable Membranes. Sinauer Associates, Incorporated.

Hindmarsh, A.C., 1983. ODEPACK, a systematized collection of ODE solvers, in: R.S., S. (Ed.), Scientific Computing, IMACS transactions on scientific computation. Amsterdam, The Netherlands. volume 1, pp. 55–64.

Hindmarsh, A.C., Brown, P.N., Grant, K.E., Lee, S.L., Serban, R., Shumaker, D.E., Woodward, C.S., 2005. SUNDIALS: Suite of nonlinear and differential/algebraic equation solvers. ACM Transactions on Mathematical Software 31, 363–396.

Hodgkin, A., 1950. Conduction of the nervous impulse: some recent experiments. British Medical Bulletin 6, 322–325.

Hodgkin, A.L., Huxley, A., Katz, B., 1952. Measurement of current-voltage relations in the membrane of the giant axon of Loligo. The Journal of Physiology 116, 424–448.

Hodgkin, A.L., Huxley, A.F., 1952a. The components of membrane conductance in the giant axon of Loligo. The Journal of Physiology 116, 473–496.

Hodgkin, A.L., Huxley, A.F., 1952b. Currents carried by sodium and potassium ions through the membrane of the giant axon of Loligo. The Journal of Physiology 116, 449–472.

Hodgkin, A.L., Huxley, A.F., 1952c. The dual effect of membrane potential on sodium conductance in the giant axon of Loligo. The Journal of Physiology 116, 497–506.

Hodgkin, A.L., Huxley, A.F., 1952d. A quantitative description of membrane current and its application to conduction and excitation in nerve. The Journal of Physiology 117, 500–544.

Hoefen, R., Reumann, M., Goldenberg, I., Moss, A.J., Jin, O., Gu, Y., McNitt, S., Zareba, W., Jons, C., Kanters, J.K., et al., 2012. In silico cardiac risk assessment in patients with long QT syndrome: type 1: clinical predictability of cardiac models. Journal of the American College of Cardiology 60, 2182–2191.

Holst, A.G., Calloe, K., Jespersen, T., Cedergreen, P., Winkel, B.G., Jensen, H.K., Leren, T.P., Haunso, S., Svendsen, J.H., Tfelt-Hansen, J., 2009. A novel SCN5A mutation in a patient with coexistence of Brugada syndrome traits and ischaemic heart disease. Case Reports in Medicine 2009.

Holst, A.G., Liang, B., Jespersen, T., Bundgaard, H., Haunso, S., Svendsen, J.H., Tfelt-Hansen, J., 2010. Sick sinus syndrome, progressive cardiac conduction disease, atrial flutter and ventricular tachycardia caused by a novel SCN5A mutation. Cardiology 115, 311–316.

Hong, K., Berruezo-Sanchez, A., Poungvarin, N., Oliva, A., Vatta, M., Brugada, J., Brugada, P., Towbin, J.A., Dumaine, R., Piñero-Galvez, C., et al., 2004. Phenotypic characterization of a large European family with Brugada syndrome displaying a sudden unexpected death syndrome mutation in SCN5A. Journal of Cardiovascular Electrophysiology 15, 64–69.

Hong, K., Hu, J., Yu, J., Brugada, R., 2012. Concomitant Brugada-like and short QT electrocardiogram linked to SCN5A mutation. European Journal of Human Genetics 20, 1189–1192.

Horne, A.J., Eldstrom, J., Sanatani, S., Fedida, D., 2011. A novel mechanism for LQT3 with 2:1 block: a pore-lining mutation in NaV1.5 significantly affects voltage-dependence of activation. Heart Rhythm 8, 770–777.

Hoshi, M., Du, X.X., Shinlapawittayatorn, K., Liu, H., Chai, S., Wan, X., Ficker, E., Deschênes, I., 2014. Brugada syndrome disease phenotype explained in apparently benign sodium channel mutations. Circulation: Cardiovascular Genetics 7, 123.

Hsueh, C.H., Chen, W.P., Lin, J.L., Tsai, C.T., Liu, Y.B., Juang, J.M., Tsao, H.M., Su, M.J., Lai, L.P., 2009. Distinct functional defect of three novel Brugada syndrome related cardiac sodium channel mutations. Journal of Biomedical Science 16, 1.

Hu, D., Barajas-Martinez, H., Nesterenko, V.V., Pfeiffer, R., Guerchicoff, A., Cordeiro, J.M., Curtis, A.B., Pollevick, G.D., Wu, Y., Burashnikov, E., et al., 2010. Dual variation in SCN5A and CACNB2b underlies the development of cardiac conduction disease without Brugada syndrome. Pacing and Clinical Electrophysiology 33, 274–285.

Hu, D., Barajas-Martínez, H., Terzic, A., Park, S., Pfeiffer, R., Burashnikov, E., Wu, Y., Borggrefe, M., Veltmann, C., Schimpf, R., et al., 2014. ABCC9 is a novel Brugada and early repolarization syndrome susceptibility gene. International Journal of Cardiology 171, 431–442.

Hu, D., Viskin, S., Oliva, A., Carrier, T., Cordeiro, J.M., Barajas-Martinez, H., Wu, Y., Burashnikov, E., Sicouri, S., Brugada, R., et al., 2007. Novel mutation in the SCN5A gene associated with arrhythmic storm development during acute myocardial infarction. Heart Rhythm 4, 1072–1080.

Hu, R.M., Tan, B.H., Tester, D.J., Song, C., He, Y., Dovat, S., Peterson, B.Z., Ackerman, M.J., Makielski, J.C., 2015. Arrhythmogenic biophysical phenotype for SCN5A mutation S1787N depends upon splice variant background and intracellular acidosis. PLOS ONE 10, e0124921.

Huang, H., Millat, G., Rodriguez-Lafrasse, C., Rousson, R., Kugener, B., Chevalier, P., Chahine, M., 2009. Biophysical characterization of a new SCN5A mutation S1333Y in a SIDS infant linked to long QT syndrome. FEBS Letters 583, 890–896.

Huang, H., Zhao, J., Barrane, F.Z., Champagne, J., Chahine, M., 2006. NaV1.5/R1193Q polymorphism is associated with both long QT and Brugada syndromes. Canadian Journal of Cardiology 22, 309–313.

Hucka, M., Finney, A., Sauro, H.M., Bolouri, H., Doyle, J.C., Kitano, H., Arkin, A.P., Bornstein, B.J., Bray, D., Cornish-Bowden, A., et al., 2003. The systems biology markup language (SBML): a medium for representation and exchange of biochemical network models. Bioinformatics 19, 524–531.

Hund, T.J., Rudy, Y., 2004. Rate dependence and regulation of action potential and calcium transient in a canine cardiac ventricular cell model. Circulation 110, 3168–3174.

Hunter, J.D., 2007. Matplotlib: A 2D graphics environment. Computing in Science & Engineering 9, 90–95.

Hunter, P., 2004. The IUPS Physiome project: a framework for computational physiology. Progress in Biophysics and Molecular Biology 85, 551–569.

Huxley, A., 2002. From overshoot to voltage clamp. Trends in Neurosciences 25, 553–558.

Inada, S., Hancox, J., Zhang, H., Boyett, M., 2009. One-dimensional mathematical model of the atrioventricular node including atrio-nodal, nodal, and nodal-his cells. Biophysical Journal 97, 2117–2127.

Iribe, G., Kohl, P., Noble, D., 2006. Modulatory effect of calmodulin-dependent kinase II (CaMKII) on sarcoplasmic reticulum Ca2+ handling and interval-force relations: a modelling study. Philosophical Transactions of the Royal Society of London A: Mathematical, Physical and Engineering Sciences 364, 1107–1133.

Irvine, L.A., Saleet Jafri, M., Winslow, R.L., 1999. Cardiac sodium channel Markov model with temperature dependence and recovery from inactivation. Biophysical Journal 76, 1868–1885.

Itoh, H., Shimizu, M., Mabuchi, H., Imoto, K., 2005a. Clinical and electrophysiological characteristics of Brugada syndrome caused by a missense mutation in the S5-pore site of SCN5A. Journal of Cardiovascular Electrophysiology 16, 378–383.

Itoh, H., Shimizu, M., Takata, S., Mabuchi, H., Imoto, K., 2005b. A novel missense mutation in the SCN5A gene associated with Brugada syndrome bidirectionally affecting blocking actions of antiarrhythmic drugs. Journal of Cardiovascular Electrophysiology 16, 486–493.

Itoh, H., Tsuji, K., Sakaguchi, T., Nagaoka, I., Oka, Y., Nakazawa, Y., Yao, T., Jo, H., Ashihara, T., Ito, M., et al., 2007. A paradoxical effect of lidocaine for the N406S mutation of SCN5A associated with Brugada syndrome. International Journal of Cardiology 121, 239–248.

Iyer, V., Mazhari, R., Winslow, R.L., 2004. A computational model of the human left-ventricular epicardial myocyte. Biophysical Journal 87, 1507–1525.

John, G.H., Langley, P., 1995. Estimating continuous distributions in bayesian classifiers, in: Proceedings of the Eleventh conference on Uncertainty in artificial intelligence, Morgan Kaufmann Publishers Inc. pp. 338–345.

Johnstone, R.H., Chang, E.T., Bardenet, R., De Boer, T.P., Gavaghan, D.J., Pathmanathan, P., Clayton, R.H., Mirams, G.R., 2016. Uncertainty and variability in models of the cardiac action potential: Can we build trustworthy models? Journal of Molecular and Cellular Cardiology 96, 49–62.

Jones, E., Oliphant, T., Peterson, P., et al., 2001. SciPy: Open source scientific tools for Python. [Online; accessed 2015-01-14].

Joyner, D., Čertík, O., Meurer, A., Granger, B.E., 2012. Open source computer algebra systems: SymPy. ACM Communications in Computer Algebra 45, 225–234.

Juang, J.M.J., Lu, T.P., Lai, L.C., Hsueh, C.H., Liu, Y.B., Tsai, C.T., Lin, L.Y., Yu, C.C., Hwang, J.J., Chiang, F.T., et al., 2014. Utilizing multiple in silico analyses to identify putative causal SCN5A variants in Brugada syndrome. Scientific Reports 4, 3850.

Kambouris, N.G., Nuss, H.B., Johns, D.C., Marbán, E., Tomaselli, G.F., Balser, J.R., 2000. A

revised view of cardiac sodium channel “blockade” in the long-QT syndrome. The Journal of Clinical Investigation 105, 1133–1140.

Kapa, S., Tester, D.J., Salisbury, B.A., Harris-Kerr, C., Pungliya, M.S., Alders, M., Wilde, A.A., Ackerman, M.J., 2009. Genetic testing for long-QT syndrome distinguishing pathogenic mutations from benign variants. Circulation 120, 1752–1760.

Kapplinger, J., Giudicessi, J., Ye, D., Tester, D., Callis, T., Valdivia, C., Makielski, J., Wilde, A., Ackerman, M., 2015. Enhanced classification of Brugada syndrome-associated and long-QT syndrome-associated genetic variants in the SCN5A-encoded Na(v)1.5 cardiac sodium channel. Circulation: Cardiovascular Genetics 8, 582–595.

Kapplinger, J.D., Tester, D.J., Alders, M., Benito, B., Berthet, M., Brugada, J., Brugada, P., Fressart, V., Guerchicoff, A., Harris-Kerr, C., et al., 2010. An international compendium of mutations in the SCN5A-encoded cardiac sodium channel in patients referred for Brugada syndrome genetic testing. Heart Rhythm 7, 33–46.

Kato, K., Makiyama, T., Wu, J., Ding, W.G., Kimura, H., Naiki, N., Ohno, S., Itoh, H., Nakanishi, T., Matsuura, H., et al., 2014. Cardiac channelopathies associated with infantile fatal ventricular arrhythmias: from the cradle to the bench. Journal of Cardiovascular Electrophysiology 25, 66–73.

Katz, B., Miledi, R., 1972. The statistical nature of the acetylcholine potential and its molecular components. The Journal of Physiology 224, 665–699.

Kauferstein, S., Kiehne, N., Peigneur, S., Tytgat, J., Bratzke, H., 2013. Cardiac channelopathy causing sudden death as revealed by molecular autopsy. International Journal of Legal Medicine 127, 145–151.

Keener, J., Sneyd, J., 2009. Mathematical Physiology. Interdisciplinary Applied Mathematics: Mathematical Biology, Springer.

Keller, D.I., Huang, H., Zhao, J., Frank, R., Suarez, V., Delacrétaz, E., Brink, M., Osswald, S., Schwick, N., Chahine, M., 2006. A novel SCN5A mutation, F1344S, identified in a patient with Brugada syndrome and fever-induced ventricular fibrillation. Cardiovascular Research 70, 521–529.

Keller, D.I., Rougier, J.S., Kucera, J.P., Benammar, N., Fressart, V., Guicheney, P., Madle, A., Fromer, M., Schläpfer, J., Abriel, H., 2005. Brugada syndrome and fever: genetic and molecular characterization of patients carrying SCN5A mutations. Cardiovascular Research 67, 510–519.

Kinoshita, K., Takahashi, H., Hata, Y., Nishide, K., Kato, M., Fujita, H., Yoshida, S., Murai, K., Mizumaki, K., Nishida, K., et al., 2016. SCN5A (K817E), a novel Brugada syndrome–associated mutation that alters the activation gating of NaV1.5 channel. Heart Rhythm 13, 1113–1120.

Kléber, A.G., Rudy, Y., 2004. Basic mechanisms of cardiac impulse propagation and associated arrhythmias. Physiological Reviews 84, 431–488.

Kline, R., 1993. Harold Black and the negative-feedback amplifier. Control Systems, IEEE 13, 82–85.

Kneller, J., Ramirez, R.J., Chartier, D., Courtemanche, M., Nattel, S., 2002. Time-dependent tran-

sients in an ionically based mathematical model of the canine atrial action potential. American Journal of Physiology – Heart and Circulatory Physiology 282, H1437–H1451.

Kohl, P., Crampin, E.J., Quinn, T., Noble, D., 2010. Systems biology: an approach. Clinical Pharmacology & Therapeutics 88, 25–33.

Koivumäki, J.T., Korhonen, T., Takalo, J., Weckström, M., Tavi, P., 2009. Regulation of excitation-contraction coupling in mouse cardiac myocytes: integrative analysis with mathematical modelling. BMC Physiology 9, 16.

Kovacs, J.M., Mant, C.T., Hodges, R.S., 2006. Determination of intrinsic hydrophilicity/hydrophobicity of amino acid side chains in peptides in the absence of nearest-neighbor or conformational effects. Peptide Science 84, 283–297.

Krogh-Madsen, T., Sobie, E.A., Christini, D.J., 2016. Improving cardiomyocyte model fidelity and utility via dynamic electrophysiology protocols and optimization algorithms. The Journal of Physiology .

Kurata, Y., Hisatome, I., Imanishi, S., Shibamoto, T., 2002. Dynamical description of sinoatrial node pacemaking: improved mathematical model for primary pacemaker cell. American Journal of Physiology – Heart and Circulatory Physiology 283, H2074–H2101.

Kyndt, F., Probst, V., Potet, F., Demolombe, S., Chevallier, J.C., Baro, I., Moisan, J.P., Boisseau, P., Schott, J.J., Escande, D., et al., 2001. Novel SCN5A mutation leading either to isolated cardiac conduction defect or Brugada syndrome in a large French family. Circulation 104, 3081–3086.

Larkin, M.A., Blackshields, G., Brown, N., Chenna, R., McGettigan, P.A., McWilliam, H., Valentin, F., Wallace, I.M., Wilm, A., Lopez, R., et al., 2007. Clustal W and Clustal X version 2.0. Bioinformatics 23, 2947–2948.

Laurent, G., Saal, S., Amarouch, M.Y., Béziau, D.M., Marsman, R.F., Faivre, L., Barc, J., Dina, C., Bertaux, G., Barthez, O., et al., 2012. Multifocal ectopic Purkinje-related premature contractions: A new SCN5A-related cardiac channelopathy. Journal of the American College of Cardiology 60, 144–156.

Law, R., Levin, M., 2015. Bioelectric memory: modeling resting potential bistability in amphibian embryos and mammalian cells. Theoretical Biology and Medical Modelling 12, 1.

Lee, J., Smaill, B., Smith, N., 2006. Hodgkin–Huxley type ion channel characterization: an improved method of voltage clamp experiment parameter estimation. Journal of Theoretical Biology 242, 123–134.

Leon, L.J., Horáček, B.M., 1991. Computer model of excitation and recovery in the anisotropic myocardium: I. Rectangular and cubic arrays of excitable elements. Journal of Electrocardiology 24, 1–15.

Leong, I.U., Stuckey, A., Lai, D., Skinner, J.R., Love, D.R., 2015. Assessment of the predictive accuracy of five in silico prediction tools, alone or in combination, and two metaservers to classify long QT syndrome gene mutations. BMC Medical Genetics 16, 1.

Li, L., Niederer, S., Idigo, W., Zhang, Y., Swietach, P., Casadei, B., Smith, N., 2010. A mathematical model of the murine ventricular myocyte: a data-driven biophysically based approach applied

to mice overexpressing the canine NCX isoform. American Journal of Physiology – Heart and Circulatory Physiology 299, H1045–H1063.

Li, P., Rudy, Y., 2011. A model of canine Purkinje cell electrophysiology and Ca2+ cycling rate dependence, triggered activity, and comparison to ventricular myocytes. Circulation Research 109, 71–79.

Li, Q., Huang, H., Liu, G., Lam, K., Rutberg, J., Green, M.S., Birnie, D.H., Lemery, R., Chahine, M., Gollob, M.H., 2009. Gain-of-function mutation of NaV1.5 in atrial fibrillation enhances cellular excitability and lowers the threshold for action potential firing. Biochemical and Biophysical Research Communications 380, 132–137.

Lin, M.T., Wu, M.H., Chang, C.C., Chiu, S.N., Thériault, O., Huang, H., Christé, G., Ficker, E., Chahine, M., 2008. In utero onset of long QT syndrome with atrioventricular block and spontaneous or lidocaine-induced ventricular tachycardia: compound effects of hERG pore region mutation and SCN5A N-terminus variant. Heart Rhythm 5, 1567–1574.

Liu, C.j., Dib-Hajj, S.D., Renganathan, M., Cummins, T.R., Waxman, S.G., 2003. Modulation of the cardiac sodium channel NaV1.5 by fibroblast growth factor homologous factor 1B. Journal of Biological Chemistry 278, 1029–1036.

Liu, H., Tateyama, M., Clancy, C.E., Abriel, H., Kass, R.S., 2002. Channel openings are necessary but not sufficient for use-dependent block of cardiac Na+ channels by flecainide evidence from the analysis of disease-linked mutations. The Journal of General Physiology 120, 39–51.

Liu, K., Yang, T., Viswanathan, P.C., Roden, D.M., 2005. New mechanism contributing to drug-induced arrhythmia rescue of a misprocessed LQT3 mutant. Circulation 112, 3239–3246.

Livshitz, L.M., Rudy, Y., 2007. Regulation of Ca2+ and electrical alternans in cardiac myocytes: role of CAMKII and repolarizing currents. American Journal of Physiology – Heart and Circulatory Physiology 292, H2854–H2866.

Loewe, A., Wilhelms, M., Fischer, F., Scholz, E., Dössel, O., 2013. Impact of hERG mutations on simulated human atrial action potentials. Biomedical Engineering / Biomedizinische Technik 58.

Loewe, A., Wilhelms, M., Schmid, J., Krause, M.J., Fischer, F., Thomas, D., Scholz, E.P., Dössel, O., Seemann, G., 2016. Parameter estimation of ion current formulations requires hybrid optimization approach to be both accurate and reliable. Frontiers in Bioengineering and Biotechnology 3, 1–13.

Lombardo, D.M., Fenton, F.H., Narayan, S.M., Rappel, W.J., 2016. Comparison of detailed and simplified models of human atrial myocytes to recapitulate patient specific properties. PLOS Computational Biology 12, 1–15.

Lopez-Rincon, A., Bendahmane, M., Ainseba, B., 2015. On 3d numerical inverse problems for the bidomain model in electrocardiology. Computers & Mathematics with Applications 69, 255–274.

Lovell, N.H., Cloherty, S.L., Celler, B.G., Dokos, S., 2004. A gradient model of cardiac pacemaker myocytes. Progress in Biophysics and Molecular Biology 85, 301–323.

Luo, C.H., Rudy, Y., 1991. A model of the ventricular cardiac action potential. depolarization, repolarization, and their interaction. Circulation Research 68, 1501–1526.

Lupoglazoff, J., Cheav, T., Baroudi, G., Berthet, M., Denjoy, I., Cauchemez, B., Extramiana, F., Chahine, M., Guicheney, P., 2001. Homozygous SCN5A mutation in long-QT syndrome with functional two-to-one atrioventricular block. Circulation Research 89, e16–e21.

Ma, D., Wei, H., Zhao, Y., Lu, J., Li, G., Sahib, N.B.E., Tan, T.H., Wong, K.Y., Shim, W., Wong, P., et al., 2013. Modeling type 3 long QT syndrome with cardiomyocytes derived from patient-specific induced pluripotent stem cells. International Journal of Cardiology 168, 5277–5286.

Maastricht University Board of Deans, 2013. Regulation governing the attainment of doctoral degrees.

MacLeod, R.S., Brooks, D.H., 1998. Recent progress in inverse problems in electrocardiology. Engineering in Medicine and Biology Magazine, IEEE 17, 73–83.

Mahajan, A., Shiferaw, Y., Sato, D., Baher, A., Olcese, R., Xie, L.H., Yang, M.J., Chen, P.S., Restrepo, J.G., Karma, A., Garfinkel, A., Qu, Z., Weiss, J.N., 2008. A rabbit ventricular action potential model replicating cardiac dynamics at rapid heart rates. Biophysical Journal 94, 392–410.

Makielski, J.C., Ye, B., Valdivia, C.R., Pagel, M.D., Pu, J., Tester, D.J., Ackerman, M.J., 2003. A ubiquitous splice variant and a common polymorphism affect heterologous expression of recombinant human SCN5A heart sodium channels. Circulation Research 93, 821–828.

Makita, N., Behr, E., Shimizu, W., Horie, M., Sunami, A., Crotti, L., Schulze-Bahr, E., Fukuhara, S., Mochizuki, N., Makiyama, T., et al., 2008. The E1784K mutation in SCN5A is associated with mixed clinical phenotype of type 3 long QT syndrome. The Journal of Clinical Investigation 118, 2219–2229.

Makita, N., Horie, M., Nakamura, T., Ai, T., Sasaki, K., Yokoi, H., Sakurai, M., Sakuma, I., Otani, H., Sawa, H., et al., 2002. Drug-induced long-QT syndrome associated with a subclinical SCN5A mutation. Circulation 106, 1269–1274.

Makita, N., Sasaki, K., Groenewegen, W.A., Yokota, T., Yokoshiki, H., Murakami, T., Tsutsui, H., 2005. Congenital atrial standstill associated with coinheritance of a novel SCN5A mutation and connexin 40 polymorphisms. Heart Rhythm 2, 1128–1134.

Makita, N., Shirai, N., Nagashima, M., Matsuoka, R., Yamada, Y., Tohse, N., Kitabatake, A., 1998. A de novo missense mutation of human cardiac Na+ channel exhibiting novel molecular mechanisms of long QT syndrome. FEBS Letters 423, 5–9.

Makiyama, T., Akao, M., Shizuta, S., Doi, T., Nishiyama, K., Oka, Y., Ohno, S., Nishio, Y., Tsuji, K., Itoh, H., et al., 2008. A novel SCN5A gain-of-function mutation M1875T associated with familial atrial fibrillation. Journal of the American College of Cardiology 52, 1326–1334.

Maleckar, M.M., Greenstein, J.L., Trayanova, N.A., Giles, W.R., 2008. Mathematical simulations of ligand-gated and cell-type specific effects on the action potential of human atrium. Progress in Biophysics and Molecular Biology 98, 161–170.

Maltsev, V.A., Kyle, J.W., Mishra, S., Undrovinas, A., 2008. Molecular identity of the late sodium current in adult dog cardiomyocytes identified by Nav1.5 antisense inhibition. American Journal of Physiology – Heart and Circulatory Physiology 295, H667–H676.

Mangoni, M.E., Couette, B., Marger, L., Bourinet, E., Striessnig, J., Nargeot, J., 2006. Voltage-dependent calcium channels and cardiac pacemaker activity: from ionic currents to genes. Progress in Biophysics and Molecular Biology 90, 38–63.

Mann, S.A., Castro, M.L., Ohanian, M., Guo, G., Zodgekar, P., Sheu, A., Stockhammer, K., Thompson, T., Playford, D., Subbiah, R., et al., 2012. R222Q SCN5A mutation is associated with reversible ventricular ectopy and dilated cardiomyopathy. Journal of the American College of Cardiology 60, 1566–1573.

Mann, S.A., Imtiaz, M., Winbo, A., Rydberg, A., Perry, M.D., Couderc, J.P., Polonsky, B., McNitt, S., Zareba, W., Hill, A.P., et al., 2016. Convergence of models of human ventricular myocyte electrophysiology after global optimization to recapitulate clinical long QT phenotypes. Journal of Molecular and Cellular Cardiology 100, 25–34.

Marangoni, S., Di Resta, C., Rocchetti, M., Barile, L., Rizzetto, R., Summa, A., Severi, S., Sommariva, E., Pappone, C., Ferrari, M., et al., 2011. A Brugada syndrome mutation (p.S216L) and its modulation by p.H558R polymorphism: standard and dynamic characterization. Cardiovascular Research 91, 606–616.

Marder, E., Goaillard, J.M., 2006. Variability, compensation and homeostasis in neuron and network function. Nature Reviews Neuroscience 7, 563–574.

Marsh, M.E., Ziaratgahi, S.T., Spiteri, R.J., 2012. The secrets to the success of the Rush–Larsen method and its generalizations. IEEE Transactions on Biomedical Engineering 59, 2506–2515.

Mason, S.J., Graham, N.E., 2002. Areas beneath the relative operating characteristics (roc) and relative operating levels (rol) curves: Statistical significance and interpretation. Quarterly Journal of the Royal Meteorological Society 128, 2145–2166.

Matsuoka, S., Sarai, N., Kuratomi, S., Ono, K., Noma, A., 2003. Role of individual ionic current systems in ventricular cells hypothesized by a model study. The Japanese Journal of Physiology 53, 105–123.

Mayer, J., Khairy, K., Howard, J., 2010. Drawing an elephant with four complex parameters. American Journal of Physics 78, 648–649.

McDowell, K.S., Vadakkumpadan, F., Blake, R., Blauer, J., Plank, G., MacLeod, R.S., Trayanova, N.A., 2012. Methodology for patient-specific modeling of atrial fibrosis as a substrate for atrial fibrillation. Journal of Electrocardiology 45, 640–645.

McKay, M., Beckman, R., Conover, W., 1979. A comparison of three methods for selecting values of input variables in the analysis of output from a computer code. Technometrics 21, 239–245.

Medeiros-Domingo, A., Kaku, T., Tester, D.J., Iturralde-Torres, P., Itty, A., Ye, B., Valdivia, C., Ueda, K., Canizales-Quinteros, S., Tusié-Luna, M.T., et al., 2007. SCN4B-encoded sodium channel $\beta 4$ subunit in congenital long-QT syndrome. Circulation 116, 134–142.

Medeiros-Domingo, A., Tan, B.H., Iturralde-Torres, P., Tester, D.J., Tusié-Luna, T., Makielski, J.C., Ackerman, M.J., 2009. Unique mixed phenotype and unexpected functional effect revealed by novel compound heterozygosity mutations involving SCN5A. Heart Rhythm 6, 1170–1175.

Michailova, A., Saucerman, J., Belik, M.E., McCulloch, A.D., 2005. Modeling regulation of cardiac

K-ATP and L-type Ca2+ currents by ATP, ADP, and Mg2+. Biophysical Journal 88, 2234–2249.

Milanič, M., Jazbinšek, V., MacLeod, R.S., Brooks, D.H., et al., 2014. Assessment of regularization techniques for electrocardiographic imaging. Journal of Electrocardiology 47, 20–28.

Miller, A.K., Marsh, J., Reeve, A., Garny, A., Britten, R., Halstead, M., Cooper, J., Nickerson, D.P., Nielsen, P.F., 2010. An overview of the CellML API and its implementation. BMC Bioinformatics 11.

Mines, G.R., 1913. On dynamic equilibrium in the heart. The Journal of Physiology 46, 349–383.

Mirams, G.R., Arthurs, C.J., Bernabeu, M.O., Bordas, R., Cooper, J., Corrias, A., Davit, Y., Dunn, S.J., Fletcher, A.G., Harvey, D.G., et al., 2013. Chaste: an open source C++ library for computational physiology and biology. PLOS Computational Biology 9, e1002970.

Mirams, G.R., Pathmanathan, P., Gray, R.A., Challenor, P., Clayton, R.H., 2016. White paper: Uncertainty and variability in computational and mathematical models of cardiac physiology. The Journal of Physiology (published ahead of print).

Mirin, A.A., Richards, D.F., Glosli, J.N., Draeger, E.W., Chan, B., Fattebert, J.l., Krauss, W.D., Oppelstrup, T., Rice, J.J., Gunnels, J.A., et al., 2012. Toward real-time modeling of human heart ventricles at cellular resolution: simulation of drug-induced arrhythmias, in: Proceedings of the International Conference on High Performance Computing, Networking, Storage and Analysis, IEEE Computer Society Press. p. 2.

Mitchell, C.C., Schaeffer, D.G., 2003. A two-current model for the dynamics of cardiac membrane. Bulletin of Mathematical Biology 65, 767–793.

Mohler, P.J., Rivolta, I., Napolitano, C., LeMaillet, G., Lambert, S., Priori, S.G., Bennett, V., 2004. NaV1.5 E1053K mutation causing Brugada syndrome blocks binding to ankyrin-G and expression of NaV1.5 on the surface of cardiomyocytes. Proceedings of the National Academy of Sciences of the United States of America 101, 17533–17538.

Mok, N.S., Priori, S.G., Napolitano, C., Chan, N.Y., Chahine, M., Baroudi, G., 2003. A newly characterized SCN5A mutation underlying Brugada syndrome unmasked by hyperthermia. Journal of Cardiovascular Electrophysiology 14, 407–411.

Molleman, A., 2003. Patch clamping: an introductory guide to patch clamp electrophysiology. John Wiley & Sons.

Moraru, I.I., Schaff, J.C., Slepchenko, B.M., Blinov, M., Morgan, F., Lakshminarayana, A., Gao, F., Li, Y., Loew, L.M., 2008. Virtual Cell modelling and simulation software environment. IET Systems Biology 2, 352–362.

Moreau, A., Krahn, A.D., Gosselin-Badaroudine, P., Klein, G.J., Christé, G., Vincent, Y., Boutjdir, M., Chahine, M., 2013. Sodium overload due to a persistent current that attenuates the arrhythmogenic potential of a novel LQT3 mutation. Frontiers in Pharmacology 4, 126.

Moric, E., Herbert, E., Trusz-Gluza, M., Filipecki, A., Mazurek, U., Wilczok, T., 2003. The implications of genetic mutations in the sodium channel gene (SCN5A). Europace 5, 325–334.

Morris, C., Lecar, H., 1981. Voltage oscillations in the barnacle giant muscle fiber. Biophysical

Journal 35, 193–213.

Morris, C.E., Juranka, P.F., 2007. NaV channel mechanosensitivity: activation and inactivation accelerate reversibly with stretch. Biophysical Journal 93, 822–833.

Motoike, H.K., Liu, H., Glaaser, I.W., Yang, A.S., Tateyama, M., Kass, R.S., 2004. The Na+ channel inactivation gate is a molecular complex a novel role of the COOH-terminal domain. The Journal of General Physiology 123, 155–165.

Murphy, L.L., Moon-Grady, A.J., Cuneo, B.F., Wakai, R.T., Yu, S., Kunic, J.D., Benson, D.W., George, A.L., 2012. Developmentally regulated SCN5A splice variant potentiates dysfunction of a novel mutation associated with severe fetal arrhythmia. Heart Rhythm 9, 590–597.

Musa, H., Kline, C.F., Sturm, A.C., Murphy, N., Adelman, S., Wang, C., Yan, H., Johnson, B.L., Csepe, T.A., Kilic, A., et al., 2015. SCN5A variant that blocks fibroblast growth factor homologous factor regulation causes human arrhythmia. Proceedings of the National Academy of Sciences 112, 12528–12533.

Muszkiewicz, A., Britton, O.J., Gemmell, P., Passini, E., Sánchez, C., Zhou, X., Carusi, A., Quinn, T.A., Burrage, K., Bueno-Orovio, A., et al., 2016. Variability in cardiac electrophysiology: Using experimentally-calibrated populations of models to move beyond the single virtual physiological human paradigm. Progress in Biophysics and Molecular Biology 120, 115–127.

Nademanee, K., Veerakul, G., Chandanamattha, P., Chaothawee, L., Ariyachaipanich, A., Jirasirirojanakorn, K., Likittanasombat, K., Bhuripanyo, K., Ngarmukos, T., 2011. Prevention of ventricular fibrillation episodes in Brugada syndrome by catheter ablation over the anterior right ventricular outflow tract epicardium. Circulation 123, 1270–1279.

Nagatomo, T., Fan, Z., Ye, B., Tonkovich, G., January, C., Kyle, J., Makielski, J., 1998. Temperature dependence of early and late currents in human cardiac wild-type and long QT DeltaKPQ Na+ channels. American Journal of Physiology 275, H2016–H2024.

Nair, K., Pekhletski, R., Harris, L., Care, M., Morel, C., Farid, T., Backx, P.H., Szabo, E., Nanthakumar, K., 2012. Escape capture bigeminy: phenotypic marker of cardiac sodium channel voltage sensor mutation R222Q. Heart Rhythm 9, 1681–1688.

Nakajima, T., Kaneko, Y., Saito, A., Ota, M., Iijima, T., Kurabayashi, M., 2015. Enhanced fast-inactivated state stability of cardiac sodium channels by a novel voltage sensor SCN5A mutation, R1632C, as a cause of atypical Brugada syndrome. Heart Rhythm 12, 2296–2304.

Napolitano, C., Rivolta, I., Priori, S.G., 2003. Cardiac sodium channel diseases. Clinical Chemistry and Laboratory Medicine 41, 439–444.

Neher, E., Sakmann, B., 1976. Single-channel currents recorded from membrane of denervated frog muscle fibres. Nature 260, 799–802.

Nelder, J.A., Mead, R., 1965. A simplex method for function minimization. The Computer Journal 7, 308–313.

Neu, A., Eiselt, M., Paul, M., Sauter, K., Stallmeyer, B., Isbrandt, D., Schulze-Bahr, E., 2010. A homozygous SCN5A mutation in a severe, recessive type of cardiac conduction disease. Human Mutation 31, E1609–E1621.

Nguyen, T.P., Wang, D.W., Rhodes, T.H., George, A.L., 2008. Divergent biophysical defects caused by mutant sodium channels in dilated cardiomyopathy with arrhythmia. Circulation Research 102, 364–371.

Nickerson, D.P., Ladd, D., Hussan, J.R., Safaei, S., Suresh, V., Hunter, P.J., Bradley, C.P., 2015. Using CellML with OpenCMISS to simulate multi-scale physiology. Frontiers in Bioengineering and Biotechnology 2.

Niederer, S., Fink, M., Noble, D., Smith, N., 2009. A meta-analysis of cardiac electrophysiology computational models. Experimental Physiology 94, 486–495.

Niederer, S., Smith, N., 2007. A mathematical model of the slow force response to stretch in rat ventricular myocytes. Biophysical Journal 92, 4030–4044.

Nivala, M., de Lange, E., Rovetti, R., Qu, Z., 2012. Computational modeling and numerical methods for spatiotemporal calcium cycling in ventricular myocytes. Frontiers in Physiology 3.

Nobel Media, 1963a. Alan L. Hodgkin - Biographical [internet]. www.nobelprize.org. Accessed: 2016-06-10.

Nobel Media, 1963b. Andrew F. Huxley - Biographical [internet]. www.nobelprize.org. Accessed: 2016-06-10.

Nobel Media, 1991a. Bert Sakmann - Biographical [internet]. www.nobelprize.org. Accessed: 2016-06-10.

Nobel Media, 1991b. Erwin Neher - Biographical [internet]. www.nobelprize.org. Accessed: 2016-06-10.

Noble, D., 1960. Cardiac action and pacemaker potentials based on the Hodgkin-Huxley equations. Nature 188, 495–497.

Noble, D., 1962. A modification of the Hodgkin-Huxley equations applicable to Purkinje fibre action and pacemaker potentials. The Journal of Physiology 160, 317–352.

Noble, D., 2017. Dance to the Tune of Life: Biological Relativity. Cambridge University Press.

Noble, D., Garny, A., Noble, P.J., 2012. How the Hodgkin-Huxley equations inspired the cardiac physiome project. The Journal of Physiology 590, 2613–2628.

Noble, D., Rudy, Y., 2001. Models of cardiac ventricular action potentials: iterative interaction between experiment and simulation. Philosophical Transactions of the Royal Society of London A: Mathematical, Physical and Engineering Sciences 359, 1127–1142.

Noda, M., Ikeda, T., Suzuki, H., Takeshima, H., Takahashi, T., Kuno, M., Numa, S., 1986. Expression of functional sodium channels from cloned cDNA. Nature 322, 826–828.

Noda, M., Shimizu, S., Tanabe, T., Takai, T., Kayano, T., Ikeda, T., Takahashi, H., Nakayama, H., Kanaoka, Y., Minamino, N., 1984. Primary structure of Electrophorus electricus sodium channel deduced from cDNA sequence. Nature 312, 121–127.

Núñez, L., Barana, A., Amorós, I., de la Fuente, M.G., Dolz-Gaitón, P., Gómez, R., Rodríguez-García, I., Mosquera, I., Monserrat, L., Delpón, E., et al., 2013. p.D1690N NaV1.5 rescues p.G1748D mutation gating defects in a compound heterozygous Brugada syndrome patient. Heart

Rhythm 10, 264–272.

O'Hara, T., Virág, L., Varró, A., Rudy, Y., 2011. Simulation of the undiseased human cardiac ventricular action potential: model formulation and experimental validation. PLOS Computational Biology 7, e1002061.

O'Leary, M., Digregorio, M., Chahine, M., 2002. Closing and inactivation potentiate the cocaethylene inhibition of cardiac sodium channels by distinct mechanisms. Molecular Pharmacology 64, 1575–1585.

Olesen, M.S., Yuan, L., Liang, B., Holst, A.G., Nielsen, N., Nielsen, J.B., Hedley, P.L., Christiansen, M., Olesen, S.P., Haunsø, S., et al., 2012. High prevalence of long QT syndrome associated SCN5A variants in patients with early-onset lone atrial fibrillation. Circulation: Cardiovascular Genetics 5, 450.

Olivetti, G., Giordano, G., Corradi, D., Melissari, M., Lagrasta, C., Gambert, Anversa, P., 1995. Gender differences and aging: effects on the human heart. Journal of the American College of Cardiology 26, 1068–1079.

Onal, B., Gratz, D., Hund, T., 2016. LongQt: A cardiac electrophysiology simulation platform. MethodsX 3, 589–599.

van Oosterom, A., 1999. The use of the spatial covariance in computing pericardial potentials. IEEE Transactions on Biomedical Engineering 46, 778–787.

van Oosterom, A., 2012a. Closed-form analytical expressions for the potential fields generated by triangular monolayers with linearly distributed source strength. Medical & Biological Engineering & Computing 50, 1–9.

van Oosterom, A., 2012b. The inverse problem of bioelectricity: an evaluation. Medical & Biological Engineering & Computing 50, 891–902.

Otagiri, T., Kijima, K., Osawa, M., Ishii, K., Makita, N., Matoba, R., Umetsu, K., Hayasaka, K., 2008. Cardiac ion channel gene mutations in sudden infant death syndrome. Pediatric Research 64, 482–487.

Pace, C.N., Scholtz, J.M., 1998. A helix propensity scale based on experimental studies of peptides and proteins. Biophysical Journal 75, 422–427.

Pandit, S.V., Giles, W.R., Demir, S.S., 2003. A mathematical model of the electrophysiological alterations in rat ventricular myocytes in type-I diabetes. Biophysical Journal 84, 832–841.

Panfilov, A., Holden, A., 1993. Computer simulation of re-entry sources in myocardium in two and three dimensions. Journal of Theoretical Biology 161, 271–285.

Panfilov, A., Vasiev, B., 1991. Vortex initiation in a heterogeneous excitable medium. Physica D: Nonlinear Phenomena 49, 107–113.

Parekh, A., Buckman-Garner, S., McCune, S., ONeill, R., Geanacopoulos, M., Amur, S., Clingman, C., Barratt, R., Rocca, M., Hills, I., et al., 2015. Catalyzing the critical path initiative: FDA's progress in drug development activities. Clinical Pharmacology & Therapeutics 97, 221–233.

Park, D.S., Shekhar, A., Marra, C., Lin, X., Vasquez, C., Solinas, S., Kelley, K., Morley, G.,

Goldfarb, M., Fishman, G.I., 2016. Fhf2 gene deletion causes temperature-sensitive cardiac conduction failure. Nature Communications 7, 12966.

Pásek, M., Šimurda, J., Christé, G., 2006. The functional role of cardiac t-tubules explored in a model of rat ventricular myocytes. Philosophical Transactions of the Royal Society of London A: Mathematical, Physical and Engineering Sciences 364, 1187–1206.

Pásek, M., Šimurda, J., Orchard, C.H., Christé, G., 2008. A model of the guinea-pig ventricular cardiac myocyte incorporating a transverse-axial tubular system. Progress in Biophysics and Molecular Biology 96, 258–280.

Passini, E., Mincholé, A., Coppini, R., Cerbai, E., Rodriguez, B., Severi, S., Bueno-Orovio, A., 2016. Mechanisms of pro-arrhythmic abnormalities in ventricular repolarisation and anti-arrhythmic therapies in human hypertrophic cardiomyopathy. Journal of Molecular and Cellular Cardiology 96, 72–81.

Pathmanathan, P., Shotwell, M.S., Gavaghan, D.J., Cordeiro, J.M., Gray, R.A., 2015. Uncertainty quantification of fast sodium current steady-state inactivation for multi-scale models of cardiac electrophysiology. Progress in Biophysics and Molecular Biology 117, 4–18.

Payandeh, J., Scheuer, T., Zheng, N., Catterall, W.A., 2011. The crystal structure of a voltage-gated sodium channel. Nature 475, 353–358.

Petitprez, S., Jespersen, T., Pruvot, E., Keller, D.I., Corbaz, C., Schläpfer, J., Abriel, H., Kucera, J.P., 2008. Analyses of a novel SCN5A mutation (C1850S): conduction vs. repolarization disorder hypotheses in the Brugada syndrome. Cardiovascular Research 78, 494–504.

Pfahnl, A.E., Viswanathan, P.C., Weiss, R., Shang, L.L., Sanyal, S., Shusterman, V., Kornblit, C., London, B., Dudley, S.C., 2007. A sodium channel pore mutation causing Brugada syndrome. Heart Rhythm 4, 46–53.

Podziemski, P., Żebrowski, J.J., 2013. A simple model of the right atrium of the human heart with the sinoatrial and atrioventricular nodes included. Journal of Clinical Monitoring and Computing 27, 481–498.

Poelzing, S., Forleo, C., Samodell, M., Dudash, L., Sorrentino, S., Anaclerio, M., Troccoli, R., Iacoviello, M., Romito, R., Guida, P., et al., 2006. SCN5A polymorphism restores trafficking of a Brugada syndrome mutation on a separate gene. Circulation 114, 368–376.

Van der Pol, B., Van der Mark, J., 1928. The heartbeat considered as a relaxation oscillation, and an electrical model of the heart. The London, Edinburgh, and Dublin Philosophical Magazine and Journal of Science 6, 763–775.

Potet, F., Mabo, P., Le Coq, G., Probst, V., Schott, J.J., Airaud, F., Guihard, G., Daubert, J.C., Escande, D., Le Marec, H., 2003. Novel Brugada SCN5A mutation leading to ST segment elevation in the inferior or the right precordial leads. Journal of Cardiovascular Electrophysiology 14, 200–203.

Prudat, Y., Kucera, J.P., 2014. Nonlinear behaviour of conduction and block in cardiac tissue with heterogeneous expression of connexin 43. Journal of Molecular and Cellular Cardiology 76, 46–54.

Pullan, A.J., Cheng, L.K., Buist, M.L., 2005. Mathematically modelling the electrical activity of

the heart: From cell to body surface and back again. World Scientific.

Meijer van Putten, R., Mengarelli, I., Guan, K., Zegers, J.G., van Ginneken, A., Verkerk, A.O., Wilders, R., 2014. Ion channelopathies in human induced pluripotent stem cell derived cardiomyocytes: a dynamic clamp study with virtual IK1. Frontiers in Physiology 6, 7–7.

Quinn, T., Granite, S., Allessie, M., Antzelevitch, C., Bollensdorff, C., Bub, G., Burton, R., Cerbai, E., Chen, P., Delmar, M., et al., 2011. Minimum information about a cardiac electrophysiology experiment (MICEE): standardised reporting for model reproducibility, interoperability, and data sharing. Progress in Biophysics and Molecular Biology 107, 4–10.

Quinn, T.A., Kohl, P., 2013. Combining wet and dry research: experience with model development for cardiac mechano-electric structure-function studies. Cardiovascular Research 97, 601–611.

Ramanathan, C., Ghanem, R.N., Jia, P., Ryu, K., Rudy, Y., 2004. Noninvasive electrocardiographic imaging for cardiac electrophysiology and arrhythmia. Nature Medicine 10, 422–428.

Remme, C.A., 2013. Cardiac sodium channelopathy associated with SCN5A mutations: electrophysiological, molecular and genetic aspects. The Journal of Physiology 591, 4099–4116.

Remme, C.A., Wilde, A.A., 2014. Targeting sodium channels in cardiac arrhythmia. Current opinion in pharmacology 15, 53–60.

Remme, C.A., Wilde, A.A., Bezzina, C.R., 2008. Cardiac sodium channel overlap syndromes: different faces of SCN5A mutations. Trends in Cardiovascular Medicine 18, 78–87.

Reumann, M., Gurev, V., Rice, J.J., 2009. Computational modeling of cardiac disease: potential for personalized medicine. Personalized Medicine 6, 45–66.

Rivolta, I., Abriel, H., Tateyama, M., Liu, H., Memmi, M., Vardas, P., Napolitano, C., Priori, S.G., Kass, R.S., 2001. Inherited Brugada and long QT-3 syndrome mutations of a single residue of the cardiac sodium channel confer distinct channel and clinical phenotypes. Journal of Biological Chemistry 276, 30623–30630.

Rivolta, I., Clancy, C.E., Tateyama, M., Liu, H., Priori, S.G., Kass, R.S., 2002. A novel SCN5A mutation associated with long QT-3: altered inactivation kinetics and channel dysfunction. Physiological Genomics 10, 191–197.

Roden, D.M., 2008. Repolarization reserve; a moving target. Circulation 118, 981–982.

Roden, D.M., 2010. Brugada syndrome: Lots of questions, some answers. Heart Rhythm 7, 47–49.

Romero, L., Pueyo, E., Fink, M., Rodríguez, B., 2009. Impact of ionic current variability on human ventricular cellular electrophysiology. American Journal of Physiology – Heart and Circulatory Physiology 297, H1436–H1445.

Rook, M.B., Alshinawi, C.B., Groenewegen, W.A., van Gelder, I.C., van Ginneken, A.C., Jongsma, H.J., Mannens, M.M., Wilde, A.A., 1999. Human SCN5A gene mutations alter cardiac sodium channel kinetics and are associated with the Brugada syndrome. Cardiovascular Research 44, 507–517.

Rosenthal, J., Gilly, W.F., 1993. Amino acid sequence of a putative sodium channel expressed in the giant axon of the squid Loligo opalescens. Proceedings of the National Academy of Sciences

90, 10026–10030.

Rossenbacker, T., Carroll, S.J., Liu, H., Kuipéri, C., de Ravel, T.J., Devriendt, K., Carmeliet, P., Kass, R.S., Heidbüchel, H., 2004. Novel pore mutation in SCN5A manifests as a spectrum of phenotypes ranging from atrial flutter, conduction disease, and Brugada syndrome to sudden cardiac death. Heart Rhythm 1, 610–615.

Roux, B., Allen, T., Berneche, S., Im, W., 2004. Theoretical and computational models of biological ion channels. Quarterly Reviews of Biophysics 37, 15–103.

Ruan, Y., Denegri, M., Liu, N., Bachetti, T., Seregni, M., Morotti, S., Severi, S., Napolitano, C., Priori, S.G., 2010. Trafficking defects and gating abnormalities of a novel SCN5A mutation question gene-specific therapy in long QT syndrome type 3. Circulation Research 106, 1374–1383.

Ruan, Y., Liu, N., Bloise, R., Napolitano, C., Priori, S.G., 2007. Gating properties of SCN5A mutations and the response to mexiletine in long-QT syndrome type 3 patients. Circulation 116, 1137–1144.

Rudy, Y., Ackerman, M.J., Bers, D.M., Clancy, C.E., Houser, S.R., London, B., McCulloch, A.D., Przywara, D.A., Rasmusson, R.L., Solaro, R.J., et al., 2008. Systems approach to understanding electromechanical activity in the human heart a national heart, lung, and blood institute workshop summary. Circulation 118, 1202–1211.

Rudy, Y., Messinger-Rapport, B., 1987. The inverse problem in electrocardiography: solutions in terms of epicardial potentials. Critical Reviews in Biomedical Engineering 16, 215–268.

Rudy, Y., Silva, J.R., 2006. Computational biology in the study of cardiac ion channels and cell electrophysiology. Quarterly Reviews of Biophysics , 57–116.

Rush, S., Larsen, H., 1978. A practical algorithm for solving dynamic membrane equations. IEEE Transactions on Biomedical Engineering , 389–392.

Saber, S., Amarouch, M.Y., Fazelifar, A.F., Haghjoo, M., Emkanjoo, Z., Alizadeh, A., Houshmand, M., Gavrilenko, A.V., Abriel, H., Zaklyazminskaya, E.V., 2015. Complex genetic background in a large family with Brugada syndrome. Physiological Reports 3, e12256.

Saito, Y.A., Strege, P.R., Tester, D.J., Locke, G.R., Talley, N.J., Bernard, C.E., Rae, J.L., Makielski, J.C., Ackerman, M.J., Farrugia, G., 2009. Sodium channel mutation in irritable bowel syndrome: evidence for an ion channelopathy. American Journal of Physiology-Gastrointestinal and Liver Physiology 296, G211–G218.

Sakakibara, Y., Furukawa, T., Singer, D.H., Jia, H., Backer, C.L., Arentzen, C.E., Wasserstrom, J.A., 1993. Sodium current in isolated human ventricular myocytes. American Journal of Physiology 265, H1301–H1309.

Sakakibara, Y., Wasserstrom, J.A., Furukawa, T., Jia, H., Arentzen, C.E., Hartz, R.S., Singer, D.H., 1992. Characterization of the sodium current in single human atrial myocytes. Circulation Research 71, 535–546.

Samani, K., Wu, G., Ai, T., Shuraih, M., Mathuria, N.S., Li, Z., Sohma, Y., Purevjav, E., Xi, Y., Towbin, J.A., et al., 2009. A novel SCN5A mutation V1340I in Brugada syndrome augmenting arrhythmias during febrile illness. Heart Rhythm 6, 1318–1326.

Sampson, K.J., Iyer, V., Marks, A.R., Kass, R.S., 2010. A computational model of Purkinje fibre single cell electrophysiology: implications for the long QT syndrome. The Journal of Physiology 588, 2643–2655.

Sánchez, C., Bueno-Orovio, A., Wettwer, E., Loose, S., Simon, J., Ravens, U., Pueyo, E., Rodriguez, B., 2014. Inter-subject variability in human atrial action potential in sinus rhythm versus chronic atrial fibrillation. PLOS ONE 9, e105897.

Sarai, N., Matsuoka, S., Kuratomi, S., Ono, K., Noma, A., 2003. Role of individual ionic current systems in the SA node hypothesized by a model study. The Japanese Journal of Physiology 53, 125–134.

Sarhan, M.F., Van Petegem, F., Ahern, C.A., 2009. A double tyrosine motif in the cardiac sodium channel domain III-IV linker couples calcium-dependent calmodulin binding to inactivation gating. Journal of Biological Chemistry 284, 33265–33274.

Sarkar, A.X., Christini, D.J., Sobie, E.A., 2012. Exploiting mathematical models to illuminate electrophysiological variability between individuals. The Journal of Physiology 590, 2555–2567.

Sarkar, A.X., Sobie, E.A., 2010. Regression analysis for constraining free parameters in electrophysiological models of cardiac cells. PLOS Computational Biology 6, e1000914.

Sarkar, A.X., Sobie, E.A., 2011. Quantification of repolarization reserve to understand interpatient variability in the response to proarrhythmic drugs: a computational analysis. Heart Rhythm 8, 1749–1755.

Sato, D., Shiferaw, Y., Garfinkel, A., Weiss, J.N., Qu, Z., Karma, A., 2006. Spatially discordant alternans in cardiac tissue role of calcium cycling. Circulation Research 99, 520–527.

Sato, D., Xie, Y., Weiss, J.N., Qu, Z., Garfinkel, A., Sanderson, A.R., 2009. Acceleration of cardiac tissue simulation with graphic processing units. Medical & Biological Engineering & Computing 47, 1011–1015.

Saucerman, J.J., Bers, D.M., 2008. Calmodulin mediates differential sensitivity of CaMKII and calcineurin to local Ca2+ in cardiac myocytes. Biophysical Journal 95, 4597–4612.

Saucerman, J.J., Brunton, L.L., Michailova, A.P., McCulloch, A.D., 2003. Modeling β-adrenergic control of cardiac myocyte contractility in silico. Journal of Biological Chemistry 278, 47997–48003.

Saucerman, J.J., Healy, S.N., Belik, M.E., Puglisi, J.L., McCulloch, A.D., 2004. Proarrhythmic consequences of a kcnq1 akap-binding domain mutation computational models of whole cells and heterogeneous tissue. Circulation Research 95, 1216–1224.

Schmidt, C., Wiedmann, F., Zhou, X.B., Heijman, J., Voigt, N., Ratte, A., Lang, S., Kallenberger, S., Campana, C., Weymann, A., De Simone, R., Szabo, G., Ruhparwar, A., Kallenbach, K., Karck, M., Ehrlich, J.R., Baczkó, I., Borggrefe, M., Ravens, U., Dobrev, D., Katus, H.A., Dierk, T., 2017. Inverse remodeling of K2P3.1 K+ channel expression and action potential duration in left ventricular dysfunction and atrial fibrillation - implications for patient-specific antiarrhythmic drug therapy. European Heart Journal .

Schneider, M., Proebstle, T., Hombach, V., Hannekum, A., Rüdel, R., 1994. Characterization of

the sodium currents in isolated human cardiocytes. Pflügers Archiv 428, 84–90.

Schuetze, S.M., 1983. The discovery of the action potential. Trends in Neurosciences 6, 164–168.

Schulz, D.J., Goaillard, J.M., Marder, E., 2006. Variable channel expression in identified single and electrically coupled neurons in different animals. Nature Neuroscience 9, 356–362.

Schwartz, P.J., Priori, S.G., Dumaine, R., Napolitano, C., Antzelevitch, C., Stramba-Badiale, M., Richard, T.A., Berti, M.R., Bloise, R., 2000. A molecular link between the sudden infant death syndrome and the long-QT syndrome. New England Journal of Medicine 343, 262–267.

Seemann, G., Sachse, F.B., Weiß, D.L., Dössel, O., 2003. Quantitative reconstruction of cardiac electromechanics in human myocardium. Journal of Cardiovascular Electrophysiology 14, S219–S228.

Seyfarth, E.A., 2006. Julius Bernstein (1839–1917): pioneer neurobiologist and biophysicist. Biological Cybernetics 94, 2–8.

Shannon, T.R., Wang, F., Puglisi, J., Weber, C., Bers, D.M., 2004. A mathematical treatment of integrated Ca dynamics within the ventricular myocyte. Biophysical Journal 87, 3351–3371.

Sherman, A.J., Shrier, A., Cooper, E., 1999. Series resistance compensation for whole-cell patch-clamp studies using a membrane state estimator. Biophysical Journal 77, 2590–2601.

Sherman-Gold, R., Maertz, W.H., 2012. The Axon Guide for Electrophysiology & Biophysics: Laboratory Techniques. Molecular Devices.

Shinlapawittayatorn, K., Du, X.X., Liu, H., Ficker, E., Kaufman, E.S., Deschênes, I., 2011a. A common SCN5A polymorphism modulates the biophysical defects of SCN5A mutations. Heart Rhythm 8, 455–462.

Shinlapawittayatorn, K., Dudash, L.A., Du, X.X., Heller, L., Poelzing, S., Ficker, E., Deschênes, I., 2011b. A novel strategy using cardiac sodium channel polymorphic fragments to rescue trafficking-deficient SCN5A mutations. Circulation: Cardiovascular Genetics 4, 500–509.

Shirai, N., Makita, N., Sasaki, K., Yokoi, H., Sakuma, I., Sakurada, H., Akai, J., Kimura, A., Hiraoka, M., Kitabatake, A., 2002. A mutant cardiac sodium channel with multiple biophysical defects associated with overlapping clinical features of Brugada syndrome and cardiac conduction disease. Cardiovascular Research 53, 348–354.

Shuraih, M., Ai, T., Vatta, M., Sohma, Y., Merkle, E.M., Taylor, E., Li, Z., Xi, Y., Razavi, M., Towbin, J.A., et al., 2007. A common SCN5A variant alters the responsiveness of human sodium channels to class I antiarrhythmic agents. Journal of Cardiovascular Electrophysiology 18, 434–440.

Shy, D., Gillet, L., Ogrodnik, J., Albesa, M., Verkerk, A.O., Wolswinkel, R., Rougier, J.S., Barc, J., Essers, M.C., Syam, N., et al., 2014. PDZ domain–binding motif regulates cardiomyocyte compartment-specific NaV1.5 channel expression and function. Circulation 130, 147–160.

Sigworth, F., 1995. Electronic design of the patch clamp, in: Single-channel recording. Springer, pp. 95–127.

Silva, J.R., Pan, H., Wu, D., Nekouzadeh, A., Decker, K.F., Cui, J., Baker, N.A., Sept, D., Rudy,

Y., 2009. A multiscale model linking ion-channel molecular dynamics and electrostatics to the cardiac action potential. Proceedings of the National Academy of Sciences 106, 11102–11106.

Silva, J.R., Rudy, Y., 2010. Multi-scale electrophysiology modeling: from atom to organ. The Journal of General Physiology 135, 575–581.

Silverman, B.D., 2000. Three-dimensional moments of molecular property fields. Journal of chemical information and computer sciences 40, 1470–1476.

Simitev, R.D., Biktashev, V.N., 2006. Conditions for propagation and block of excitation in an asymptotic model of atrial tissue. Biophysical Journal 90, 2258–2269.

Simpson, R.J., 2003. Proteins and Proteomics: A Laboratory Manual. Cold Spring Harbor Laboratory Press, Cold Spring Harbor, NY, USA.

Six, I., Hermida, J.S., Huang, H., Gouas, L., Fressart, V., Benammar, N., Hainque, B., Denjoy, I., Chahine, M., Guicheney, P., 2008. The occurrence of Brugada syndrome and isolated cardiac conductive disease in the same family could be due to a single SCN5A mutation or to the accidental association of both diseases. Europace 10, 79–85.

Smith, N., Niederer, S., 2016. Is computational modeling adding value for understanding the heart? Journal of Molecular and Cellular Cardiology 96, 1.

Smits, J.P., Koopmann, T.T., Wilders, R., Veldkamp, M.W., Opthof, T., Bhuiyan, Z.A., Mannens, M.M., Balser, J.R., Tan, H.L., Bezzina, C.R., et al., 2005a. A mutation in the human cardiac sodium channel (E161K) contributes to sick sinus syndrome, conduction disease and Brugada syndrome in two families. Journal of Molecular and Cellular Cardiology 38, 969–981.

Smits, J.P., Veldkamp, M.W., Bezzina, C.R., Bhuiyan, Z.A., Wedekind, H., Schulze-Bahr, E., Wilde, A.A., 2005b. Substitution of a conserved alanine in the domain IIIS4–S5 linker of the cardiac sodium channel causes long QT syndrome. Cardiovascular Research 67, 459–466.

Soeller, C., Cannell, M., 1999. Examination of the transverse tubular system in living cardiac rat myocytes by 2-photon microscopy and digital image–processing techniques. Circulation Research 84, 266–275.

Sottas, V., Rougier, J.S., Jousset, F., Kucera, J.P., Shestak, A., Makarov, L.M., Zaklyazminskaya, E.V., Abriel, H., 2013. Characterization of 2 genetic variants of NaV1.5-Arginine 689 found in patients with cardiac arrhythmias. Journal of Cardiovascular Electrophysiology 24, 1037–1046.

Southern, J., Pitt-Francis, J., Whiteley, J., Stokeley, D., Kobashi, H., Nobes, R., Kadooka, Y., Gavaghan, D., 2008. Multi-scale computational modelling in biology and physiology. Progress in Biophysics and Molecular Biology 96, 60–89.

Splawski, I., Timothy, K.W., Tateyama, M., Clancy, C.E., Malhotra, A., Beggs, A.H., Cappuccio, F.P., Sagnella, G.A., Kass, R.S., Keating, M.T., 2002. Variant of SCN5A sodium channel implicated in risk of cardiac arrhythmia. Science 297, 1333–1336.

Stewart, P., Aslanidi, O.V., Noble, D., Noble, P.J., Boyett, M.R., Zhang, H., 2009. Mathematical models of the electrical action potential of Purkinje fibre cells. Philosophical Transactions of the Royal Society of London A: Mathematical, Physical and Engineering Sciences 367, 2225–2255.

Stoelzle, S., Obergrussberger, A., Bruggemann, A., Haarmann, C., George, M., Kettenhofen, R.F., Fertig, N., 2011. State-of-the-art automated patch clamp devices: Heat activation, action potentials and high throughput in ion channel screening. Frontiers in Pharmacology 2.

Stone, J.E., Gohara, D., Shi, G., 2010. OpenCL: A parallel programming standard for heterogeneous computing systems. Computing in Science & Engineering 12, 66.

Sugiura, S., Washio, T., Hatano, A., Okada, J., Watanabe, H., Hisada, T., 2012. Multi-scale simulations of cardiac electrophysiology and mechanics using the university of tokyo heart simulator. Progress in Biophysics and Molecular Biology 110, 380–389.

Surber, R., Hensellek, S., Prochnau, D., Werner, G.S., Benndorf, K., Figulla, H.R., Zimmer, T., 2008. Combination of cardiac conduction disease and long QT syndrome caused by mutation T1620K in the cardiac sodium channel. Cardiovascular Research 77, 740–748.

Swan, H., Amarouch, M.Y., Leinonen, J., Marjamaa, A., Kucera, J.P., Laitinen-Forsblom, P.J., Lahtinen, A.M., Palotie, A., Kontula, K., Toivonen, L., et al., 2014. A gain-of-function mutation of the SCN5A gene causes exercise-induced polymorphic ventricular arrhythmias. Circulation: Cardiovascular Genetics 7, 771–781.

Taggart, P., Sutton, P.M., Opthof, T., Coronel, R., Trimlett, R., Pugsley, W., Kallis, P., 2000. Inhomogeneous transmural conduction during early ischaemia in patients with coronary artery disease. Journal of Molecular and Cellular Cardiology 32, 621–630.

Tan, B.H., Valdivia, C.R., Rok, B.A., Ye, B., Ruwaldt, K.M., Tester, D.J., Ackerman, M.J., Makielski, J.C., 2005. Common human SCN5A polymorphisms have altered electrophysiology when expressed in PQ1077 splice variants. Heart Rhythm 2, 741–747.

Tan, B.H., Valdivia, C.R., Song, C., Makielski, J.C., 2006. Partial expression defect for the SCN5A missense mutation G1406R depends on splice variant background Q1077 and rescue by mexiletine. American Journal of Physiology – Heart and Circulatory Physiology 291, H1822–H1828.

Tan, H.L., Bink-Boelkens, M.T., Bezzina, C.R., Viswanathan, P.C., Beaufort-Krol, G.C., van Tintelen, P.J., van den Berg, M.P., Wilde, A.A., Balser, J.R., 2001. A sodium-channel mutation causes isolated cardiac conduction disease. Nature 409, 1043–1047.

Tan, H.L., Kupershmidt, S., Zhang, R., Stepanovic, S., Roden, D.M., Wilde, A.A., Anderson, M.E., Balser, J.R., 2002. A calcium sensor in the sodium channel modulates cardiac excitability. Nature 415, 442–447.

Tarradas, A., Selga, E., Beltran-Alvarez, P., Pérez-Serra, A., Riuró, H., Picó, F., Iglesias, A., Campuzano, O., Castro-Urda, V., Fernández-Lozano, I., et al., 2013. A novel missense mutation, I890T, in the pore region of cardiac sodium channel causes Brugada syndrome. PLOS ONE 8, e53220.

Tateyama, M., Kurokawa, J., Terrenoire, C., Rivolta, I., Kass, R., 2003. Stimulation of protein kinase C inhibits bursting in disease-linked mutant human cardiac sodium channels. Circulation 107, 3216–3222.

Ten Tusscher, K., Panfilov, A.V., 2003. Reentry in heterogeneous cardiac tissue described by the luo-rudy ventricular action potential model. American Journal of Physiology – Heart and

Circulatory Physiology 284, H542–H548.

Tester, D.J., Valdivia, C., Harris-Kerr, C., Alders, M., Salisbury, B.A., Wilde, A.A., Makielski, J.C., Ackerman, M.J., 2010. Epidemiologic, molecular, and functional evidence suggest A572D-SCN5A should not be considered an independent LQT3-susceptibility mutation. Heart Rhythm 7, 912–919.

Tibshirani, R., 1996. Regression shrinkage and selection via the lasso. Journal of the Royal Statistical Society. Series B (Methodological) , 267–288.

Tran, D.X., Sato, D., Yochelis, A., Weiss, J.N., Garfinkel, A., Qu, Z., 2009. Bifurcation and chaos in a model of cardiac early afterdepolarizations. Physical Review Letters 102, 258103.

Tsurugi, T., Nagatomo, T., Abe, H., Oginosawa, Y., Takemasa, H., Kohno, R., Makita, N., Makielski, J.C., Otsuji, Y., 2009. Differential modulation of late sodium current by protein kinase A in R1623Q mutant of LQT3. Life Sciences 84, 380–387.

ten Tusscher, K., Noble, D., Noble, P., Panfilov, A., 2004. A model for human ventricular tissue. American Journal of Physiology – Heart and Circulatory Physiology 286, H1573–H1589.

ten Tusscher, K.H., Panfilov, A.V., 2006. Alternans and spiral breakup in a human ventricular tissue model. American Journal of Physiology – Heart and Circulatory Physiology 291, H1088–H1100.

Valdivia, C.R., Ackerman, M.J., Tester, D.J., Wada, T., McCormack, J., Ye, B., Makielski, J.C., 2002. A novel SCN5A arrhythmia mutation, M1766L, with expression defect rescued by mexiletine. Cardiovascular Research 55, 279–289.

Valdivia, C.R., Tester, D.J., Rok, B.A., Munger, T.M., Jahangir, A., Makielski, J.C., Ackerman, M.J., 2004. A trafficking defective, Brugada syndrome-causing SCN5A mutation rescued by drugs. Cardiovascular Research 62, 53–62.

Vandenberg, J.I., Perry, M.D., Perrin, M.J., Mann, S.A., Ke, Y., Hill, A.P., 2012. hERG K+ channels: structure, function, and clinical significance. Physiological Reviews 92, 1393–1478.

Vandersickel, N., de Boer, T., Vos, M.A., Panfilov, A.V., 2016. Perpetuation of Torsade de Pointes in heterogeneous hearts: competing foci or re-entry? The Journal of Physiology .

Vatta, M., Dumaine, R., Antzelevitch, C., Brugada, R., Li, H., Bowles, N.E., Nademanee, K., Brugada, J., Brugada, P., Towbin, J.A., 2002a. Novel mutations in domain I of SCN5A cause Brugada syndrome. Molecular Genetics and Metabolism 75, 317–324.

Vatta, M., Dumaine, R., Varghese, G., Richard, T.A., Shimizu, W., Aihara, N., Nademanee, K., Brugada, R., Brugada, J., Veerakul, G., et al., 2002b. Genetic and biophysical basis of sudden unexplained nocturnal death syndrome (SUNDS), a disease allelic to Brugada syndrome. Human Molecular Genetics 11, 337–345.

Verkhratsky, A., Krishtal, O., Petersen, O.H., 2006. From Galvani to patch clamp: the development of electrophysiology. Pflügers Archiv 453, 233–247.

Vigmond, E.J., Hughes, M., Plank, G., Leon, L.J., 2003. Computational tools for modeling electrical activity in cardiac tissue. Journal of Electrocardiology 36, 69–74.

Viswanathan, P.C., Benson, D.W., Balser, J.R., 2003. A common SCN5A polymorphism modulates

the biophysical effects of an SCN5A mutation. The Journal of Clinical Investigation 111, 341–346.

Voigt, N., Heijman, J., Wang, Q., Chiang, D.Y., Li, N., Karck, M., Wehrens, X.H., Nattel, S., Dobrev, D., 2014. Cellular and molecular mechanisms of atrial arrhythmogenesis in patients with paroxysmal atrial fibrillation. Circulation 129, 145–156.

Volders, P.G., Sipido, K.R., Vos, M.A., Kulcsár, A., Verduyn, S.C., Wellens, H.J., 1998. Cellular basis of biventricular hypertrophy and arrhythmogenesis in dogs with chronic complete atrioventricular block and acquired torsade de pointes. Circulation 98, 1136–1147.

Volders, P.G., Stengl, M., van Opstal, J.M., Gerlach, U., Spätjens, R.L., Beekman, J.D., Sipido, K.R., Vos, M.A., 2003. Probing the contribution of IKs to canine ventricular repolarization key role for β-adrenergic receptor stimulation. Circulation 107, 2753–2760.

Walch, O.J., Eisenberg, M.C., 2015. Parameter identifiability and identifiable combinations in generalized Hodgkin-Huxley models. arXiv preprint arXiv:1511.05227 .

Wallman, M., Smith, N.P., Rodriguez, B., 2012. A comparative study of graph-based, eikonal, and monodomain simulations for the estimation of cardiac activation times. IEEE Transactions on Biomedical Engineering 59, 1739–1748.

Walmsley, J., 2013. Incorporating inter-sample variability into cardiac electrophysiology simulations. Ph.D. thesis. University of Oxford.

Walmsley, J., Rodriguez, J.F., Mirams, G.R., Burrage, K., Efimov, I.R., Rodriguez, B., 2013. mRNA expression levels in failing human hearts predict cellular electrophysiological remodeling: a population-based simulation study. PLOS ONE 8, e56359.

Walsh, R., Peters, N.S., Cook, S.A., Ware, J.S., 2014. Paralogue annotation identifies novel pathogenic variants in patients with Brugada syndrome and catecholaminergic polymorphic ventricular tachycardia. Journal of Medical Genetics 51, 35–44.

Waltemath, D., Adams, R., Beard, D.A., Bergmann, F.T., Bhalla, U.S., Chelliah, V., Cooling, M.T., Cooper, J., Crampin, E.J., Garny, A., et al., 2011a. Minimum information about a simulation experiment (MIASE). PLOS Computational Biology 7, e1001122_1–e1001122_4.

Waltemath, D., Adams, R., Bergmann, F.T., Hucka, M., Kolpakov, F., Miller, A.K., Moraru, I.I., Nickerson, D., Sahle, S., Snoep, J.L., et al., 2011b. Reproducible computational biology experiments with SED-ML-the simulation experiment description markup language. BMC Systems Biology 5, 198.

Wan, X., Chen, S., Sadeghpour, A., Wang, Q., Kirsch, G.E., 2001a. Accelerated inactivation in a mutant Na+ channel associated with idiopathic ventricular fibrillation. American Journal of Physiology – Heart and Circulatory Physiology 280, H354–H360.

Wan, X., Chen, S., Sadeghpour, A., Wang, Q., Kirsch, G.E., 2001b. Accelerated inactivation in a mutant Na+ channel associated with idiopathic ventricular fibrillation. American Journal of Physiology – Heart and Circulatory Physiology 280, H354–H360.

Wan, X., Wang, Q., Kirsch, G.E., 2000. Functional suppression of sodium channels by β1-subunits as a molecular mechanism of idiopathic ventricular fibrillation. Journal of Molecular and Cellular Cardiology 32, 1873–1884.

Wang, C., Wang, C., Hoch, E.G., Pitt, G.S., 2011. Identification of novel interaction sites that determine specificity between fibroblast growth factor homologous factors and voltage-gated sodium channels. Journal of Biological Chemistry 286, 24253–24263.

Wang, D.W., Crotti, L., Shimizu, W., Pedrazzini, M., Cantu, F., De Filippo, P., Kishiki, K., Miyazaki, A., Ikeda, T., Schwartz, P.J., et al., 2008. Malignant perinatal variant of long-QT syndrome caused by a profoundly dysfunctional cardiac sodium channel. Circulation: Arrhythmia and Electrophysiology 1, 370–378.

Wang, D.W., Desai, R.R., Crotti, L., Arnestad, M., Insolia, R., Pedrazzini, M., Ferrandi, C., Vege, A., Rognum, T., Schwartz, P.J., et al., 2007a. Cardiac sodium channel dysfunction in sudden infant death syndrome. Circulation 115, 368–376.

Wang, D.W., Makita, N., Kitabatake, A., Balser, J.R., George, A.L., 2000. Enhanced Na+ channel intermediate inactivation in Brugada syndrome. Circulation Research 87, e37–e43.

Wang, D.W., Viswanathan, P.C., Balser, J.R., George, A.L., Benson, D.W., 2002. Clinical, genetic, and biophysical characterization of SCN5A mutations associated with atrioventricular conduction block. Circulation 105, 341–346.

Wang, D.W., Yazawa, K., George, A.L., Bennett, P.B., 1996. Characterization of human cardiac Na+ channel mutations in the congenital long QT syndrome. Proceedings of the National Academy of Sciences 93, 13200–13205.

Wang, H.G., Zhu, W., Kanter, R.J., Silva, J.R., Honeywell, C., Gow, R.M., Pitt, G.S., 2016. A novel NaV1.5 voltage sensor mutation associated with severe atrial and ventricular arrhythmias. Journal of Molecular and Cellular Cardiology 92, 52–62.

Wang, L., Meng, X., Yuchi, Z., Zhao, Z., Xu, D., Fedida, D., Wang, Z., Huang, C., 2015. De novo mutation in the SCN5A gene associated with Brugada syndrome. Cellular Physiology and Biochemistry 36, 2250–2262.

Wang, L., Zhang, H., Wong, K.C., Liu, H., Shi, P., 2010. Physiological-model-constrained noninvasive reconstruction of volumetric myocardial transmembrane potentials. IEEE Transactions on Biomedical Engineering 57, 296–315.

Wang, L.J., Sobie, E.A., 2008. Mathematical model of the neonatal mouse ventricular action potential. American Journal of Physiology – Heart and Circulatory Physiology 294, H2565–H2575.

Wang, Q., Chen, S., Chen, Q., Wan, X., Shen, J., Hoeltge, G., Timur, A., Keating, M., Kirsch, G., 2004. The common SCN5A mutation R1193Q causes LQTS-type electrophysiological alterations of the cardiac sodium channel. Journal of Medical Genetics 41, e66–e66.

Wang, S.Y., Tikhonov, D.B., Mitchell, J., Zhorov, B., Wang, G.K., 2007b. Irreversible block of cardiac mutant Na+ channels by batrachotoxin. Channels 1, 179–188.

Watanabe, H., Nogami, A., Ohkubo, K., Kawata, H., Hayashi, Y., Ishikawa, T., Makiyama, T., Nagao, S., Yagihara, N., Takehara, N., et al., 2011a. Electrocardiographic characteristics and SCN5A mutations in idiopathic ventricular fibrillation associated with early repolarization. Circulation: Arrhythmia and Electrophysiology 4, 874–881.

Watanabe, H., Yang, T., Stroud, D.M., Lowe, J.S., Harris, L., Atack, T.C., Wang, D.W., Hipkens, S.B., Leake, B., Hall, L., et al., 2011b. Striking in vivo phenotype of a disease-associated human SCN5A mutation producing minimal changes in vitro. Circulation 124, 1001–1011.

Watanabe, H., Yang, T., Stroud, D.M., Lowe, J.S., Harris, L., Atack, T.C., Wang, D.W., Hipkens, S.B., Leake, B., Hall, L., et al., 2011c. Striking in vivo phenotype of a disease-associated human SCN5A mutation producing minimal changes in vitro. Circulation 124, 1001–1011.

Wedekind, H., Smits, J.P., Schulze-Bahr, E., Arnold, R., Veldkamp, M.W., Bajanowski, T., Borggrefe, M., Brinkmann, B., Warnecke, I., Funke, H., et al., 2001. De novo mutation in the SCN5A gene associated with early onset of sudden infant death. Circulation 104, 1158–1164.

Wehrens, X., Abriel, H., Cabo, C., Benhorin, J., Kass, R., 2000. Arrhythmogenic mechanism of an lqt-3 mutation of the human heart na+ channel α-subunit a computational analysis. Circulation 102, 584–590.

Wehrens, X.H., Rossenbacker, T., Jongbloed, R.J., Gewillig, M., Heidbüchel, H., Doevendans, P.A., Vos, M.A., Wellens, H.J., Kass, R.S., 2003. A novel mutation L619F in the cardiac Na+ channel SCN5A associated with long-QT syndrome (LQT3): a role for the I-II linker in inactivation gating. Human Mutation 21, 552–552.

Wei, J., Wang, D.W., Alings, M., Fish, F., Wathen, M., Roden, D.M., George, A.L., 1999. Congenital long-QT syndrome caused by a novel mutation in a conserved acidic domain of the cardiac Na+ channel. Circulation 99, 3165–3171.

Weiss, J.N., Garfinkel, A., Karagueuzian, H.S., Nguyen, T.P., Olcese, R., Chen, P.S., Qu, Z., 2015. Perspective: A dynamics-based classification of ventricular arrhythmias. Journal of Molecular and Cellular Cardiology 82, 136–152.

Weiss, J.N., Karma, A., MacLellan, W.R., Deng, M., Rau, C.D., Rees, C.M., Wang, J., Wisniewski, N., Eskin, E., Horvath, S., Qu, Z., Wang, Y., Lusis, A.J., 2012. "Good enough solutions" and the genetics of complex diseases. Circulation Research 111, 493–504.

Wellens, H.J., Vermeulen, A., Durrer, D., 1972. Ventricular fibrillation occurring on arousal from sleep by auditory stimuli. Circulation 46, 661–665.

Welsh, A.J., Greco, E.F., Fenton, F.H., 2017. Dynamics of a human spiral wave. Physics Today 70, 78–79.

WHO, 2016. Cardiovascular diseases [internet]. www.who.int/cardiovascular_diseases/en. Accessed: 2016-06-03.

Wilde, A.A., Brugada, R., 2011. Phenotypical manifestations of mutations in the genes encoding subunits of the cardiac sodium channel. Circulation Research 108, 884–897.

Wilhelms, M., 2013. Multiscale modeling of cardiac electrophysiology: adaptation to atrial and ventricular rhythm disorders and pharmacological treatment. KIT Scientific Publishing.

Willms, A.R., Baro, D.J., Harris-Warrick, R.M., Guckenheimer, J., 1999. An improved parameter estimation method for Hodgkin-Huxley models. Journal of Computational Neuroscience 6, 145–168.

Wimalaratne, S.M., Halstead, M.D., Lloyd, C.M., Cooling, M.T., Crampin, E.J., Nielsen, P., 2009. A method for visualizing CellML models. Bioinformatics 25, 3012–3019.

Winkel, B.G., Larsen, M.K., Berge, K.E., Leren, T.P., Nissen, P.H., Olesen, M.S., Hollegaard, M.V., Jespersen, T., Yuan, L., Nielsen, N., et al., 2012. The prevalence of mutations in KCNQ1, KCNH2, and SCN5A in an unselected national cohort of young sudden unexplained death cases. Journal of Cardiovascular Electrophysiology 23, 1092–1098.

Yan, G.X., Antzelevitch, C., 1999. Cellular basis for the Brugada syndrome and other mechanisms of arrhythmogenesis associated with ST-segment elevation. Circulation 100, 1660–1666.

Yang, P., Kanki, H., Drolet, B., Yang, T., Wei, J., Viswanathan, P.C., Hohnloser, S.H., Shimizu, W., Schwartz, P.J., Stanton, M., et al., 2002. Allelic variants in long-QT disease genes in patients with drug-associated torsades de pointes. Circulation 105, 1943–1948.

Ye, B., Valdivia, C.R., Ackerman, M.J., Makielski, J.C., 2003. A common human SCN5A polymorphism modifies expression of an arrhythmia causing mutation. Physiological Genomics 12, 187–193.

Yokoi, H., Makita, N., Sasaki, K., Takagi, Y., Okumura, Y., Nishino, T., Makiyama, T., Kitabatake, A., Horie, M., Watanabe, I., et al., 2005. Double SCN5A mutation underlying asymptomatic Brugada syndrome. Heart Rhythm 2, 285–292.

Yong, S.L., Ni, Y., Zhang, T., Tester, D.J., Ackerman, M.J., Wang, Q.K., 2007. Characterization of the cardiac sodium channel SCN5A mutation, N1325S, in single murine ventricular myocytes. Biochemical and Biophysical Research Communications 352, 378–383.

Young, K.A., Caldwell, J.H., 2005. Modulation of skeletal and cardiac voltage-gated sodium channels by calmodulin. The Journal of Physiology 565, 349–370.

Yu, T., Lloyd, C.M., Nickerson, D.P., Cooling, M.T., Miller, A.K., Garny, A., Terkildsen, J.R., Lawson, J., Britten, R.D., Hunter, P.J., et al., 2011. The Physiome model repository 2. Bioinformatics 27, 743–744.

Zeng, Z., Zhou, J., Hou, Y., Liang, X., Zhang, Z., Xu, X., Xie, Q., Li, W., Huang, Z., 2013. Electrophysiological characteristics of a SCN5A voltage sensors mutation R1629Q associated with Brugada syndrome. PLOS ONE 8, e78382.

Zhang, J., Chen, Y., Yang, J., Xu, B., Wen, Y., Xiang, G., Wei, G., Zhu, C., Xing, Y., Li, Y., 2015. Electrophysiological and trafficking defects of the SCN5A T353I mutation in Brugada syndrome are rescued by alpha-allocryptopine. European Journal of Pharmacology 746, 333–343.

Zhang, Y., Wang, T., Ma, A., Zhou, X., Gui, J., Wan, H., Shi, R., Huang, C., Grace, A., Huang, C.H., et al., 2008. Correlations between clinical and physiological consequences of the novel mutation R878C in a highly conserved pore residue in the cardiac Na+ channel. Acta Physiologica 194, 311–323.

Zimmer, T., Surber, R., 2008. SCN5A channelopathies – an update on mutations and mechanisms. Progress in Biophysics and Molecular Biology 98, 120–136.